

**PHYSICS BEYOND THE STANDARD MODEL:  
SUPERSYMMETRY, DARK MATTER, AND LHC  
PHENOMENOLOGY**

**BY ROUVEN ESSIG**

A dissertation submitted to the  
Graduate School—New Brunswick  
Rutgers, The State University of New Jersey  
in partial fulfillment of the requirements  
for the degree of  
Doctor of Philosophy  
Graduate Program in Physics and Astronomy

Written under the direction of

Professor Scott Thomas

and approved by

---

---

---

---

---

New Brunswick, New Jersey

October, 2008

## ABSTRACT OF THE DISSERTATION

# Physics Beyond the Standard Model: Supersymmetry, Dark Matter, and LHC Phenomenology

by Rouven Essig

Dissertation Director: Professor Scott Thomas

The Standard Model (SM) of particle physics is remarkably successful and has survived two decades of precision tests at high energy particle accelerators. However, it is known to be incomplete, and there are reasons to believe that there is new physics at energy scales that will soon be probed in greater detail than ever before by the Large Hadron Collider (LHC), a proton-proton accelerator being built near Geneva.

This thesis contains a diverse set of topics that may broadly be described as physics beyond the SM.

In Chapter 2, implications of current experimental constraints are presented for the stop masses and mixing in the Minimal Supersymmetric Standard Model (MSSM), a well-motivated candidate for physics beyond the SM. It is found, for example, that lower bounds on the stop masses are as large as 1 TeV assuming no stop-mixing.

Chapter 3 presents the regions in the MSSM with the minimal amount of fine-tuning of electroweak symmetry breaking. The minimal amount of tuning increases enormously for a Higgs mass beyond 120 GeV.

Supersymmetry cannot be an exact symmetry, and one possibility is that our Universe is in a long-lived metastable state with broken supersymmetry. In Chapter 4, a generic model with this property is constructed in which all the relevant parameters, including the supersymmetry breaking scale, are generated dynamically. This model has several interesting model-building features including an explicitly and spontaneously broken R-symmetry, a singlet, a large global symmetry, naturalness, renormalizability, and a “pseudo-runaway” direction.

In Chapter 5, a simple extension of the SM with weakly interacting non-chiral dark matter particles is presented. Such particles can be detected at a future direct-detection experiment.

There are a wide variety of possible discovery signatures for new physics at the LHC. A discovery signature with a large SM background that has not been well studied involves multi-jet events without leptons and/or missing energy. In Chapter 6, it is found that using innovative search strategies pair production of new coloured adjoint fermions producing a pure six-jet final state can be detected up to a mass of about 650-700 GeV with  $10 \text{ fb}^{-1}$  of integrated luminosity.

## Acknowledgements

There are many people who have helped me over the years either professionally, or personally, or both.

I do not know if I would have tried to follow a career in physics if my high school physics teacher, Mr. Gerhold, would not have introduced me to physics and shown me how exciting a field it is. Without him I may very well have followed a different path, and so I thank him for his infectious enthusiasm.

During my undergraduate years at Wits University in Johannesburg, I had the good fortune to meet Professor Robert de Mello-Koch. Robert is a shining light in the field of theoretical physics in South Africa and has been very inspirational to me. I thank him for guiding me in my first few years as an aspiring physicist.

By coming to the USA and to Rutgers on a Fulbright scholarship, I have received all the opportunities that I ever could have asked for. I thank the Fulbright commission in South Africa for giving me the scholarship, the University of the Witwatersrand for giving me an overseas scholarship, and the Rutgers Physics Department and the New High Energy Theory Center for their support throughout.

The person that is most responsible for helping me make use of these opportunities is my advisor Scott Thomas. Scott has taught me an immense amount of physics. He not only guided me on all the topics in my thesis, but like any good advisor also pushed me to become an independent researcher. His door was always open, and he was always happy to answer my many physics questions. I very much appreciate his genuine love for the subject, and I sincerely thank him for his advise and guidance.

Among the other faculty at Rutgers I would like to thank in particular Professors Tom

Banks, Michael Douglas, Daniel Friedan, Eva Halkiadakis, Jack Hughes, Amit Lath, Ronald Ransome, and Matthew Strassler. It is a true privilege to have such great faculty to turn to for help and advise.

All the staff in the Rutgers physics department have always been very helpful, but Diane Soyak deserves a special mention. Diane is a wonderfully warm person and has gone out of her way to help me with a million different things. Thank you.

During the first few days after I first arrived in the USA, my host family Olwen and Theo van Es made sure I did not have to sleep out on the streets, and I really value their warmth and hospitality.

I am grateful to the support of the many friends that I have made over the last few years among my fellow graduate students, past and present, including Evgeny Andriyash, Arvind Ayyer, Eleonora Dell'Aquila, Sourabh Dube, Carl-Johan Eklund, Alberto Garcia - Raboso, Rafael Greenblatt, Gareth Hughes, José Juknevich, Sam Klevtsov, Tim Koeth, Sergio Lukic, Dmitry Melnikov, Haile Owusu, Sridhar Ramanujam, Naseem Rangwala, Brian Vancil, Aaron Warren, Jessica Warren, and Iskander Ziyatdinov. I am especially grateful to my fellow graduate student and collaborators Jean-François Fortin, Kuver Sinha, Gonzalo Torroba, and Korneel van den Broek. I have learned so much from you, and I hope you realize just how valuable your support has been to me over the last few years.

I also had the good fortune of having several friends outside the Rutgers physics department. In particular I would like to thank my long-time friends from South Africa, Michael Abbott, Grant Anderson, Sonja Currie, Mark Dalton, George Konidaris, Greg Lewis, Iris Oren, and Gene Phillips, as well as the people at 10 Handy Street who gave me a home away from home during the first few years in the USA. I especially want to thank my good friends Searle Silverman and Robin Phillips for always being there when I needed them.

Finally, and most importantly, I thank my two sisters, Sandra and Diana, and especially both my parents and Neelima, for their continued love and support, and for always believing in me. I'm not sure I could have done this without them.

## Dedication

*For*

*Mom,*

*Dad,*

*&*

*Neelima*

# Table of Contents

<b>Abstract</b> . . . . .	ii
<b>Acknowledgements</b> . . . . .	iv
<b>Dedication</b> . . . . .	vi
<b>List of Tables</b> . . . . .	x
<b>List of Figures</b> . . . . .	xii
<b>1. Introduction</b> . . . . .	1
<b>References</b> . . . . .	12
<b>2. Implications of the CERN LEP Higgs Bounds for the MSSM Stop Sector</b> .	13
2.1. Introduction . . . . .	13
2.2. LEP constraints on the Higgs sector and implications for the MSSM stop sector .	15
2.3. Lower bounds on the stop masses . . . . .	20
2.4. Implications of new physics constraints for the lower bounds on the stop masses .	37
2.5. Implications for Electroweak Symmetry Breaking . . . . .	46
2.6. Conclusions . . . . .	50
2.7. Appendix: Mixing in the Two Doublet Higgs Sector . . . . .	53
2.8. Appendix: Quasi-Fixed Point for the Stop Trilinear Coupling $A_t$ . . . . .	56
<b>References</b> . . . . .	59
<b>3. The Minimally Tuned Minimal Supersymmetric Standard Model</b> . . . . .	63
3.1. Introduction . . . . .	63

3.2. Electroweak Symmetry Breaking . . . . .	66
3.3. The Tuning Measure . . . . .	70
3.4. Minimal Model Independent Tuning . . . . .	72
3.5. Minimal Fine-Tuning as a Function of the Higgs Mass . . . . .	86
3.6. Conclusions . . . . .	91
3.7. Appendix: Semi-numerical Solutions of the MSSM One-Loop RG-Equations . . . . .	93
3.8. Appendix: Fine-tuning Components . . . . .	98
<b>References . . . . .</b>	<b>100</b>
<b>4. Meta-Stable Dynamical Supersymmetry Breaking Near Points of Enhanced Symmetry . . . . .</b>	<b>104</b>
4.1. Introduction . . . . .	104
4.2. The Model and its Supersymmetric Vacua . . . . .	106
4.3. Metastability near enhanced symmetry points . . . . .	112
4.4. Particle Spectrum and R-symmetry . . . . .	121
4.5. Meta-Stability Near Generic Points of Enhanced Symmetry . . . . .	125
4.6. Conclusions . . . . .	128
<b>References . . . . .</b>	<b>130</b>
<b>5. Direct Detection of Non-Chiral Dark Matter . . . . .</b>	<b>133</b>
5.1. Introduction . . . . .	133
5.2. Chiral Electroweak Dark Matter . . . . .	135
5.3. Non-Chiral Dark Matter . . . . .	137
5.4. Higgs contribution to the Direct Detection Cross-Section and Singlet Dark Matter . . . . .	152
5.5. Conclusions . . . . .	156
<b>References . . . . .</b>	<b>158</b>

<b>6. Extracting Hadronic Resonances using Jet Ensemble Correlations . . . . .</b>	<b>161</b>
6.1. Introduction . . . . .	162
6.2. Simulation Tools and Overview of Analysis . . . . .	164
6.3. Analysis and Results . . . . .	169
6.4. Conclusions . . . . .	186
6.5. Appendix: Comparison of the PGS 4 and CMSSW detector simulations . . . . .	187
6.6. Appendix: Other Kinematic Correlations . . . . .	191
6.7. Appendix: Three-Jet Resonance Figures . . . . .	193
<b>References . . . . .</b>	<b>204</b>
<b>Vita . . . . .</b>	<b>205</b>

## List of Tables

2.1. Minimum allowed values of the combination $(m_{\tilde{t}_L}^2 + m_{\tilde{t}_R}^2 +  A_t ^2)^{1/2}$ consistent with a physical Higgs boson mass of $m_h \geq 114.4$ GeV in the Higgs decoupling limit for large $\tan \beta$ , taking into account only the LEP Higgs sector bounds. The minimum allowed values increase with decreasing $\tan \beta$ . . . . .	48
3.1. Low-scale values for the stop soft trilinear coupling, the average of the left- and right-handed stop soft masses and the two physical stop masses. These low scale values give the minimal fine-tuning for arbitrary messenger scales. . . . .	77
6.1. Lorentz and gauge invariant color flow restrictions on resonant and two-body production and decay modes to quarks and gluons of fermion and scalar triplet, quix, and octet representations transforming as $\mathbf{3}$ or $\bar{\mathbf{3}}$ , $\mathbf{6}$ or $\bar{\mathbf{6}}$ , or $\mathbf{8}$ under $SU(3)_C$ , respectively. Shown in parenthesis are the possible resonances. . . . .	163
6.2. Data samples generated, their cross-sections, number of events in sample, and integrated luminosity. The cross-sections include a 5 GeV cut on the jets within PYTHIA, and assume $ \eta  < 3.0$ . . . . .	169
6.3. High level triggers and event selection on $p_T$ ordered jets. For the high level triggers see the CMS TDR [12, 13]. . . . .	170
6.4. $\sigma(pp \rightarrow X \rightarrow 6j)$ cross sections in pb for adjoint Majorana fermion pair production, top quark pair production and QCD, $X = \{QQ, t\bar{t}, \text{QCD}\}$ , with the triggers and event selection given in Table 6.3, and with additional $\sum_{j=1}^6 p_{T,j}$ and $p_{T,6}$ cuts on the $p_T$ ordered jets. . . . .	173

6.5.	Correct matching probability fraction of $p_T$ ordered reconstructed jet triplets to the parton level $Q \rightarrow qqq, \overline{qqq}$ resonance for $m_Q = 290$ GeV as obtained from Monte Carlo information. The probability fractions and the ordering of the reconstructed jet triplets remain roughly unchanged for different $m_Q$ . Note that the table only shows the jet triplets that can be made up from the six hardest jet. The 11 best jet-triplets are found among triplets consisting only of the six hardest jets. . . . .	177
6.6.	Shown are the various kinematic and diagonal cuts used in the analysis for different values of $m_Q$ . Also shown is the “Diagonal Cut Yield on 16-Ensemble”, for the signal ( $QQ$ ) and the pure QCD background, which is the number of jet-triplets (out of a maximum of 16) from each event that on average pass all the cuts (including the diagonal cut). The ratio $S_{16}^{\text{res}}/B_{16}^{\text{res}}$ is the number of jet-triplets from the signal that are within the resonance peak after all the cuts, divided by the corresponding number for the pure QCD background. The significance given by $S_{16}^{\text{res}}/\sqrt{B_{16}^{\text{res}}}$ for integrated luminosities $\mathcal{L} = 0.1, 1, \text{ and } 10 \text{ fb}^{-1}$ , respectively, are also given in the table. All numbers are obtained from averaging 1000 pseudo-experiments. . . . .	185

## List of Figures

2.1. Minimum stop soft masses, $m_{\tilde{t}} \equiv m_{\tilde{t}_L} = m_{\tilde{t}_R}$ , for $m_h \geq 114.4$ GeV as a function of $\tan\beta$ for stop mixing $X_t/m_{\tilde{t}} = 0, \pm 1, \pm 2$ . All squark, slepton, and gaugino soft masses are equal to the stop soft masses, $\mu = 200$ GeV, $m_A = 1000$ GeV, $m_t = 173$ GeV, and all soft trilinear couplings are equal to $A_t = X_t + \mu \cot\beta$ . . . . .	25
2.2. Minimum physical stop masses, $m_{\tilde{t}_1}$ and $m_{\tilde{t}_2}$ , for $m_h \geq 114.4$ GeV as a function of $\tan\beta$ for vanishing stop mixing ( $X_t = 0$ ) and natural maximal stop mixing ( $X_t/m_{\tilde{t}} = -2$ ). Other parameters are as given in Fig. 2.1. . . . .	26
2.3. Minimum stop soft masses, $m_{\tilde{t}} \equiv m_{\tilde{t}_L} = m_{\tilde{t}_R}$ , for $m_h \geq 114.4$ GeV as a function of $\tan\beta$ for vanishing stop mixing ( $X_t = 0$ ) for a top quark mass of $m_t = 168, 173, 178$ GeV. Other parameters are as given in Fig. 2.1. . . . .	26
2.4. Minimum stop soft masses, $m_{\tilde{t}} \equiv m_{\tilde{t}_L} = m_{\tilde{t}_R}$ , for $m_h \geq 114.4$ GeV as a function of $\tan\beta$ for intermediate stop mixing ( $X_t/m_{\tilde{t}} = -1$ ) for a top quark mass of $m_t = 168, 173, 178$ GeV. Other parameters are as given in Fig. 2.1. . . . .	27
2.5. Minimum stop soft masses, $m_{\tilde{t}} \equiv m_{\tilde{t}_L} = m_{\tilde{t}_R}$ , for $m_h \geq 114.4$ GeV as a function of $\tan\beta$ for natural maximal stop mixing ( $X_t/m_{\tilde{t}} = -2$ ) for a top quark mass of $m_t = 168, 173, 178$ GeV. Other parameters are as given in Fig. 2.1. . . . .	27
2.6. Minimum stop soft masses, $m_{\tilde{t}} \equiv m_{\tilde{t}_L} = m_{\tilde{t}_R}$ , for $m_h \geq 114.4$ GeV as a function of $\tan\beta$ for various values of the bino, wino, and gluino soft masses, $M_1, M_2, M_3$ . The upper three lines are for vanishing stop mixing ( $X_t = 0$ ) and the lower three for natural maximal stop mixing ( $X_t/m_{\tilde{t}} = -2$ ). Other parameters are as given in Fig. 2.1. . . . .	28

- 2.7. Minimum stop soft masses,  $m_{\tilde{t}} \equiv m_{\tilde{t}_L} = m_{\tilde{t}_R}$ , for  $m_h \geq 114.4$  GeV as a function of  $\tan \beta$  for natural maximal stop mixing ( $X_t/m_{\tilde{t}} = -2$ ) with  $\mu = -500, 200, 500$  GeV and bino, wino, and gluino soft masses of  $M_1 = 100$  GeV,  $M_2 = 200$  GeV,  $M_3 = 800$  GeV. Other parameters are as given in Fig. 2.1. . . . . 29
- 2.8. Minimum stop soft masses,  $m_{\tilde{t}} \equiv m_{\tilde{t}_L} = m_{\tilde{t}_R}$ , as a function of  $m_h$ . All squark and slepton soft masses are equal to the stop soft masses,  $\mu = 200$  GeV,  $m_t = 173$  GeV,  $\{M_1, M_2\} = \{100, 200\}$  GeV,  $\tan \beta = 30$ , and all the soft trilinear couplings are equal to  $A_t = X_t + \mu \cot \beta$ . In the figure, the curved lines from left to right are as follows: the dotted line is for no mixing ( $X_t/m_{\tilde{t}} = 0$ ), the dash-dot line for intermediate mixing ( $X_t/m_{\tilde{t}} = -1$ ), the dashed line for natural maximal mixing ( $X_t/m_{\tilde{t}} = -2$ ), and the solid line for the  $m_h^{\max}$  benchmark scenario ( $X_t/m_{\tilde{t}} = +2$ ) [24]. The gluino mass is set to be  $M_3 = 800$  GeV in all cases except in the  $m_h^{\max}$  benchmark scenario, where  $M_3 = 0.8m_{\tilde{t}}$ . The vertical dotted line is at  $m_h = 114.4$  GeV, which is the lower bound set by LEP on  $m_h$  in the decoupling limit. . . . . 30
- 2.9. Minimum stop soft masses,  $m_{\tilde{t}} \equiv m_{\tilde{t}_L} = m_{\tilde{t}_R}$ , for  $m_h \simeq 93$  GeV,  $m_H \geq 114.4$  GeV, and  $\cos^2(\beta - \alpha) \geq 0.8$ , as a function of  $\tan \beta$  for stop mixing  $X_t/m_{\tilde{t}} = 0, \pm 1, \pm 2$ . All squark, slepton, and gaugino soft mass parameters are equal to the stop soft masses,  $\mu = 200$  GeV,  $m_t = 173$  GeV, and all soft trilinear couplings are equal to  $A_t = X_t + \mu \cot \beta$ . This figure may be compared with Fig. 2.1. . . . 34
- 2.10. Minimum stop soft masses,  $m_{\tilde{t}} \equiv m_{\tilde{t}_L} = m_{\tilde{t}_R}$ , for  $m_h \simeq 93$  GeV,  $m_H \geq 114.4$  GeV, and  $\cos^2(\beta - \alpha) \geq 0.8$ , as a function of  $\tan \beta$  for vanishing stop mixing ( $X_t/m_{\tilde{t}} = 0$ ) for a top quark mass of  $m_t = 168, 173, 178$  GeV. Other parameters are given as in Fig. 2.9. This figure may be compared with Fig. 2.3. . . . . 34

2.11. Minimum stop soft masses, $m_{\tilde{t}} \equiv m_{\tilde{t}_L} = m_{\tilde{t}_R}$ , for $m_h \simeq 93$ GeV, $m_H \geq 114.4$ GeV, and $\cos^2(\beta - \alpha) \geq 0.8$ , as a function of $\tan \beta$ for intermediate stop mixing ( $X_t/m_{\tilde{t}} = -1$ ) for a top quark mass of $m_t = 168, 173, 178$ GeV. Other parameters are given as in Fig. 2.9. This figure may be compared with Fig. 2.4. . . . . .	35
2.12. Minimum stop soft masses, $m_{\tilde{t}} \equiv m_{\tilde{t}_L} = m_{\tilde{t}_R}$ , for $m_h \simeq 93$ GeV, $m_H \geq 114.4$ GeV, and $\cos^2(\beta - \alpha) \geq 0.8$ , as a function of $\tan \beta$ for natural maximal stop mixing ( $X_t/m_{\tilde{t}} = -2$ ) for a top quark mass of $m_t = 168, 173, 178$ GeV. Other parameters are given as in Fig. 2.9. This figure may be compared with Fig. 2.5. . . . . .	35
2.13. Minimum stop soft masses, $m_{\tilde{t}} \equiv m_{\tilde{t}_L} = m_{\tilde{t}_R}$ , as a function of $\tan \beta$ , for no stop mixing ( $X_t/m_{\tilde{t}} = 0$ ). The solid line shows the minimum stop soft masses for $m_h \simeq 93$ GeV, $m_H \geq 114.4$ GeV, and $\cos^2(\beta - \alpha) \geq 0.8$ , consistent with the LEP Higgs bounds. The dashed and dash-dot lines are not consistent with the LEP bounds and used for comparison. The dashed line shows the minimum soft masses for $m_h \simeq 93$ GeV and $\cos^2(\beta - \alpha) \geq 0.8$ and without a constraint on $m_H$ . The dash-dot line shows the minimum soft masses for $m_h \simeq 93$ GeV and without constraints on $m_H$ and $\cos^2(\beta - \alpha)$ . Other parameters are given as in Fig. 2.9. . . . . .	36
2.14. Minimum stop soft masses, $m_{\tilde{t}} \equiv m_{\tilde{t}_L} = m_{\tilde{t}_R}$ , as a function of $\tan \beta$ , for intermediate stop mixing ( $X_t/m_{\tilde{t}} = -1$ ). The other parameters and the different lines are as for Fig. 2.13. . . . . .	36
2.15. Minimum stop soft masses, $m_{\tilde{t}} \equiv m_{\tilde{t}_L} = m_{\tilde{t}_R}$ , as a function of $\tan \beta$ , for natural maximal stop mixing ( $X_t/m_{\tilde{t}} = -2$ ). The other parameters and the different lines are as for Fig. 2.13. . . . . .	37
2.16. $\mathcal{B}(B \rightarrow X_s \gamma)$ versus $\mu$ with stop soft masses $m_{\tilde{t}} \equiv m_{\tilde{t}_L} = m_{\tilde{t}_R} = 283$ GeV, and natural maximal stop mixing ( $X_t/m_{\tilde{t}} = -2$ ). All squark, slepton, and gaugino soft mass parameters are equal to the stop soft masses, $m_t = 173$ GeV, $m_A = 1000$ GeV, $\tan \beta = 20$ , and all the soft trilinear couplings are equal to $A_t = X_t + \mu \cot \beta$ . . . . . .	43

2.17. Relationship between the $\text{Re}(H_u) - \text{Re}(H_d)$ and $H_{\parallel} - H_{\perp}$ bases and $h - H$ mass eigenstates for the two doublet Higgs sector. . . . .	53
3.1. The coefficients $c_{ij}$ defined in equation (3.5) for $\tan\beta = 10$ as a function of the messenger scale $M_S$ . . . . .	69
3.2. The minimal fine-tuning as a function of the messenger scale $M_S$ for $\tan\beta = 10$ . The top black line is the total minimal fine-tuning as defined in equation (3.10) which includes all the individual contributions. The individual contributions to the fine-tuning from $\mu^2$ , $m_{H_u}^2$ , the gaugino masses $M_1^2$ , $M_2^2$ and $M_3^2$ , and the stop soft trilinear coupling $A_t^2$ are included. Moreover, the average fine-tuning of the stop soft masses $m_{\tilde{t}_L}^2$ and $m_{\tilde{t}_R}^2$ is included as in equation (3.11). . . . .	75
3.3. The messenger scale values of $M_3$ , $M_2$ , $M_1$ , $A_t$ and the average of the stop soft masses squared, $m_{\tilde{t}}$ , that give the minimal fine-tuning (MFT) as a function of the messenger scale $M_S$ and for $\tan\beta = 10$ . The high-scale values of $M_2$ and $A_t$ , and to a lesser extent $M_1$ and $m_{\tilde{t}}$ , in the minimal fine-tuned region are roughly constant. The high-scale value of $M_3$ , however, decreases significantly as the messenger scale is increased. The reason for this is that the coefficient of $M_3^2$ in the expression for $m_{\tilde{t}}$ increases as a function of $M_S$ , and thus the minimal fine-tuned region requires the value of $M_3$ to decrease as $M_S$ increases. . . . .	76
3.4. The low-scale values of the gaugino masses $M_1$ , $M_2$ and $M_3$ , the stop soft trilinear coupling $A_t$ and the average of the stop soft masses squared $m_{\tilde{t}}$ that give the minimal fine-tuning (MFT) for the messenger scale $M_S$ (with $\tan\beta = 10$ ). While the low-scale values of $M_2$ , $A_t$ and $m_{\tilde{t}}$ that give the minimal fine-tuning are roughly the same for all $M_S$ , the values of $M_1$ and $M_3$ decrease for larger $M_S$ . . . . .	78

- 3.5. The RG-evolution of  $A_t/M_3$  for various boundary conditions at the low-scale for  $A_t(m_Z) / M_3(m_Z) = \{-2.0, -1.5, \dots, 1.5, 2.0\}$  and  $\tan\beta = 10$ . The strongly attractive infrared quasi-fixed point near  $A_t/M_3 \simeq -1$  is clearly visible. The gaugino masses have been set to their minimal fine-tuned values for the case  $M_S = M_{\text{GUT}}$ , i.e.  $M_3(m_Z) \simeq 335$  GeV,  $M_2(m_Z) \simeq 430$  GeV, and  $M_1(m_Z) \simeq 830$  GeV. . . . . 79
- 3.6. The RG-trajectories of the minimal fine-tuned region if the messenger scale is  $M_S=M_{\text{GUT}}$  ( $\tan\beta$  has been set to 10). At the scale  $m_Z$ , the parameter values are  $m_{\tilde{t}} \simeq 305$  GeV,  $m_{\tilde{t}_1} \simeq 110$  GeV,  $m_{\tilde{t}_2} \simeq 475$  GeV,  $M_3(m_Z) \simeq 335$  GeV, and  $\mu(m_Z) = 140$  GeV. The minimal fine-tuned value is obtained for *natural maximal-mixing*, i.e.  $A_t \simeq -2m_{\tilde{t}}$ . . . . . 80
- 3.7. The minimal fine-tuning as a function of the lower bound on the Higgs mass  $m_h$ , where the calculation of  $m_h$  only includes the one-loop corrections from the top-stop sector ( $\tan\beta = 10$ ,  $m_A = 250$  GeV,  $m_t = 170.9$  GeV). . . . . 87

3.8. The minimal fine-tuning as a function of the lower bound on the Higgs mass  $m_h$  calculated with `FeynHiggs` 2.6.0 ( $\tan\beta = 10$ ,  $m_A = 250$  GeV,  $m_t = 170.9$  GeV). Throughout this paper the fine-tuning is minimized subject to a constraint on  $m_h$ , where  $m_h$  is estimated with a one-loop formula as described in Section 3.4.1. The different lines arise from different assumptions made about  $A_t$ , or  $\mu$  and  $M_2$ , when minimizing the fine-tuning. These different assumptions give rise to different low-energy spectra that present the least fine-tuned parameter choices satisfying these assumptions. These low-energy spectra may then be used in `FeynHiggs` to calculate  $m_h$ . Although  $M_2$ ,  $\mu$  and the sign of  $A_t$  do not affect the one-loop estimate of  $m_h$  which only contains the dominant corrections, they do affect the `FeynHiggs` estimate of  $m_h$ . For the solid black line no constraint was set on  $A_t$ , and  $\mu$  and  $M_2$  were only required to be above 100 GeV. It is the same line as in Figure 3.7, but with  $m_h$  estimated by `FeynHiggs` instead of the one-loop formula. The dashed blue line assumes  $A_t$  is positive and near maximal mixing, also with  $M_2$  and  $\mu$  only required to be above 100 GeV. The dash-dot green curve makes no assumption about  $A_t$  but sets  $\mu = 100$  GeV and  $M_2 = 100$  GeV. The dotted red line assumes  $A_t = 0$ , and again only requires  $\mu$  and  $M_2$  to be larger than 100 GeV. Further details and explanations are given in the text. 90

4.1. A plot showing the global shape of the potential.  $M$  has been expanded around zero as in equation (3.8). Note the runaway in the direction  $X \rightarrow -\infty$  and  $\phi \rightarrow 0$ . The singularity at  $\phi = 0$  and the “drain”  $W_\phi = 0$  are clearly visible. Also visible is the Coleman-Weinberg channel near  $X = 0$  and  $\phi$  large, discussed later. This plot was generated with the help of [37]. . . . . 115

4.2.	A plot showing the shape of the potential, including the one-loop Coleman-Weinberg corrections, near the metastable minimum. In the $\phi$ -direction the potential is a parabola, whereas in the $X$ -direction it is a side of a hill with a minimum created due to quantum corrections. This plot was generated with the help of [37]. . . . .	117
4.3.	A plot of the classical potential (dashed line) and the total potential including one-loop corrections (solid line) for fixed $ \phi  =  \phi_0 $ , where $ \phi_0 $ is the position of the metastable minimum in the $\phi$ -direction, defined in (4.32). In the figure, $N_f = 3$ , $N_c = 2$ , $N'_f = 1$ and $N'_c = 2$ . The values were scaled so that the position of the “drain”, $W_\phi = 0$ , equals 1 on both axes. In these units, the position of the metastable minimum is on the order of $10^{-4}$ . This plot was generated with the help of [37]. . . . .	121
4.4.	Table showing the classical mass spectrum, grouped in sectors of $\text{Str } M^2 = 0$ for $N_f = N_c + 1$ . The $O(m^2)$ fields in $(\phi, \text{tr } X)$ are not degenerate. Although supersymmetry is spontaneously broken, there is no goldstino at the classical level. . . . .	122
4.5.	Table showing the mass spectrum, including one-loop corrections, grouped in sectors of $\text{Str } M^2 = 0$ for $N_f = N_c + 1$ . Notice the appearance of the goldstino in the $(\phi, \text{tr } X)$ sector. The $O(m^2)$ fields in $(\phi, \text{tr } X)$ are not degenerate; here $m_{CW}^2 = bh^3m \phi_0 $ . . . . .	123
4.6.	Table showing the classical mass spectrum, grouped in sectors of $\text{Str } m^2 = 0$ , for $N_f > N_c + 1$ . After gauging $SU(\tilde{N}_c)$ , the traceless goldstone bosons from $(\chi, \bar{\chi})$ are eaten, giving a mass $m_W^2 = g^2m \phi_0 /h$ to the gauge bosons. Further, from $V_D = 0$ , the noncompact goldstones also acquire a mass $m_W^2$ . Including CW corrections, $\text{tr } X$ acquires mass $m_{CW}^2$ and one of the fermions becomes massless. . . . .	123

- 5.1. Feynman diagrams for the irreducible one-loop couplings between non-chiral dark matter and quarks. For real representations of  $SU(2)_L \times U(1)_Y$ , there are only  $W$ -bosons within the loop. For complex representations of  $SU(2)_L \times U(1)_Y$ , there are both  $W$ - and  $Z$ -bosons in the loop. The symbol  $h$  denotes the Standard Model Higgs boson,  $\chi$  denotes the dark matter particle, and  $q$  refers to quarks. There is also a cross-diagram for the diagram on the left which needs to be included. . . . . 145
- 5.2. Feynman diagrams generating a coupling between dark matter  $\chi$  and gluons  $G$ . For real representations of  $SU(2)_L \times U(1)_Y$ , there are only  $W$ -bosons within the loop. For complex representations of  $SU(2)_L \times U(1)_Y$ , there are both  $W$ - and  $Z$ -bosons in the loop. The symbol  $h$  denotes the Standard Model Higgs boson and  $q$  refers to quarks. . . 149

- 5.3. A comparison of the results presented in this paper with current and projected experimental bounds for the cross-section of dark matter scattering off a nucleon. Shown are the current experimental upper bounds from XENON10 (solid black line) [14], and the projected upper bounds for SuperCDMS 2-ST at Soudan (blue dashed line), SuperCDMS 25kg / 7-ST at Snolab (green dashed line), XENON1T (magenta dashed line) and SuperCDMS Phase C (red dashed line) [15, 16, 17]. The dashed black horizontal line is the theoretical lower bound on the cross-section for chiral electroweak dark matter scattering coherently off nuclei via the exchange of a  $Z$ -boson, see §5.2. The black dot (●) is the predicted cross-section for a 1 TeV non-chiral dark-matter particle part of two  $SU(2)_L$  doublets with opposite hypercharge (a complex representation of  $SU(2)_L$ ), assuming its coupling to the  $Z$ -boson is forbidden by splitting the Dirac state into a pseudo-Dirac state; see §5.3.2. Without the latter assumption, the cross-section is given by the open circle (○) and would be ruled out. The black square (■) is the predicted cross-section for a 2 TeV non-chiral dark matter particle part of an  $SU(2)_L$  triplet with zero hypercharge (a real representation of  $SU(2)_L$ ), see §5.3.1. Dark matter from higher order real or complex representations has a larger direct-detection cross-section than those represented by the black square or by the black dot, respectively, see §5.3. The dotted diagonal lines represent the Higgs contribution to dark matter scattering off nucleons for a range of magnitudes of the Higgs to dark matter coupling. This coupling also determines what fraction,  $f_{m_{\text{ewsb}}} \equiv m_{\text{ewsb}}/m_\chi$ , of the dark matter mass comes from electroweak symmetry breaking, and the lines shown are for various  $f_{m_{\text{ewsb}}}$ . The experimental results shown in this figure were obtained through [40]. . . . 153
- 6.1. The decay of two gluinos to six quarks, via an intermediate off-shell squark, producing a six jet final state. Events of this type were generated with PYTHIA using the Minimal Supersymmetric Standard Model with R-parity violation. . . 165
- 6.2. The distribution of the events in the  $p_{T,6}$  versus  $\sum_{i=1}^6 p_{T,i}$  plane for signal and pure QCD background. . . . . 172

- 6.3. The figures show the three-jet invariant mass which was found as follows: form all 10 pairs of three-jet invariant mass combinations from the six hardest jets within an event and calculate the difference between the invariant masses of the two members of each pair. Find the pair with the smallest difference, and plot the smaller of the two invariant masses from this pair. All the trigger-level and event selection cuts as discussed in §6.3.1 are included. Also included are the two kinematic cuts  $\sum_{j=1}^6 p_{T,j} \geq 600$  GeV and  $p_{T,6} \geq 90$  GeV. The luminosity used in these plots is  $\mathcal{L}=250$  pb<sup>-1</sup>. . . . . 175
- 6.4. The three-jet invariant mass using Monte Carlo matching information for the same signal data as used in Fig. 6.3, i.e. for  $m_Q = 290$  GeV, including all the trigger-level and event selection cuts as discussed in §6.3.1, and also including the two kinematic cuts  $\sum_{j=1}^6 p_{T,j} \geq 600$  GeV and  $p_{T,6} \geq 90$  GeV. The luminosity used in this plot is  $\mathcal{L}=250$  pb<sup>-1</sup>. . . . . 176
- 6.5. The figures show the invariant mass,  $M_{ijk} \equiv \sqrt{(p_i + p_j + p_k)^2}$ , versus the scalar sum of the transverse momenta,  $|p_{T,i}| + |p_{T,j}| + |p_{T,k}|$  for signal, pure QCD and  $t\bar{t}$ . Here  $ijk$  form a jet-triplet, and the figures include all the best 16 jet-triplets that most often come from the decay of a  $Q$ , as shown in Table 6.5. There are thus 16 entries for each event. All the trigger-level and event selection cuts as discussed in §6.3.1 are included, as well as the two kinematic cuts  $\sum_{j=1}^6 p_{T,j} \geq 600$  GeV and  $p_{T,6} \geq 90$  GeV. The luminosity shown here is  $\mathcal{L}=250$  pb<sup>-1</sup>. . . . . 179
- 6.6. The invariant mass of all the jet-triplets, chosen among the 16 best triplets, that satisfy (6.1) for the signal with  $m_Q = 290$  GeV. All the trigger-level and event selection cuts as discussed in §6.3.1 are included, as well as the two kinematic cuts  $\sum_{j=1}^6 p_{T,j} \geq 600$  GeV and  $p_{T,6} \geq 90$  GeV. The offset in equation (6.1) is -100 GeV for this plot. . . . . 182

6.7.	The invariant mass of the best 16 jet-triplets that satisfy (6.1) for the signal with $m_Q = 290$ GeV, the pure QCD background, and the $t\bar{t}$ background (stacked on top of each other from top to bottom, respectively). Included are all the trigger-level and event selection cuts as discussed in §6.3.1, as well as the two kinematic cuts $\sum_{j=1}^6 p_{T,j} \geq 600$ GeV and $p_{T,6} \geq 90$ GeV. The offset in equation (6.1) is -100 GeV. The luminosity shown here is $\mathcal{L} = 1\text{fb}^{-1}$ . . . . .	184
6.8.	The Monte Carlo matched jet-triplet invariant masses for different detector simulations and, in some cases, with an additional smearing of the jet energy resolution. The signal has $m_Q = 290$ GeV. Only trigger-level cuts are included, without any additional kinematic cuts. In Figure (a), the events were run through the PGS 4 detector simulation, while in Figure (b) they were run through the full CMSSW detector simulation. Figure (c) includes events run through PGS 4, but each jet receives an additional smearing as described in the text, in order to have an overall jet energy resolution as that found in CMSSW. Figure (d) includes jets run through PGS 4, with the same additional smearing as in Figure (c), but with an additional smearing of about 10% as given by (6.5). This additional 10% smearing is described in the CMS TDR as being more realistic, but is not included in the CMSSW detector simulation. The luminosity shown in the figures is about $\mathcal{L} \simeq 300 \text{pb}^{-1}$ . . . . .	189
6.9.	The invariant mass of the best 16 jet-triplets that satisfy (6.1) for the signal with $m_Q = 290$ GeV. Included are all the trigger-level and event selection cuts as discussed in §6.3.1, as well as the two kinematic cuts $\sum_{j=1}^6 p_{T,j} \geq 600$ GeV and $p_{T,6} \geq 90$ GeV. The offset in equation (6.1) is -100 GeV. The luminosity shown here is $\mathcal{L} = 300 \text{pb}^{-1}$ , except for Figure (d) which only has $\mathcal{L} = 58 \text{pb}^{-1}$ and suffers slightly from low statistics. Figures (a)-(d) assume the same detector/jet energy resolution as described in Fig. 6.8. . . . .	190

- 6.10.  $M_{ijk} \equiv \sqrt{(p_i + p_j + p_k)^2}$  versus various other kinematic quantities made out of three jets, for the signal with  $m_Q = 420$  GeV. Here  $ijk$  form a jet-triplet, and the figures include all the best 16 jet-triplets that most often come from the decay of a  $Q$ , as shown in Table 6.5. Each plot thus contains 16 entries for each event. All the trigger-level and event selection cuts as discussed in §6.3.1 are included, as well as the two kinematic cuts  $\sum_{j=1}^6 p_{T,j} \geq 600$  GeV and  $p_{T,6} \geq 90$  GeV. The luminosity shown here is  $\mathcal{L} = 2 \text{ fb}^{-1}$ . . . . . 192
- 6.11. The invariant mass of the 16 best jet-triplets that satisfy (6.1) for the signal with  $m_Q = 290$  GeV and offset value given in each subfigure caption. Included are all the trigger-level and event selection cuts (§6.3.1), a kinematic cut  $\sum_{j=1}^6 p_{T,j} \geq 600$  GeV, and a cut on  $p_{T,6}$  as detailed in each subfigure caption.  $\mathcal{L} = 1\text{fb}^{-1}$ . . . 193
- 6.12. The invariant mass of the 16 best jet-triplets that satisfy (6.1) for the signal with  $m_Q = 290$  GeV and offset value given in each subfigure caption. Included are all the trigger-level and event selection cuts (§6.3.1), a kinematic cut  $\sum_{j=1}^6 p_{T,j} \geq 600$  GeV, and a cut on  $p_{T,6}$  as detailed in each subfigure caption.  $\mathcal{L} = 1\text{fb}^{-1}$ . . . 194
- 6.13. The invariant mass of the 16 best jet-triplets that satisfy (6.1) for the signal with  $m_Q = 420$  GeV and offset value given in each subfigure caption. Included are all the trigger-level and event selection cuts (§6.3.1), a kinematic cut  $\sum_{j=1}^6 p_{T,j} \geq 700$  GeV, and a cut on  $p_{T,6}$  as detailed in each subfigure caption.  $\mathcal{L} = 1\text{fb}^{-1}$ . . . 195
- 6.14. The invariant mass of the 16 best jet-triplets that satisfy (6.1) for the signal with  $m_Q = 420$  GeV and offset value given in each subfigure caption. Included are all the trigger-level and event selection cuts (§6.3.1), a kinematic cut  $\sum_{j=1}^6 p_{T,j} \geq 700$  GeV, and a cut on  $p_{T,6}$  as detailed in each subfigure caption.  $\mathcal{L} = 1\text{fb}^{-1}$ . . . 196
- 6.15. The invariant mass of the 16 best jet-triplets that satisfy (6.1) for the signal with  $m_Q = 660$  GeV and offset value given in each subfigure caption. Included are all the trigger-level and event selection cuts (§6.3.1), a kinematic cut  $\sum_{j=1}^6 p_{T,j} \geq 1100$  GeV, and a cut on  $p_{T,6}$  as detailed in each subfigure caption.  $\mathcal{L} = 1\text{fb}^{-1}$ . . . 197

- 6.16. The invariant mass of the 16 best jet-triplets that satisfy (6.1) for the signal with  $m_Q = 660$  GeV and offset value given in each subfigure caption. Included are all the trigger-level and event selection cuts (§6.3.1), a kinematic cut  $\sum_{j=1}^6 p_{T,j} \geq 1100$  GeV, and a cut on  $p_{T,6}$  as detailed in each subfigure caption.  $\mathcal{L} = 1\text{fb}^{-1}$ . . . . . 198
- 6.17. The invariant mass of the 16 best jet-triplets that satisfy (6.1), with an offset value given in each subfigure caption, for the signal with  $m_Q = 290$  GeV, the pure QCD background, and the  $t\bar{t}$  background. Included are all the trigger-level and event selection cuts (§6.3.1), a kinematic cut  $\sum_{j=1}^6 p_{T,j} \geq 600$  GeV, and a cut on  $p_{T,6}$  as detailed in each subfigure caption.  $\mathcal{L} = 1\text{fb}^{-1}$ . . . . . 199
- 6.18. The invariant mass of the 16 best jet-triplets that satisfy (6.1), with an offset value given in each subfigure caption, for the signal with  $m_Q = 420$  GeV, the pure QCD background, and the  $t\bar{t}$  background. Included are all the trigger-level and event selection cuts (§6.3.1), a kinematic cut  $\sum_{j=1}^6 p_{T,j} \geq 700$  GeV, and a cut on  $p_{T,6}$  as detailed in each subfigure caption.  $\mathcal{L} = 1\text{fb}^{-1}$ . . . . . 200
- 6.19. The invariant mass of the 16 best jet-triplets that satisfy (6.1), with an offset value given in each subfigure caption, for the signal with  $m_Q = 420$  GeV, the pure QCD background, and the  $t\bar{t}$  background. Included are all the trigger-level and event selection cuts (§6.3.1), a kinematic cut  $\sum_{j=1}^6 p_{T,j} \geq 700$  GeV, and a cut on  $p_{T,6}$  as detailed in each subfigure caption.  $\mathcal{L} = 1\text{fb}^{-1}$ . . . . . 201
- 6.20. The invariant mass of the 16 best jet-triplets that satisfy (6.1), with an offset value given in each subfigure caption, for the signal with  $m_Q = 660$  GeV, the pure QCD background, and the  $t\bar{t}$  background. Included are all the trigger-level and event selection cuts (§6.3.1), a kinematic cut  $\sum_{j=1}^6 p_{T,j} \geq 1100$  GeV, and a cut on  $p_{T,6}$  as detailed in each subfigure caption.  $\mathcal{L} = 1\text{fb}^{-1}$ . . . . . 202

6.21. The invariant mass of the 16 best jet-triplets that satisfy (6.1), with an offset value given in each subfigure caption, for the signal with  $m_Q = 660$  GeV, the pure QCD background, and the  $t\bar{t}$  background. Included are all the trigger-level and event selection cuts (§6.3.1), a kinematic cut  $\sum_{j=1}^6 p_{T,j} \geq 1100$  GeV, and a cut on  $p_{T,6}$  as detailed in each subfigure caption.  $\mathcal{L} = 1\text{fb}^{-1}$ . . . . . 203

# Chapter 1

## Introduction

This thesis is being completed at the beginning of a very exciting time in the field of high energy physics. The standard model of particle physics is remarkably successful and has withstood two decades of precision tests at high energy particle accelerators. It does, however, leave unanswered several fundamental questions, such as how electroweak symmetry is broken, the weakness of gravity, the origin of the mass of fundamental particles, and whether there are additional symmetries in nature, such as supersymmetry. Starting in 2008, particle physicists will enter a new era in which the prospects of finding answers to these questions and others are great. This era will be dominated by a new machine built to probe the high energy frontier, the Large Hadron Collider (LHC), a proton-proton accelerator being built at CERN outside of Geneva along the French-Swiss border.

This thesis consists of a diverse set of topics that may broadly be described as physics beyond the standard model. It consists of five main chapters which discuss the implications of current experimental constraints on the Minimal Supersymmetric Standard Model (MSSM), fine-tuning in the MSSM, a model in which supersymmetry is broken in a metastable vacuum, the prospects for direct detection of a particular dark matter candidate, and some Large Hadron Collider (LHC) phenomenology.

I shall first give a broad introduction which attempts to place these topics in a larger context. I shall then briefly summarize each of the chapters in turn.

The Standard Model of particle physics is known to describe the properties and interactions of all the known fundamental particles down to distances of about  $10^{-16}$  cm or, equivalently, up to the electroweak energy scale of about 250 GeV. It is undoubtedly one of the most successful

theories of physics and has withstood testing from a variety of experiments, mainly from particle accelerators. Many of these experiments have probed its structure to an incredibly large precision and found no significant deviation [1].

This success is a reason to celebrate, but for many it has also been a large source of frustration. Part of this frustration is because the Higgs boson in the Standard Model has not yet been found, despite intense efforts spent looking for it. However, the frustration really goes beyond not having found the Higgs. There is reason to believe that there should be new physics somewhere between the electroweak and the TeV scale ( $\mathcal{O}(1000 \text{ GeV})$ ), possibly with a whole slew of new particles, and the frustration stems from the sheer number of ways that the Standard Model has been tested, sometimes with staggering precision, without any sign of this new physics. It is not only that no new particles have been directly produced and detected, but also that new particles, if they are not too heavy, indirectly affect precision observables, and no significant deviations from the Standard Model predictions of these precision observables have been found to date.

Why should there be new physics around the TeV scale or below? We know that the Standard Model is an incomplete description of fundamental physics, but most of its failures do not actually point to new TeV scale physics. We will first briefly discuss some of these failures, before turning to the reason of why it is believed that there should be new physics at the TeV scale.

One of the Standard Model's big failures, of course, is that it does not include a description of quantum gravity. However, gravitational effects are not important for particle physics experiments at the energies that have been probed so far. Moreover, since quantum gravitational effects presumably only become important near the Planck scale  $M_P \sim 10^{19} \text{ GeV}$ , they will never be important in any particle physics experiment that can conceivably be built.

A further obvious problem with the Standard Model is that the neutrinos as described in the Standard Model have zero mass, which is now known to be incorrect from neutrino oscillation experiments. However, it is easy to give the neutrinos in the Standard Model non-zero masses

by, for example, adding a right-handed neutrino to the Standard Model. Although much still needs to be understood about the neutrino sector, a non-zero neutrino mass does not point to new physics around the TeV scale (if anything, it points to new physics at energies of about  $10^{15}$  GeV).

Arguably the biggest failure in our understanding of fundamental physics is that we have no good explanation for the “dark energy” that is driving the acceleration of the cosmic expansion and makes up about 72% of today’s energy density of the Universe [2]. It is true that the Universe’s acceleration can be easily described with Einstein’s theory of general relativity by the addition of the “cosmological constant” term to Einstein’s equations, which describes the energy of the vacuum of space. This term can explain and is so far completely consistent with combined data from astronomical measurements of supernovae, the cosmic microwave background radiation, and galaxy cluster masses. However, its measured value is about 120 orders of magnitude too small than what would have been expected from quantum field theory. The resolution of this “cosmological constant problem” may have to wait for a better understanding of quantum gravity. It is, however, unlikely to be resolved by any new physics at the TeV scale.

Astronomical measurements have not only provided striking evidence for the existence of dark energy, but they have also pointed to the existence of additional matter in the Universe. This so-called dark matter makes up about 23% of the current energy density in the Universe, which is to be contrasted with the 5% that consists of Standard Model particles. Although the identity of the dark matter particle is not known, there are many suggestions for what it could be (it is known that it is not part of the Standard Model). An intriguing possibility is that it is a particle that could soon be produced and detected at the LHC. This possibility gets some credence from the observation that any weakly interacting massive particle (WIMP), i.e. a particle charged under the Standard Model electroweak gauge group  $SU(2)_L \times U(1)_Y$  and interacting with the  $W$ - and  $Z$ -bosons, has the correct dark matter relic density if its mass is on the order of several 100 GeV. At this stage this is only an intriguing observation, since there is nothing that requires the dark matter in the Universe to be a WIMP. However, it does suggest the possibility that

any new physics around the TeV scale may also have a suitable dark matter candidate.

None of the previous shortcomings or failures of the Standard Model require new physics around the TeV scale or below. The reason for the belief that there *should* be something new somewhere around this scale really comes from trying to find a solution to the *hierarchy problem*. Finding a solution to the hierarchy problem has been the driving force behind model building for physics beyond the standard model for the last 30 years. Let us now briefly review the breaking of electroweak symmetry in the Standard Model and the definition of the hierarchy problem.

The Standard Model is a gauge theory with gauge group  $SU(3)_C \times SU(2)_L \times U(1)_Y$ . Gauge symmetry requires the Standard Model Lagrangian to be written in terms of massless spin-half fields describing the fermions and massless spin-one fields describing the gauge bosons. It is not yet clear how fermions as well as some gauge bosons get mass. In particular, experiments show that the electroweak symmetry, described in the Standard Model Lagrangian by massless gauge fields that transform under  $SU(2) \times U(1)$ , is broken, since three of the four carriers of the electroweak force, the vector bosons  $W^+$ ,  $W^-$  and  $Z$ , are massive. The set of particles and interactions responsible for electroweak symmetry breaking is generically called the *Higgs sector*. The *minimal Higgs sector* is the most popular choice for the Higgs sector of the Standard Model as it consists of a single Higgs field which is a complex  $SU(2)$  doublet. One of the components of the  $SU(2)$  doublet acquires a vacuum expectation value (VEV)  $v$  and automatically generates mass terms for the vector bosons via the *Higgs mechanism*, as well as mass terms for fermions via Yukawa couplings between the Higgs field and the fermions. The Higgs field has four degrees of freedom. Three are the would-be Goldstone bosons that ‘get eaten’ and form the longitudinal component of the vector bosons, and the one remaining degree of freedom is a scalar field, the long-sought after *Higgs boson*,  $h$ . The Standard Model does not predict the mass of  $h$  which, at tree-level, can be written in terms of the Higgs self-coupling  $\lambda$  as  $m_h = \sqrt{2\lambda}v$ , with  $v \approx 246$  GeV. Precision measurements of the electroweak parameters, however, put *indirect* constraints on the Higgs mass of about  $129^{+74}_{-49}$  GeV and limit it to less than 285 GeV at the 95% confidence level

[1]. Data from the Large Electron Positron (LEP) collider in CERN, Geneva, which operated at center of mass energies of 91 - 209 GeV, put a lower bound of 114.4 GeV at the 95% confidence level on its mass [4]. There are theoretical reasons for needing  $m_h$  to be larger than  $\approx 70$  GeV (vacuum stability) and less than  $\approx 800$  GeV (triviality).

The Higgs mass is thus expected to be somewhere around the electroweak scale. If  $m_h$  is more than about 180 GeV,  $\lambda$  blows up somewhere before the Planck scale, which means that the Higgs sector becomes strongly coupled, and there may be some new physics below the Planck scale. However, if  $m_h$  is less than about 180 GeV, none of the the Standard Model couplings (including  $\lambda$ ) blow up before the Planck scale, and the Standard Model can be a perfectly consistent weakly interacting theory all the way up to the Planck scale. In either case, however, a *naturalness* argument makes it doubtful that the Standard Model really is a low-energy effective theory valid to very high energies. All particle masses and couplings receive quantum corrections which makes them sensitive to the scale, denoted by  $\Lambda$ , at which new physics becomes relevant. Fermion masses and dimensionless couplings are only logarithmically sensitive to  $\Lambda$ . However, scalar masses like the Higgs mass are quadratically sensitive to  $\Lambda$ . In particular, if  $(m_h^2)_0$  denotes the fundamental Higgs mass-squared parameter in the theory, then the observable Higgs mass-squared  $m_h^2$  is given by

$$m_h^2 = (m_h^2)_0 - \frac{k}{16\pi^2}\Lambda^2, \quad (1.1)$$

where the second term comes from quantum corrections involving the Standard Model particles, and  $k$  is a coupling of  $\mathcal{O}(1)$ . If  $\Lambda^2$  is of order  $M_P^2$  (where  $M_P$  is the Planck scale), then  $(m_h^2)_0$  must also be of order  $M_P^2$ , and a very unnatural “fine-tuned” cancelation of 1 part in  $10^{30}$  between the two contributions must give  $m_h$  of order the electroweak scale. This fine-tuning is called the *hierarchy problem*. It can be solved if  $\Lambda$  is not too large and below the TeV scale.

It is important to note that the hierarchy problem is not a logically compelling argument proving the existence of new physics below the TeV scale. It is simply based on the common-sense belief that there should not be any strange coincidences, and that therefore the Higgs mass should not be fine-tuned. But it is perfectly possible that there is nothing beyond the

Standard Model all the way up to the Planck scale. In fact, recently, there is evidence in string theory for the existence of a “landscape” of possible vacua, each of which could be a Universe in itself. It may then be that a simple anthropic argument is correct: since a low Higgs mass is one of the conditions for life to exist, it is not surprising that we find ourselves in a Universe where the Higgs mass is small. It is irrelevant then that our Universe has a hierarchy problem.

Whatever one’s feelings about the hierarchy problem, it is a fact that it has been the driving force behind the model building community to go beyond the Standard Model. Let us assume that it is a real problem that is solved by having new physics below the TeV scale so that there is no fine-tuning. There are several suggestions of what this new physics is, and one of the most promising candidates is supersymmetry (SUSY).

How does SUSY solve the hierarchy problem [5]? SUSY posits the existence of a bosonic superpartner to every Standard Model fermion, and a fermionic superpartner to every Standard Model boson. If SUSY is exact, the Standard Model particle and its superpartner are degenerate in mass. In addition to the usual term from quantum corrections to the Higgs mass from Standard Model particles in (1.1), there would be a similar contribution to the Higgs mass *with the opposite sign and the same magnitude* from the superpartners. These two terms exactly cancel in the limit of exact SUSY, and there is thus no hierarchy problem. Since it is obviously not the case that there are superpartners degenerate in mass with their Standard Model counterparts, SUSY cannot be an exact symmetry of our world at low energies, and the cancelation between the two contributions is not exact and instead leaves a small remnant. To avoid a large fine-tuning to the Higgs mass, this remnant cannot be too big. This means that the superpartners should have a mass of order the electroweak or TeV scale if SUSY solves the hierarchy problem. The fact that no superpartners have been detected to this date, and the fact that also no indirect effects of their presence have been observed, requires them to be heavier than they need to be for SUSY to completely solve the hierarchy problem. This latter observation is called the “little hierarchy problem”.

We now turn to a brief discussion of each of the chapters in the thesis.

*Chapter 2: Implications of the CERN LEP Higgs Bounds for the MSSM Stop Sector [7]*

Chapters 2 and 3 deal with fine-tuning and related issues in the context of the Minimal Supersymmetric Standard Model (MSSM). The MSSM is the minimal extension of the Standard Model which incorporates SUSY, with the interesting properties that the gauge couplings unify at the Grand Unified Theory (GUT) scale of about  $2 \times 10^{16}$  GeV and that there can be a viable WIMP dark matter candidate. In addition to the Standard Model it contains a superpartner for every Standard Model particle. Since the exact supersymmetry breaking mechanism is not known, we parameterise our ignorance by including explicit supersymmetry breaking terms in the MSSM Lagrangian. In addition, to avoid anomalies and to give mass to all the quarks and leptons, the minimal Standard Model Higgs sector needs to be modified and the minimal MSSM Higgs sector consists of two complex  $SU(2)$  doublets with opposite hypercharge. The MSSM Higgs sector thus has eight degrees of freedom, of which three are the would-be Goldstone bosons that again get “eaten”, whereas the remaining five form two charged scalars ( $H^\pm$ ), one CP-odd neutral scalar ( $A^0$ ), and two CP-even neutral scalars ( $h^0$  and  $H^0$ , with  $m_{H^0} \geq m_{h^0}$  by definition). Unlike the Standard Model, SUSY requires that the Higgs self-couplings are not free parameters but are proportional to the electroweak couplings. This constrains the tree-level mass of the lighter Higgs,  $h^0$ , to be less than the mass of the  $Z$ -boson (91 GeV). If the actual mass of  $h^0$  lies above 91 GeV, then we require radiative corrections. These would come mainly from loops involving the heavy top quark and its superpartner, the scalar top quark, or “stop”, and for *large stop masses* are able to push  $m_{h^0}$  up to around 115-125 GeV, or even higher, depending on the size of various MSSM parameters.

The best experimental bounds on the MSSM Higgs bosons come from LEP [6]. In Chapter 2, the implications of the LEP Higgs bounds on the MSSM stop masses and mixing are compared in two different regions of the Higgs parameter space. The first region is the Higgs decoupling limit, in which the bound on the mass of the lighter Higgs is the same as the Standard Model Higgs bound of  $m_h \geq 114.4$  GeV, and the second region is near a non-decoupling limit with

$m_h \simeq 93$  GeV, in which the masses of all the physical Higgs bosons are required to be light. In both regions it is found, for example, that the lower bound on the stop mass is about 1000 GeV if there is no stop-mixing. Additional constraints are considered from the electroweak  $S$ - and  $T$ -parameter and the decays  $B \rightarrow X_s \gamma$  and  $B_s \rightarrow \mu^+ \mu^-$ , which also constrain the Higgs and/or stop sector. In some regions of the MSSM parameter space these additional constraints are stronger than the LEP Higgs bounds. The implications of this analysis for the tuning of electroweak symmetry breaking are mentioned.

*Chapter 3: The Minimally Tuned Minimal Supersymmetric Standard Model [8]*

The work in Chapter 2 shows that the stop masses and mixings are required to be rather large for the MSSM to be consistent with current experimental bounds. Large values for the stop masses, however, can be shown to increase the size of the fine-tuning. Since the MSSM contains many parameters, it may be possible to decrease the fine-tuning by changing the value of some other parameter. An interesting question then is what regions in the MSSM parameter space have the least amount of fine-tuning of electroweak symmetry breaking. In Chapter 3, an analysis will be presented that not only discusses the regions in the MSSM with the minimal amount of fine-tuning of electroweak symmetry breaking, but also shows how the minimal amount of tuning increases enormously for a Higgs mass beyond 120 GeV. The upshot of the analysis is that there is not much room left in which the Higgs mass can lie before the MSSM begins to look extremely fine-tuned.

*Chapter 4: Meta-Stable Dynamical Supersymmetry Breaking Near Points of Enhanced Symmetry [10, 11]*

Since the theoretical discovery of SUSY, much work has gone into trying to see how it could be realized in nature. As we have discussed, if SUSY exists, it cannot be an exact symmetry at low energies, and a very important problem in physics is to determine how it gets broken. Over the years many models of SUSY breaking were built, but many of them were rather

complicated and elaborate. These models usually contained stable vacua in which SUSY was broken. It turns out that the requirement of stability is rather stringent, and severely limits the kind of models that can be built. However, recently there has been a renewed interest in building SUSY breaking models after Intriligator, Seiberg and Shih [9] found meta-stable supersymmetry breaking vacua in a surprisingly simple model, namely  $\mathcal{N} = 1$  supersymmetric QCD with massive flavors. The fact that SUSY breaking vacua were found in such a simple theory suggested that they may in fact be ubiquitous, and that many models could contain similar vacua. Indeed, it was found that by relaxing the requirement that the SUSY breaking vacua be stable, it is much easier to build models of SUSY breaking. Our universe could be in such a metastable state as long as the probability for the vacuum to decay is very small and thus not in obvious conflict with observations.

In Chapter 4, the construction of a generic model with long-lived metastable vacua is discussed in which all the relevant parameters, including the SUSY breaking scale, are generated dynamically. The model consists of two supersymmetric QCD sectors coupled by a singlet. It has several desirable features including an explicitly and spontaneously broken R-symmetry, a singlet, a large global symmetry, naturalness and renormalizability. The metastable vacua are produced near a point of enhanced symmetry by a combination of nonperturbative gauge effects and perturbative effects coming from the one-loop Coleman-Weinberg potential. An interesting feature is the existence of "pseudo-runaway" directions, which correspond to runaway directions that are lifted by perturbative quantum corrections.

#### *Chapter 5: Direct Detection of Non-Chiral Dark Matter [3]*

As we have discussed, although the existence of dark matter is rather well established, the identity of the dark matter particle remains a mystery. Current experimental constraints on the properties of dark matter particles come from particle accelerators and from two other types of experiments, called indirect and direct detection experiments. While the indirect detection experiments look for the particles that are produced from annihilating dark matter, the direct

detection experiments attempt to infer the presence of dark matter particles as they scatter off nuclei within detectors by looking for the resulting nuclear recoil.

The rationale for the direct detection experiments is that the dark matter lies in a halo which encompasses our Milky Way galaxy. As the earth and sun rotate around the galactic center, detectors on the earth move through the halo and intersect the path of dark matter particles, which are expected to scatter off the nuclei inside the detectors.

Strong constraints have already been set from the direct detection experiments. They, for example, rule out fermion dark matter that is a chiral representation of the electroweak gauge group. Non-chiral real, complex and singlet representations, however, provide viable fermion dark matter candidates, as will be discussed in Chapter 5. Although any one of these candidates will be virtually impossible to detect at the LHC, it is shown that they may be detected at future planned direct detection experiments. For the real case, an irreducible radiative coupling to quarks may allow a detection. The complex case in general has an experimentally ruled out tree-level coupling to quarks via  $Z$ -boson exchange. However, in the case of two  $SU(2)_L$  doublets, a higher dimensional coupling to the Higgs can suppress this coupling, and a remaining irreducible radiative coupling may allow a detection. Singlet dark matter could be detected through a coupling to quarks via Higgs exchange. Since all non-chiral dark matter can have a coupling to the Higgs, at least some of its mass can be obtained from electroweak symmetry breaking, and this mass is a useful characterization of its direct detection cross-section.

*Chapter 6: Extracting Hadronic Resonances using Jet Ensemble Correlations [12]*

We have discussed above how a large number of models have been developed in response to the hierarchy problem. Although they differ slightly in their success in solving the hierarchy problem, they generically predict new particles to be near or below the TeV scale. This is why there is great excitement in the particle physics community about the coming LHC era.

Due to the large number of different possible models, there is a vast array of possibilities for new particles with different interactions and with masses just above the electroweak scale.

Moreover, if one takes a top-down approach motivated by a more fundamental theory such as string theory, the possibilities become even more numerous and varied. We thus need to be prepared to extract new physics from a plethora of possible discovery signatures.

Chapter 6 discusses a discovery signature that has not been well studied to date. This discovery signature involves multi-jet events, both with and without leptons and/or missing energy. Jets are produced in QCD hard scattering processes that create high transverse momentum quarks or gluons. Since quarks and gluons carry a color charge, QCD confinement does not allow them to be detected directly in their free form and instead they turn into a spray of hadrons confined to a narrow cone, called a jet. Jets are ubiquitously produced in Standard Model QCD processes which will dominate at the LHC, and this may easily hide new physics beyond the Standard Model that also produces jets. This is why much of the community is focused on extracting new physics from more conventional discovery signals, such as multi-leptons and missing energy with no, or very few, jets, which do not have such a large Standard Model background. However, there are many new physics signals that could only, or predominantly, involve jets, so an analysis of discovery signatures which involve many jets is essential. Moreover, new particles which produce multi-jet events tend to have a rather large production cross-section at the LHC. This opens up the possibility that they could be among the first things to be discovered at the LHC, provided that suitable search strategies are developed.

This work considers pair production of a new heavy colored particle ( $Q$ ) undergoing a three-body decay into jets and producing a six-jet final state. Since the  $Q$ 's undergo a three-body decay into three jets, they should be seen as a resonance in a histogram of the invariant mass of three jets. It is hard to extract this resonance due to the very large number of background events which can completely swamp the signal, and also due to the large amount of combinatoric confusion from not knowing how to select the three jets coming from the decay of one of the  $Q$ 's. However, innovative cuts that make use of correlations and kinematic features among the observables formed from the jets that come from the  $Q$ 's can be used to extract the resonance. It is worth emphasizing that the search strategies developed here are more widely applicable.

## References

- [1] W. M. Yao *et al.* [Particle Data Group], J. Phys. G **33**, 1 (2006).
- [2] E. Komatsu *et al.* [WMAP Collaboration], arXiv:0803.0547 [astro-ph].
- [3] R. Essig, Phys. Rev. D **78**, 015004 (2008), arXiv:0710.1668 [hep-ph]
- [4] R. Barate *et al.* [LEP Working Group for Higgs boson searches], Phys. Lett. B **565**, 61 (2003), arXiv:hep-ex/0306033.
- [5] S. P. Martin, arXiv:hep-ph/9709356.
- [6] S. Schael *et al.* [ALEPH Collaboration], Eur. Phys. J. C **47**, 547 (2006), arXiv:hep-ex/0602042.
- [7] R. Essig, Phys. Rev. D **75**, 095005 (2007), arXiv:hep-ph/0702104.
- [8] R. Essig and J. F. Fortin, JHEP **0804**, 073 (2008), arXiv:0709.0980 [hep-ph].
- [9] K. Intriligator, N. Seiberg and D. Shih, JHEP **0604**, 021 (2006), arXiv:hep-th/0602239.
- [10] R. Essig, K. Sinha and G. Torroba, JHEP **0709**, 032 (2007), arXiv:0707.0007 [hep-th].
- [11] R. Essig, K. Sinha and G. Torroba, arXiv:0710.4311 [hep-th].
- [12] S.-H. Chuang, R. Essig, E. Halkiadakis, A. Lath, and S. Thomas, “Extracting Hadronic Resonances using Jet Ensemble Correlations”, in preparation.

## Chapter 2

# Implications of the CERN LEP Higgs Bounds for the MSSM Stop Sector

This chapter appears in print in Phys.Rev.D75:095005, 2007, arxiv:hep-ph/0702104.

The implications of the LEP Higgs bounds on the MSSM stop masses and mixing are compared in two different regions of the Higgs parameter space. The first region is the Higgs decoupling limit, in which the bound on the mass of the lighter Higgs is  $m_h \geq 114.4$  GeV, and the second region is near a non-decoupling limit with  $m_h \simeq 93$  GeV, in which the masses of all the physical Higgs bosons are required to be light. Additional constraints from the electroweak  $S$ - and  $T$ -parameter and the decays  $B \rightarrow X_s \gamma$  and  $B_s \rightarrow \mu^+ \mu^-$ , which also constrain the Higgs and/or stop sector, are considered. In some regions of the MSSM parameter space these additional constraints are stronger than the LEP Higgs bounds. Implications for the tuning of electroweak symmetry breaking are also discussed.

### 2.1 Introduction

The Higgs sector in the Minimal Supersymmetric Standard Model (MSSM) consists of two  $SU(2)_L$  doublets,  $H_d$  and  $H_u$ , with opposite hypercharge. Five physical states remain after electroweak symmetry breaking (EWSB). Assuming there are no CP-violating phases, these physical states consist of two neutral CP-even states  $h$  and  $H$  with masses  $m_h \leq m_H$ , one neutral CP-odd state  $A$ , and two charged states  $H^\pm$ . The tree-level masses of  $h$  and  $H$  are bounded,  $m_h^{\text{tree}} \leq m_Z \leq m_H^{\text{tree}}$ , with  $m_Z \simeq 91$  GeV.

Using the Large Electron Positron (LEP) collider, the LEP collaboration searched for these

Higgs bosons and published bounds on their masses [1]. Their results have ruled out substantial regions of the MSSM Higgs parameter space, and in much of the remaining allowed regions it is clear that large radiative corrections to the tree-level Higgs masses are required to satisfy the LEP bounds. However, two very different scenarios are still possible. One scenario is obtained in the Higgs decoupling limit in which  $h$  behaves like the Standard Model (SM) Higgs and all the other Higgs bosons become heavy and decouple from the low energy theory. Here the bound on  $m_h$  coincides with the bound on the mass of the SM Higgs, namely  $m_h \geq 114.4$  GeV [2]. The other scenario is obtained in the Higgs “non-decoupling” limit in which  $H$  behaves like the SM Higgs and the Higgs sector is required to be light. It allows for  $93$  GeV  $\lesssim m_h < 114.4$  GeV, where the value of 93 GeV is the (somewhat model dependent) lower bound that the LEP collaboration has obtained for  $m_h$  assuming various decay scenarios for  $h$  and a variety of different “benchmark” parameter choices for the MSSM parameters. If  $m_h$  is near 93 GeV, it seems to naively require much smaller radiative corrections to the tree-level Higgs mass than when  $m_h$  is near 114.4 GeV. Since the dominant radiative corrections to the tree-level CP-even Higgs mass matrix, which determines  $m_h$  and  $m_H$ , come from loops involving the top quark and stop squarks, one might naively suspect that  $m_h$  near 93 GeV allows for much smaller stop masses than  $m_h$  near 114.4 GeV. Moreover, larger stop masses would in general imply a more fine-tuned MSSM, and one might therefore suspect that the MSSM is less fine-tuned for  $m_h$  near 93 GeV. In this paper, we present lower bounds on the stop masses consistent with the LEP Higgs bounds, both in the Higgs decoupling region, with  $m_h \geq 114.4$  GeV, as well as near the Higgs non-decoupling region, with  $m_h \simeq 93$  GeV. We compare the constraints on the stop masses in these two regions of the Higgs parameter space, and show that in certain regions of the MSSM parameter space the lower bounds on the stop masses are not significantly different from each other. Furthermore, although there are regions in which the lower bounds are smaller, there are also regions in which they are larger.

There are other constraints on new physics that may further tighten bounds on the stop or Higgs sector. These additional constraints include the electroweak  $S$ - and  $T$ -parameter, and the

decays  $B \rightarrow X_s \gamma$  and  $B_s \rightarrow \mu^+ \mu^-$ . In this paper, we discuss the regions of the MSSM parameter space in which these additional constraints are important in restricting the stop and/or Higgs sector further.

The outline of this paper is as follows. In Section 2.2, we investigate the LEP constraints on the neutral MSSM Higgs sector and its implication for the stop sector in more detail. This will allow us to obtain a simple numerical estimate of the lower bound on the stop masses in a particular limit of the MSSM parameter space. This estimate is independent of the size of  $m_h$ . Section 2.3 contains the main results of this paper. We give lower bounds on the stop masses consistent with the LEP Higgs bounds. The analysis will include all the important radiative corrections to the CP-even Higgs mass matrix, and we discuss the importance of the top mass, the stop mixing the gaugino masses and the supersymmetric Higgsino mass parameter ( $\mu$ ) on the lower bounds of the stop masses. In addition, we present results on how the lower bounds on the soft stop masses vary in the decoupling limit as a function of  $m_h$ . In Section 2.4, we discuss how other constraints on new physics impact the results in Section 2.3. In particular, we investigate the effect of the electroweak  $S$ - and  $T$ -parameters,  $B \rightarrow X_s \gamma$ , and  $B_s \rightarrow \mu^+ \mu^-$ . Section 2.5 contains a discussion of the implications of our analysis for electroweak symmetry breaking and the supersymmetric little hierarchy problem. In Section 2.6, we summarize the results of this paper. Appendix 2.7 gives the relevant background to understand the LEP results for the MSSM Higgs sector. In Appendix 2.8, we review the quasi-fixed point for the stop soft trilinear coupling,  $A_t$ . The trilinear coupling is the main ingredient in determining the amount of stop mixing, and we use the quasi-fixed point value for  $A_t$  in some of the main results of this paper.

## 2.2 LEP constraints on the Higgs sector and implications for the MSSM stop sector

In this section, we first review the LEP Higgs constraints, before going on to discuss the implications of these constraints for the stop sector.

### 2.2.1 Constraints from LEP on the MSSM Higgs-sector

The LEP collaboration searched for the production of Higgs bosons in both the Higgsstrahlung ( $e^+e^- \rightarrow Z \rightarrow Zh$  (or  $ZH$ )) and pair production ( $e^+e^- \rightarrow Z \rightarrow Ah$  (or  $AH$ )) channels. The results from these channels have been used to set upper bounds on the couplings  $ZZh$  ( $ZZH$ ) and  $ZAh$  ( $ZAH$ ) as a function of the Higgs masses. These couplings are proportional to either  $\sin^2(\beta - \alpha)$  or  $\cos^2(\beta - \alpha)$ . Here  $\beta$  is determined from the ratio of the two vacuum expectation values  $v_u \equiv \langle \text{Re}(H_u^0) \rangle$  and  $v_d \equiv \langle \text{Re}(H_d^0) \rangle$  as  $\tan \beta = v_u/v_d$ , and  $\alpha$  is the neutral CP-even Higgs mixing angle.

Within the MSSM, the results from the Higgsstrahlung channel give an upper bound on  $\sin^2(\beta - \alpha)$  and  $\cos^2(\beta - \alpha)$  as a function of  $m_h$  and  $m_H$ , respectively (see Fig. 2 in [1]). The pair production channel, on the other hand, gives an upper bound on  $\cos^2(\beta - \alpha)$  and  $\sin^2(\beta - \alpha)$  as a function of  $m_h + m_A$  and  $m_H + m_A$ , respectively (see Fig. 4 in [1]). Appendix 2.7 contains a review on how these functions of  $\alpha$  and  $\beta$  appear in the MSSM, and why LEP bounds them.

The LEP results from the Higgsstrahlung channel put several interesting bounds on  $m_h$ ,  $m_H$  and  $\sin^2(\beta - \alpha)$ . In the decoupling limit,  $h$  behaves like the SM Higgs so that  $\sin^2(\beta - \alpha) \rightarrow 1$  and the bound on its mass is given by

$$m_h \geq 114.4 \text{ GeV}, \quad \sin^2(\beta - \alpha) \rightarrow 1. \quad (2.1)$$

If  $m_h$  is less than 114.4 GeV, smaller values of  $\sin^2(\beta - \alpha)$  are required in order to suppress the production of  $h$  in the Higgsstrahlung channel and to allow it to have escaped detection. For  $m_h \simeq 93$  GeV,  $\sin^2(\beta - \alpha)$  needs to be less than about 0.2, so that  $\cos^2(\beta - \alpha) \gtrsim 0.8$  (from Fig. 2 in [1]). Larger values of  $\cos^2(\beta - \alpha)$ , however, increase the  $HZZ$  coupling so that now  $m_H$  needs to be large enough to suppress the production of  $H$  in the Higgsstrahlung channel, and allow it, in turn, to have escaped detection. We find that  $m_H \gtrsim 114.0$  GeV (from Fig. 2 in [1]). If  $\sin^2(\beta - \alpha)$  is even smaller and approaches zero, i.e.  $\cos^2(\beta - \alpha) \rightarrow 1$ , it is  $H$  which behaves like the SM Higgs so that the bound on its mass is given by  $m_H \geq 114.4$  GeV (this will be referred to as the Higgs “non-decoupling” limit).

In Section 2.3, we present lower bounds on the stop soft masses for two regions in the Higgs parameter space. These two regions are given by equation (2.1) and by

$$m_h \simeq 93 \text{ GeV}, \quad \cos^2(\beta - \alpha) \geq 0.8, \quad m_H \geq 114.4 \text{ GeV}. \quad (2.2)$$

(We choose  $m_H$  in equation (2.2) to be at least above 114.4 GeV, in order to allow the full range  $0.8 \leq \cos^2(\beta - \alpha) \leq 1$ .)

We note that the bounds given in the previous paragraphs assume that the MSSM Higgs boson  $h$  decays like the SM Higgs boson (see [1]). If we assume different Higgs decay branching ratios, somewhat different bounds can be obtained. For example, assuming  $h$  decays completely into  $\tau\bar{\tau}$  gives a stricter bound on the  $hZZ$  coupling for a wide range of  $m_h$ . The LEP collaboration even considered the extreme case in which the Higgs decays invisibly. In this case, the bound on the  $hZZ$  coupling as a function of  $m_h$  is in general not much worse than if we assume that the Higgs decays like a SM Higgs. In fact, for some range of  $m_h$  the bound is even stricter if we assume that the Higgs decays invisibly [3].

The lower bound on  $m_h$  is also model dependent. For example, in [1], figures are presented that show excluded regions in the MSSM parameter space for a variety of “benchmark” scenarios that consist of different choices for the MSSM parameters. The LEP collaboration found that the lower bound on  $m_h$  can be slightly less than 93 GeV in certain cases. Moreover, the authors in [4] claim that there are certain regions in parameter space for which the  $ZZh$  coupling and the  $h/A \rightarrow b\bar{b}$  branching ratios are both suppressed and that this allows  $m_h$  to be substantially less than 93 GeV.

## 2.2.2 Implications for the MSSM stop sector

Since the tree-level mass of the lighter neutral Higgs is bounded above by  $m_Z$ , it is clear that substantial radiative corrections are required to push the lighter Higgs mass above 114.4 GeV in the Higgs decoupling limit.

We now discuss why substantial radiative corrections to the tree-level Higgs masses are also

required if the lighter Higgs mass is near 93 GeV. This is most easily seen in the large  $\tan\beta$  limit. In this limit, the CP-even Higgs mass squared matrix in the  $(H_d, H_u)$  basis is particularly simple if we only include the tree-level pieces and the dominant radiative corrections. Since  $\tan\beta$  is large, the vacuum expectation value  $v_d$  vanishes in this limit, and the Higgs vacuum expectation value is thus completely determined by  $v_u$ . In the absence of any radiative corrections, one of the physical Higgs mass eigenstates lies completely in the  $H_u$  direction and thus behaves like the SM Higgs (with a mass equal to  $m_Z$ ), whereas the other mass eigenstate lies completely in the  $H_d$  direction (with a mass equal to the mass of the CP-odd Higgs,  $m_A$ ). This alignment of the two physical CP-even Higgs mass eigenstates with the  $H_u$  and  $H_d$  direction, respectively, remains unchanged when only the dominant radiative correction is added. The reason for this is that, due to the large top Yukawa coupling, the dominant radiative corrections to the Higgs sector are to the up-type Higgs soft supersymmetry breaking Lagrangian mass and come from loops involving the top quark and stop squarks [5, 6, 7]. This gives a correction to the  $H_u$ - $H_u$  component of the CP-even Higgs mass squared matrix. The matrix is thus particularly simple for large  $\tan\beta$ , and is given by

$$\mathcal{M}^2 \approx \begin{pmatrix} m_A^2 & 0 \\ 0 & m_Z^2 + \delta\mathcal{M}_{uu}^2 \end{pmatrix} \quad (\text{for large } \tan\beta), \quad (2.3)$$

where  $\delta\mathcal{M}_{uu}^2$  is the dominant top/stop correction. Since the  $H_u$ - $H_u$  component for large  $\tan\beta$  gives the mass of the physical Higgs that behaves like the SM Higgs, its value is bounded below by 114.4 GeV, i.e.

$$m_Z^2 + \delta\mathcal{M}_{uu}^2 \gtrsim (114.4 \text{ GeV})^2. \quad (2.4)$$

The result in equation (2.4) is independent of whether the lighter or the heavier Higgs lies in the  $H_u$  direction (this depends on the size of  $m_A$ ). It also shows that the lower bound on the size of the required radiative corrections is fixed and independent of the mass of the lighter Higgs, at least in the large  $\tan\beta$  limit including only the leading corrections. Moreover, it is

$m_H$  which acquires the dominant radiative corrections for  $m_h \simeq 93$  GeV.

A simple estimate of the lower bounds on the stop masses in the large  $\tan\beta$  limit may be obtained using equation (2.4). For large  $\tan\beta$ , the dominant radiative correction is given by

$$\delta\mathcal{M}_{uu}^2 \simeq \frac{3g^2 m_t^4}{8\pi^2 m_W^2} \left\{ \ln\left(\frac{m_{\tilde{t}}^2}{m_t^2}\right) + \frac{X_t^2}{m_t^2} \left(1 - \frac{X_t^2}{12m_t^2}\right) \right\}, \quad (2.5)$$

where  $m_t$  is the top mass,  $g$  is the  $SU(2)_L$  gauge coupling, and  $m_W$  is the mass of the  $W$ -bosons [5, 6, 7]. Furthermore, equation (2.5) assumes that the stop soft masses are equal to  $m_{\tilde{t}}$ , with  $m_{\tilde{t}} \gg m_t$ . The stop mixing parameter is given by  $X_t = A_t - \mu \cot\beta$  ( $\simeq A_t$  for large  $\tan\beta$ ), where  $A_t$  denotes the stop soft trilinear coupling and  $\mu$  is the supersymmetric Higgsino mass parameter. The dependence on the top mass to the fourth power is particularly noteworthy. The first term in equation (2.5) comes from renormalization group running of the Higgs quartic coupling below the stop mass scale and vanishes in the limit of exact supersymmetry. It grows logarithmically with the stop mass. The second term is only present for non-zero stop mixing and comes from a finite threshold correction to the Higgs quartic coupling at the stop mass scale. It is independent of the stop mass for fixed  $X_t/m_{\tilde{t}}$ , and grows linearly as  $(X_t/m_{\tilde{t}})^2$  for small  $X_t/m_{\tilde{t}}$ .

It is apparent from equation (2.5) that the mixing term is important for determining lower bounds on the stop masses. Using equation (2.5) and assuming no mixing ( $X_t = 0$ ), we require  $m_{\tilde{t}} \gtrsim 570$  GeV in order to satisfy the LEP bound in (2.4). This value was obtained using a running top mass of  $m_t(m_t) \simeq 167$  GeV [8, 9]. The second (mixing) term in equation (2.5), however, reaches a maximum of 3 for  $X_t = \sqrt{6}m_{\tilde{t}}$ , called *maximal-mixing*. In order for the logarithm of the first term to be of the same order,  $m_{\tilde{t}}$  needs to be about 750 GeV. Thus the mixing term alone is more than enough to give the required radiative corrections to satisfy the LEP bound. Mixing in the stop sector therefore allows for much smaller stop masses.

There are other radiative corrections to the Higgs masses which are important, including negative radiative corrections that come from charginos, for example. In Section 2.3, we include all the important radiative corrections to determine more accurate lower bounds on the stop

masses. For example, for no stop mixing and  $\tan\beta = 50$ , a more accurate lower bound is given by  $m_{\tilde{t}} \gtrsim 980$  GeV, assuming a physical top mass of 173 GeV,  $\mu = 200$  GeV, and a bino and wino mass of 100 GeV and 200 GeV, respectively. This shows the importance of including higher order corrections to the Higgs sector. Moreover, the lower bound is approximately the same for  $m_h \simeq 93$  GeV and for  $m_h \geq 114.4$  GeV, as expected for large  $\tan\beta$ .

The above discussion assumes that  $\tan\beta$  is large. In Section 2.3, we obtain lower bounds on  $m_{\tilde{t}}$  also for small and moderate values of  $\tan\beta$ , for which the off-diagonal elements in the Higgs mass matrix become important. In general, we find that the stop masses and/or mixing have to be sizeable for all values of  $\tan\beta$  and for both the Higgs decoupling and non-decoupling regions. However, depending on the size of the stop mixing, the lower bounds on the stop masses for moderate values of  $\tan\beta$  can be smaller for  $m_h \simeq 93$  GeV than for  $m_h \geq 114.4$  GeV (see also [10]). Moreover, for small values of  $\tan\beta$ , the lower bounds on the stop masses become larger for  $m_h \simeq 93$  GeV than for  $m_h \geq 114.4$  GeV.

### 2.3 Lower bounds on the stop masses

In this section, we present lower bounds on the stop masses consistent with the LEP Higgs bounds, and we discuss their dependence on some of the other MSSM parameters. In particular, we set lower bounds on the left-handed and right-handed stop soft mass,  $m_{\tilde{t}_L}$  and  $m_{\tilde{t}_R}$ , respectively, taking both equal to a common value, which we denote by  $m_{\tilde{t}}$ . We denote the lower bound on  $m_{\tilde{t}}$  consistent with the LEP Higgs bounds by  $m_{\tilde{t},\min}$ . We consider the two scenarios given in equations (2.1) and (2.2), namely the Higgs decoupling limit with  $m_h \geq 114.4$  GeV (Section 2.3.1), and near the Higgs non-decoupling limit with  $m_h \simeq 93$  GeV, and the additional constraints  $\cos^2(\beta - \alpha) \geq 0.8$  and  $m_H \geq 114.4$  GeV (Section 2.3.3). In addition, in Section 2.3.2, we give lower bounds on the stop soft masses as a function of the physical Higgs boson mass  $m_h$  in the decoupling limit. All the lower bounds on the stop masses that we present are consistent with the  $2\sigma$  constraint on  $\delta\rho$  (which is related to the electroweak  $T$ -parameter). In Section 2.4, we discuss the importance of this parameter, as well as others, in constraining the

stop masses.

### 2.3.1 Lower bounds on the stop masses for $m_h \geq 114.4$ GeV

For a given set of parameters, we minimize  $m_{\tilde{t}}$  by starting it at the lowest value that gives physical stop masses above 100 GeV and increasing it until  $m_h$  is above 114.4 GeV. We choose the physical stop mass to be at least 100 GeV since this bound is illustrative of the actual, slightly model dependent, lower bound obtained from the Tevatron [11]. The Higgs masses were calculated with version 2.2.7 of the program `FeynHiggs` which includes all the important radiative corrections to the Higgs sector [12, 13, 14, 15]. We set  $m_A = 1000$  GeV to ensure that we are in the Higgs decoupling limit.

In Fig. 2.1, we show  $m_{\tilde{t},\min}$  as a function of  $\tan\beta$  for stop mixing  $X_t/m_{\tilde{t}} = 0, \pm 1$ , and  $\pm 2$ . All squark, slepton, and gaugino soft masses are equal to  $m_{\tilde{t}}$ ,  $\mu = 200$  GeV,  $m_t = 173$  GeV, and all the soft trilinear couplings are equal to the stop soft trilinear coupling,  $A_t = X_t + \mu \cot\beta$ . The lower solid line shows the *maximal-mixing* scenario,<sup>1</sup>  $X_t = 2m_{\tilde{t}}$ , which approximately maximizes the radiative corrections to the Higgs sector for a given set of parameters [19]. The dot-dashed line shows the *no-mixing* scenario,  $X_t = 0$ , which approximately minimizes the radiative corrections to the Higgs sector for a given set of parameters. The lower dashed line shows the results for  $X_t = m_{\tilde{t}}$ . An *intermediate-mixing* scenario with  $X_t = -m_{\tilde{t}}$  is represented by the upper dashed line. We choose this scenario since  $A_t$  has a strongly attractive infrared quasi-fixed point at  $A_t = -M_3$ , see Appendix 2.8. Thus,  $A_t$  prefers to be negative due to renormalization group evolution from the high scale down to the low scale (we choose the convention in which  $M_3$  is positive). In addition, we consider a scenario which maximizes the Higgs mass for negative stop mixing, and call it *natural maximal mixing*. This scenario is given by  $X_t = -2m_{\tilde{t}}$  and is represented by the upper solid-line in the figure.

---

<sup>1</sup>The word ‘‘maximal’’ refers to the size of the radiative corrections, not to the amount of mixing. Maximal mixing in `FeynHiggs` is obtained by setting  $X_t \simeq 2m_{\tilde{t}}$ , and not  $X_t = \sqrt{6}m_{\tilde{t}}$  as in Section 2.2.2. In the former case,  $X_t$  is defined in the on-shell scheme used in the diagrammatic two-loop results incorporated into `FeynHiggs`, whereas in the latter it is defined in the  $\overline{MS}$ -scheme used in the RG approach. Moreover,  $m_h$  is not symmetric with respect to  $X_t$  in the full two-loop diagrammatic calculation in the on-shell scheme. For example,  $m_h$  can be up to 5 GeV larger for  $X_t = +2m_{\tilde{t}}$  than for  $X_t = -2m_{\tilde{t}}$ . The difference arises from non-logarithmic two-loop contributions to  $m_h$ , see [16, 17, 18].

A feature that is common to all the curves is that  $m_{\tilde{\tau}}$  becomes very large for small  $\tan\beta$ . This is because the tree-level contribution to the Higgs mass in the decoupling limit is given by  $m_h^{\text{tree}} \simeq |\cos 2\beta| m_Z$ , and goes to zero as  $\tan\beta$  approaches 1. Larger radiative corrections, and thus larger stop masses, are therefore required for smaller  $\tan\beta$  to push  $m_h$  above 114.4 GeV.

Fig. 2.1 clearly shows that mixing in the stop sector has a large impact on the values of  $m_{\tilde{\tau},\text{min}}$ , with larger mixing allowing much smaller values of  $m_{\tilde{\tau},\text{min}}$  (see also [20, 21]). For large  $\tan\beta$ , the difference in  $m_{\tilde{\tau},\text{min}}$  between no mixing and maximal mixing is about 1000 GeV, with  $m_{\tilde{\tau},\text{min}} = 1260$  GeV for  $\tan\beta = 50$  in the no-mixing case.

A plot of the two *physical* stop masses,  $m_{\tilde{t}_1}$  and  $m_{\tilde{t}_2}$ , versus  $\tan\beta$  is given in Fig. 2.2 for no mixing and for natural maximal mixing. For no mixing, there is no discernible difference in the two stop masses since the only difference that arises is from small  $SU(2)_L$  and  $U(1)_Y$  D-term quartic interactions. For appreciable mixing, the two physical stop masses are split by an amount that is on the order of  $\sim \sqrt{m_t X_t}$ . For  $X_t = -2m_{\tilde{\tau}}$  and  $\tan\beta \geq 7$ ,  $m_{\tilde{\tau},\text{min}}$  is small enough that the lighter physical stop mass is all the way down at its experimental lower bound of roughly 100 GeV. For this range of  $\tan\beta$ , we find that  $m_{\tilde{\tau}}$  is larger than that which is required to get  $m_h$  just above 114.4 GeV, and thus  $m_h$  is several GeV above 114.4 GeV here.

The current value of the top mass from the CDF and D0 experiments at Fermilab is  $m_t = 171.4 \pm 2.1$  GeV [22]. The values obtained for  $m_{\tilde{\tau},\text{min}}$  are, however, extremely sensitive to slight variations in the value of the top mass (see also [20]). It is thus illustrative to plot  $m_{\tilde{\tau},\text{min}}$  as a function of  $\tan\beta$  for various amounts of stop mixing and for three choices of the top mass: 168 GeV, 173 GeV and 178 GeV. The plots are shown in Fig. 2.3, 2.4 and 2.5 for  $X_t/m_{\tilde{\tau}} = 0, -1,$  and  $-2$ , respectively. These plots again assume that all squark, slepton, and gaugino soft masses are equal to  $m_{\tilde{\tau}}$ ,  $\mu = 200$  GeV, and all the soft trilinear couplings are equal to  $A_t$ .

All three figures show that  $m_{\tilde{\tau},\text{min}}$  is extremely sensitive to small changes in  $m_t$  for small  $\tan\beta$ . For intermediate and vanishing stop mixing, this sensitivity persists for large  $\tan\beta$ . For example, in the no-mixing case for  $\tan\beta = 50$ , we find  $m_{\tilde{\tau},\text{min}} \simeq 870$  GeV, 1260 GeV, and 2570 GeV for  $m_t = 178$  GeV, 173 GeV, and 168 GeV, respectively. The very large value of  $m_{\tilde{\tau},\text{min}}$

for  $m_t = 168$  GeV is particularly noteworthy, especially if the central value of the measured top mass keeps decreasing slightly as more data from the Tevatron becomes available.

So far we assumed that the gaugino masses are all equal to  $m_{\tilde{t}}$ . The bino and wino masses,  $M_1$  and  $M_2$ , as well as  $\mu$  contribute to the Higgs masses at one loop, whereas the gluino mass,  $M_3$ , only appears at two loops (see e.g. [9, 13, 23] and references therein). Since large values of  $M_1$ ,  $M_2$  and  $\mu$  can give important *negative* contributions to the Higgs masses [24], smaller values of  $m_{\tilde{t},\min}$  are possible for smaller values of  $M_1$ ,  $M_2$  and  $\mu$ . For example, setting  $M_1 = 100$  GeV,  $M_2 = 200$  GeV and  $M_3 = 800$  GeV, we find in the no-mixing case for  $\tan\beta = 50$  that  $m_{\tilde{t},\min} \simeq 760$  GeV, 980 GeV, and 1410 GeV for  $m_t = 178$  GeV, 173 GeV and 168 GeV, respectively. This may be compared with the values given in the previous paragraph for the case where all the gaugino masses are equal to  $m_{\tilde{t}}$ . Thus, setting the bino and wino masses to smaller values decreases the size of  $m_{\tilde{t},\min}$ , especially if  $m_t$  is small. However, the large value of  $m_{\tilde{t},\min}$  for  $m_t = 168$  GeV is still noteworthy.

We show a further example of how a different choice for  $M_1$  and  $M_2$  affects  $m_{\tilde{t},\min}$  in Fig. 2.6 for the no-mixing and natural-maximal-mixing scenario. For each scenario, this figure shows a case for which  $M_1$  and  $M_2$  are both large ( $M_1 = M_2 = 800$  GeV) or both small ( $M_1 = 100$  GeV,  $M_2 = 200$  GeV). In both cases,  $M_3$  is fixed to be 800 GeV,  $\mu = 200$  GeV,  $m_t = 173$  GeV, all squark and slepton soft masses are equal to the stop soft masses, and all the soft trilinear couplings are equal to  $A_t$ . The plots show that  $m_{\tilde{t},\min}$  is smaller for smaller values of  $M_1$  and  $M_2$ . For example,  $m_{\tilde{t},\min}$  is about 160 GeV smaller in the no-mixing case for  $\tan\beta = 50$  when choosing the smaller set of values for  $M_1$  and  $M_2$ , and the difference in  $m_{\tilde{t},\min}$  grows as  $\tan\beta$  decreases. For natural maximal mixing, no difference can be seen for most  $\tan\beta$  values, since here the condition  $m_{\tilde{t}_1} \geq 100$  GeV again requires larger values of  $m_{\tilde{t},\min}$  than the condition  $m_h \geq 114.4$  GeV. However, there is a difference in  $m_{\tilde{t},\min}$  for smaller  $\tan\beta$ , which again grows as  $\tan\beta$  decreases.

Fig. 2.6 also shows how a change in the gluino mass,  $M_3$ , affects  $m_{\tilde{t},\min}$ . In general,  $m_h$  tends to be maximized for  $M_3 \simeq 0.8m_{\tilde{t}}$  [13]. In this figure, we compare  $m_{\tilde{t},\min}$  for two different

gluino masses, namely  $M_3 = 800$  GeV and  $M_3 = 1500$  GeV. The figure shows that the effect is not very large for this choice of parameters. However, the gluino mass can significantly affect the Higgs masses, and therefore  $m_{\tilde{t},\min}$ , for large  $\tan\beta$  and large and *negative*  $\mu$ .

The variation of  $m_h$  as a function of  $\mu$  does not generally exceed about 3 GeV [13]. However, it can become very large if one includes the all-order resummation of the  $\tan\beta$  enhanced terms of order  $\mathcal{O}(\alpha_b(\alpha_s \tan\beta)^n)$ , where  $\alpha_b = \lambda_b^2/4\pi$  and  $\lambda_b$  is the bottom Yukawa coupling [25, 26, 27, 28, 29, 30, 31]. This resummation is included in `FeynHiggs`. The origin of the enhancement is a change in the bottom Yukawa coupling due to a loop containing, for example, a gluino and a sbottom squark. The leading corrections to the bottom Yukawa coupling can be incorporated into the one-loop result for the Higgs masses by the use of an effective bottom mass,  $m_b^{\text{eff}}$ . Large  $|\mu| \tan\beta$  can substantially change the effective bottom mass  $m_b^{\text{eff}}$  from its  $\overline{\text{MS}}$  value. *Positive*  $\mu$  can substantially *decrease*  $m_b^{\text{eff}}$ , making the sbottom/bottom sector corrections to  $m_h$  negligible. *Negative*  $\mu$  on the other hand can substantially *increase*  $m_b^{\text{eff}}$ , making the sbottom/bottom sector corrections to  $m_h$  important. The bottom/sbottom corrections to  $m_h$  are negative in the latter case. Larger stop masses are then required for large and negative  $\mu$  as  $\tan\beta$  increases to enhance the positive radiative corrections from the stop/top.

This effect can be seen in Fig. 2.7 where we compare  $\mu = +200$  GeV and  $\mu = \pm 500$  GeV for natural maximal stop mixing. This figure again assumes that all squark, slepton, and gaugino soft masses are equal to the stop soft masses,  $m_t = 173$  GeV, and all the soft trilinear couplings are equal to  $A_t$ . For large  $\tan\beta$ , slightly larger  $m_{\tilde{t},\min}$  are required for  $\mu = -500$  GeV than when  $\mu$  is positive (the effect would be stronger for even larger negative  $\mu$ ). Note that for small values of  $\tan\beta$  there is a region for which  $m_{\tilde{t}}$  is larger for both  $\mu = -500$  GeV and  $\mu = +500$  GeV than for  $\mu = 200$  GeV. As we discussed above, this is because larger chargino and neutralino masses decrease the size of  $m_h$ .

Since the gluino mass also enters the equation that determines  $m_b^{\text{eff}}$ , it can have a significant impact on  $m_h$  for large  $\tan\beta$  and large negative values of  $\mu$  as demonstrated in [31]. Thus, some non-negligible dependence of  $m_{\tilde{t},\min}$  on the gluino mass is expected for negative and large

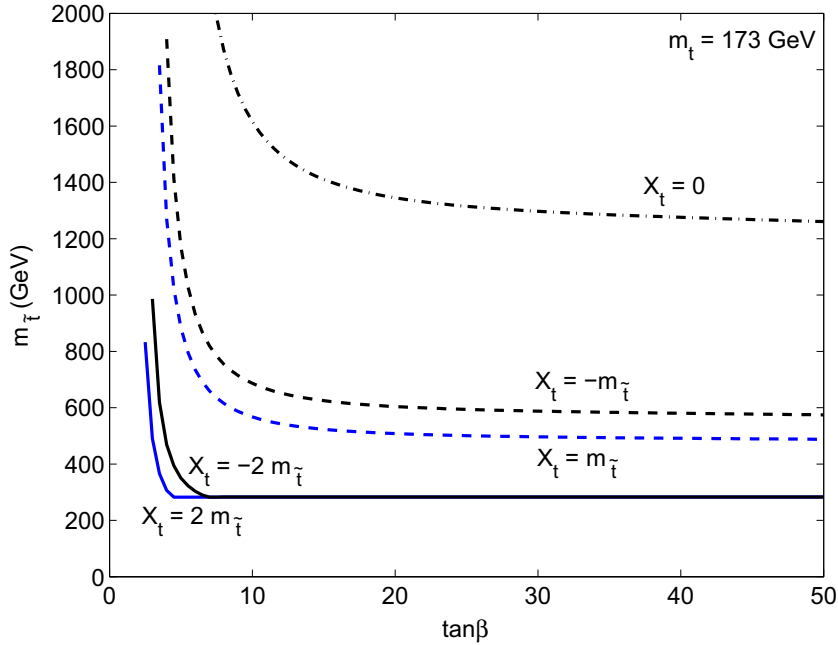


Figure 2.1: Minimum stop soft masses,  $m_{\tilde{t}} \equiv m_{\tilde{t}_L} = m_{\tilde{t}_R}$ , for  $m_h \geq 114.4$  GeV as a function of  $\tan\beta$  for stop mixing  $X_t/m_{\tilde{t}} = 0, \pm 1, \pm 2$ . All squark, slepton, and gaugino soft masses are equal to the stop soft masses,  $\mu = 200$  GeV,  $m_A = 1000$  GeV,  $m_t = 173$  GeV, and all soft trilinear couplings are equal to  $A_t = X_t + \mu \cot\beta$ .

$\mu$ .

### 2.3.2 Lower bounds on the stop masses as function of the Higgs mass

In this section, we present lower bounds on the stop soft masses,  $m_{\tilde{t}} \equiv m_{\tilde{t}_L} = m_{\tilde{t}_R}$ , as a function of the Higgs mass,  $m_h$ . We assume the decoupling limit ( $m_A = 1000$  GeV), and we set all squark and slepton soft masses equal to the stop soft masses,  $\mu = 200$  GeV,  $m_t = 173$  GeV,  $M_1 = 100$  GeV,  $M_2 = 200$  GeV,  $M_3 = 800$  GeV,  $\tan\beta = 30$ , and all the soft trilinear couplings equal to  $A_t$ . We allow  $m_h$  to range from 100 GeV upwards. This means that the values obtained for  $m_{\tilde{t}}$  in the range  $m_h \in [100, 114.4]$  GeV will be lower than those consistent with the LEP results, since we set no additional constraints on  $\cos^2(\beta - \alpha)$  and  $m_H$ . However, the main point here is to show the dependence of  $m_{\tilde{t}}$  on  $m_h$  without any other constraints. The lower bounds on  $m_{\tilde{t}}$  are required to give physical stop masses not less than 100 GeV.

We show the results for different amounts of stop mixing in Fig. 2.8. This figure shows

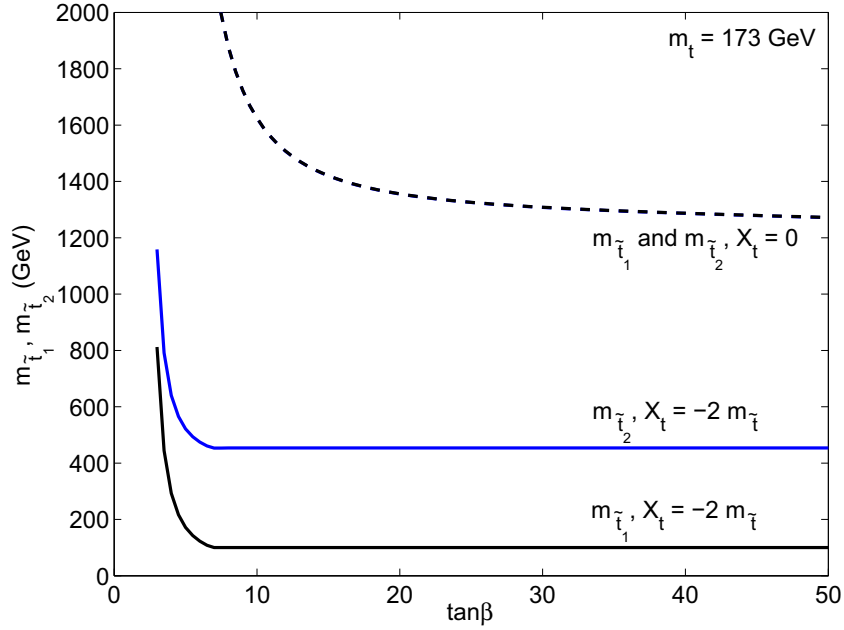


Figure 2.2: Minimum physical stop masses,  $m_{\tilde{t}_1}$  and  $m_{\tilde{t}_2}$ , for  $m_h \geq 114.4$  GeV as a function of  $\tan\beta$  for vanishing stop mixing ( $X_t = 0$ ) and natural maximal stop mixing ( $X_t/m_{\tilde{t}} = -2$ ). Other parameters are as given in Fig. 2.1.

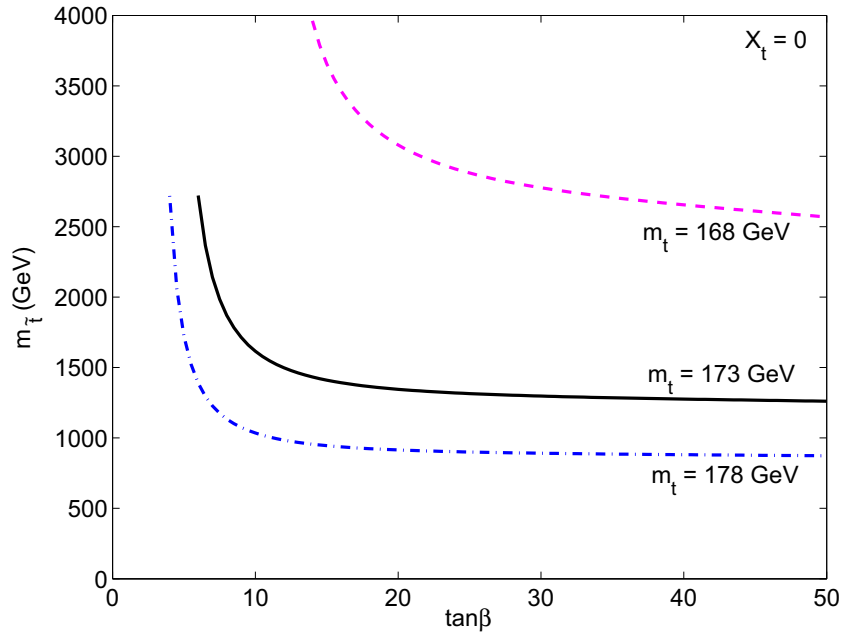


Figure 2.3: Minimum stop soft masses,  $m_{\tilde{t}} \equiv m_{\tilde{t}_L} = m_{\tilde{t}_R}$ , for  $m_h \geq 114.4$  GeV as a function of  $\tan\beta$  for vanishing stop mixing ( $X_t = 0$ ) for a top quark mass of  $m_t = 168, 173, 178$  GeV. Other parameters are as given in Fig. 2.1.

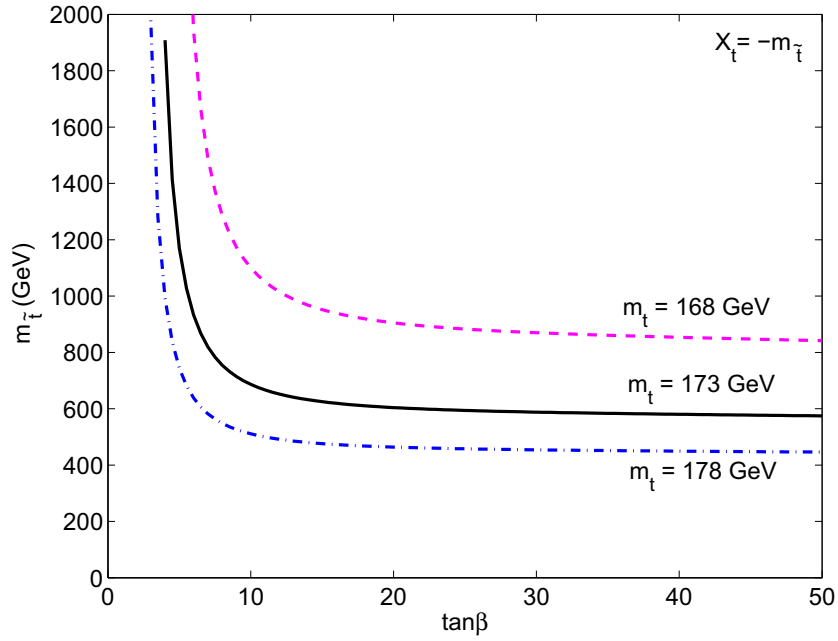


Figure 2.4: Minimum stop soft masses,  $m_{\tilde{t}} \equiv m_{\tilde{t}_L} = m_{\tilde{t}_R}$ , for  $m_h \geq 114.4$  GeV as a function of  $\tan\beta$  for intermediate stop mixing ( $X_t/m_{\tilde{t}} = -1$ ) for a top quark mass of  $m_t = 168, 173, 178$  GeV. Other parameters are as given in Fig. 2.1.

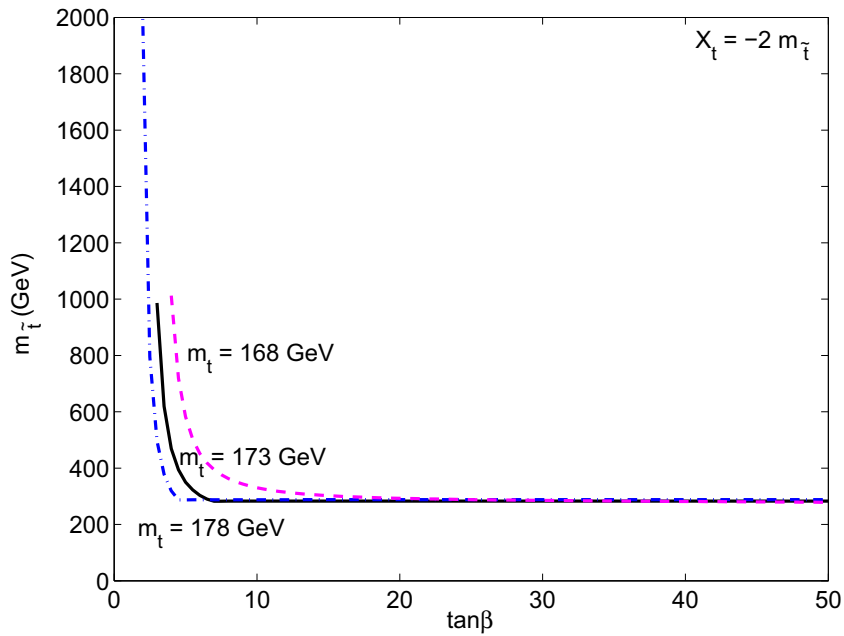


Figure 2.5: Minimum stop soft masses,  $m_{\tilde{t}} \equiv m_{\tilde{t}_L} = m_{\tilde{t}_R}$ , for  $m_h \geq 114.4$  GeV as a function of  $\tan\beta$  for natural maximal stop mixing ( $X_t/m_{\tilde{t}} = -2$ ) for a top quark mass of  $m_t = 168, 173, 178$  GeV. Other parameters are as given in Fig. 2.1.

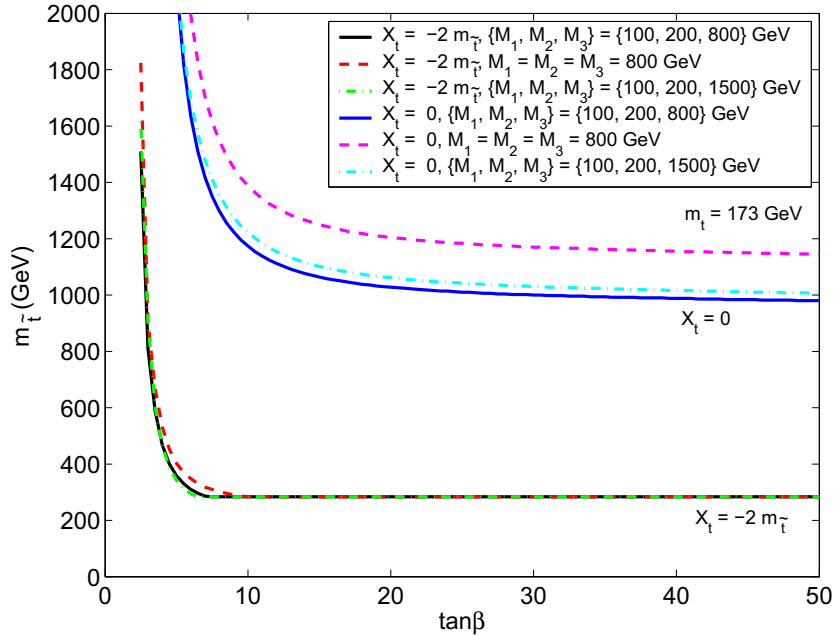


Figure 2.6: Minimum stop soft masses,  $m_{\tilde{t}} \equiv m_{\tilde{t}_L} = m_{\tilde{t}_R}$ , for  $m_h \geq 114.4$  GeV as a function of  $\tan\beta$  for various values of the bino, wino, and gluino soft masses,  $M_1, M_2, M_3$ . The upper three lines are for vanishing stop mixing ( $X_t = 0$ ) and the lower three for natural maximal stop mixing ( $X_t/m_{\tilde{t}} = -2$ ). Other parameters are as given in Fig. 2.1.

how an increase in  $m_h$  requires an exponential increase in  $m_{\tilde{t}}$ . In addition to the no-mixing, intermediate-mixing and natural-maximal-mixing cases, we also include the  $m_h^{\max}$  benchmark scenario ( $X_t = +2m_{\tilde{t}}$ ) (but with  $\mu = +200$  GeV, not  $\mu = -200$  GeV) [24]. This benchmark scenario is designed to maximize the Higgs mass for a given set of parameters. Moreover, we choose  $M_3 = 800$  GeV for all cases, with the exception of the latter one. In the latter benchmark scenario, we choose the benchmark value  $M_3 = 0.8m_{\tilde{t}}$  instead, which gives slightly higher values for  $m_h$  [24].

It is clear from the figure that there is some value of  $m_h$  at which a further small increase in  $m_h$  would require an extremely large increase in the stop masses. It is instructive to obtain the values of  $m_h$  from the figure if, for example,  $m_{\tilde{t}} = 3000$  GeV. We find for no stop mixing,  $m_h \simeq 121$  GeV, for intermediate stop mixing,  $m_h \simeq 126$  GeV, for natural maximal stop mixing,  $m_h \simeq 131$  GeV, and for the  $m_h^{\max}$  benchmark scenario,  $m_h \simeq 134$  GeV (see also [32], for example, and references therein).

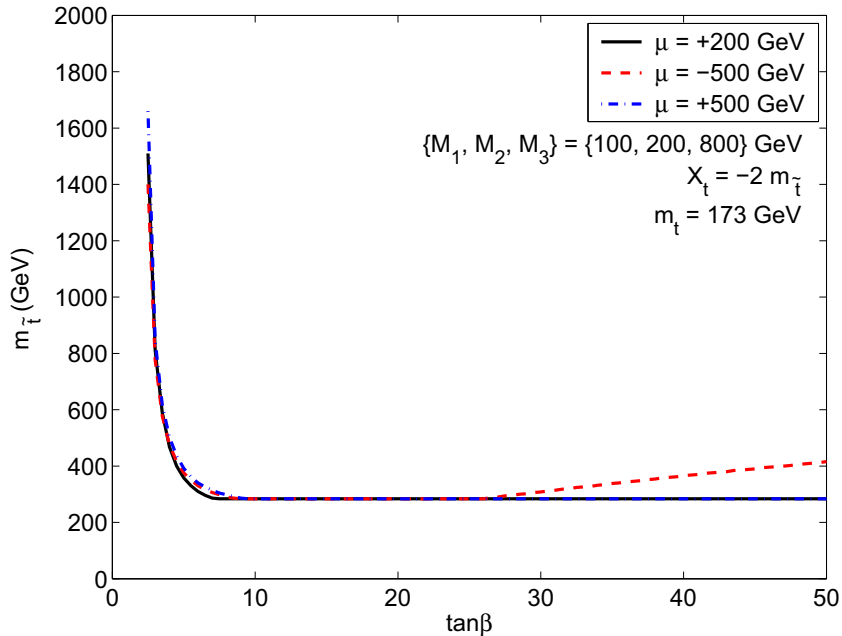


Figure 2.7: Minimum stop soft masses,  $m_{\tilde{t}} \equiv m_{\tilde{t}_L} = m_{\tilde{t}_R}$ , for  $m_h \geq 114.4$  GeV as a function of  $\tan\beta$  for natural maximal stop mixing ( $X_t/m_{\tilde{t}} = -2$ ) with  $\mu = -500, 200, 500$  GeV and bino, wino, and gluino soft masses of  $M_1 = 100$  GeV,  $M_2 = 200$  GeV,  $M_3 = 800$  GeV. Other parameters are as given in Fig. 2.1.

Since  $A_t$  and  $M_3$  most naturally have the opposite sign due to renormalization group running and the presence of a strongly attractive quasi-fixed point (see Appendix 2.8), a negative value of  $A_t$  is more natural. For negative  $A_t$ , the upper bound of  $m_h$  in the MSSM is around 131 GeV.

### 2.3.3 Lower bounds on the stop masses for $m_h \simeq 93$ GeV

In this section, we present results for the minimum stop soft masses,  $m_{\tilde{t}} \equiv m_{\tilde{t}_L} = m_{\tilde{t}_R}$ , as a function of  $\tan\beta$ , for various choices of the other MSSM parameters, and consistent with the following set of constraints on the Higgs sector obtained by LEP:  $m_h \simeq 93$  GeV,  $\cos^2(\beta-\alpha) \geq 0.8$  and  $m_H \geq 114.4$  GeV (see equation (2.2)).

The mass  $m_A$  is allowed to be a free parameter, since  $m_{\tilde{t}}$  needs to be minimized without enforcing the decoupling limit. We vary  $m_A$  between 93.5 GeV and 1000 GeV from the bottom up for a given choice of  $m_{\tilde{t}}$  and other MSSM parameters, until the conditions  $93 \text{ GeV} \leq m_h \leq$

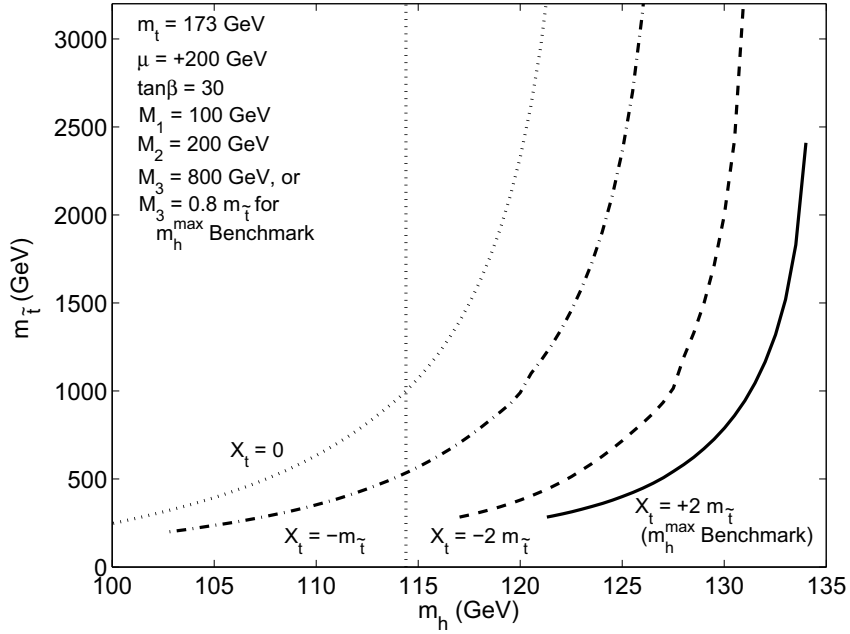


Figure 2.8: Minimum stop soft masses,  $m_{\tilde{t}} \equiv m_{\tilde{t}_L} = m_{\tilde{t}_R}$ , as a function of  $m_h$ . All squark and slepton soft masses are equal to the stop soft masses,  $\mu = 200 \text{ GeV}$ ,  $m_t = 173 \text{ GeV}$ ,  $\{M_1, M_2\} = \{100, 200\} \text{ GeV}$ ,  $\tan\beta = 30$ , and all the soft trilinear couplings are equal to  $A_t = X_t + \mu \cot\beta$ . In the figure, the curved lines from left to right are as follows: the dotted line is for no mixing ( $X_t/m_{\tilde{t}} = 0$ ), the dash-dot line for intermediate mixing ( $X_t/m_{\tilde{t}} = -1$ ), the dashed line for natural maximal mixing ( $X_t/m_{\tilde{t}} = -2$ ), and the solid line for the  $m_h^{\max}$  benchmark scenario ( $X_t/m_{\tilde{t}} = +2$ ) [24]. The gluino mass is set to be  $M_3 = 800 \text{ GeV}$  in all cases except in the  $m_h^{\max}$  benchmark scenario, where  $M_3 = 0.8m_{\tilde{t}}$ . The vertical dotted line is at  $m_h = 114.4 \text{ GeV}$ , which is the lower bound set by LEP on  $m_h$  in the decoupling limit.

95 GeV,  $\cos^2(\beta - \alpha) \geq 0.8$ , and  $m_H \geq 114.4$  GeV are satisfied. (The lower bound of 93.5 GeV for  $m_A$  is the approximate lower bound obtained within the same benchmark scenarios as the bound on  $m_h$ ; it turns out that the actual values obtained for  $m_A$  are slightly larger). If these conditions cannot all be satisfied, we keep increasing  $m_{\tilde{t}}$  until they are satisfied. Note that we require the lower bounds on  $m_{\tilde{t}}$  to give physical stop masses of at least 100 GeV. We again denote the lower bounds on  $m_{\tilde{t}}$  consistent with the LEP Higgs bounds by  $m_{\tilde{t},\min}$ .

The Higgs masses,  $m_h$  and  $m_H$ , are calculated with `FeynHiggs`, and  $\cos^2(\beta - \alpha)$  is calculated using the `FeynHiggs` output of the radiatively corrected CP-even Higgs mixing angle  $\alpha$ .

In Fig. 2.9, we show  $m_{\tilde{t},\min}$  as a function of  $\tan\beta$  for stop mixing  $X_t/m_{\tilde{t}} = 0, \pm 1$ , and  $\pm 2$ . All squark, slepton, and gaugino soft masses are equal to the stop soft masses,  $\mu = 200$  GeV,  $m_t = 173$  GeV, and all the soft trilinear couplings are equal to the stop soft trilinear coupling,  $A_t$ . This figure may be compared with Fig. 2.1 in which we require  $m_h \geq 114.4$  GeV in the Higgs decoupling limit.

Next, we show  $m_{\tilde{t},\min}$  as a function of  $\tan\beta$  for different values of the top mass (168 GeV, 173 GeV and 178 GeV) and for different amounts of mixing. Fig. 2.10 is for no mixing, Fig. 2.11 is for intermediate mixing, and Fig. 2.12 is for natural maximal mixing. All squark, slepton, and gaugino soft masses are again equal to the stop soft masses,  $\mu = 200$  GeV, and all the soft tri-linear couplings are equal to  $A_t$ . These figures may be compared with the figures in which we require  $m_h \geq 114.4$  GeV in the decoupling limit, namely Figs. 2.3, 2.4 and 2.5, respectively.

We first compare  $m_{\tilde{t},\min}$  in the two scenarios  $m_h \simeq 93$  GeV and  $m_h \geq 114.4$  GeV for large  $\tan\beta$ . Here, the figures show that  $m_{\tilde{t},\min}$  is the same in the case of maximal or natural maximal mixing. For intermediate and vanishing stop mixing,  $m_{\tilde{t},\min}$  is only slightly smaller for  $m_h \simeq 93$  GeV than for  $m_h \geq 114.4$  GeV. Assuming  $m_t = 173$  GeV and  $\tan\beta = 50$ , the difference is only about 15 GeV for  $X_t = -m_{\tilde{t}}$  and 70 GeV for  $X_t = 0$ . We expected the values for  $m_{\tilde{t},\min}$  to be so similar from the discussion in Section 2.2.2.

For moderate  $\tan\beta$ ,  $m_{\tilde{t},\min}$  can be substantially smaller for  $m_h \simeq 93$  GeV than for  $m_h \geq 114.4$  GeV. This is true in particular for the no-mixing and intermediate-mixing cases, with

the difference being more pronounced for smaller values of  $m_t$ . For example, the maximum difference between  $m_{\tilde{t},\min}$  in the two scenarios is about 600 GeV for  $\tan\beta = 12.5$  if there is no mixing and  $m_t = 173$  GeV.

As  $\tan\beta$  decreases further, however,  $m_{\tilde{t},\min}$  for  $m_h \simeq 93$  GeV rises very steeply, and becomes larger than for  $m_h \geq 114.4$  GeV.

Understanding this behavior of  $m_{\tilde{t},\min}$  as a function of  $\tan\beta$  requires an understanding of the importance of the constraints  $\cos^2(\beta - \alpha) \geq 0.8$  and  $m_H \geq 114.4$  GeV. To this end, we compare  $m_{\tilde{t},\min}$  versus  $\tan\beta$  for the case that the constraint on  $m_H$  is ignored, for the case that both constraints are ignored, and for the case consistent with the LEP bounds that includes both constraints. We again make the comparison for various amounts of mixing in the stop sector. Fig. 2.13 shows the results for no mixing, Fig. 2.14 for intermediate mixing, and Fig. 2.15 for natural maximal mixing. Each of these figures has three lines. The solid line shows the results which are consistent with the LEP bounds, i.e. it includes the two constraints  $\cos^2(\beta - \alpha) \geq 0.8$  and  $m_H \geq 114.4$  GeV, in addition to requiring  $m_h \simeq 93$  GeV. The dashed line, on the other hand, does not include the constraint on  $m_H$ , but does require  $\cos^2(\beta - \alpha) \geq 0.8$  and  $m_h \simeq 93$  GeV. The dash-dot line only requires  $m_h \simeq 93$  GeV, and ignores the constraints on  $\cos^2(\beta - \alpha)$  and  $m_H$ .

As expected, both constraints from LEP in general increase  $m_{\tilde{t},\min}$ . The constraint  $\cos^2(\beta - \alpha) \geq 0.8$  is more important as  $\tan\beta$  becomes smaller, but less important as  $\tan\beta$  gets larger. The constraint  $m_H \geq 114.4$  GeV, however, is more important for larger  $\tan\beta$  (if stop mixing is not too large), but is less important as  $\tan\beta$  becomes smaller. We now explain these observations.

If the only condition is  $m_h \simeq 93$  GeV, the theory tends to be in the Higgs decoupling limit where  $\cos^2(\beta - \alpha) \rightarrow 0$ . The reason for this is that for a given set of parameters, including a given value of  $m_{\tilde{t}}$ ,  $m_h$  is maximized in the decoupling limit. (This is also the reason why ignoring both constraints is in general equivalent to ignoring only the constraint  $\cos^2(\beta - \alpha) \geq 0.8$  but keeping  $m_H \geq 114.4$  GeV as a constraint.) The constraint  $\cos^2(\beta - \alpha) \geq 0.8$ , however, forces all the MSSM Higgs masses to be quite small. In particular,  $m_A$  is forced to be relatively

small and degenerate with  $m_h$ , so that larger  $m_{\tilde{t}}$  are required to obtain the same value for  $m_h$ .<sup>2</sup> Moreover, the maximum value reached by  $\cos^2(\beta - \alpha)$  decreases as  $\tan\beta$  decreases. Larger radiative corrections, in particular larger values of  $m_{\tilde{t}}$  or more stop mixing, can increase the maximum value of  $\cos^2(\beta - \alpha)$ . However, if  $\tan\beta$  decreases too far, exponentially larger values of  $m_{\tilde{t}}$  are required to allow  $\cos^2(\beta - \alpha)$  to be greater than 0.8.

For a given set of parameters,  $m_h$  in general decreases as  $\tan\beta$  decreases. This is not the case for  $m_H$ , which in general decreases as  $\tan\beta$  increases. This explains why the constraint on  $m_H$  is more important for larger values of  $\tan\beta$ . In the decoupling limit,  $m_H$  is approximately degenerate with  $m_A$ , and larger values of  $m_{\tilde{t}}$  do not affect  $m_H$  much. In the non-decoupling limit, however, larger values of  $m_{\tilde{t}}$  can increase  $m_H$ . In fact, if we define  $m_h^{\text{max}}$  to be equal to  $m_h$  in the decoupling limit, then  $m_H \simeq m_h^{\text{max}}$  for large  $\tan\beta$  and  $\cos^2(\beta - \alpha) \simeq 1$ . This may be explained with the formula

$$m_h^2 \sin^2(\beta - \alpha) + m_H^2 \cos^2(\beta - \alpha) = (m_h^{\text{max}})^2, \quad (2.6)$$

valid for large  $\tan\beta$  [32, 33, 34, 35], and explains why larger  $m_{\tilde{t}}$  increases the value of  $m_H$  in, or near, the non-decoupling region (see also Section 2.2.2).

---

<sup>2</sup>The results for  $m_A$  for the case consistent with the LEP results (which includes both constraints) are  $m_A \in [96.1 \text{ GeV}, 99.5 \text{ GeV}]$  for natural maximal mixing,  $m_A \in [94.3 \text{ GeV}, 97.7 \text{ GeV}]$  for intermediate mixing, and  $m_A \in [95.1 \text{ GeV}, 97.7 \text{ GeV}]$  for no mixing. When the constraint on  $m_H$  is ignored,  $m_A$  lies roughly in the same range. Note that from the pair-production channel these values of  $m_h + m_A$  give upper bounds on  $\cos^2(\beta - \alpha)$  consistent with  $\cos^2(\beta - \alpha) \geq 0.8$ , depending on what one assumes for the Higgs decay branching ratios, see [1].

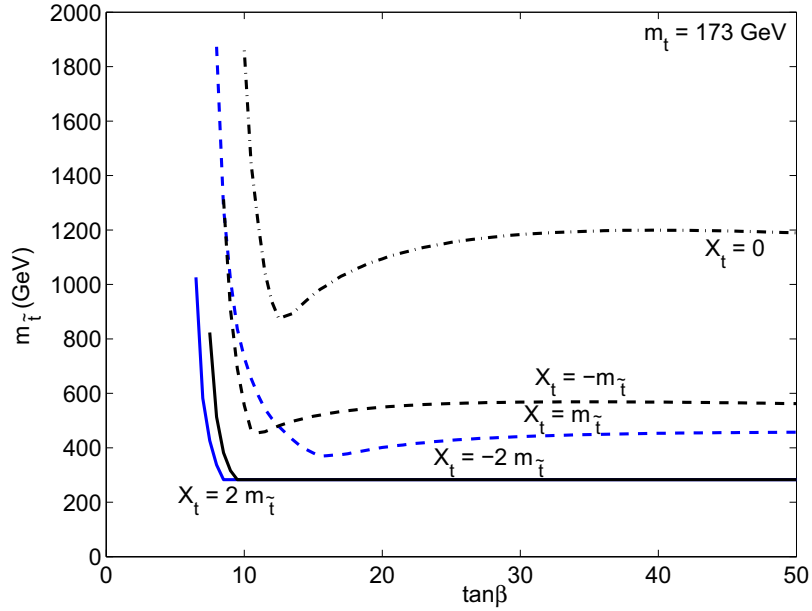


Figure 2.9: Minimum stop soft masses,  $m_{\tilde{t}} \equiv m_{\tilde{t}_L} = m_{\tilde{t}_R}$ , for  $m_h \simeq 93$  GeV,  $m_H \geq 114.4$  GeV, and  $\cos^2(\beta - \alpha) \geq 0.8$ , as a function of  $\tan\beta$  for stop mixing  $X_t/m_{\tilde{t}} = 0, \pm 1, \pm 2$ . All squark, slepton, and gaugino soft mass parameters are equal to the stop soft masses,  $\mu = 200$  GeV,  $m_t = 173$  GeV, and all soft trilinear couplings are equal to  $A_t = X_t + \mu \cot\beta$ . This figure may be compared with Fig. 2.1.

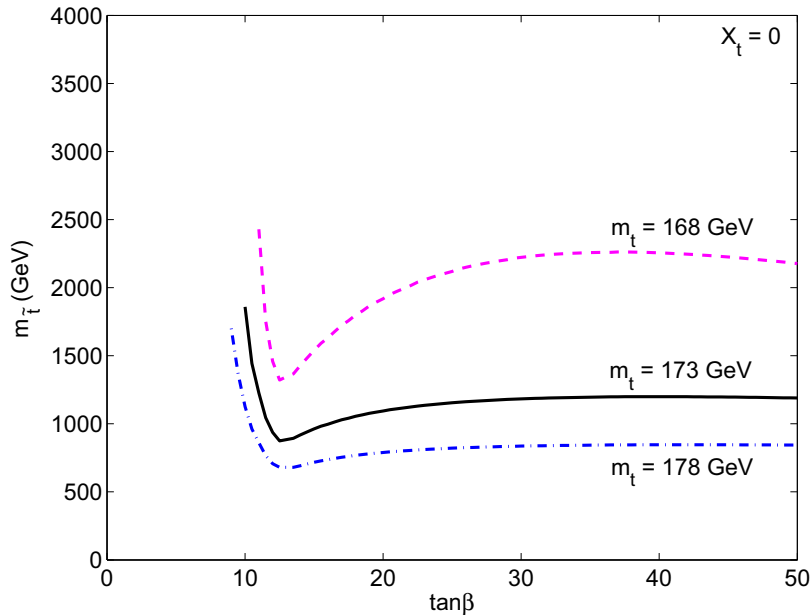


Figure 2.10: Minimum stop soft masses,  $m_{\tilde{t}} \equiv m_{\tilde{t}_L} = m_{\tilde{t}_R}$ , for  $m_h \simeq 93$  GeV,  $m_H \geq 114.4$  GeV, and  $\cos^2(\beta - \alpha) \geq 0.8$ , as a function of  $\tan\beta$  for vanishing stop mixing ( $X_t/m_{\tilde{t}} = 0$ ) for a top quark mass of  $m_t = 168, 173, 178$  GeV. Other parameters are given as in Fig. 2.9. This figure may be compared with Fig. 2.3.

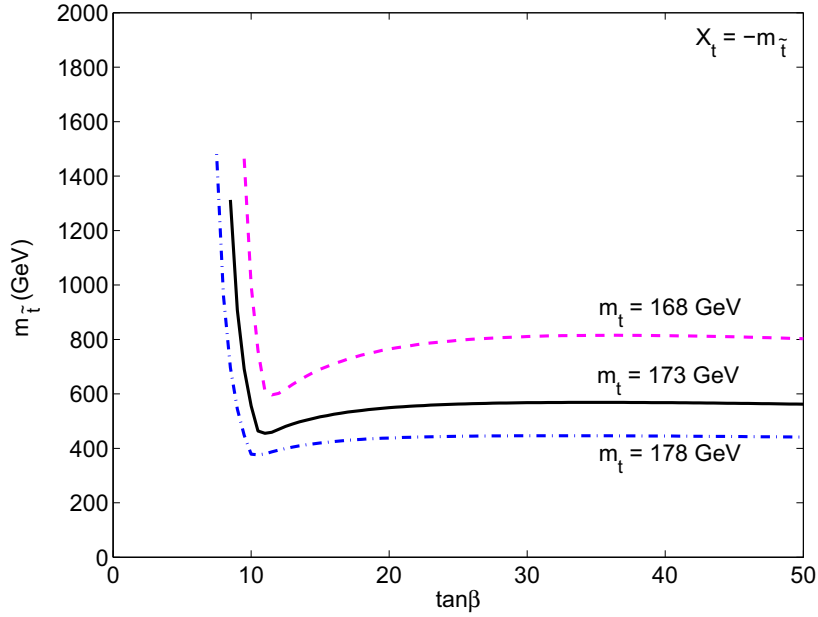


Figure 2.11: Minimum stop soft masses,  $m_{\tilde{t}} \equiv m_{\tilde{t}_L} = m_{\tilde{t}_R}$ , for  $m_h \simeq 93$  GeV,  $m_H \geq 114.4$  GeV, and  $\cos^2(\beta - \alpha) \geq 0.8$ , as a function of  $\tan\beta$  for intermediate stop mixing ( $X_t/m_{\tilde{t}} = -1$ ) for a top quark mass of  $m_t = 168, 173, 178$  GeV. Other parameters are given as in Fig. 2.9. This figure may be compared with Fig. 2.4.

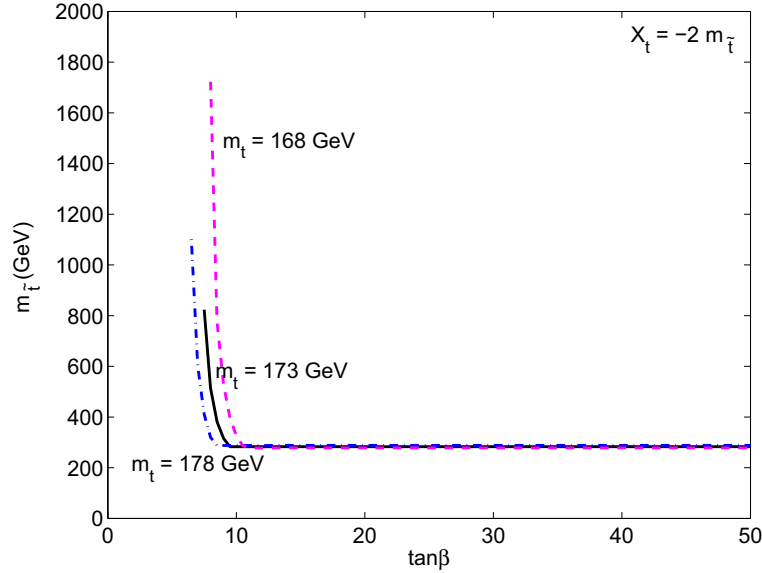


Figure 2.12: Minimum stop soft masses,  $m_{\tilde{t}} \equiv m_{\tilde{t}_L} = m_{\tilde{t}_R}$ , for  $m_h \simeq 93$  GeV,  $m_H \geq 114.4$  GeV, and  $\cos^2(\beta - \alpha) \geq 0.8$ , as a function of  $\tan\beta$  for natural maximal stop mixing ( $X_t/m_{\tilde{t}} = -2$ ) for a top quark mass of  $m_t = 168, 173, 178$  GeV. Other parameters are given as in Fig. 2.9. This figure may be compared with Fig. 2.5.

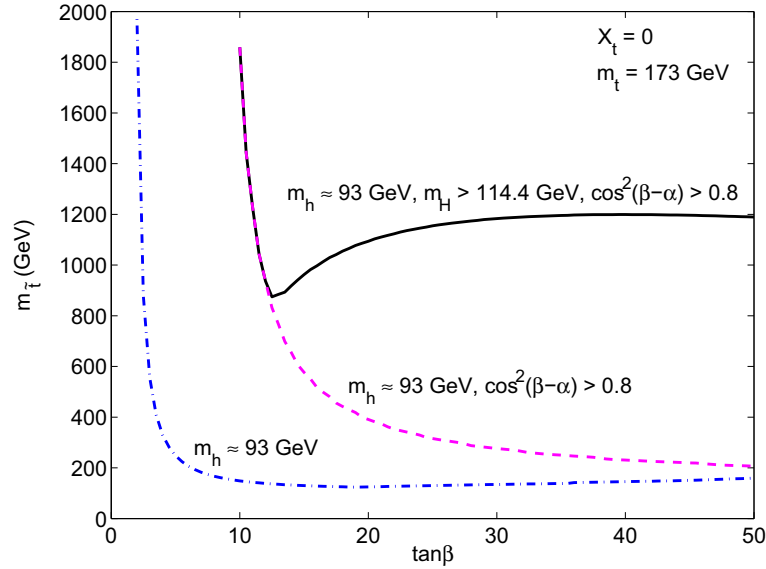


Figure 2.13: Minimum stop soft masses,  $m_{\tilde{t}} \equiv m_{\tilde{t}_L} = m_{\tilde{t}_R}$ , as a function of  $\tan\beta$ , for no stop mixing ( $X_t/m_{\tilde{t}} = 0$ ). The solid line shows the minimum stop soft masses for  $m_h \simeq 93$  GeV,  $m_H \geq 114.4$  GeV, and  $\cos^2(\beta - \alpha) \geq 0.8$ , consistent with the LEP Higgs bounds. The dashed and dash-dot lines are not consistent with the LEP bounds and used for comparison. The dashed line shows the minimum soft masses for  $m_h \simeq 93$  GeV and  $\cos^2(\beta - \alpha) \geq 0.8$  and without a constraint on  $m_H$ . The dash-dot line shows the minimum soft masses for  $m_h \simeq 93$  GeV and without constraints on  $m_H$  and  $\cos^2(\beta - \alpha)$ . Other parameters are given as in Fig. 2.9.

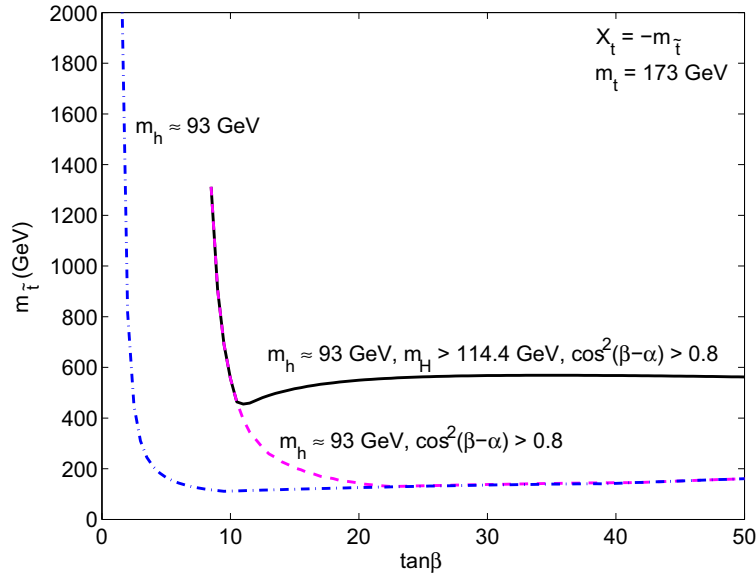


Figure 2.14: Minimum stop soft masses,  $m_{\tilde{t}} \equiv m_{\tilde{t}_L} = m_{\tilde{t}_R}$ , as a function of  $\tan\beta$ , for intermediate stop mixing ( $X_t/m_{\tilde{t}} = -1$ ). The other parameters and the different lines are as for Fig. 2.13.

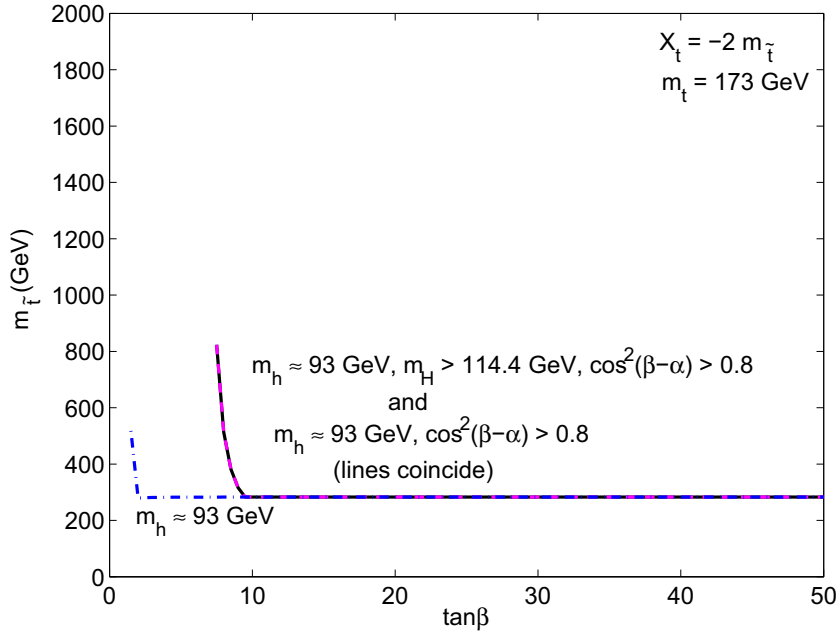


Figure 2.15: Minimum stop soft masses,  $m_{\tilde{t}} \equiv m_{\tilde{t}_L} = m_{\tilde{t}_R}$ , as a function of  $\tan\beta$ , for natural maximal stop mixing ( $X_t/m_{\tilde{t}} = -2$ ). The other parameters and the different lines are as for Fig. 2.13.

## 2.4 Implications of new physics constraints for the lower bounds on the stop masses

In Section 2.3, we presented lower bounds on the stop soft masses that are consistent with the LEP Higgs bounds (we again denote these bounds by  $m_{\tilde{t},\min}$ ). In this section, we consider additional constraints from the electroweak  $S$ - and  $T$ -parameter and the decays  $B \rightarrow X_s \gamma$  and  $B_s \rightarrow \mu^+ \mu^-$ , which also constrain the Higgs and/or stop sector. Some of these constraints may provide more stringent lower bounds on the stop masses than those provided by the constraints from LEP on the Higgs sector, or they might indirectly constrain the Higgs sector more tightly than the LEP results.

### 2.4.1 Constraints from Electroweak Precision Measurements: T- and S-parameters

The oblique parameters  $T$  and  $S$  parameterize new physics contributions to electroweak vacuum-polarization diagrams. They give a good parametrization if these diagrams are the dominant corrections to electroweak precision observables [36]. Strong constraints on these parameters already exist [11, 37].

The MSSM includes new  $SU(2)_L$  doublets that contribute to the  $T$ - and  $S$ -parameter (which are defined to be zero from SM contributions alone). The  $T$ -parameter is a measure of how strongly the vector part of  $SU(2)_L$  is broken, and is non-zero, for example, for heavy, non-degenerate multiplets of fermions or scalars. The  $S$ -parameter is a measure of how strongly the axial part of  $SU(2)_L$  is broken, and is non-zero, for example, for heavy, degenerate multiplets of chiral fermions [11].

The main contribution in the MSSM to the  $T$ -parameter in general comes from the stop / sbottom doublet [38]. In particular, large mixing in the stop and/or sbottom sectors can lead to large differences amongst the two stop and two sbottom masses, which gives a large contribution to the  $T$ -parameter. Moreover, for a given set of parameters and fixed  $X_t/m_{\tilde{t}}$ , decreasing  $m_{\tilde{t}}$  tends to increase the value of the  $T$ -parameter. For these reasons the  $T$ -parameter could provide more stringent lower bounds on  $m_{\tilde{t}}$  than those coming from the LEP Higgs bounds when the mixing in the stop sector is large, since then the stop and sbottom masses are split by large amounts and the LEP Higgs constraints allow for small  $m_{\tilde{t}}$ .

We estimate the  $T$ -parameter with version 2.2.7 of `FeynHiggs`. This program calculates  $\delta\rho$  which measures the deviation of the electroweak  $\rho$ -parameter from unity. The  $T$ -parameter and  $\delta\rho$  are related by  $\delta\rho = \alpha T$ , where  $\alpha$  is the QED coupling. All the results presented in this paper are consistent with the  $2\sigma$  constraint on the upper bound of  $\delta\rho$ , namely  $\delta\rho \leq 0.0026$  [11]. The  $T$ - and  $S$ -parameters are correlated, so that this bound corresponds to the  $2\sigma$  bound on  $T$  for  $S = 0$ .

We find that the  $2\sigma$  constraint on  $\delta\rho$  does not provide an additional constraint on the stop masses in essentially all the analyses presented in this paper.

For (natural) maximal stop mixing with  $m_{\tilde{t}} = m_{\tilde{t},\min}$ , the value of  $\delta\rho$  is not consistent with its  $1\sigma$  bound, although it is consistent with its  $2\sigma$  bound (for intermediate and less mixing, it is consistent also with the  $1\sigma$  bound). For example,  $m_{\tilde{t},\min} = 283$  GeV for large  $\tan\beta$  and natural maximal stop mixing ( $X_t = -2m_{\tilde{t}}$ ) in order to obtain  $m_h \geq 114.4$  GeV in the Higgs decoupling limit (this assumes all squark, slepton, and gaugino soft mass parameters are equal to  $m_{\tilde{t}}$ ,  $\mu = 200$  GeV,  $m_t = 173$  GeV, and all the soft trilinear couplings are equal to  $A_t$ ). This gives a value of  $\delta\rho = 0.0014$ . Increasing  $m_{\tilde{t}}$  while keeping all other parameters fixed decreases  $\delta\rho$ , and for  $m_{\tilde{t}} = 420$  GeV,  $\delta\rho$  is consistent with its  $1\sigma$  upper bound of 0.0009 found in the latest PDG review [11]. With  $m_{\tilde{t}} = 530$  GeV,  $\delta\rho$  is consistent with its  $1\sigma$  upper bound of 0.0006 found in the previous PDG review [39].<sup>3</sup>

The  $S$ -parameter in the MSSM is in general not very important [11]. We estimated it using the formulae in [40]. Including contributions from all squarks and sleptons, the  $S$ -parameter does not reach a value higher than about 0.05 for  $m_{\tilde{t}} = m_{\tilde{t},\min}$  in those cases that have large stop mixing, with the main contribution coming from the stop/sbottom doublet. For intermediate and vanishing mixing it is negligible. The constraint on  $S$  depends on  $T$ , but the  $1\sigma$  upper bound on  $S$  is about 0.07 for  $T = 0$ , whereas a positive value for  $T$  allows for larger values of  $S$ . Thus the  $S$ -parameter is a weaker constraint on the stop masses than the LEP Higgs sector bounds.

#### 2.4.2 Constraints from $B \rightarrow X_s\gamma$

New physics can contribute at one loop to the decay  $B \rightarrow X_s\gamma$ , and can therefore be just as important as the SM contribution mediated by a  $W$ -boson and the top quark. This makes the

---

<sup>3</sup>As this paper was being completed, we noticed that version 2.5.1 of `FeynHiggs` now uses sbottom masses with the SM and MSSM QCD corrections added when calculating  $\delta\rho$ . This can give different values of  $\delta\rho$ , especially for small sbottom masses, and it makes  $\delta\rho$  more sensitive to  $\mu$ . The results quoted in this paragraph change as follows. For  $m_{\tilde{t}} = 283$  GeV,  $\delta\rho = 0.0011$ . Increasing  $m_{\tilde{t}}$  to 310 GeV gives  $\delta\rho = 0.0009$ , and  $m_{\tilde{t}} = 380$  GeV gives  $\delta\rho = 0.0006$ . Qualitatively the conclusions presented in this section are unaffected. We thank S. Heinemeyer for clarifying the difference between the older and newer versions.

decay  $B \rightarrow X_s \gamma$  an important tool in constraining new physics.

The SM contribution to the branching ratio  $\mathcal{B}(B \rightarrow X_s \gamma)$  is predicted to be

$$\mathcal{B}(B \rightarrow X_s \gamma)_{\text{SM}} \simeq (2.98 \pm 0.26) \times 10^{-4}, \quad (2.7)$$

see [41], whereas the experimental bound is given by

$$\mathcal{B}(B \rightarrow X_s \gamma)_{\text{expt}} \simeq (3.55 \pm 0.26) \times 10^{-4}, \quad (2.8)$$

see [42]. This allows, but does not require, new physics contributions [41].

There are several contributions to the decay  $B \rightarrow X_s \gamma$  from the additional particles in the MSSM, which we now discuss.

Within the Higgs sector, the charged Higgs ( $H^+$ ) contributes at one loop to the decay  $B \rightarrow X_s \gamma$ . The contribution is larger for smaller  $m_{H^+}$ . If one only considers this contribution, as one would in the two-Higgs-doublet model of type II (2HDM (II)), then this sets a rather stringent lower bound on  $m_{H^+}$ . The bound of course depends on the SM prediction and experimental measurement of  $\mathcal{B}(B \rightarrow X_s \gamma)$ , and in the past used to be about  $m_{H^+} \gtrsim 350$  GeV, see [43], [44] and references therein. The latest results quoted in equations (2.7) and (2.8) are expected to change this bound slightly, but we do not explore this in more detail [41]. It is clear, however, that this bound is much stronger than the bound coming from a direct search of  $H^+$  at LEP which is given by  $m_{H^+} \gtrsim 78.6$  GeV [45]. Note that the charged Higgs contribution is mostly independent of  $\tan \beta$ ; only for very small values of  $\tan \beta$  does it increase substantially.

The charged Higgs, thus, does not contribute much to  $B \rightarrow X_s \gamma$  in the decoupling limit for large  $m_A$ , since here  $m_{H^+}$  is large. In the region  $m_h \simeq 93$  GeV with  $\cos^2(\beta - \alpha) \geq 0.8$  and  $m_H \geq 114.4$  GeV, however,  $m_{H^+} \simeq 125$  GeV. The contribution from the charged Higgs to  $\mathcal{B}(B \rightarrow X_s \gamma)$  is then roughly  $7.7 \times 10^{-4}$ , more than a factor of two larger than the SM contribution. We estimated this using version 2.5.1 of the program **FeynHiggs**,<sup>4</sup> in the limit of

---

<sup>4</sup>Note that **FeynHiggs** gives  $\mathcal{B}(B \rightarrow X_s \gamma)_{\text{SM}} \simeq 3.63 \times 10^{-4}$  which is larger than the latest value quoted in equation (2.7). This is not of qualitative importance here.

large sparticle masses. Therefore, the constraint on  $\mathcal{B}(B \rightarrow X_s \gamma)$  rules out this region of the Higgs parameter space if one only considers the charged Higgs contribution.

There are, however, also chargino, neutralino and gluino contributions to  $B \rightarrow X_s \gamma$  within the MSSM with minimal flavor violation (MFV).<sup>5</sup> NLO contributions can be very important and need to be included in order to get an accurate estimate of  $\mathcal{B}(B \rightarrow X_s \gamma)$  [44]. The contribution from a chargino together with a stop in the loop is often the most important one. The chargino-stop contribution can become very large for small chargino and small stop masses, and it is proportional to  $\tan \beta$  in the amplitude. However, it vanishes in the limit of large stop or chargino masses. From studying the mSUGRA model, it is known that usually the chargino-stop contribution to the branching ratio interferes constructively with the SM and the charged Higgs contribution if the sign of  $\mu A_t$  is positive, whereas it interferes destructively if the sign of  $\mu A_t$  is negative [44].

This means that the region  $m_h \simeq 93$  GeV is not necessarily ruled out, since a light stop and a light chargino could cancel the charged Higgs contribution [10, 47, 48]. Using version 2.5.1 of `FeynHiggs` to calculate the branching ratio of  $B \rightarrow X_s \gamma$ , we verify this claim in the case of intermediate and larger stop mixing, at least for  $\tan \beta$  not too small. We find that the contribution to  $B \rightarrow X_s \gamma$  from the chargino-stop loop can easily be large enough to interfere destructively with the charged Higgs contribution and thus give an experimentally allowed value of  $\mathcal{B}(B \rightarrow X_s \gamma)$ . Moreover, in some cases for sizeable stop mixing, the chargino-stop contribution can be made much larger than the SM and charged Higgs contribution. Thus, an experimentally consistent value of  $\mathcal{B}(B \rightarrow X_s \gamma)$  can also often be obtained by finding a chargino mass that gives a chargino-stop amplitude equal to the negative of the charged Higgs amplitude plus the negative of twice the SM amplitude. We note that an experimentally consistent value for  $\mathcal{B}(B \rightarrow X_s \gamma)$  can always be found without requiring the stop masses to be larger than  $m_{\tilde{t}, \min}$ ,

---

<sup>5</sup>There are other possibilities for flavor violation within the MSSM, and therefore additional contributions to  $B \rightarrow X_s \gamma$  are possible. The additional flavor violation is small, however, assuming that the only source of flavor violation comes from the mixing among the squarks and assuming that this is of the same form as the mixing among the quarks, i.e. described by the Cabibbo-Kobayashi-Maskawa (CKM) matrix. This assumption is usually called minimal flavor violation (MFV). The MSSM with general flavor violation allows for more contributions to the decay  $B \rightarrow X_s \gamma$ , which can sometimes weaken constraints on parameters in the MSSM with MFV [46].

but by adjusting the chargino mass alone.

If  $\tan\beta$  is small enough then  $m_{\tilde{t},\min}$  becomes exponentially large, and the constraint on  $\mathcal{B}(B \rightarrow X_s\gamma)$  rules out the  $m_h \simeq 93$  GeV region since the chargino-stop contribution cannot cancel the charged Higgs contribution.

In the case of vanishing stop mixing with *degenerate* stop soft masses,  $m_{\tilde{t},\min}$  is so large that the chargino-stop contribution to  $B \rightarrow X_s\gamma$  is too small to cancel the charged Higgs contribution. However, even in the no-mixing case one of the stops can be chosen to be light by setting one of the stop soft masses to a small value. In this case the other stop soft mass needs to be very large in order for the radiative corrections to the Higgs sector to be large enough to satisfy the LEP bounds. One light stop, however, is able to give a sizeable chargino-stop contribution that can cancel the charged Higgs contribution. For example, we find  $m_{\tilde{t},\min} \simeq 1100$  GeV for  $m_h \simeq 93$  GeV,  $\cos^2(\beta - \alpha) \geq 0.8$  and  $m_H \geq 114.4$  GeV, with  $\tan\beta = 20$ ,  $\mu = 200$  GeV,  $m_A \simeq 96$  GeV, and  $m_t = 173$  GeV (this assumes that all squark, slepton, and gaugino soft masses are equal to  $m_{\tilde{t}}$ , and all the soft trilinear couplings are equal to  $A_t$ ). Since the charged Higgs then essentially provides the only contribution to  $B \rightarrow X_s\gamma$  beyond that of the SM itself, the branching ratio is again about  $7.7 \times 10^{-4}$ . However, choosing, for example,  $m_{\tilde{t}_L} = 350$  GeV,  $m_{\tilde{t}_R} = 2000$  GeV, all the gaugino soft masses equal to  $m_{\tilde{t}_L}$ , and keeping all other squark and slepton soft masses equal to 1100 GeV, gives a consistent branching ratio of  $3.6 \times 10^{-4}$ .

In the Higgs decoupling limit, for which  $m_h \geq 114.4$  GeV, the charged Higgs contribution vanishes. Since  $m_{\tilde{t},\min}$  is large for very small  $\tan\beta$  or vanishing stop mixing, the chargino-stop contribution to  $\mathcal{B}(B \rightarrow X_s\gamma)$  is small, and there is no inconsistency with the experimental bound. On the other hand,  $m_{\tilde{t},\min}$  can be so low for appreciable amounts of mixing (and if  $\tan\beta$  is not too small) that the chargino-stop contribution can easily be too large. In this case, however, we can find a chargino mass that gives a branching ratio of  $B \rightarrow X_s\gamma$  within the experimentally allowed region, and again we find no further constraint on  $m_{\tilde{t}}$ . We can achieve this by setting the chargino mass to a very large value, in which case the chargino-stop contribution becomes vanishingly small. For negative  $\mu A_t$ , however, the chargino-stop loop

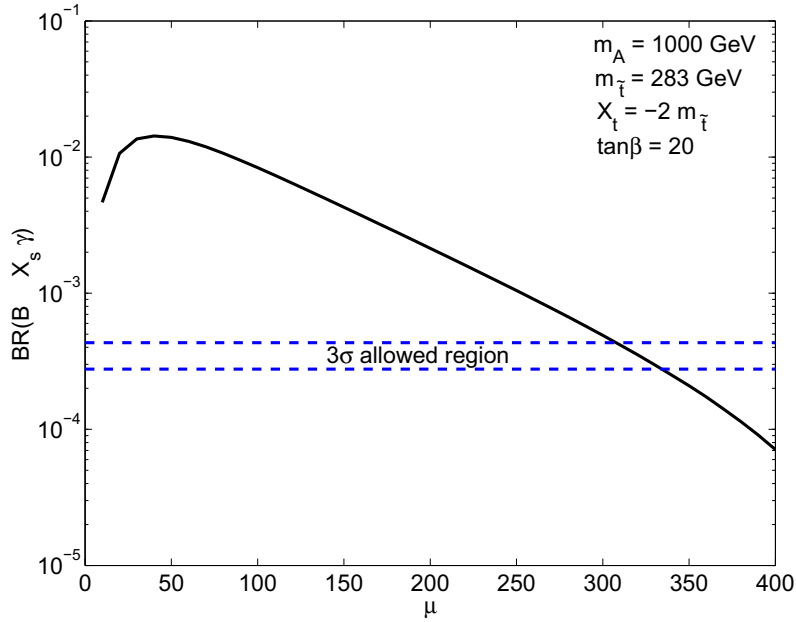


Figure 2.16:  $\mathcal{B}(B \rightarrow X_s \gamma)$  versus  $\mu$  with stop soft masses  $m_{\tilde{t}} \equiv m_{\tilde{t}_L} = m_{\tilde{t}_R} = 283$  GeV, and natural maximal stop mixing ( $X_t/m_{\tilde{t}} = -2$ ). All squark, slepton, and gaugino soft mass parameters are equal to the stop soft masses,  $m_t = 173$  GeV,  $m_A = 1000$  GeV,  $\tan \beta = 20$ , and all the soft trilinear couplings are equal to  $A_t = X_t + \mu \cot \beta$ .

interferes destructively with the SM contribution so that we can also adjust the chargino mass until the chargino-stop amplitude is equal to the negative of twice the SM amplitude. This is what happens in the case depicted in Fig. 2.16, where we show the branching ratio of  $B \rightarrow X_s \gamma$  as a function of  $\mu$ . In this figure, all squark, slepton, and gaugino soft masses are equal to the stop soft masses, which are given by  $m_{\tilde{t}, \min} = 283$  GeV,  $m_t = 173$  GeV,  $\tan \beta = 20$ ,  $X_t = -2m_{\tilde{t}}$ , and all the soft trilinear couplings are equal to the stop soft trilinear coupling,  $A_t$ . We find an experimentally allowed value for  $\mathcal{B}(B \rightarrow X_s \gamma)$  in this case by choosing  $\mu \simeq 330$  GeV. We note that  $\mu$  has to be chosen within about a 30 GeV window for  $\mathcal{B}(B \rightarrow X_s \gamma)$  to fall within the  $3\sigma$  allowed region.

### 2.4.3 Constraints from $B_s \rightarrow \mu^+\mu^-$

The decay  $B_s \rightarrow \mu^+\mu^-$  has not yet been observed. The SM contribution to this decay is dominated by penguin diagrams involving the  $Z$ -boson and box diagrams involving the  $W$ -bosons [49]. (The SM Higgs does contribute to the decay  $B_s \rightarrow \mu^+\mu^-$  within the SM, but relative to the dominant contribution it is suppressed by  $m_\mu m_{b,s}/m_W^2$ , where  $m_\mu$ ,  $m_b$  and  $m_s$  are the masses of the muon, b-quark and s-quark, respectively, and  $m_W$  is the mass of the  $W$ -bosons [50].) The SM contribution to the branching ratio is quite small since it is fourth order in the weak interactions. It is predicted to be

$$\mathcal{B}(B_s \rightarrow \mu^+\mu^-)_{\text{SM}} = (3.42 \pm 0.54) \times 10^{-9} \quad (2.9)$$

(see [51] and references therein). This is well below the current experimental bound from the CDF experiment at the Tevatron given by

$$\mathcal{B}(B_s \rightarrow \mu^+\mu^-)_{\text{expt}} < 1.5 \times 10^{-7} \quad (2.10)$$

at the 90% confidence level [51].

There are several contributions to the decay  $B_s \rightarrow \mu^+\mu^-$  from the additional particles in the MSSM, which we now discuss.

The contributions to the decay  $B_s \rightarrow \mu^+\mu^-$  coming only from the MSSM Higgs sector are the same as those found in the 2HDM (II). They can be enhanced by two powers of  $\tan\beta$  in the amplitude, which can compensate for the suppression by the muon mass. One can set an approximate bound on  $m_{H^+}$  assuming this is the *only* contribution within the MSSM. This bound depends on  $\tan\beta$ , but for  $\tan\beta = 50$  one finds an experimentally allowed value for  $\mathcal{B}(B_s \rightarrow \mu^+\mu^-)$  if  $m_{H^+} \gtrsim 35$  GeV (see for example [52, 53]). As we discussed in Section 2.4.2, within the 2HDM (II) the constraint on  $\mathcal{B}(B \rightarrow X_s\gamma)$  alone forces  $m_{H^+}$  to be larger than about 350 GeV. Such a large value for  $m_{H^+}$  guarantees that  $\mathcal{B}(B_s \rightarrow \mu^+\mu^-)$  is roughly of the same size as the SM result even for quite large  $\tan\beta$ , so that it alone provides no further constraint

on the parameter space within the 2HDM (II) [54].

In the MSSM there are, however, further contributions to the decay  $B_s \rightarrow \mu^+ \mu^-$  coming from box and penguin diagrams that involve charginos and up-type squarks [53, 54, 55, 56, 57, 58, 59]. The penguin diagrams also contain the neutral Goldstone and Higgs bosons. The self-energy MSSM Higgs penguin diagrams give the leading contribution to  $\mathcal{B}(B_s \rightarrow \mu^+ \mu^-)$  for non-negligible mixing in the stop sector. (In an effective Lagrangian approach these diagrams may be viewed as inducing a non-holomorphic coupling between down-type quarks and the up-type Higgs field.) For large  $\tan \beta$ , this leading contribution is roughly proportional to  $A_t^2 \tan^6 \beta / m_A^4$ , and can thus be significantly larger than the contributions from the Higgs sector alone. Moreover, this contribution becomes small for very small  $\mu$ . This contribution does not vanish for degenerate squark masses, nor in the limit of large sparticle masses. Thus, although the branching ratio depends on the size of the stop masses, it is much more sensitive to the size of the Higgs masses,  $\tan \beta$  and the amount of stop mixing. A light Higgs sector can give a branching ratio of  $B_s \rightarrow \mu^+ \mu^-$  that is more than three orders of magnitude above the SM prediction and thus well ruled out, especially if the stop mixing and  $\tan \beta$  are large. Moreover, this is the case even for large sparticle masses. Furthermore, such large values for  $\mathcal{B}(B_s \rightarrow \mu^+ \mu^-)$  can be reached within the MSSM without violating any other constraints, including, for example, those on  $\mathcal{B}(B \rightarrow X_s \gamma)$  [54, 60].

There are further contributions to  $\mathcal{B}(B_s \rightarrow \mu^+ \mu^-)$  which also have a  $\tan^6 \beta / m_A^4$  behavior, even assuming that the CKM matrix is the only source of flavor violation in the squark sector. These appear if the left-handed up-type soft squark masses of the three generations are not all equal, so that the left-handed down-type soft squark mass-squared matrix has off-diagonal terms. These lead to contributions from loops involving a neutralino or a gluino and a down-type squark [53, 55, 58, 59, 60]. Cancellations between the chargino and gluino contributions can occur and the neutralino contribution, although usually smaller, can then be important (see, for example, [60]).

We estimated the values for  $\mathcal{B}(B_s \rightarrow \mu^+ \mu^-)$  with the program `MicrOMEGAS` 1.3 [61, 62] and

the subroutine `IsaBMM` from `IsaTools/IsaJet` [58, 63]. We find that the branching ratio of  $B_s \rightarrow \mu^+\mu^-$  is well within experimental limits for the region  $m_h \simeq 93$  GeV,  $m_H \geq 114.4$  GeV and  $\cos^2(\beta - \alpha) \geq 0.8$  in the case of no (or very little) stop mixing and degenerate squark soft masses. For intermediate mixing with degenerate squark masses near  $m_{\tilde{t},\min}$ ,  $\mathcal{B}(B_s \rightarrow \mu^+\mu^-)$  is consistent with experimental limits for  $\tan\beta \lesssim 20 - 25$ . For natural maximal mixing,  $\mathcal{B}(B_s \rightarrow \mu^+\mu^-)$  is consistent with experimental limits for  $\tan\beta \lesssim 15$ . For larger  $\tan\beta$ , as well as for non-degenerate squark soft masses, a scan over all relevant MSSM parameters is necessary in order to see whether we can find an experimentally consistent value of  $\mathcal{B}(B_s \rightarrow \mu^+\mu^-)$  for such a light Higgs sector. However, for large stop mixing, it will become increasingly difficult to find a parameter set that gives a branching ratio consistent with experiments as  $\tan\beta$  is increased. Of course, this assumes that there are no fortuitous cancelations between the different contributions, and also that there are no other flavor-violating contributions such as from R-parity violating couplings. A scan over the relevant MSSM parameters, even assuming MFV, is beyond the scope of this paper. The reader is referred to the references found in the previous two paragraphs, and especially [48], bearing in mind that the current CDF bound on  $\mathcal{B}(B_s \rightarrow \mu^+\mu^-)$ , equation (2.10), is stronger than the one used in these references.

In the Higgs decoupling limit, the dominant flavor-violating effects involving loops of neutral Higgs bosons decouple, and these large contributions to  $B_s \rightarrow \mu^+\mu^-$  become negligible. Using `MicrOMEGAS 1.3`, one may explicitly check that the decay  $B_s \rightarrow \mu^+\mu^-$  does not provide stronger constraints on the stop masses than do the LEP Higgs bounds in the decoupling limit found in Section 2.3.1.

## 2.5 Implications for Electroweak Symmetry Breaking

In Section 2.3, we presented lower bounds on the stop masses consistent with the LEP Higgs bounds, and in Section 2.4, we discussed whether the electroweak  $S$ - and  $T$ -parameter and the decays  $B \rightarrow X_s\gamma$  and  $B_s \rightarrow \mu^+\mu^-$  indirectly put further constraints on the Higgs and/or stop sector. In this section, we look at the implications for electroweak symmetry breaking.

The mechanism of radiative electroweak symmetry breaking arises rather naturally in supersymmetric extensions of the Standard Model [64, 65, 66]. Because of the large top Yukawa coupling, quantum fluctuations of the stop squarks significantly modify the up-type Higgs potential, as studied numerically for the physical Higgs boson mass in the previous sections. The leading effect, however, is a tachyonic contribution to the up-type Higgs soft supersymmetry breaking Lagrangian mass. Over much of parameter space this tachyonic contribution is sufficient to result in a stop squark quantum fluctuation-induced phase transition for the Higgs fields, which is generally referred to as radiative electroweak symmetry breaking.

The leading quantum contribution to the up-type Higgs soft mass comes from renormalization group evolution below the supersymmetry breaking messenger scale. The one-loop  $\beta$ -function for the up-type Higgs soft mass-squared is, neglecting effects proportional to gauge couplings,

$$16\pi^2\beta_{m_{H_u}^2} \simeq 6\lambda_t^2(m_{H_u}^2 + m_{\tilde{t}_L}^2 + m_{\tilde{t}_R}^2 + |A_t|^2) \quad (2.11)$$

The light Higgs mass bounds require rather large stop masses and/or stop mixing, where the stop soft trilinear coupling is related to the mixing parameter by  $A_t = X_t + \mu \cot \beta$ . This implies that the stop contributions to the  $\beta$ -function in (2.11) proportional to the combination  $(m_{\tilde{t}_L}^2 + m_{\tilde{t}_R}^2 + |A_t|^2)$  are also sizeable, at least at the low scale. Moreover, for generic parameters this combination remains sizeable over the entire renormalization group trajectory up to the messenger scale. For generic messenger scale values of the up-type Higgs soft mass squared,  $m_{H_u}^2$ , the large value of the combination  $(m_{\tilde{t}_L}^2 + m_{\tilde{t}_R}^2 + |A_t|^2)$ , along with the sizeable coefficient in the  $\beta$ -function (2.11), then imply that  $m_{H_u}^2$  evolves relatively rapidly under renormalization group evolution.

This evolution is towards tachyonic values of  $m_{H_u}^2$  which reduce the magnitude of the  $\beta$ -function (2.11). For running into the deep infrared, the up-type Higgs mass squared would be driven to values near the zero of the  $\beta$ -function (2.11) for which

$X_t/m_{\tilde{t}}$	$m_t = 168$ GeV	$m_t = 173$ GeV	$m_t = 178$ GeV
0	3630	1780	1240
-1	1460	1000	770
-2	680	690	710

Table 2.1: Minimum allowed values of the combination  $(m_{\tilde{t}_L}^2 + m_{\tilde{t}_R}^2 + |A_t|^2)^{1/2}$  consistent with a physical Higgs boson mass of  $m_h \geq 114.4$  GeV in the Higgs decoupling limit for large  $\tan\beta$ , taking into account only the LEP Higgs sector bounds. The minimum allowed values increase with decreasing  $\tan\beta$ .

$$m_{H_u}^2 \simeq -(m_{\tilde{t}_L}^2 + m_{\tilde{t}_R}^2 + |A_t|^2). \quad (2.12)$$

Although this relation is not strictly obtained with finite running, the up-type Higgs mass squared can approach this value for very high messenger scale. In Table 2.1, we show the minimum allowed values of the combination  $(m_{\tilde{t}_L}^2 + m_{\tilde{t}_R}^2 + |A_t|^2)^{1/2}$  deduced from the results of section 2.3.1 consistent with  $m_h \geq 114.4$  GeV in the Higgs decoupling limit for large  $\tan\beta$ . The minimum allowed values increase with decreasing  $\tan\beta$ .

The full Lagrangian mass squared for the up-type Higgs is a sum of the soft mass squared and square of the superpotential Higgs mass,  $m^2 = m_{H_u}^2 + |\mu|^2$ . To leading order in  $1/\tan^2\beta$ , and ignoring the finite quantum corrections to the Higgs potential which are not of qualitative importance for the present discussion, this is equal to minus half the  $Z$ -boson mass squared in the ground state with broken electroweak symmetry

$$\frac{1}{2}m_Z^2 \simeq -(m_{H_u}^2 + |\mu|^2). \quad (2.13)$$

For  $m_{H_u}^2$  near the zero of its  $\beta$ -function given by (2.12), the bounds given in Table 2.1 imply that obtaining the observed value of the  $Z$ -boson mass,  $m_Z \simeq 91$  GeV, requires a rather sensitive cancelation between the up-type Higgs soft mass and  $\mu$ -parameter. The numerical magnitude of this tuning (which has come to be known as the supersymmetric little hierarchy problem) is apparent in the numerical data in Table 2.1, at least for regions of parameter space which are driven under renormalization group flow to near the zero of the  $\beta$ -function (2.11).

The minimum allowed value of the combination  $(m_{\tilde{t}_L}^2 + m_{\tilde{t}_R}^2 + |A_t|^2)$  for a given lower limit on the Higgs mass decreases with increasing stop mixing. This may be understood from the leading expression for the quantum corrected Higgs mass given in equation (2.5). For no stop mixing,  $X_t = 0$ , the leading correction to the Higgs mass squared comes only from renormalization group running of the Higgs quartic coupling below the stop mass scale, and is therefore proportional to  $\ln(m_{\tilde{t}}^2/m_t^2)$ . A linear increase in the Higgs mass squared in this case requires an exponential increase in  $m_{\tilde{t}}$ . However, the stop mixing correction to the Higgs mass squared with  $X_t \neq 0$  comes from a finite threshold correction to the Higgs quartic coupling at the stop mass scale and is independent of  $m_{\tilde{t}}$  for fixed  $X_t/m_{\tilde{t}}$ . In this case a linear increase in the Higgs mass squared only requires a linear increase in  $(X_t/m_{\tilde{t}})^2$ . So increasing stop mixing allows exponentially lighter stop masses in order to obtain a given Higgs mass. While such a decrease clearly reduces the soft stop mass contributions to  $\beta_{m_{H_u}^2}$  [20, 67] this is partially offset by an increase in the mixing contribution from the stop trilinear coupling. From the data in Table 2.1, it is clear that large stop mixing can decrease the magnitude of  $\beta_{m_{H_u}^2}$  (2.11) by up to a factor of a few depending on the top mass. However, the magnitude of the total stop contribution including mixing is still quite sizeable for a Higgs mass bound of  $m_h \geq 114.4$  GeV. So large stop mixing alone cannot appreciably ameliorate the tuning of supersymmetric electroweak symmetry breaking or satisfactorily solve the supersymmetric little hierarchy problem.<sup>6</sup>

This conclusion essentially remains unchanged for a physical Higgs boson mass of  $m_h \simeq 93$  GeV with  $\cos^2(\beta - \alpha) \geq 0.8$  and  $m_H \geq 114.4$  GeV, as seen from the numerical results in Section 2.3.3. In general, one should bear in mind that indirect constraints on new physics, especially from  $\mathcal{B}(B_s \rightarrow \mu^+ \mu^-)$ , severely restrict the allowed MSSM parameter space for  $m_h \simeq 93$  GeV (see Section 2.4). However, for less than maximal stop mixing, the stop masses can be somewhat smaller for moderate  $\tan\beta$  near the Higgs non-decoupling limit than in the Higgs decoupling

---

<sup>6</sup>Although this conclusion is valid for a generic choice of messenger scale values for the sparticle masses, it is possible to reduce the amount of tuning coming from the running of  $m_{H_u}^2$  by a more judicious choice. One example is to choose negative stop masses squared at the high scale which allows the contribution to the tuning from the running of  $m_{H_u}^2$  to be arbitrarily small, as well allow for the (natural) maximal mixing scenario to be radiatively generated at the low scale [68].

limit (see also [10]). The combination  $(m_{\tilde{t}_L}^2 + m_{\tilde{t}_R}^2 + |A_t|^2)^{1/2}$  is in fact the smallest in the Higgs non-decoupling region near intermediate values for the stop mixing and for  $\tan\beta$  near 10. It reaches as low as about 650 GeV for  $m_t = 178$  GeV,  $\tan\beta = 10.5$ ,  $X_t = -m_{\tilde{t}}$ , and gaugino masses equal to  $m_{\tilde{t}}$ . It can be decreased slightly further by setting the bino and wino masses to smaller values. (For maximal stop mixing, the combination is actually larger since here the Tevatron bound on the lighter stop mass forces the stop soft masses to be larger than required from the LEP Higgs bounds alone.) The combination always remains sizeable though, and thus the tuning of electroweak symmetry breaking cannot be ameliorated by much in the  $m_h \simeq 93$  GeV region.

## 2.6 Conclusions

The dominant radiative corrections to the tree-level CP-even Higgs mass matrix, which determines  $m_h$  and  $m_H$ , come from loops involving the top quark and stop squarks, with larger stop masses implying larger radiative corrections. In this paper, we presented lower bounds on the stop masses consistent with the LEP Higgs bounds in two different regions in the MSSM Higgs parameter space. The one region is the Higgs decoupling limit, in which the bound on the mass of the lighter Higgs is equal to the bound on the SM Higgs,  $m_h \geq 114.4$  GeV. The other region is near the Higgs “non-decoupling” limit with  $m_h \simeq 93$  GeV in which the Higgs sector is required to be light. In the latter region, there are two additional constraints. One is on the mass of the heavier Higgs, which now behaves like the SM Higgs, i.e.  $m_H \gtrsim 114.4$  GeV. The other constraint is on size of the coupling of the lighter Higgs to two  $Z$  bosons which is controlled by the parameter  $\sin^2(\beta - \alpha)$  and here needs to be less than about 0.2 (i.e.  $\cos^2(\beta - \alpha) \gtrsim 0.8$ ) for the lighter Higgs to have escaped detection at LEP. We denote the lower bounds on the stop masses consistent with the LEP Higgs bounds by  $m_{\tilde{t},\min}$ .

We presented  $m_{\tilde{t},\min}$  as a function of  $\tan\beta$  in both these regions in the Higgs parameter space for a variety of MSSM parameter choices. In particular, we further elucidated the importance of the top mass and stop mixing, and investigated numerically how larger top masses and more

stop mixing allow for substantially smaller values of  $m_{\tilde{t},\min}$ . We also showed numerically how larger gaugino masses and larger values of  $\mu$  increase  $m_{\tilde{t},\min}$ . Moreover, we saw how much  $m_{\tilde{t},\min}$  increases if  $\mu$  is negative compared to  $\mu$  positive if both  $\tan\beta$  and the magnitude of  $\mu$  are large. In the non-decoupling region, we discussed how the constraints on  $\cos^2(\beta - \alpha)$  and on  $m_H$  lead to increased values for  $m_{\tilde{t},\min}$ .

We also considered how  $m_{\tilde{t},\min}$  changes as a function of  $m_h$ . Since  $A_t$  and  $M_3$  most naturally have the opposite sign at low scales due to renormalization group running, a negative value of  $A_t$  is more natural in a convention where  $M_3$  is positive. For negative  $A_t$  and stop masses less than a few TeV, the upper bound of  $m_h$  in the MSSM is around 131 GeV.

We demonstrated that the two regions in the Higgs parameter space have roughly the same  $m_{\tilde{t},\min}$  if  $\tan\beta$  is large. For moderate values of  $\tan\beta$  and non-maximal stop mixing,  $m_{\tilde{t},\min}$  is larger in the Higgs decoupling region than in the Higgs non-decoupling region. As  $\tan\beta$  decreases, however,  $m_{\tilde{t},\min}$  is larger in the Higgs non-decoupling region than in the Higgs decoupling region.

We also considered additional constraints from the electroweak  $S$ - and  $T$ -parameter and the decays  $B \rightarrow X_s \gamma$  and  $B_s \rightarrow \mu^+ \mu^-$ , which also constrain the Higgs and/or stop sector.

The main contribution to the  $T$ -parameter within the MSSM usually comes from the stop / sbottom doublet and, for a given set of parameters, is larger for larger stop (and sbottom) mixing as well as for smaller stop and sbottom masses. We found that the value of the  $T$ -parameter is well within its  $2\sigma$  bound for stop masses equal to  $m_{\tilde{t},\min}$ . In fact, only for maximal stop mixing do we find small enough values for  $m_{\tilde{t},\min}$  that give a contribution to the  $T$ -parameter that does not also fall within its  $1\sigma$  bound. For such large stop mixing one must then increase the stop masses by a small amount above  $m_{\tilde{t},\min}$  to also satisfy the  $1\sigma$  bound on the  $T$ -parameter.

We found that the contribution to the  $S$ -parameter is not large, and that the  $S$ -parameter therefore does not provide an additional constraint on the stop masses.

The indirect constraint on  $\mathcal{B}(B \rightarrow X_s \gamma)$  in many cases does not provide an additional constraint on the stop masses. In the Higgs non-decoupling region for  $m_h \simeq 93$  GeV, the Higgs

sector is required to be light, and the charged Higgs contribution to  $B \rightarrow X_s \gamma$  is large. The charged Higgs contribution can usually be canceled by the chargino-stop contribution through a judicious choice of the chargino mass. However, for vanishing stop mixing and assuming degenerate stop soft masses,  $m_{\tilde{t},\min}$  is so large that the chargino-stop contribution is too small to cancel the charged Higgs contribution. For vanishing stop mixing, we therefore require non-degenerate stop soft masses with one light stop so that the chargino-stop contribution can be large enough to give an experimentally consistent value for  $\mathcal{B}(B \rightarrow X_s \gamma)$  (the other stop must then be very heavy so that the LEP Higgs constraints are satisfied). In the Higgs decoupling limit, the charged Higgs contribution vanishes. We find no further constraint on the stop masses. Even for large stop mixing, for which  $m_{\tilde{t},\min}$  can be very small, one can always obtain an experimentally consistent value for  $\mathcal{B}(B \rightarrow X_s \gamma)$  by adjusting the chargino mass.

The main contributions to the flavor-violating decay  $B_s \rightarrow \mu^+ \mu^-$  come from flavor violating Higgs couplings, and these decouple in the Higgs decoupling limit. Thus, the indirect constraint on  $\mathcal{B}(B_s \rightarrow \mu^+ \mu^-)$  is only important in the Higgs non-decoupling region. In this region, however, it is able to severely restrict the allowed parameter space, since the flavor violation does not decouple in the limit of large sparticle masses. In fact, the region for such a light Higgs sector is ruled out if stop mixing and  $\tan \beta$  are large, unless there are fortuitous cancelations amongst the various contributions, or there are additional flavor-violating contributions from, for example, R-parity violating couplings that cancel these contributions.

We note that we did not consider the constraint on the anomalous magnetic moment of the muon,  $(g-2)_\mu$ , since it decouples in the limit of large sneutrino and smuon masses. It alone is thus unable to directly provide a further constraint on the Higgs sector or on the stop masses.

Lastly, we discussed the implications of our numerical analysis for electroweak symmetry breaking. Large stop mixing generically decreases the tuning of supersymmetric electroweak symmetry breaking, but is unable to do so sufficiently to solve the supersymmetric little hierarchy problem. Moreover, the tuning can be ameliorated only slightly in the  $m_h \simeq 93$  GeV region compared to the  $m_h \geq 114.4$  GeV region (for intermediate values of the stop mixing

and moderate values of  $\tan \beta$ ), and thus the supersymmetric little hierarchy problem cannot be satisfactorily solved in either of the two regions.

## 2.7 Appendix: Mixing in the Two Doublet Higgs Sector

A Higgs sector with electroweak symmetry broken to electromagnetism,  $SU(2)_L \times U(1)_Y \rightarrow U(1)_Q$ , by two  $SU(2)_L$  doublets,  $H_u$  and  $H_d$ , with hypercharge  $Y = \pm 1$  respectively, has two physical scalars,  $h$  and  $H$ , a pseudoscalar,  $A$ , and a charged scalar,  $H^\pm$ . The couplings of the scalar mass eigenstates,  $h$  and  $H$ , to the gauge bosons are determined by the associated amplitudes of the neutral components of the gauge eigenstate doublets,  $H_u^0$  and  $H_d^0$ . It is instructive to consider various vectors in the  $\text{Re}(H_d^0) - \text{Re}(H_u^0)$  plane in order to describe these couplings and the relationship between the mass and gauge interaction eigenstates.

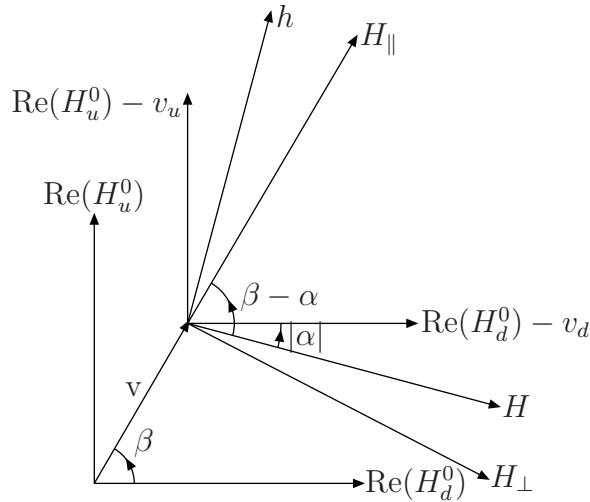


Figure 2.17: Relationship between the  $\text{Re}(H_u) - \text{Re}(H_d)$  and  $H_{\parallel} - H_{\perp}$  bases and  $h - H$  mass eigenstates for the two doublet Higgs sector.

Electroweak symmetry is broken by the expectation values  $\langle \text{Re}(H_u^0) \rangle = v_u$  and  $\langle \text{Re}(H_d^0) \rangle = v_d$ . These expectation values define a vector in the  $\text{Re}(H_d^0) - \text{Re}(H_u^0)$  plane with an angle  $\beta$  defined by  $\tan \beta = v_u/v_d$  as indicated in Fig. 2.17. The two physical neutral CP-even scalar mass eigenstates are fluctuations about the expectation value in this plane and are related by a rotation to the gauge eigenstates conventionally defined by an angle  $\alpha$  as [69]

$$\begin{pmatrix} H \\ h \end{pmatrix} = \sqrt{2} \begin{pmatrix} \cos \alpha & \sin \alpha \\ -\sin \alpha & \cos \alpha \end{pmatrix} \begin{pmatrix} \text{Re}(H_d^0) - v_d \\ \text{Re}(H_u^0) - v_u \end{pmatrix} \quad (2.14)$$

Vectors in the  $\text{Re}(H_d^0) - \text{Re}(H_u^0)$  plane which are parallel and perpendicular,  $H_{\parallel}$  and  $H_{\perp}$ , to the expectation value vector may also be defined as indicated in Fig. 2.17

$$\begin{pmatrix} H_{\perp} \\ H_{\parallel} \end{pmatrix} = \sqrt{2} \begin{pmatrix} \sin \beta & -\cos \beta \\ \cos \beta & \sin \beta \end{pmatrix} \begin{pmatrix} \text{Re}(H_d^0) - v_d \\ \text{Re}(H_u^0) - v_u \end{pmatrix}, \quad (2.15)$$

see also [10]. The physical mass eigenstates are related to these by a rotation

$$\begin{pmatrix} H \\ h \end{pmatrix} = \begin{pmatrix} \sin(\beta - \alpha) & \cos(\beta - \alpha) \\ -\cos(\beta - \alpha) & \sin(\beta - \alpha) \end{pmatrix} \begin{pmatrix} H_{\perp} \\ H_{\parallel} \end{pmatrix}. \quad (2.16)$$

The neutral Goldstone pseudoscalar boson,  $G$ , which is eaten by the  $Z$ -boson is by definition the imaginary part of the linear combination of the components of the neutral Higgs doublets which are aligned with the expectation value, and the physical pseudoscalar Higgs boson,  $A$ , is the perpendicular combination

$$\begin{aligned} A &= \text{Im}(H_{\perp}) \\ G &= \text{Im}(H_{\parallel}) \end{aligned} \quad (2.17)$$

These states are related to the gauge eigenstates through a rotation by the angle  $\beta$

$$\begin{pmatrix} A \\ G \end{pmatrix} = \sqrt{2} \begin{pmatrix} -\sin \beta & \cos \beta \\ \cos \beta & \sin \beta \end{pmatrix} \begin{pmatrix} \text{Im}(H_d^0) \\ \text{Im}(H_u^0) \end{pmatrix}. \quad (2.18)$$

The charged Goldstone bosons,  $G^{\pm}$ , and the charged Higgs mass eigenstates,  $H^{\pm}$ , are defined similarly as

$$\begin{aligned} H^{\pm} &= \text{Im}(H_{\perp}^{\pm}) \\ G^{\pm} &= \text{Im}(H_{\parallel}^{\pm}) \end{aligned}, \quad (2.19)$$

where  $H_{\perp}^{\pm}$  and  $H_{\parallel}^{\pm}$  are defined in analogy with equation (2.15).

We may consider Higgs decoupling limits of the two doublet Higgs sector in which  $m_H$ ,  $m_A$ ,  $m_{H^\pm} \gg m_h$  so that only a single light Higgs doublet remains in the low energy theory. A particular decoupling limit is one for which the physical mass eigenstate of the light Higgs doublet is aligned with the expectation value vector so that  $H_\parallel$  is the single Higgs doublet of the low energy theory and  $H_\perp$  contains the heavy mass eigenstates. This is the unique decoupling limit available to the tree-level Higgs potential of the MSSM, although other misaligned decoupling limits may be realized for more general two doublet potentials. In the aligned decoupling limit  $h = H_\parallel$  with  $\sin(\beta - \alpha) = 1$  and  $\cos(\beta - \alpha) = 0$ .

The couplings of physical Higgs bosons to gauge bosons arise from the gauge kinetic terms of the Higgs fields

$$(D_\mu H_u)^* D^\mu H_u + (D_\mu H_d)^* D^\mu H_d \quad (2.20)$$

where  $D_\mu = \partial_\mu + ig' \frac{1}{2} Y B_\mu + ig T^a W_\mu^a$  is the covariant derivative including the  $SU(2)_L \times U(1)_Y$  gauge connections  $W_\mu^a$  and  $B_\mu$ . A coupling of two gauge bosons to a single physical Higgs boson arises from (2.20) with a gauge field in each covariant derivative, a physical Higgs boson in one Higgs field, and an expectation value in the other Higgs field. In terms of the  $H_\parallel - H_\perp$  basis these couplings are particularly simple. Since it is only  $H_\parallel$  which is parallel to the expectation value, only this component appears in these couplings

$$(D_\mu v)^* D^\mu H_\parallel + (D_\mu H_\parallel)^* D^\mu v, \quad (2.21)$$

where of course  $D_\mu v$  contains only gauge field couplings since  $\partial_\mu v = 0$ . In terms of the physical gauge bosons, the couplings in (2.21) give rise to  $WWH_\parallel$  and  $ZZH_\parallel$  interactions. In terms of the physical Higgs scalar eigenstates  $h$  and  $H$  related to  $H_\parallel$  in (2.16) these couplings give interactions  $WWh$  and  $ZZh$  proportional to  $\sin(\beta - \alpha)$  and interactions  $WWH$  and  $ZZH$  proportional to  $\cos(\beta - \alpha)$ . In the Higgs aligned decoupling limit the latter interactions vanish since  $H = H_\perp$  in this limit with  $\cos(\beta - \alpha) = 0$ . Note that there are no interactions of two gauge bosons with a single charged Higgs boson of the form  $W^\pm ZH^\mp$ , since from (2.19) the

physical charged Higgs boson resides in  $H_\perp$ , while from (2.21) these type of interactions arise only for  $H_\parallel$ . This result generalizes to any number of Higgs doublets.

A coupling of a single gauge boson to two physical Higgs bosons arises from (2.20) with a single gauge field in one of the covariant derivatives, physical Higgs bosons in each Higgs field, and a derivative acting on one of the Higgs fields

$$(D_\mu H^*)\partial^\mu H + (\partial_\mu H)^* D^\mu H \quad (2.22)$$

where the covariant derivatives  $D_\mu$  are again understood to only contain gauge fields here. This subset of couplings represents the Higgs current coupling to a single gauge boson, and therefore must contain at least one imaginary component of a Higgs field. Now from equations (2.17) and (2.19) the imaginary components of the Higgs fields appear in the physical mass eigenstates only through  $H_\perp$ . So the couplings (2.22) to physical mass eigenstates are contained in

$$(D_\mu H_\perp)^* \partial^\mu H_\perp + (\partial_\mu H_\perp)^* D^\mu H_\perp \quad (2.23)$$

In terms of the physical  $Z$  gauge boson these couplings give rise to  $ZH_\perp H_\perp$  interactions. In terms of the physical eigenstates  $h$  and  $H$  related to  $H_\perp$  in (2.16), these couplings give the interaction  $ZAH$  proportional to  $\sin(\beta - \alpha)$  and  $ZAh$  proportional to  $\cos(\beta - \alpha)$ . In the Higgs aligned decoupling limit the latter interaction vanishes since  $h = H_\parallel$  in this limit with  $\cos(\beta - \alpha) = 0$ .

## 2.8 Appendix: Quasi-Fixed Point for the Stop Trilinear Coupling $A_t$

The MSSM has a number of quasi-fixed points for various couplings that make a relation in the low energy theory between them and other parameters quite natural. These couplings include the top Yukawa and top trilinear coupling. Consider first the so called Pendleton-Ross quasi-fixed point for the top Yukawa [70]. The one-loop  $\beta$ -functions for the top Yukawa  $\lambda_t$  and  $SU(3)_C$  gauge coupling  $g_3$  in the MSSM are

$$16\pi^2\beta_{\lambda_t} = \lambda_t(6\lambda_t^2 - \frac{16}{3}g_3^2) \quad (2.24)$$

$$16\pi^2\beta_{g_3} = -3g_3^3 \quad (2.25)$$

where  $SU(2)_L$  and  $U(1)_Y$  gauge interactions have been neglected in  $\beta_{\lambda_t}$ . These  $\beta$ -functions give a one-loop  $\beta$ -function for the logarithm of the ratio of couplings of

$$16\pi^2\beta_{\ln(\lambda_t/g_3)} = 6\lambda_t^2 - \frac{7}{3}g_3^2. \quad (2.26)$$

Vanishing of this  $\beta$ -function implies that the ratio of the top Yukawa to  $SU(3)_C$  gauge coupling,  $\lambda_t/g_3$ , is independent of renormalization group scale at one-loop. Since  $\beta_{g_3}$  does not vanish at one-loop,  $g_3$  is renormalization scale dependent. So the vanishing of  $\beta_{\ln(\lambda_t/g_3)}$  defines a quasi-fixed point for  $\lambda_t$  rather than a scale-independent fixed-point relation. With the above approximations the Pendleton-Ross quasi-fixed point in the MSSM occurs for

$$\lambda_t^2 = \frac{7}{18}g_3^2. \quad (2.27)$$

Since  $\beta_{g_3}$  is independent of  $\lambda_t$  at one-loop, and the coefficient of the  $\lambda_t^2$  term in  $\beta_{\ln(\lambda_t/g_3)}$  is positive, this quasi-fixed point is attractive for  $\lambda_t/g_3$  both above and below the quasi-fixed point value. Moreover, since  $\beta_{\lambda_t}$  is cubic in  $\lambda_t$ , it is very strongly attractive from above.

The top trilinear coupling and gluino mass have a similar quasi-fixed point relation [71, 72].

The one-loop  $\beta$ -functions for the top trilinear coupling,  $A_t$ , and gluino mass,  $M_3$ , are

$$16\pi^2\beta_{A_t} = 12\lambda_t^2 A_t + \frac{32}{3}g_3^2 M_3 \quad (2.28)$$

$$16\pi^2\beta_{M_3} = -2g_3^2 M_3 \quad (2.29)$$

where  $SU(2)_L$  and  $U(1)_Y$  gauge interactions have been neglected in  $\beta_{A_t}$ . Adding these  $\beta$ -functions gives

$$16\pi^2\beta_{(A_t+M_3)} = 12\lambda_t^2 A_t + \frac{14}{3}g_3^2 M_3. \quad (2.30)$$

At the Pendleton-Ross quasi-fixed point (2.27) for the top Yukawa in the MSSM this reduces to

$$16\pi^2\beta_{(A_t+M_3)} = \frac{14}{3}g_3^2(A_t + M_3). \quad (2.31)$$

The vanishing of  $\beta_{A_t+M_3}$  again defines a quasi-fixed point for  $A_t$  rather than a scale independent fixed point relation. With the above approximations at the Pendleton-Ross quasi-fixed point, the top trilinear then has a quasi-fixed point of

$$A_t = -M_3. \quad (2.32)$$

Since the coefficient of  $\beta_{A_t+M_3}$  is positive, this quasi-fixed point is attractive. Moreover, since it is proportional to  $g_3^2$  with a sizeable coefficient it is rather strongly attractive. Because of this it is most natural for  $A_t$  and  $M_3$  to have opposite sign and be comparable in magnitude at low scales due to renormalization group evolution. This conclusion is rather insensitive to messenger scale boundary conditions for  $A_t$ , at least for large enough messenger scales.

## References

- [1] **ALEPH, DELPHI, L3 and OPAL** Collaboration, The LEP Working Group for Higgs Boson Searches, “Search for neutral MSSM Higgs bosons at LEP,” [hep-ex/0602042](#).
- [2] The LEP Working Group for Higgs boson searches: Barate *et al.*, “Search for the standard model Higgs boson at LEP,” *Phys. Lett.* **B565** (2003) 61–75, [hep-ex/0306033](#).
- [3] The LEP Working Group for Higgs boson searches, “Searches for invisible Higgs bosons: Preliminary combined results using LEP data collected at energies up to 209 GeV,” [hep-ex/0107032](#).
- [4] A. Belyaev, Q.-H. Cao, D. Nomura, K. Tobe, and C. P. Yuan, “Light MSSM Higgs boson scenario and its test at hadron colliders,” [hep-ph/0609079](#).
- [5] Y. Okada, M. Yamaguchi, and T. Yanagida, “Upper bound of the lightest Higgs boson mass in the minimal supersymmetric standard model,” *Prog. Theor. Phys.* **85** (1991) 1–6.
- [6] J. R. Ellis, G. Ridolfi, and F. Zwirner, “Radiative corrections to the masses of supersymmetric Higgs bosons,” *Phys. Lett.* **B257** (1991) 83–91.
- [7] H. E. Haber and R. Hempfling, “Can the mass of the lightest Higgs boson of the minimal supersymmetric model be larger than  $m(Z)$ ?” *Phys. Rev. Lett.* **66** (1991) 1815–1818.
- [8] M. Carena, J. R. Espinosa, M. Quiros, and C. E. M. Wagner, “Analytical expressions for radiatively corrected Higgs masses and couplings in the MSSM,” *Phys. Lett.* **B355** (1995) 209–221, [hep-ph/9504316](#).
- [9] H. E. Haber, R. Hempfling, and A. H. Hoang, “Approximating the radiatively corrected Higgs mass in the minimal supersymmetric model,” *Z. Phys.* **C75** (1997) 539–554, [hep-ph/9609331](#).
- [10] S. G. Kim *et al.*, “A solution for little hierarchy problem and  $b \rightarrow s \gamma$ ,” *Phys. Rev.* **D74** (2006) 115016, [hep-ph/0609076](#).
- [11] W.-M. Yao *et al.*, “Review of Particle Physics,” *Journal of Physics G* **33** (2006) 1+.
- [12] S. Heinemeyer, W. Hollik, and G. Weiglein, “FeynHiggs: A program for the calculation of the masses of the neutral CP-even Higgs bosons in the MSSM,” *Comput. Phys. Commun.* **124** (2000) 76–89, [hep-ph/9812320](#).
- [13] S. Heinemeyer, W. Hollik, and G. Weiglein, “The masses of the neutral CP-even Higgs bosons in the MSSM: Accurate analysis at the two-loop level,” *Eur. Phys. J.* **C9** (1999) 343–366, [hep-ph/9812472](#).
- [14] G. Degrandi, S. Heinemeyer, W. Hollik, P. Slavich, and G. Weiglein, “Towards high-precision predictions for the MSSM Higgs sector,” *Eur. Phys. J.* **C28** (2003) 133–143, [hep-ph/0212020](#).
- [15] M. Frank *et al.*, “The Higgs boson masses and mixings of the complex MSSM in the Feynman-diagrammatic approach,” [hep-ph/0611326](#).

- [16] J. R. Espinosa and R.-J. Zhang, “MSSM lightest CP-even Higgs boson mass to  $O(\alpha(s)\alpha(t))$ : The effective potential approach,” *JHEP* **03** (2000) 026, [hep-ph/9912236](#).
- [17] M. Carena *et al.*, “Reconciling the two-loop diagrammatic and effective field theory computations of the mass of the lightest CP-even Higgs boson in the MSSM,” *Nucl. Phys.* **B580** (2000) 29–57, [hep-ph/0001002](#).
- [18] S. Heinemeyer, “MSSM Higgs physics at higher orders,” [hep-ph/0407244](#).
- [19] S. Heinemeyer, W. Hollik, and G. Weiglein, “The mass of the lightest MSSM Higgs boson: A compact analytical expression at the two-loop level,” *Phys. Lett.* **B455** (1999) 179–191, [hep-ph/9903404](#).
- [20] R. Kitano and Y. Nomura, “Supersymmetry, naturalness, and signatures at the LHC,” *Phys. Rev.* **D73** (2006) 095004, [hep-ph/0602096](#).
- [21] R. Dermisek and I. Low, “Probing the stop sector and the sanity of the MSSM with the Higgs boson at the LHC,” [hep-ph/0701235](#).
- [22] Tevatron Electroweak Working Group, “Combination of CDF and D0 results on the mass of the top quark,” [hep-ex/0608032](#).
- [23] H. E. Haber and R. Hempfling, “The Renormalization group improved Higgs sector of the minimal supersymmetric model,” *Phys. Rev.* **D48** (1993) 4280–4309, [hep-ph/9307201](#).
- [24] M. Carena, S. Heinemeyer, C. E. M. Wagner, and G. Weiglein, “Suggestions for improved benchmark scenarios for Higgs- boson searches at LEP2,” [hep-ph/9912223](#).
- [25] T. Banks, “Supersymmetry and the quark mass matrix,” *Nucl. Phys.* **B303** (1988) 172.
- [26] L. J. Hall, R. Rattazzi, and U. Sarid, “The Top quark mass in supersymmetric SO(10) unification,” *Phys. Rev.* **D50** (1994) 7048–7065, [hep-ph/9306309](#).
- [27] R. Hempfling, “Yukawa coupling unification with supersymmetric threshold corrections,” *Phys. Rev.* **D49** (1994) 6168–6172.
- [28] M. Carena, M. Olechowski, S. Pokorski, and C. E. M. Wagner, “Electroweak symmetry breaking and bottom - top Yukawa unification,” *Nucl. Phys.* **B426** (1994) 269–300, [hep-ph/9402253](#).
- [29] M. Carena, D. Garcia, U. Nierste, and C. E. M. Wagner, “Effective Lagrangian for the anti-t b H+ interaction in the MSSM and charged Higgs phenomenology,” *Nucl. Phys.* **B577** (2000) 88–120, [hep-ph/9912516](#).
- [30] H. Eberl, K. Hidaka, S. Kraml, W. Majerotto, and Y. Yamada, “Improved SUSY QCD corrections to Higgs boson decays into quarks and squarks,” *Phys. Rev.* **D62** (2000) 055006, [hep-ph/9912463](#).
- [31] S. Heinemeyer, W. Hollik, H. Rzehak, and G. Weiglein, “High-precision predictions for the MSSM Higgs sector at  $O(\alpha(b)\alpha(s))$ ,” *Eur. Phys. J.* **C39** (2005) 465–481, [hep-ph/0411114](#).
- [32] M. Carena and H. E. Haber, “Higgs boson theory and phenomenology. ((V)),” *Prog. Part. Nucl. Phys.* **50** (2003) 63–152, [hep-ph/0208209](#).
- [33] J. M. Moreno, D. H. Oaknin, and M. Quiros, “Sphalerons in the MSSM,” *Nucl. Phys.* **B483** (1997) 267–290, [hep-ph/9605387](#).
- [34] J. R. Espinosa and J. F. Gunion, “A no-lose theorem for Higgs searches at a future linear collider,” *Phys. Rev. Lett.* **82** (1999) 1084–1087, [hep-ph/9807275](#).

- [35] M. Carena, S. Mrenna, and C. E. M. Wagner, “The complementarity of LEP, the Tevatron and the LHC in the search for a light MSSM Higgs boson,” *Phys. Rev.* **D62** (2000) 055008, [hep-ph/9907422](#).
- [36] M. E. Peskin and T. Takeuchi, “Estimation of oblique electroweak corrections,” *Phys. Rev.* **D46** (1992) 381–409.
- [37] J. Erler, “Precision electroweak physics,” [hep-ph/0604035](#).
- [38] S. Heinemeyer, W. Hollik, and G. Weiglein, “Electroweak precision observables in the minimal supersymmetric standard model,” *Phys. Rept.* **425** (2006) 265–368, [hep-ph/0412214](#).
- [39] S. Eidelman *et al.*, “Review of particle physics,” *Phys. Lett.* **B592** (2004) 1.
- [40] T. Inami, C. S. Lim, and A. Yamada, “Radiative correction parameter S in beyond the standard models,” *Mod. Phys. Lett.* **A7** (1992) 2789–2798.
- [41] T. Becher and M. Neubert, “Analysis of  $\text{Br}(B \rightarrow X/s \text{ gamma})$  at NNLO with a cut on photon energy,” *Phys. Rev. Lett.* **98** (2007) 022003, [hep-ph/0610067](#).
- [42] Heavy Flavor Averaging Group (HFAG), “Averages of b-hadron properties at the end of 2005,” [hep-ex/0603003](#).
- [43] P. Gambino and M. Misiak, “Quark mass effects in anti- $B \rightarrow X/s \text{ gamma}$ ,” *Nucl. Phys.* **B611** (2001) 338–366, [hep-ph/0104034](#).
- [44] T. Hurth, “Present status of inclusive rare B decays,” *Rev. Mod. Phys.* **75** (2003) 1159–1199, [hep-ph/0212304](#).
- [45] The LEP Working Group for Higgs boson searches, “Search for charged Higgs bosons: Preliminary combined results using LEP data collected at energies up to 209 GeV,” [hep-ex/0107031](#).
- [46] K. Okumura and L. Roszkowski, “Weakened constraints from  $b \rightarrow s \text{ gamma}$  on supersymmetry flavor mixing due to next-to-leading-order corrections,” *Phys. Rev. Lett.* **92** (2004) 161801.
- [47] M. Drees, “A supersymmetric explanation of the excess of Higgs-like events at LEP,” *Phys. Rev.* **D71** (2005) 115006, [hep-ph/0502075](#).
- [48] D. Hooper and T. Plehn, “Dark matter and collider phenomenology with two light supersymmetric Higgs bosons,” *Phys. Rev.* **D72** (2005) 115005, [hep-ph/0506061](#).
- [49] T. Inami and C. S. Lim, “Effects of superheavy quarks and leptons in low-energy weak processes  $K(L) \rightarrow \mu \text{ anti-}\mu$ ,  $K^+ \rightarrow \pi^+ \text{ neutrino anti-neutrino}$   $K^0 \leftrightarrow \text{anti-}K^0$ ,” *Prog. Theor. Phys.* **65** (1981) 297.
- [50] B. Grzadkowski and P. Krawczyk, “Higgs particle effects in flavor changing transitions,” *Z. Phys.* **C18** (1983) 43–45.
- [51] CDF Collaboration, A. Abulencia *et al.*, “Search for  $B_s \rightarrow \mu^+ \mu^-$  and  $B_d \rightarrow \mu^+ \mu^-$  decays in  $p\bar{p}$  collisions with CDF II,” *Phys. Rev. Lett.* **95** (2005) 221805, [hep-ex/0508036](#).
- [52] H. E. Logan and U. Nierste, “ $B/s, d \rightarrow l^+ l^-$  in a two-Higgs-doublet model,” *Nucl. Phys.* **B586** (2000) 39–55, [hep-ph/0004139](#).
- [53] P. H. Chankowski and L. Slawianowska, “ $B^0/d, s \rightarrow \mu^- \mu^+$  decay in the MSSM,” *Phys. Rev.* **D63** (2001) 054012, [hep-ph/0008046](#).

- [54] C. Bobeth, T. Ewerth, F. Kruger, and J. Urban, “Analysis of neutral Higgs-boson contributions to the decays  $\text{anti-B/s} \rightarrow l^+ l^-$  and  $\text{anti-B} \rightarrow K l^+ l^-$ ,” *Phys. Rev.* **D64** (2001) 074014, [hep-ph/0104284](#).
- [55] K. S. Babu and C. F. Kolda, “Higgs-mediated  $B_0 \rightarrow \mu^+ \mu^-$  in minimal supersymmetry,” *Phys. Rev. Lett.* **84** (2000) 228–231, [hep-ph/9909476](#).
- [56] A. J. Buras, P. H. Chankowski, J. Rosiek, and L. Slawianowska, “ $\Delta(M(d,s))$ ,  $B/(d,s)_0 \rightarrow \mu^+ \mu^-$  and  $B \rightarrow X/s \gamma$  in supersymmetry at large  $\tan(\beta)$ ,” *Nucl. Phys.* **B659** (2003) 3, [hep-ph/0210145](#).
- [57] A. Dedes and A. Pilaftsis, “Resummed effective Lagrangian for Higgs-mediated FCNC interactions in the CP-violating MSSM,” *Phys. Rev.* **D67** (2003) 015012, [hep-ph/0209306](#).
- [58] J. K. Mizukoshi, X. Tata, and Y. Wang, “Higgs-mediated leptonic decays of B/s and B/d mesons as probes of supersymmetry,” *Phys. Rev.* **D66** (2002) 115003, [hep-ph/0208078](#).
- [59] A. Dedes, “The Higgs penguin and its applications: An overview,” *Mod. Phys. Lett.* **A18** (2003) 2627–2644, [hep-ph/0309233](#).
- [60] C. Bobeth, T. Ewerth, F. Kruger, and J. Urban, “Enhancement of  $B(\text{anti-B/d} \rightarrow \mu^+ \mu^-)/B(\text{anti-B/s} \rightarrow \mu^+ \mu^-)$  in the MSSM with minimal flavour violation and large  $\tan \beta$ ,” *Phys. Rev.* **D66** (2002) 074021, [hep-ph/0204225](#).
- [61] G. Belanger, F. Boudjema, A. Pukhov, and A. Semenov, “MicrOMEGAs: A program for calculating the relic density in the MSSM,” *Comput. Phys. Commun.* **149** (2002) 103–120, [hep-ph/0112278](#).
- [62] G. Belanger, F. Boudjema, A. Pukhov, and A. Semenov, “MicrOMEGAs: Version 1.3,” *Comput. Phys. Commun.* **174** (2006) 577–604, [hep-ph/0405253](#).
- [63] F. E. Paige, S. D. Protopopescu, H. Baer, and X. Tata, “ISAJET 7.69: A Monte Carlo event generator for p p, anti-p p, and e+ e- reactions,” [hep-ph/0312045](#).
- [64] L. E. Ibanez and G. G. Ross, “ $SU(2)_L \times U(1)$  Symmetry Breaking as a Radiative Effect of Supersymmetry Breaking in GUTs,” *Phys. Lett.* **B110** (1982) 215–220.
- [65] J. R. Ellis, D. V. Nanopoulos, and K. Tamvakis, “Grand Unification in Simple Supergravity,” *Phys. Lett.* **B121** (1983) 123.
- [66] L. Alvarez-Gaume, J. Polchinski, and M. B. Wise, “Minimal Low-Energy Supergravity,” *Nucl. Phys.* **B221** (1983) 495.
- [67] G. L. Kane, T. T. Wang, B. D. Nelson, and L.-T. Wang, “Theoretical implications of the LEP Higgs search,” *Phys. Rev.* **D71** (2005) 035006, [hep-ph/0407001](#).
- [68] R. Dermisek and H. D. Kim, “Radiatively generated maximal mixing scenario for the Higgs mass and the least fine tuned minimal supersymmetric standard model,” *Phys. Rev. Lett.* **96** (2006) 211803, [hep-ph/0601036](#).
- [69] J. F. Gunion, H. E. Haber, G. L. Kane, and S. Dawson, *The Higgs Hunter’s Guide*. Alan M. Wylde, 1990.
- [70] B. Pendleton and G. G. Ross, “Mass and Mixing Angle Predictions from Infrared Fixed Points,” *Phys. Lett.* **B98** (1981) 291.
- [71] P. M. Ferreira, I. Jack, and D. R. T. Jones, “Infrared soft universality,” *Phys. Lett.* **B357** (1995) 359–364, [hep-ph/9506467](#).
- [72] M. Lanzagorta and G. G. Ross, “Infrared fixed point structure of soft supersymmetry breaking mass terms,” *Phys. Lett.* **B364** (1995) 163–174, [hep-ph/9507366](#).

## Chapter 3

# The Minimally Tuned Minimal Supersymmetric Standard Model

This chapter appears in print in JHEP04(2008)073, arxiv:0709.0980 [hep-ph], and consists of work done with Jean-François Fortin.

The regions in the Minimal Supersymmetric Standard Model with the minimal amount of fine-tuning of electroweak symmetry breaking are presented for general messenger scale. No a priori relations among the soft supersymmetry breaking parameters are assumed and fine-tuning is minimized with respect to all the important parameters which affect electroweak symmetry breaking. The superpartner spectra in the minimally tuned region of parameter space are quite distinctive with large stop mixing at the low scale and negative squark soft masses at the high scale. The minimal amount of tuning increases enormously for a Higgs mass beyond roughly 120 GeV.

### 3.1 Introduction

The Minimal Supersymmetric Standard Model, or MSSM, is a well-motivated candidate for physics beyond the Standard Model (SM). The gauge couplings within the MSSM unify to within a few percent at the grand unified theory (GUT) scale,  $M_{\text{GUT}} \simeq 2 \times 10^{16}$  GeV, and the lightest supersymmetric particle is a good dark matter candidate provided that R-parity is conserved. Supersymmetry (SUSY) can also naturally stabilize the hierarchy between the electroweak (EW) and the GUT or Planck scale. It does this by providing a radiative mechanism for electroweak symmetry breaking (EWSB) where large quantum fluctuations of the scalar top

squarks due to the large Yukawa coupling destabilize the origin of the Higgs potential. In much of the MSSM parameter space this quite naturally leads to the right EWSB scale, as long as the soft SUSY breaking parameters lie near it.

The absence of any direct experimental evidence from collider searches for the MSSM scalar particles and the Higgs boson has, however, ruled out significant regions in the MSSM parameter space. Indirect evidence from EW precision measurements and searches for flavor changing neutral currents, CP violating effects and rare decays has not been forthcoming either, providing additional severe constraints. As a result, the soft SUSY breaking parameters must lie well above the EW scale in order to satisfy the experimental constraints, especially the constraints on the Higgs mass from the results of the CERN LEP collider ( $m_h \gtrsim 114.4$  GeV [1]).

Soft SUSY breaking parameters well above the EW scale reintroduce a small hierarchy and require some fine-tuning (FT) among the SUSY parameters in order to obtain EWSB [2]-[22]. This is usually referred to as the supersymmetric little hierarchy problem.

Different choices for the soft SUSY breaking parameters lead to different amounts of FT. This paper presents the minimally tuned MSSM (or MTMSSM), i.e. the MSSM parameter region that has the least model-independent FT of EWSB. Model-independent means that no relations are assumed between the soft SUSY breaking parameters at the scale at which they are generated (which will be referred to as the messenger scale). Rather, each of them is taken to be an independent parameter which is free at the messenger scale, and which therefore can contribute to the total FT of the EWSB scale. The messenger scale itself is varied between 2 TeV and  $M_{\text{GUT}}$  and the effect of this on the minimal FT is discussed.

In Section 3.2, EWSB in the MSSM will be reviewed. Section 3.3 discusses the tuning measure used in this paper. The parameters taken to contribute to the tuning are  $|\mu|^2$ ,  $m_{H_u}^2$ , the gaugino masses  $M_1$ ,  $M_2$  and  $M_3$ , the stop soft masses  $m_{t_L}^2$  and  $m_{t_R}^2$ , and the stop soft trilinear coupling  $A_t$ .

Section 3.4 contains some of the main results. The low- and high-scale MSSM spectrum which leads to the least model-independent FT is found. This is done for various messenger

scales by numerically minimizing the FT expression subject to constraints on the Higgs, stop, and gaugino masses. The results are then motivated analytically. The least FT is found to be about 5% if the messenger scale coincides with the GUT scale. An important feature of the least FT region is negative stop soft masses at the messenger scale (first pointed out in [19]). Even for messenger scales as low as 2 TeV, the stop soft masses are tachyonic at the messenger scale (threshold effects in the RG-running were neglected throughout). This does not lead to any problems with charge and/or color breaking minima. Another feature of the least FT region is that the trilinear stop soft coupling,  $A_t$ , is negative and lies near “natural” maximal mixing, i.e.  $A_t \simeq -2m_{\tilde{t}}$ , where  $m_{\tilde{t}}$  is the average of the two stop soft masses. This value for  $A_t$  maximizes the radiative corrections to  $m_h$ . The large stop mixing leads to a sizeable splitting between the two stop mass eigenstates. Moreover, the gluino mass,  $M_3$ , is much smaller than the wino mass,  $M_2$ , at the high scale. The wino mass, in turn, is much smaller than the bino mass  $M_1$ . Phenomenological consequences of the low-scale spectrum are briefly summarized.

Section 3.5 contains the rest of the main results of the paper. The FT is minimized as a function of the lower bound on the Higgs mass (with the messenger scale set to  $M_{\text{GUT}}$ ). Although the numerical minimization procedure contains the dominant one-loop expression for  $m_h$  as a constraint, the resulting least FT spectra are used to calculate  $m_h$  more accurately with the program `FeynHiggs` [23, 24, 25, 26, 27]. The result is a plot of the minimal FT as a function of  $m_h$ , where  $m_h$  now includes all the important higher order corrections. There are several striking features of this plot. First of all, for  $m_h$  larger than a certain value, the FT increases very rapidly and at least as fast as an exponential. Secondly, around this  $m_h$ , the value of  $A_t$  in the least FT region makes a sudden transition from lying near  $-2m_{\tilde{t}}$  to lying near  $+2m_{\tilde{t}}$ . The third striking feature is that this value of  $m_h$  is surprisingly low. The precise value is only slightly dependent on the parameters in the Higgs sector and can be taken to lie around 120 GeV. It has been mentioned before that the FT increases exponentially as a function of  $m_h$ , see for example [8, 14]. Previously, these results were obtained by assuming a specific set of boundary conditions at the messenger scale and without taking into account important

higher-order corrections to the Higgs mass which are included in `FeynHiggs`. The results here do not assume particular boundary values for any of the important parameters contributing to EWSB - rather, the spectrum that leads to the least amount of tuning is found. Moreover, the higher-order Higgs mass corrections are included. It is shown that the *minimal* amount of tuning still increases at least as fast as an exponential.

Section 3.6 contains a summary of the results and the conclusions. Appendix 3.7 reviews the semi-numerical solutions of the MSSM one-loop renormalization - group (RG) equations. These are used to calculate the expression for the FT employed in this paper. Appendix 3.8 contains a list of expressions for the FT with respect to various parameters.

### 3.2 Electroweak Symmetry Breaking

In the Higgs decoupling limit of the MSSM, the lower bound on the mass of the lighter CP-even Higgs mass eigenstate  $h$  coincides with the 114.4 GeV bound on the mass of the SM Higgs boson [1]. The mass of  $h$  may be approximated by

$$m_h^2 \simeq m_Z^2 \cos^2 2\beta + \frac{3}{4\pi^2} \frac{m_t^4}{v^2} \left[ \log \frac{m_{\tilde{t}}^2}{m_t^2} + \frac{X_t^2}{m_{\tilde{t}}^2} \left( 1 - \frac{X_t^2}{12m_{\tilde{t}}^2} \right) \right] \quad (3.1)$$

which, in addition to the tree-level Higgs mass, includes the dominant one-loop quantum corrections coming from top and stop loops [28, 29, 30, 31, 32, 33]. Here  $m_t$  is the top mass,  $m_{\tilde{t}}^2$  is the arithmetic mean of the two squared stop masses and  $v = \sqrt{2}m_W/g \simeq 174.1$  GeV where  $g$  is the  $SU(2)$  gauge coupling and  $m_W$  is the mass of the  $W$ -boson. Furthermore, equation (3.1) assumes  $m_{\tilde{t}} \gg m_t$ . The stop mixing parameter is given by  $X_t = A_t - \mu \cot \beta$  ( $\simeq A_t$  for large  $\tan \beta$ ), where  $A_t$  denotes the stop soft trilinear coupling and  $\mu$  is the supersymmetric Higgsino mass parameter. The first term in equation (3.1) is the tree-level contribution to the Higgs mass. The first term in square brackets comes from renormalization group running of the Higgs quartic coupling below the stop mass scale and vanishes in the limit of exact supersymmetry. It grows logarithmically with the stop mass. The second term in square brackets is only present

for non-zero stop mixing and comes from a finite threshold correction to the Higgs quartic coupling at the stop mass scale. It is independent of the stop mass for fixed  $X_t/m_{\tilde{t}}$ , and grows as  $(X_t/m_{\tilde{t}})^2$  for small  $X_t/m_{\tilde{t}}$ .

Equation (3.1) implies a combination of three things which are required to satisfy the bound on  $m_h$ , namely a large tree-level contribution, large stop masses and/or large stop mixing<sup>1</sup>. A large tree-level contribution to  $m_h$  requires  $\tan\beta$  to be at least of a moderate size ( $\gtrsim 5 - 10$ ). Although the stop masses must be rather large, their lower bound is very sensitive to the size of the stop mixing, with larger mixing allowing for much smaller stop masses (see [34] for a recent study on this). The reason for this sensitive dependence is due to the Higgs mass depending logarithmically on the stop masses in contrast to the polynomial dependence on the stop mixing.

The soft masses are not only directly constrained from the LEP Higgs bounds but also indirectly by constraints on flavor changing neutral currents, electroweak precision measurements and CP-violation. Besides these, however, the Higgs sector parameters are also constrained by requiring that the electroweak symmetry is broken. This leads to the following two tree-level relations at the low scale

$$\sin 2\beta = \frac{2m_{12}^2}{m_{H_u}^2 + m_{H_d}^2 + 2|\mu|^2} = \frac{2m_{12}^2}{m_A^2} \quad (3.2)$$

$$\frac{m_Z^2}{2} = -|\mu|^2 + \frac{m_{H_d}^2 - m_{H_u}^2 \tan^2\beta}{\tan^2\beta - 1}, \quad (3.3)$$

where  $m_A$  is the CP-odd Higgs mass, and  $\beta$  is determined from the ratio of the two vacuum expectation values  $v_u \equiv \langle \text{Re}(H_u^0) \rangle$  and  $v_d \equiv \langle \text{Re}(H_d^0) \rangle$  as  $\tan\beta = v_u/v_d$ . The masses  $m_{H_u}^2$ ,  $m_{H_d}^2$  and  $m_{12}^2$  are the three soft mass parameters in the MSSM Higgs sector. For a given value of  $\tan\beta$ ,  $m_{12}^2$  may be eliminated in favor of  $m_A^2$  with equation (3.2). Equation (3.3) gives an expression for  $m_Z^2$  in terms of the supersymmetric mass parameter  $\mu$  and the soft masses  $m_{H_u}^2$  and  $m_{H_d}^2$ . Since  $\tan\beta$  should be sizeable, the contribution from  $m_{H_d}^2$  to the expression for  $m_Z^2$

---

<sup>1</sup>Although it is not obvious, it is important to note that these statements remain the same even away from the Higgs decoupling limit, see e.g. [34]. Moreover, as mentioned in [34], the fine-tuning in the Higgs decoupling limit is comparable to the fine-tuning in the Higgs non-decoupling limit. Thus the least fine-tuned regions found in this paper do not depend in an essential way on the fact that the analysis is done in the Higgs decoupling limit.

may be neglected and (3.3) simplifies to

$$m_Z^2 = -2|\mu|^2 - 2m_{H_u}^2. \quad (3.4)$$

Close to the Higgs decoupling limit,  $m_A$  is relatively large. However, since  $|\mu|^2, m_{H_u}^2 \sim \mathcal{O}(m_Z^2)$  to avoid large cancellations,  $m_A$  may not be too large, otherwise  $m_{H_d}^2$  would also be sizeable and equation (3.4) would break down (unless the value of  $\tan\beta$  is increased accordingly). By choosing  $\tan\beta = 10$  and  $m_A = 250$  GeV in the numerical analysis throughout, equation (3.4) holds to a very good approximation.

Equation (3.4) holds at tree-level, and although quantum corrections may add  $\mathcal{O}(10$  GeV) to the right hand side of (3.4), this has negligible impact on the amount of fine-tuning to be discussed below.

The parameters  $m_{H_u}^2$  and  $|\mu|^2$  in equation (3.4) are evaluated at the scale  $m_Z$ . Since the fine-tuning of EWSB is a measure of the sensitivity of some low-scale EWSB parameter (usually taken to be  $m_Z^2$ ) to a change in high-scale input parameters,  $|\mu|^2$  and  $m_{H_u}^2$  need to be evolved to a high scale using their RG equations (the one-loop RG equations will be sufficient for the purposes of discussing fine-tuning). Under RG running many of the soft parameters mix, and as a result of this mixing, the expression for  $m_Z^2$  in terms of parameters that are evaluated at the messenger scale  $M_S$  differs significantly from the simple form given in (3.4). The RG-equations may be integrated (see Appendix 3.7) and the expression for  $m_Z^2$  may generically be written as [35, 36]

$$m_Z^2 = \sum_{i,j} c_{ij}(\tan\beta, M_S) m_i(M_S) m_j(M_S). \quad (3.5)$$

For moderate and not too large values of  $\tan\beta$  with an appropriate  $m_A$ , the simplified expression for  $m_Z^2$  is applicable (equation (3.4)) and contributions from the bottom/sbottom and tau/stau sectors may still be neglected<sup>2</sup>. The most important parameters appearing in (3.5) then are  $\mu^2$ ,  $m_{H_u}^2$ , the gaugino masses  $M_1$ ,  $M_2$  and  $M_3$ , the stop soft masses  $m_{\tilde{t}_L}^2$  and  $m_{\tilde{t}_R}^2$ , and the stop soft

---

<sup>2</sup>For large  $\tan\beta$ , bottom/sbottom and tau/stau sector contributions must be included. Large  $\tan\beta$  allows the tree-level Higgs mass to be increased by about 2 GeV compared to its value for  $\tan\beta = 10$ . Higher-order corrections to the Higgs mass from the bottom/sbottom sector, however, can in some regions lead to rather large negative contributions. The effect on the least fine-tuned regions found in this paper will not be discussed in detail, but it is unlikely that the main features of the least fine-tuned spectrum will change.

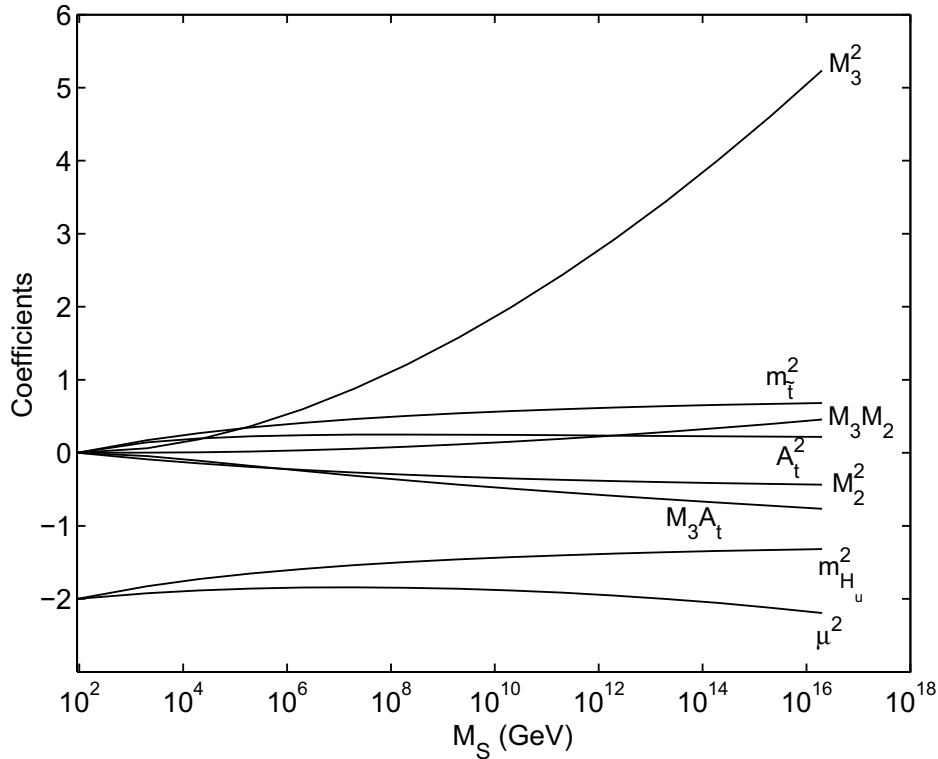


Figure 3.1: The coefficients  $c_{ij}$  defined in equation (3.5) for  $\tan\beta = 10$  as a function of the messenger scale  $M_S$ .

trilinear coupling  $A_t$ . The coefficients  $c_{ij}$  depend on  $\tan\beta$  and the messenger scale  $M_S$ . The most important coefficients are shown in Figure 3.1 for  $\tan\beta = 10$  as a function of  $M_S$ .

At the scale  $m_Z$ , the coefficients of  $m_{H_u}^2$  and  $\mu^2$  are  $-2$  while the coefficients of the other soft parameters are zero in agreement with equation (3.4). Since  $\mu^2$  is a supersymmetric parameter, it gets renormalized multiplicatively and its RG evolution does not give rise to soft parameters (see equation (3.45)). Figure 3.1 shows that the coefficient of  $\mu^2$  does not vary much and remains close to  $-2$  all the way up to the GUT scale. The RG evolution of  $m_{H_u}^2$  to higher messenger scales, however, generates non-zero coefficients for the other soft parameters. The  $\beta$ -function of  $m_{H_u}^2$ ,

$$8\pi^2\beta_{m_{H_u}^2} = 3\lambda_t^2(m_{H_u}^2 + m_{t_L}^2 + m_{t_R}^2 + |A_t|^2) - 3g_2^2|M_2|^2 - g_Y^2|M_1|^2 - \frac{1}{2}g_Y^2 S_Y, \quad (3.6)$$

depends on the stop sector parameters  $\{m_{t_L}^2, m_{t_R}^2, A_t\}$ , the wino and bino masses  $M_2$  and

$M_1$ , and  $S_Y \equiv \frac{1}{2}\text{Tr}(Y_i m_i^2)$ , which thus get generated immediately under RG evolution. The coefficients of  $M_2$  and especially  $M_1$  and  $S_Y$  in (3.6) are small and lead to small coefficients in the expression for  $m_Z^2$  (3.5). Although  $\beta_{m_{H_u}^2}$  does not explicitly depend on the gluino mass, a non-zero coefficient for  $M_3$  is generated indirectly since the stop sector  $\beta$ -functions depend on  $M_3$ . Moreover,  $M_3$  appears with a large coefficient in these  $\beta$ -functions, and thus the coefficient of  $M_3$  in equation (3.5) dominates after a few decades of RG evolution. For example, at a messenger scale of  $M_S = M_{\text{GUT}} \equiv 2 \times 10^{16}$  GeV, the expression for  $m_Z^2$  (for  $\tan \beta = 10$ ) is

$$\begin{aligned}
m_Z^2 = & -2.19 \hat{\mu}^2 - 1.32 \hat{m}_{H_u}^2 + 0.68 \hat{m}_{\tilde{t}_L}^2 + 0.68 \hat{m}_{\tilde{t}_R}^2 + 5.24 \hat{M}_3^2 - 0.44 \hat{M}_2^2 \\
& - 0.01 \hat{M}_1^2 + 0.22 \hat{A}_t^2 - 0.77 \hat{A}_t \hat{M}_3 - 0.17 \hat{A}_t \hat{M}_2 - 0.02 \hat{A}_t \hat{M}_1 \\
& + 0.46 \hat{M}_3 \hat{M}_2 + 0.07 \hat{M}_3 \hat{M}_1 + 0.01 \hat{M}_2 \hat{M}_1 + 0.05 \hat{S}_Y,
\end{aligned} \tag{3.7}$$

where the hatted parameters on the right-hand side are all evaluated at  $M_S$ . This expression may be used to calculate the FT as discussed next.

### 3.3 The Tuning Measure

A variety of tuning measures have been used in the literature (a list of references has been provided in the Introduction). Since the concept of fine-tuning (FT) is inherently subjective, there is no absolute definition of a FT measure. The most common definition of the sensitivity of an observable  $\mathcal{O}(\{a_i\})$  on a parameter  $a_i$ , denoted by  $\Delta(\mathcal{O}, a_i)$ , is given by [2, 3]

$$\Delta(\mathcal{O}, a_i) = \left| \frac{\partial \log \mathcal{O}}{\partial \log a_i} \right| = \left| \frac{a_i}{\mathcal{O}} \frac{\partial \mathcal{O}}{\partial a_i} \right|. \tag{3.8}$$

$\Delta(\mathcal{O}, a_i)$  thus measures the percentage variation of the observable under a percentage variation of the parameter. A large value of  $\Delta(\mathcal{O}, a_i)$  signifies that a small change in the parameter leads to a large change in the observable, and suggests that the observable is fine-tuned with respect to that parameter. In the literature, the FT of  $\mathcal{O}$  is often defined to be  $\max_i \Delta(\mathcal{O}(a_i))$ , e.g. [2, 3]. This FT measure arguably underestimates the ‘‘total amount’’ of FT if there is more than one parameter  $a_i$ . This can be a drawback especially if there are many parameters that are tuned by roughly the same amount. This motivates the use of a FT measure which considers

the tuning of all the parameters simultaneously. Assuming that the individual  $\Delta(\mathcal{O}, a_i)$  are uncorrelated, the following FT measure may be used (see also [16, 37])

$$\mathcal{F}(\mathcal{O}) = \sqrt{\sum_i \left(\Delta(\mathcal{O}, a_i)\right)^2}. \quad (3.9)$$

Of interest in this paper is to quantify the sensitivity of EWSB in the MSSM on (soft) supersymmetric parameters at the messenger scale  $M_S$ . To this end, the observable to consider is  $m_Z^2$  as a function of the supersymmetric Higgsino mass squared and the soft supersymmetry breaking parameters, collectively denoted by  $m_i^2(M_S)$  (in the FT measure, all parameters are taken to have mass dimension two). The sensitivity of  $m_Z^2$  with respect to each parameter may be calculated as in (3.8) with  $\mathcal{O} = m_Z^2$ , and the total FT of  $m_Z^2$  on parameters evaluated at the messenger scale  $M_S$  may be quantified by

$$\mathcal{F}(m_Z^2; M_S) = \sqrt{\sum_i \left(\Delta(m_Z^2, m_i^2(M_S))\right)^2}. \quad (3.10)$$

Note that  $\mathcal{F}(m_Z^2; M_S)$  may be interpreted as the length of a “fine-tuning vector” with components  $\Delta(m_Z^2, m_i^2(M_S))$ . This fine-tuning vector is formally a vector field defined by the gradient of the scalar field  $\log m_Z^2$ , a function of  $\log m_i^2$ , along surfaces of constant  $\log m_Z^2$ .

There are several possible drawbacks to this FT measure, see for example [22, 38]. One of these is that the individual  $\Delta(m_Z^2, m_i^2(M_S))$  are assumed to be uncorrelated. Within a given model of supersymmetry breaking, there may be relations among the parameters at the messenger scale. This would imply that the FT vector is projected onto a subspace, and the resulting FT is necessarily less. In other words, the tuning of one parameter is correlated with the tuning of another, so that the total FT is less<sup>3</sup> than that given by (3.10). Moreover, within a given model the values of the parameters at the messenger scale may be restricted to certain ranges, whereas (3.10) assumes that all values are equally likely. However, no model for supersymmetry breaking will be assumed here. Instead, the minimal FT will be found as a function of the messenger scale  $M_S$  assuming no relations or restrictions among the high-scale

---

<sup>3</sup>Note, however, that if a given model assumes relations among the high scale parameters which do not allow the parameters to fall within the least fine-tuned regions found in this paper, then the FT of such a model will most likely be substantially larger than the model-independent minimal FT, *despite* there being relations among the high scale parameters.

input parameters. For this “model-independent” tuning it is satisfactory to use the FT measure (3.10).

Note that to find the tuning of a model, one should in principle consider the tuning of all observables, since the absence of tuning in one observable does not necessarily imply it is small in others, see e.g. [17]. In this paper, however, only the tuning of EWSB will be considered.

Finally, note that the FT with respect to a single parameter is by definition (3.8) zero if that parameter happens to be zero at the messenger scale. An extreme version of this is found in the no-scale model [39], where all scalar soft masses are much smaller than the gaugino masses at the high scale. Setting them to zero, and using (3.8) and (3.10) the FT could be expected to be small. However, it may be shown that this does not minimize the FT, since  $M_3$  and  $\mu$  need to be quite large at the high scale to satisfy all the low-energy experimental bounds (see [13]). In the results presented in this paper, no parameter is found to be zero at the high scale.

### 3.4 Minimal Model Independent Tuning

In this section the minimal model independent tuning will be found as a function of the messenger scale.

#### 3.4.1 Discussion of Minimization Procedure and Constraints

The FT given by equation (3.10) is written in terms of parameters evaluated at the messenger scale. In order to find the minimal FT (MFT) for a given messenger scale that is consistent with low-energy experimental constraints, it is easiest to rewrite the FT expression in terms of parameters that are evaluated at the low scale. This can be done by expressing each high-scale parameter in terms of low-scale parameters, see Appendix 3.7. Once the FT is written in terms of low-scale parameters,  $m_{H_u}^2(m_Z)$  may be eliminated by using equation (3.4) (neglecting contributions from  $m_{H_d}^2$ ).

The low-energy constraints considered in this paper include bounds on the (physical) sparticle masses, on the gaugino masses, and on the Higgs mass<sup>4</sup>. The physical top quark mass  $m_t^{\text{pole}}$  is set to the central value of the latest Tevatron mass measurement of  $170.9 \pm 1.8$  GeV [40]. The physical stop masses are required to be at least 100 GeV which is illustrative of the actual, slightly model dependent, lower bound obtained from the Tevatron [41]. It is found that the region of MFT does not quite saturate this bound, although a slightly larger value for the top mass would allow the lighter stop to be as low as 100 GeV. The gaugino masses  $M_1$  and  $M_2$ , as well as  $\mu$ , are taken to have a lower bound of 100 GeV. The gluino mass is found to be never smaller than 335 GeV in the numerical results presented in this section, and this does not generically violate any experimental bounds.

The most important constraint is the Higgs mass bound of 114.4 GeV (valid in the decoupling limit), since it turns out that this bound is always saturated when minimizing the FT. In the numerical results presented in this paper, the Higgs mass is calculated using the formulas found in [42] (see also [28, 29, 30, 31, 32, 43]). These formulas include the one-loop corrections coming from the top/stop sector and are simple enough to be used as constraints in the FT minimization (but note that the sign convention used here for  $A_t$  is that of [44]). In order to capture some of the important leading two-loop contributions to the Higgs mass, a running top mass  $m_t(m_t) \simeq 162.5$  GeV (evaluated in the  $\overline{MS}$ -scheme) is used instead of the physical top mass  $m_t^{\text{pole}}$ . There are, however, further higher-order corrections to the Higgs mass that play a very important role, and more accurate Higgs masses may be obtained with the program `FeynHiggs` which includes many of them. These additional corrections often tend to lower the Higgs mass, and the one-loop formula used in the minimization procedure here does not capture this effect. In order to compensate for some of these additional higher-order corrections and thus obtain a more accurate estimate of the MFT, a lower bound for the Higgs mass of 121.5 GeV is used in the FT minimization, instead of the SM lower bound of 114.4 GeV. It turns

---

<sup>4</sup>Constraints from measurements of  $B \rightarrow X_s \gamma$  or the electroweak  $S$ - and  $T$ -parameter do not significantly affect the results presented below, since an experimentally consistent value can be obtained by only small adjustments (if at all necessary) in the least fine-tuned parameters - see also [34].

out that the typical low energy sparticle spectrum obtained in the analysis below then leads to a Higgs mass that lies just above 114.4 GeV when these additional corrections are taken into account (calculated with `FeynHiggs`, version 2.6.0, assuming real parameters). The issue of higher-order corrections to the Higgs mass will be revisited in Section 3.5.

Sequential Quadratic Programming (SQP) in Maple is used as a minimization algorithm. Given the FT function (3.10) written in terms of low scale parameters, as well as linear constraints on the gaugino masses and  $\mu$ , non-linear constraints on the physical stop and Higgs masses, and an initial guess, SQP generates a less FT point until the minimum is found. Unlike other minimization algorithms, SQP can handle arbitrary constraints which is essential here due to the highly non-linear physical stop mass and Higgs mass constraints.

### 3.4.2 Numerical Results

Figure 3.2 shows a plot of the MFT as a function of the messenger scale  $M_S$ . Shown are the individual contributions  $\Delta(m_Z^2, m_i^2(M_S))$  to the FT, with  $m_i^2$  given by  $M_3^2$ ,  $M_2^2$ ,  $M_1^2$ ,  $A_t^2$ ,  $\mu^2$ , or  $m_{H_u}^2$ . The FT of  $m_{t_L}^2$  and  $m_{t_R}^2$  have been included as

$$\Delta(m_Z^2, m_t^2) = \left( \frac{1}{2} \left[ \left( \Delta(m_Z^2, m_{t_L}^2) \right)^2 + \left( \Delta(m_Z^2, m_{t_R}^2) \right)^2 \right] \right)^{1/2}. \quad (3.11)$$

The (top) black line shows the total FT as defined by (3.10).

From the plot it is clear that the MFT increases as a function of the messenger scale  $M_S$ . This is expected since a higher messenger scale implies more RG running to the low scale so that small differences in high-scale input parameters are magnified. For  $M_S = M_{\text{GUT}}$ , the total MFT is about 22, i.e. 4.5%. (As an aside, for  $\tan\beta = 30$  and  $m_A = 1000$ , the MFT for a Higgs mass of 114 GeV is about 11, i.e. 9%.) The largest contribution to the total minimal FT comes from  $M_3^2$  and  $A_t^2$  which are both comparable for all values of  $M_S$ . The next most important contribution is that from  $M_2^2$ . The contributions from  $\mu^2$ , as well as  $m_{t_L}^2$  and  $m_{t_R}^2$  are less important and increase only slightly as a function of  $M_S$ . The FT from  $m_{H_u}^2$  is very small for all messenger scales while the contribution from  $M_1^2$  is negligible for small and large

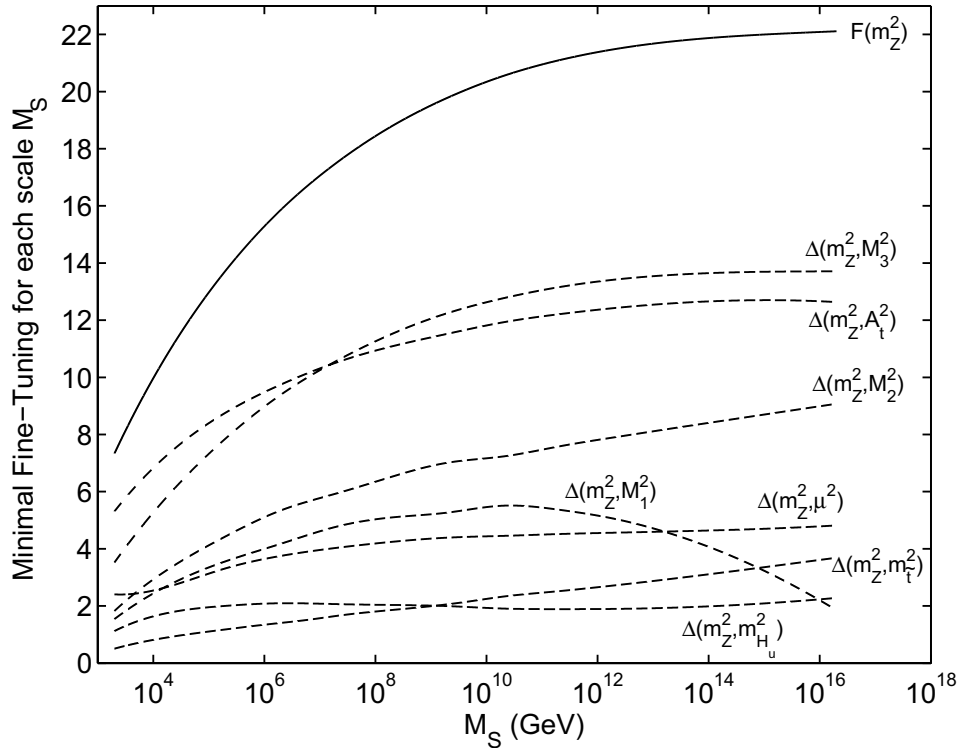


Figure 3.2: The minimal fine-tuning as a function of the messenger scale  $M_S$  for  $\tan\beta = 10$ . The top black line is the total minimal fine-tuning as defined in equation (3.10) which includes all the individual contributions. The individual contributions to the fine-tuning from  $\mu^2$ ,  $m_{H_u}^2$ , the gaugino masses  $M_1^2$ ,  $M_2^2$  and  $M_3^2$ , and the stop soft trilinear coupling  $A_t^2$  are included. Moreover, the average fine-tuning of the stop soft masses  $m_{t_L}^2$  and  $m_{t_R}^2$  is included as in equation (3.11).

$M_S$  but larger for intermediate messenger scales.

The large contribution from  $M_3^2$  is mainly because it has the largest (in magnitude) coefficient in the expression for  $m_Z^2$ , at least for  $M_S \gtrsim 10^{10}$  GeV, see Figure 3.1. The coefficients of the cross-terms  $A_t M_3$ ,  $M_2 M_3$  and  $M_1 M_3$  are smaller (see Appendix 3.8), but together still contribute about 40% of the FT with respect to  $M_3^2$  for  $M_S = M_{\text{GUT}}$ . The reason that the cross-term contributions are so large is that the MFT values of  $A_t$ ,  $M_2$ , and  $M_1$  are rather sizeable at the messenger scale when compared with  $M_3$  (at least for  $M_S \gtrsim 10^4$  GeV). This is depicted in Figure 3.3.

The FT of  $m_Z^2$  with respect to  $A_t^2$  is also very large even though the coefficients of  $A_t^2$  and the cross-terms  $A_t M_3$ ,  $A_t M_2$  and  $A_t M_1$  in the expression for  $m_Z^2$  are rather small (for  $M_S = M_{\text{GUT}}$ ,

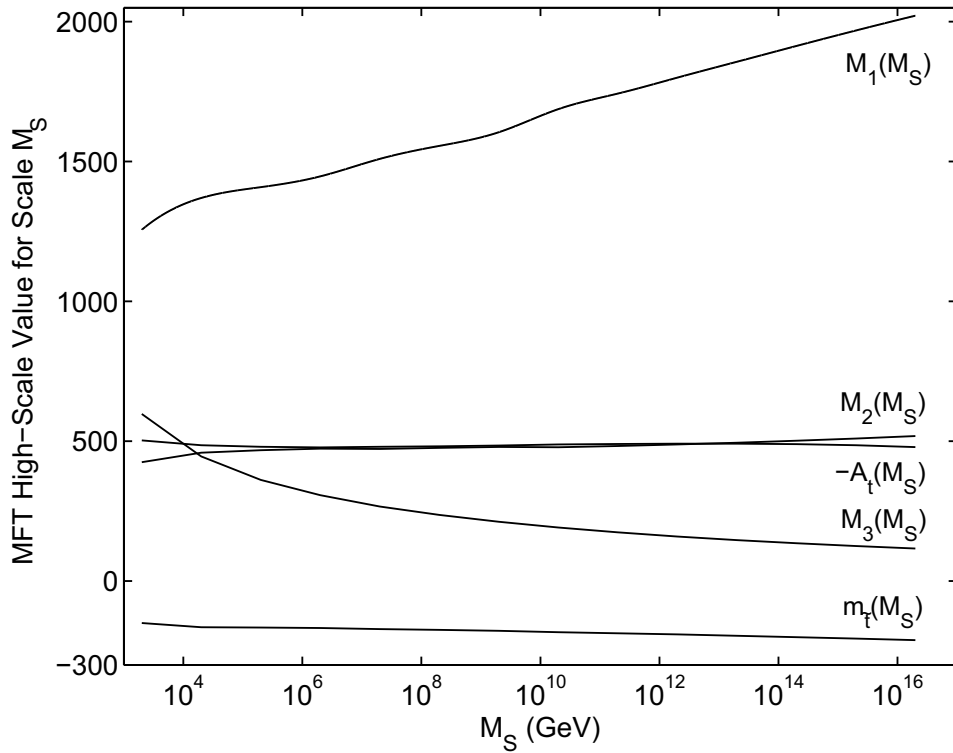


Figure 3.3: The messenger scale values of  $M_3$ ,  $M_2$ ,  $M_1$ ,  $A_t$  and the average of the stop soft masses squared,  $m_{\tilde{t}}$ , that give the minimal fine-tuning (MFT) as a function of the messenger scale  $M_S$  and for  $\tan\beta = 10$ . The high-scale values of  $M_2$  and  $A_t$ , and to a lesser extent  $M_1$  and  $m_{\tilde{t}}$ , in the minimal fine-tuned region are roughly constant. The high-scale value of  $M_3$ , however, decreases significantly as the messenger scale is increased. The reason for this is that the coefficient of  $M_3^2$  in the expression for  $m_Z^2$  increases as a function of  $M_S$ , and thus the minimal fine-tuned region requires the value of  $M_3$  to decrease as  $M_S$  increases.

about 50% of the FT comes from the cross-terms). This is again because  $A_t$ ,  $M_2$  and  $M_1$  are sizeable at  $M_S$ . The contribution to the FT from  $M_2^2$  is large for similar reasons.

The FT with respect to  $\mu^2$  increases only slightly as a function of  $M_S$  since the coefficient of  $\mu^2$  in the expression for  $m_Z^2$  does not vary much, and since the high-scale value of  $\mu^2$  increases only slightly as  $M_S$  is increased. The contribution from  $\mu^2$  is smaller than those from  $M_3^2$ ,  $M_2^2$  and  $A_t^2$  because the value of  $\mu$  is comparatively small and also because there are no cross-terms in the FT expression that involve  $\mu$  and other (large) soft parameters. Similar reasoning holds for the contributions from  $m_{H_u}^2$ ,  $m_{\tilde{t}_L}^2$  and  $m_{\tilde{t}_R}^2$ .

The low-energy spectrum that gives the MFT for a given messenger scale remains roughly unchanged as the messenger scale changes. The value of the stop soft trilinear coupling at the

$A_t$	$\sqrt{\frac{1}{2}(m_{\tilde{t}_L}^2 + m_{\tilde{t}_R}^2)}$	$m_{\tilde{t}_1}$	$m_{\tilde{t}_2}$
-610 GeV	305 GeV	110 GeV	475 GeV

Table 3.1: Low-scale values for the stop soft trilinear coupling, the average of the left- and right-handed stop soft masses and the two physical stop masses. These low scale values give the minimal fine-tuning for arbitrary messenger scales.

low scale is always about -610 GeV, with the two physical stop masses around 110 GeV and 475 GeV, respectively, see Table 3.1 and Figure 3.4. These values of the stop-sector parameters are essentially determined by the constraint on the Higgs mass and from the minimization of  $\Delta(m_Z^2, m_{H_u}^2(M_S))$ . The ratio  $X_t/m_{\tilde{t}}$  is approximately -2, where  $X_t \equiv A_t - \mu \cot \beta$ , and  $m_{\tilde{t}} \equiv \sqrt{\frac{1}{2}(m_{\tilde{t}_L}^2 + m_{\tilde{t}_R}^2)}$ . The MFT is thus found for the *natural maximal-mixing* scenario which approximately maximizes the radiative corrections to the Higgs sector for a given set of parameters and for *negative*  $A_t$  [34, 45, 46, 47]. Small deviations of  $A_t$  (and to a lesser extent  $m_{\tilde{t}_L}$  and  $m_{\tilde{t}_R}$ ) from its MFT value at the low scale lead to a very large increase in the FT, mainly from  $\Delta(m_Z^2, m_{H_u}^2(M_S))$ . This can be seen from (3.23), which shows that the largest coefficients in the expression for  $m_{H_u}^2(M)$  in terms of low-scale parameters all involve powers of  $A_t$ . Note that for generic points in the still allowed parameter space,  $\Delta(m_Z^2, m_{H_u}^2)$  would give one of the largest contribution to the FT. To minimize the FT it is thus best to minimize  $\Delta(m_Z^2, m_{H_u}^2(M_S))$  which essentially determines the values of the stop-sector parameters (see the discussion in Section 3.4.3). The other contributions to the FT are then not at their minimum, but they are much smaller and less sensitive to variations in the parameters.

The low-scale values of the gaugino masses that give the MFT for a given messenger scale are shown in Figure 3.4. While the value of  $M_2$  that gives the MFT is roughly the same for all  $M_S$ , the values of  $M_1$  and  $M_3$  decrease for larger  $M_S$ . Changing  $M_1$  away from its MFT value does affect the FT but not excessively so, while a change in  $M_3$  has a larger effect. The  $\mu$ -parameter is always found to be less than 150 GeV for the MFT region at any messenger scale. Choosing it to be closer to 100 GeV instead has a negligible impact on the FT, and allows a neutralino to be the lightest SM superpartner (LSP), instead of the lighter stop, which

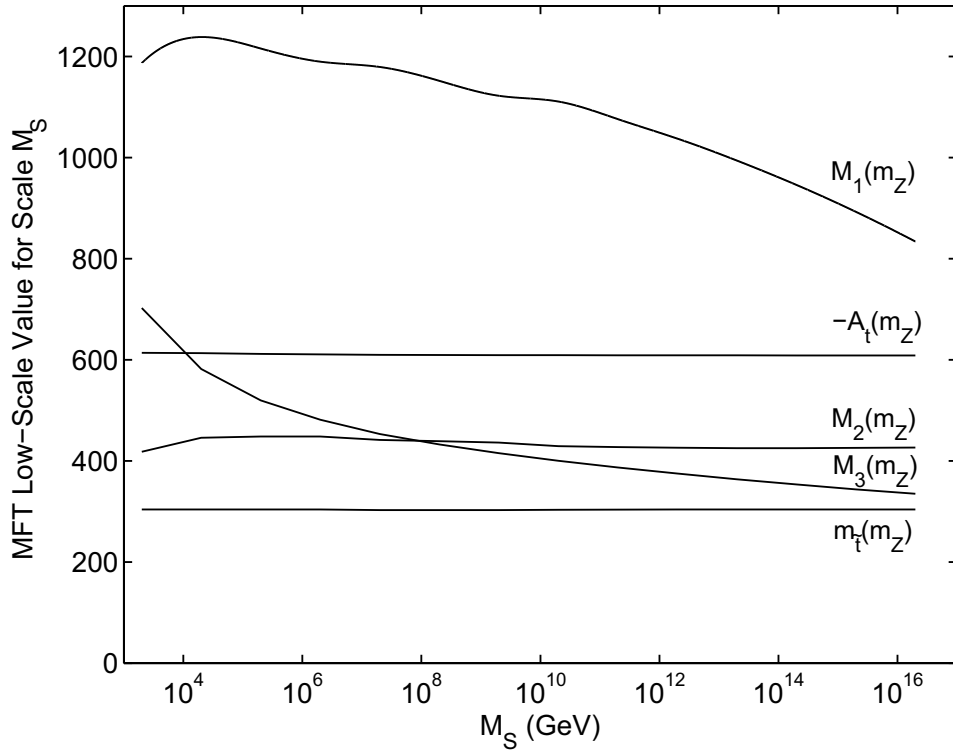


Figure 3.4: The low-scale values of the gaugino masses  $M_1$ ,  $M_2$  and  $M_3$ , the stop soft trilinear coupling  $A_t$  and the average of the stop soft masses squared  $m_{\tilde{t}}$  that give the minimal fine-tuning (MFT) for the messenger scale  $M_S$  (with  $\tan\beta = 10$ ). While the low-scale values of  $M_2$ ,  $A_t$  and  $m_{\tilde{t}}$  that give the minimal fine-tuning are roughly the same for all  $M_S$ , the values of  $M_1$  and  $M_3$  decrease for larger  $M_S$ .

is found to be the LSP in the numerical minimization procedure.

Negative  $A_t$  may be expected to lead to less FT than positive  $A_t$  because  $A_t$  has a strongly attractive infrared quasi-fixed point near [48, 49]

$$A_t \simeq -M_3. \quad (3.12)$$

(This relation is strictly valid only at the Pendleton-Ross quasi-fixed point for the top Yukawa [50], and neglecting  $SU(2)_L$  and  $U(1)_Y$  gauge interactions.) Because of this it is most natural for  $A_t$  and  $M_3$  to have opposite sign and be comparable in magnitude at low scales due to renormalization group evolution, see Figure 3.5. For positive  $A_t$  and maximal-mixing in the stop-sector,  $A_t$  would have to be an order of magnitude larger than  $M_3$  at the messenger scale (see Figure 3.5) which would lead to a much more FT parameter region. The MFT region here

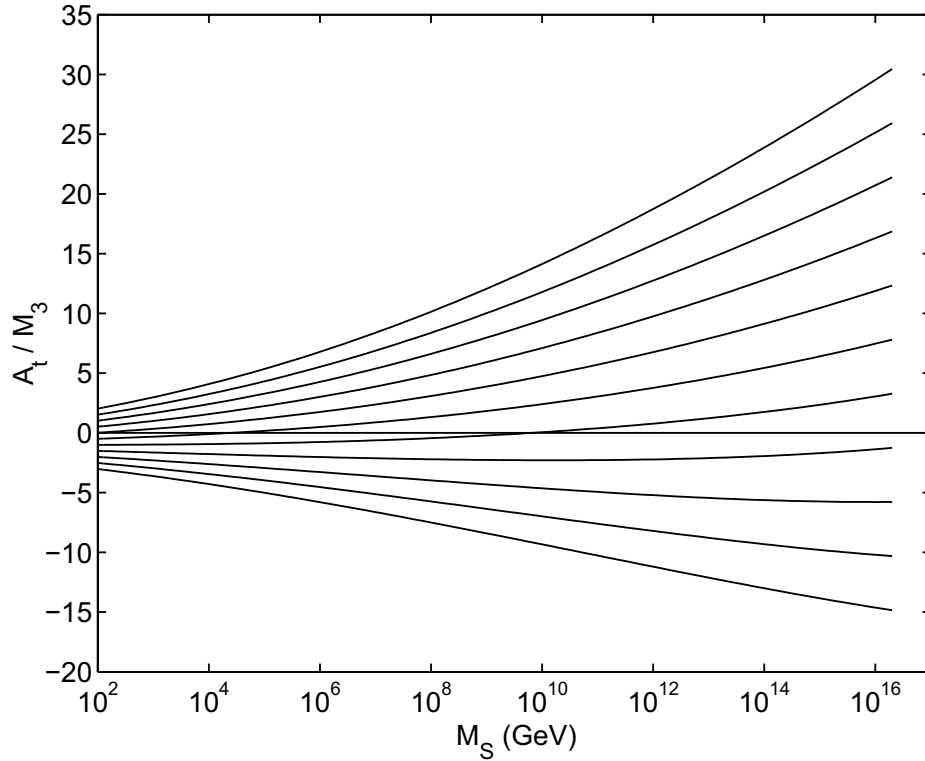


Figure 3.5: The RG-evolution of  $A_t/M_3$  for various boundary conditions at the low-scale for  $A_t(m_Z)/M_3(m_Z) = \{-2.0, -1.5, \dots, 1.5, 2.0\}$  and  $\tan\beta = 10$ . The strongly attractive infrared quasi-fixed point near  $A_t/M_3 \simeq -1$  is clearly visible. The gaugino masses have been set to their minimal fine-tuned values for the case  $M_S = M_{\text{GUT}}$ , i.e.  $M_3(m_Z) \simeq 335$  GeV,  $M_2(m_Z) \simeq 430$  GeV, and  $M_1(m_Z) \simeq 830$  GeV.

does not satisfy (3.12) exactly, but instead  $A_t/M_3 \simeq -1.8$  at the low scale, for  $M_S = M_{\text{GUT}}$ .

In order to satisfy (3.12) exactly,  $M_3$  would have to be larger (assuming  $A_t$  remains fixed).

This would increase the size of the stop masses under RG evolution as can be seen from their  $\beta$ -functions, see (3.50) and (3.51), which would lead to increased FT.

The MTMSSM has negative soft squark squared masses at the messenger scale (see also [19]). This remains the case even if the messenger scale is very low and only on the order of a few TeV (for very low messenger scales, finite threshold corrections should really be included). Under RG-evolution the masses get driven positive very quickly within about a decade of running. It is the sizeable values of the gaugino masses that pull them up towards positive values. For smaller messenger scales the MFT region has a larger gluino mass, which drives the squark

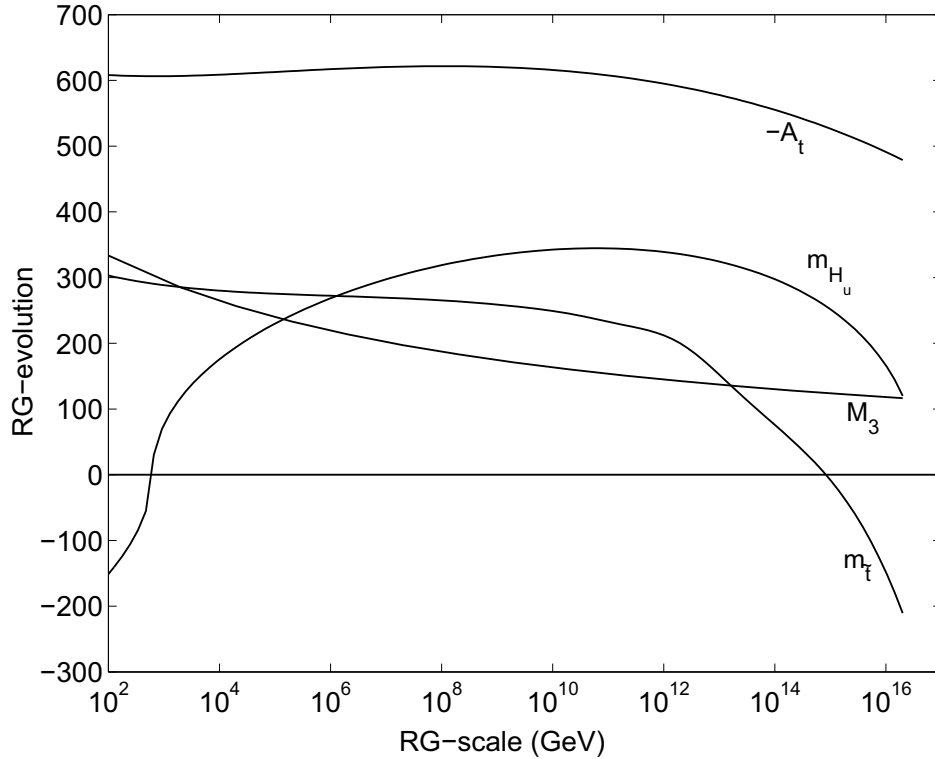


Figure 3.6: The RG-trajectories of the minimal fine-tuned region if the messenger scale is  $M_S=M_{\text{GUT}}$  ( $\tan\beta$  has been set to 10). At the scale  $m_Z$ , the parameter values are  $m_{\tilde{t}} \simeq 305$  GeV,  $m_{\tilde{t}_1} \simeq 110$  GeV,  $m_{\tilde{t}_2} \simeq 475$  GeV,  $M_3(m_Z) \simeq 335$  GeV, and  $\mu(m_Z) = 140$  GeV. The minimal fine-tuned value is obtained for *natural maximal-mixing*, i.e.  $A_t \simeq -2m_{\tilde{t}}$ .

masses to positive values even faster while running towards the infrared. Equations (3.22) and (3.24) or (3.25) in Appendix 3.7 show that negative squarks at the messenger scale lead to more stop-mixing at the low scale, as was pointed out in [19]. Figure 3.6 shows the RG-trajectories of the MFT region if the messenger scale is  $M_S=M_{\text{GUT}}$ .

The presence of tachyonic squarks at the messenger scale [51, 52] and/or very large  $A_t$  [53, 54] may lead to dangerous color and/or charge breaking (CCB) minima.

Very large  $A_t$  may result in dangerous CCB minima around the EW scale. These CCB minima occur in the  $(\tilde{t}_L, \tilde{t}_R, H_u)$  plane [55]. The condition that the EW minimum is the global minimum may be estimated by going along the D-flat direction  $|\tilde{t}_L| = |\tilde{t}_R| = |H_u|$  and is given by [56]

$$A_t^2 + 3\mu^2 \lesssim 3(m_{\tilde{t}_L}^2 + m_{\tilde{t}_R}^2). \quad (3.13)$$

Assuming instead that the EW minimum is only metastable but has a large enough lifetime gives the weaker constraint [56]

$$A_t^2 + 3\mu^2 \lesssim 7.5(m_{\tilde{t}_L}^2 + m_{\tilde{t}_R}^2). \quad (3.14)$$

The MTMSSM easily satisfies the second condition, as well as satisfying the first condition. There are thus no dangerous CCB minima resulting from large  $A_t$ .

Tachyonic stops at the messenger scale may result in an unbounded from below potential along D-flat directions involving the stop fields, as well as first and/or second generation squark fields or slepton fields. Loop corrections give rise to an effective potential which is not unbounded from below, but they generically introduce a CCB minimum with a vacuum expectation value (VEV) on the order of the messenger scale. The MTMSSM may thus have CCB minima with a VEV around the EW scale if the messenger scale is low, or CCB minima with a VEV large compared to the EW scale if the messenger scale is high. Since the EW minimum is metastable and long-lived for  $m_{\tilde{t}} \gtrsim \frac{1}{6}M_3$  [57], it turns out that these CCB minima are not dangerous in the MTMSSM. Moreover, the MTMSSM does not determine the masses of the sleptons or first and second generation squarks since these do not play an important role in the FT. It is thus always possible to choose them in such a way to avoid CCB minima without changing the above FT results.

Finally, it is interesting to note that there are several near degenerate parameter subspaces along which the FT does not change much. The first and second generation particles and their superpartners do not contribute much to the FT because in equation (3.5) they appear only with a small coefficient. The parameter  $S_Y$  is also not very important for the same reason. A more interesting near degenerate subspace is that the FT is rather insensitive to changes in the *difference* of the two stop soft mass squared parameters at the low scale as long as their sum is kept fixed. This may be understood from the expression for  $m_Z^2$ , e.g. equation (3.7), in which only their sum appears (using the one-loop RG equations). However, even with only one-loop RG equations this degeneracy is not exact since small discrepancies appear in the FT measure from equations (3.24) and (3.25). Moreover, the difference in the two stop soft mass

squared parameters appears in the calculation of the physical stop masses and this affects the size of the Higgs mass, which is the most crucial low-energy constraint when calculating the FT. The FT only starts to change by an order one number when  $\sqrt{|m_{\tilde{t}_L}^2 - m_{\tilde{t}_R}^2|} \sim 300$  GeV for  $M_S = M_{\text{GUT}}$ .

### 3.4.3 Analytic Motivation for Numerical Results

The numerical results presented in section 3.4.2 may be motivated analytically. The discussion will for now assume  $M_S = M_{\text{GUT}}$ , but generalizes to arbitrary  $M_S$  with a few caveats discussed below.

In order to get a physical Higgs mass satisfying the experimental bound without generating large FT for the EWSB, it is natural to maximize the radiative corrections to  $m_h$ . Due to the strongly attractive quasi-fixed point for  $A_t$ , this is achieved for negative  $A_t$  near (natural) maximal mixing (at least for  $m_h$  not too large, see Section 3.5).

The most important contribution to the FT comes from  $\Delta(m_Z^2, m_{H_u}^2(M_S))$  since it has the largest coefficients, see Appendix 3.8. Eliminating  $\hat{m}_{H_u}^2$  with the EWSB equation (3.7) and using the average stop soft mass squared  $\hat{m}_t^2 = (\hat{m}_{\tilde{t}_L}^2 + \hat{m}_{\tilde{t}_R}^2)/2$  gives

$$\begin{aligned} m_Z^2 \Delta(m_Z^2, \hat{m}_{H_u}^2) = & \quad | -m_Z^2 - 2.19 \hat{\mu}^2 + 1.36 \hat{m}_t^2 + 5.24 \hat{M}_3^2 \\ & - 0.44 \hat{M}_2^2 + 0.46 \hat{M}_3 \hat{M}_2 - 0.77 \hat{A}_t \hat{M}_3 - 0.17 \hat{A}_t \hat{M}_2 \\ & - 0.01 \hat{M}_1^2 + 0.22 \hat{A}_t^2 |. \end{aligned} \quad (3.15)$$

It is possible to have cancelations among the various terms in this expression.  $\Delta(m_Z^2, M_3^2(M_S))$  also has large coefficients, but cancelations among its terms are impossible since  $\hat{A}_t$  is negative (see Appendix 3.8).

Ignoring  $\hat{\mu}^2$ , cancelation of the largest terms in equation (3.15), i.e. the gluino term and the average stop soft mass squared term, decreases the FT by setting  $\hat{m}_{H_u}^2 \simeq m_{H_u}^2$  and leads to tachyonic squarks at the messenger scale [19]

$$\hat{m}_t^2 \simeq -3.9 \hat{M}_3^2. \quad (3.16)$$

Next, the four terms on the second line of equation (3.15) can cancel by taking

$$\hat{M}_3 \simeq \frac{0.96\hat{M}_2 + 0.37\hat{A}_t}{1 - 1.67\frac{\hat{A}_t}{\hat{M}_2}}. \quad (3.17)$$

Assuming  $\hat{M}_2 \simeq -\hat{A}_t$ , this simplifies to  $\hat{M}_2 \simeq 4.5\hat{M}_3$ . Furthermore, keeping only the most important terms, the natural maximal-mixing scenario implies

$$\begin{aligned} -2 \simeq \frac{A_t}{m_{\tilde{t}}} &\simeq (0.32\hat{A}_t - 2.13\hat{M}_3 - 0.27\hat{M}_2 - 0.03\hat{M}_1) \left[ 0.66\hat{m}_{\tilde{t}}^2 + 5.15\hat{M}_3^2 \right. \\ &\quad \left. + 0.11\hat{M}_2^2 + 0.02\hat{M}_1^2 + 0.19\hat{A}_t\hat{M}_3 + 0.04\hat{A}_t\hat{M}_2 - 0.05\hat{A}_t^2 \right]^{-1/2} \\ &= (-4.80\hat{M}_3 - 0.03\hat{M}_1) \left[ 2.16\hat{M}_3^2 + 0.02\hat{M}_1^2 \right]^{-1/2} \end{aligned} \quad (3.18)$$

which leads to  $\hat{M}_1 \simeq 15\hat{M}_3$ , again assuming  $\hat{M}_2 \simeq -\hat{A}_t$ . It is now possible to compute the ratio of the soft trilinear coupling with the gluino mass at the EWSB scale,

$$\frac{A_t}{M_3} \simeq \frac{0.32\hat{A}_t - 2.13\hat{M}_3 - 0.27\hat{M}_2 - 0.03\hat{M}_1}{2.88\hat{M}_3} \simeq -1.8. \quad (3.19)$$

These results agree well with the numerical results presented in section 3.4.2.

Note that a GUT scale model which predicts degenerate and negative squark and slepton soft masses at the GUT scale would need very large wino and bino masses in comparison to the gluino mass in order to drive the slepton soft masses to positive values under RG running to the EWSB scale [58]. This is due to the small coefficients of the bino and wino masses in the  $\beta$ -functions of the slepton soft masses. It is interesting that the MFT region prefers the bino mass larger than the wino mass and, in turn, the wino mass larger than the gluino mass.

Although this cancelation pattern holds to a good approximation for higher messenger scales,  $\hat{m}_{\tilde{t}}^2$  does not exactly cancel  $\hat{M}_3^2$  as the messenger scale decreases. For lower messenger scales,  $\hat{m}_{\tilde{t}}^2$  becomes less tachyonic while  $\hat{M}_3^2$  increases, allowing the stop masses to be driven positive faster under RG running to the EWSB scale. Moreover, the coefficient of  $\hat{M}_3^2$  in the expression for  $m_Z^2$  (3.5) decreases significantly, as can be seen in Figure 3.1. Therefore the cancelation pattern in  $\Delta(m_Z^2, \hat{m}_{H_u}^2)$  discussed above does not hold since the  $\hat{m}_{\tilde{t}}^2$  contribution decreases while the  $\hat{M}_3^2$  term gives a comparable contribution for all messenger scales (except for very small messenger scales). On the other hand, being a supersymmetric parameter,  $\hat{\mu}$  and its

coefficient in equation (3.5) does not change much for different messenger scales. Compared to  $\hat{M}_3^2$  and  $\hat{m}_t^2$ , its contribution becomes important at lower messenger scales and a lower FT can be obtained by canceling the three contributions together. The other relations in the above cancelation pattern holds to a good approximation for lower messenger scales, although for  $M_S \lesssim 10^5$  the cancelation pattern becomes more involved.

### 3.4.4 Summary of Phenomenological Implications

The above analysis shows that the MTMSSM has small values for  $\mu$ , the stop masses and the gluino mass. The gluino in the MTMSSM is around 335 GeV for  $M_S = M_{\text{GUT}}$ , but heavier for lower  $M_S$ . There is large mixing in the stop-sector which introduces a significant splitting between the two physical stop masses. They have masses of around 115 GeV and 475 GeV respectively, see Table 3.1. Thus the MTMSSM may have a stop as the LSP. However, as mentioned before,  $\mu$  can be chosen to be small enough so that a neutralino is the LSP without affecting FT by much.

At the Large Hadron Collider, gluino pair-production in the MTMSSM is thus rather large and comparable to top quark pair-production. The production of  $\tilde{t}_1\tilde{t}_1$  is also of the same order.

The gluinos are Majorana particles, and can decay into the lightest stop via  $\tilde{g}\tilde{g} \rightarrow t\tilde{t}_1\tilde{t}_1$  producing same-sign top quarks 50% of the time. The top quarks each decay into  $Wb$ , and the events with two same-sign top quarks will contain two same-sign leptons if the  $W$  decays leptonically. If a neutralino and a chargino are lighter than the stop, the decay  $\tilde{t}_1 \rightarrow \chi_1^+ b$  is possible, with  $\chi_1^+$  further decaying into a neutralino and soft jets or leptons. The events thus also contain missing energy and a number of  $b$ -jets, some of which are soft if the  $\tilde{t}_1 - \chi_1^+$  mass splitting is small.

If  $\tilde{t}_1$  is the LSP a number of further interesting signatures are possible, see [59]. The lighter stop can either be pair-produced directly or from gluino decays. Even though it is the lightest SM superpartner, it may decay into a lighter goldstino  $\tilde{G}$  via the flavor-violating decay  $\tilde{t}_1 \rightarrow c\tilde{G}$  or via the three-body decay  $\tilde{t}_1 \rightarrow bW\tilde{G}$ . The decay rate depends on the messenger scale, with

lower messenger scales leading to larger decay rates. For reasonable messenger scales, its decay length easily exceeds the hadronization length scale, and the stop in general hadronizes before it decays [59]. For messenger scales less than a few hundred TeV, the decay length is small enough so that the decay products seem to originate from the interaction region. The three-body decay leads to a similar signature as the top decay but can be distinguished from it, see [60]. For larger messenger scales,  $\tilde{t}_1$  decays inside a hadronized mesino or sbaryon and a variety of interesting signatures are possible [59], including mesino-anti-mesino oscillations [61].

Another interesting possibility is the direct pair-production of the heavier stop  $\tilde{t}_2$ . Since the two physical stop masses are split by a large amount, the decay mode  $\tilde{t}_2 \rightarrow \tilde{t}_1 + Z$  is kinematically allowed and has a sizeable branching ratio [62]. The resulting signature depends on the  $\tilde{t}_1$  decay channel as discussed above. For  $\chi_1^+$  and  $\chi_0^1$  lighter than  $\tilde{t}_1$ , the authors of [62] propose to look for the inclusive signature  $Z(l^+, l^-)bb\cancel{E}_T X$ , where the two leptons  $l^+$  and  $l^-$  have an invariant mass equal to the  $Z$ -mass. Detecting this signature would give evidence for the maximal-mixing scenario but requires a large integrated luminosity (at least  $\mathcal{O}(100 \text{ fb}^{-1})$ ) [62]. Since the mass difference between  $\tilde{t}_1$  and the LSP is small in the MTMSSM this signature will be very hard to see since the jet from the decay  $\tilde{t}_1 \rightarrow \chi_1^+ b$  is soft which makes it more difficult to separate the signal from the SM background [62].

An alternative way to measure the parameters in the stop-sector is to use the Higgs boson as a probe [63]. A measurement of the Higgs mass and its production rate in the gluon fusion channel allows the average of the two stop soft masses as well as the stop mixing to be determined in many regions of the still allowed MSSM parameter space, and especially in regions where the FT is small [63].

### 3.4.5 Fine-Tuning with Respect to Other Parameters

This subsection briefly discusses other parameters that may in principle contribute to the FT.

If the goal is to find the MFT region of a model and make a prediction of what parameter region is preferred for the model from a FT point of view, there is no reason to include the FT

of experimentally known parameters such as  $g_Y$ ,  $g_2$ ,  $g_3$ , or  $\lambda_t$ . Taking into account the known parameters in the minimization procedure would most likely lead to other MFT values for all parameters, including MFT values for the known parameters which would in all likelihood not match the experimental values.

If the goal, however, is to find the FT of a given model, one should in principle include contributions from experimentally known parameters. For example, FT with respect to  $\lambda_t$ ,  $\Delta(m_Z^2, \lambda_t(M_S))$ , may give a large contribution to the total FT due to the large top mass. Indeed, with the MFT values for  $M_S = M_{\text{GUT}}$ ,  $\Delta(m_Z^2, \lambda_t(M_{\text{GUT}})) \simeq 8$ . This, however, increases the total FT only by a small amount from 22.1 to 23.5.

What about FT with respect to  $m_{12}^2$  and  $\tan\beta$ ? These parameters are unknown and in principle they should be included in the minimization procedure. With the help of equation (3.3) and symmetries, it is however easy to see that  $\Delta(m_Z^2, m_{12}^2(M_S)) = 0$ . Indeed  $m_{12}^2$  does not appear directly in the expression for  $m_Z^2$ . Furthermore it breaks a  $U(1)_{\text{PQ}}$ - and a  $U(1)_R$ -symmetry and consequently does not feed back into any other  $\beta$ -functions since no other parameter breaks both symmetries. Thus  $m_{12}^2$  cannot appear in equation (3.3) and is therefore completely free, which allows  $m_A$  to be chosen accordingly as discussed in Section 3.2.

The FT of  $\tan\beta$  has not been taken into account in the minimization procedure since an explicit expression for  $m_Z^2$  can only be obtained assuming a specific value for  $\tan\beta$ , because  $\lambda_t$  depends on  $\tan\beta$  through  $m_t$ . Moreover, since  $\tan\beta$  is then a free parameter the approximation leading to equation (3.4) may not be valid anymore and  $m_{H_d}^2$  should be reintroduced. Contributions from bottom/sbottom and tau/stau sectors should also be included if  $\tan\beta$  becomes large.

### 3.5 Minimal Fine-Tuning as a Function of the Higgs Mass

The Higgs mass  $m_h$  is the most important low-energy constraint that determines the amount of minimal fine-tuning (MFT). It is therefore interesting to look at how the MFT is affected when the lower bound on  $m_h$  is changed. Figure 3.7 shows a plot of the MFT as a function of the

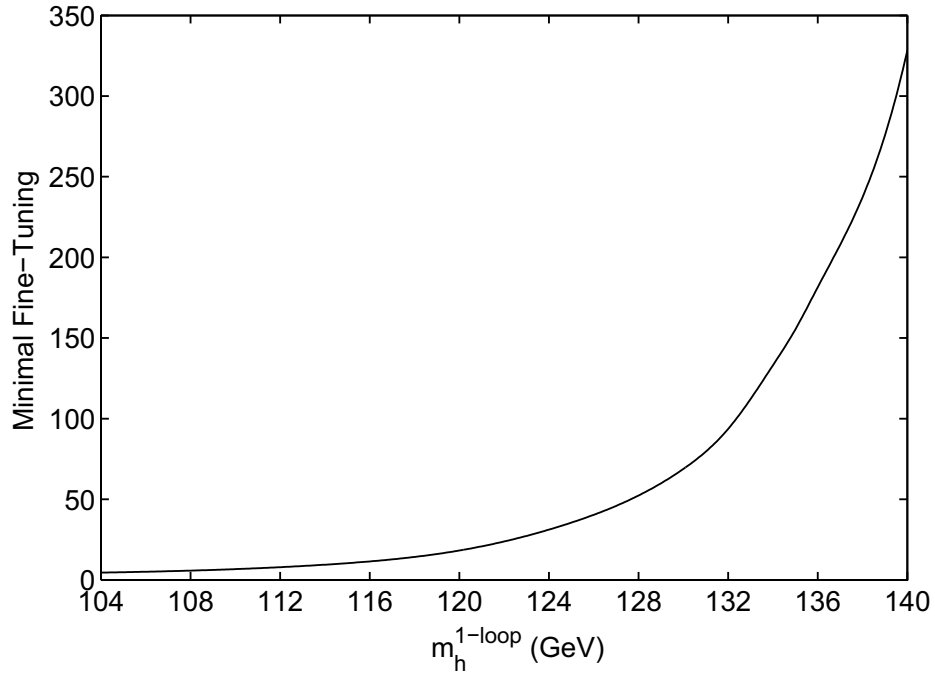


Figure 3.7: The minimal fine-tuning as a function of the lower bound on the Higgs mass  $m_h$ , where the calculation of  $m_h$  only includes the one-loop corrections from the top-stop sector ( $\tan\beta = 10$ ,  $m_A = 250$  GeV,  $m_t = 170.9$  GeV).

lower bound on  $m_h$ , where the calculation of  $m_h$  is the same one used in the FT minimization described in Section 3.4.1, and only includes the one-loop corrections from the top-stop sector (with  $m_A = 250$  GeV,  $\tan\beta = 10$ ,  $m_t = 170.9$  GeV, and  $M_S = M_{\text{GUT}}$ ). The Higgs mass calculated with the one-loop corrections will be denoted by  $m_h^{1\ell}$ . The region of MFT always saturates the bound on  $m_h^{1\ell}$  and has negative  $A_t$ . The minimal FT is about 1% for  $m_h^{1\ell} \simeq 132$  GeV.

There are, however, other important one-loop and two-loop corrections that can significantly affect  $m_h$ , and these need to be included in order to get a more accurate idea of how the MFT changes as a function of the lower bound on  $m_h$ . With these additional corrections,  $m_h$  is not anymore a symmetric function of the stop-mixing parameter  $X_t = A_t - \mu \cot\beta \simeq A_t$ , where the latter approximation is good for sizeable  $\tan\beta$ . It can be up to 5 GeV larger for  $X_t = +2m_{\tilde{t}}$  than for  $X_t = -2m_{\tilde{t}}$ , the difference arising from non-logarithmic two-loop contributions to  $m_h$ , see [64, 65, 66]. Moreover, large chargino masses, i.e. large values of  $M_2$  and  $\mu$ , can give

important negative contributions to  $m_h$  [67]. These corrections are also not included in  $m_h^{1\ell}$ . Two-loop corrections that allow the gluino mass to affect  $m_h$  can also be important but are smaller in general - this will be ignored in the following discussion since the impact on the results presented below is negligible.

The MFT spectrum that was found with the minimization procedure may be used to calculate  $m_h$  with `FeynHiggs`. The `FeynHiggs` estimate for  $m_h$  will be denoted by  $m_h^{\text{FH}}$ . The result is the solid black line in Figure 3.8. This MFT spectrum characteristically has large chargino masses and a negative value for  $A_t$  near the “natural” maximal mixing scenario.

Comparing the solid black line in Figure 3.8 with the curve in Figure 3.7 shows the well-known fact that the higher-order corrections to  $m_h$  are extremely important. There are two additional very striking features. First of all, as  $m_h^{\text{FH}}$  increases and approaches 120 GeV, the FT increases enormously. Any further small increase in the Higgs mass results in an enormous increase in the FT. The reason is that as  $m_h^{\text{FH}}$  approaches 120 GeV here, it only grows logarithmically as a function of the stop masses. The stop masses therefore become exponentially large and thus increase the FT at least exponentially (see also [34]).

The second striking feature of this curve is that the value of the Higgs mass at which the FT starts to increase enormously is rather low (the MFT is already 1% for  $m_h^{\text{FH}} \simeq 119$  GeV). This value of  $m_h$  may be increased by just under 2 GeV by choosing larger  $\tan\beta$  and  $m_A$  (recall that throughout this discussion  $\tan\beta = 10$  and  $m_A = 250$  GeV). Note that the latest Tevatron top mass value ( $m_t = 170.9$  GeV) has been used in the calculation, and a slightly different value can also change  $m_h$  by a few GeV.

An obvious question is whether the MFT region is significantly different if  $m_h^{\text{FH}}$  were used in the minimization procedure instead of  $m_h^{1\ell}$  (the former is too complicated to be used). For MSSM spectra that give small  $m_h$  this is certainly not the case, since there is not a very large discrepancy between the two Higgs mass estimates  $m_h^{1\ell}$  and  $m_h^{\text{FH}}$ . The difference between the two Higgs mass estimates becomes significant, however, for MSSM spectra that give a large  $m_h$ , and the approximation  $m_h^{\text{FH}}$  can be substantially smaller than  $m_h^{1\ell}$ . Also, as mentioned

above,  $m_h^{\text{FH}}$  can be substantially larger for positive  $A_t$  (near maximal mixing) than for negative  $A_t$  (near “natural” maximal mixing), and increases as the chargino masses decrease. On the other hand,  $m_h^{1\ell}$  remains unaffected by the sign of  $A_t$  and the size of the chargino masses. It is thus possible that the MFT region does not coincide with the region obtained in the above minimization procedure as the lower bound on  $m_h$  increases. This is indeed the case, as will now be discussed.

The FT may be minimized with the constraint that the chargino masses are small. Since the effect of varying  $\mu$  and  $M_2$  on the FT are noticeable but not substantial, the resulting spectrum will be characterized by gluino and stop masses that are only slightly larger than those obtained in the MFT region discussed in this paper. The value of  $A_t$  is still negative. This spectrum may be used to calculate  $m_h^{\text{FH}}$ . The result is shown by the dash-dot green curve in Figure 3.8. For  $m_h^{\text{FH}}$  not too large, the solid black curve lies below the dash-dot green curve because the MFT region has large values of  $M_2$ , see Section 3.4. As  $m_h^{\text{FH}}$  increases further, however, the FT becomes very large since the stop masses become exponentially large. Smaller chargino masses lead to larger values of  $m_h^{\text{FH}}$ , and the two curves show that for  $m_h$  just below 120 GeV, a smaller FT may be obtained by decreasing the size of  $M_2$ . This behavior cannot be captured by  $m_h^{1\ell}$  which is unaffected by a change in the chargino masses. Note that the transition between the two regions described by the two curves is smooth, and that it occurs when the MFT is already more than 1%.

Next, the FT may be minimized with the constraint that  $A_t$  is positive and near maximal mixing. The resulting low-energy spectrum is characterized by small chargino and gluino masses. This spectrum may then be used to calculate  $m_h^{\text{FH}}$ , and the MFT as a function of this value of  $m_h^{\text{FH}}$  is displayed by the dashed blue line in Figure 3.8. Comparing the solid black line or dash-dot green line with the dashed blue line, it is clear that for small  $m_h^{\text{FH}}$  the MFT region has negative values of  $A_t$ . Even though negative  $A_t$  might be expected to always give less FT than positive  $A_t$  due to the IR quasi-fixed point, the increase in  $m_h^{\text{FH}}$  by several GeV by making  $A_t$  positive is substantial, and as  $m_h^{\text{FH}}$  approaches about 123 GeV, the two curves cross. Thus,

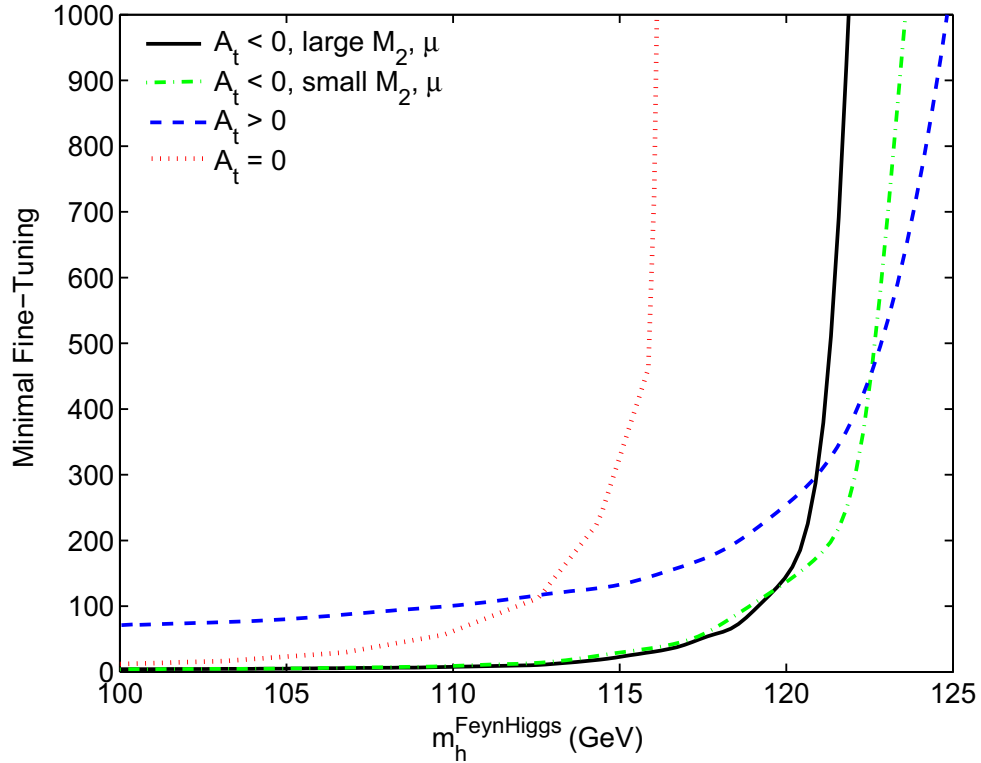


Figure 3.8: The minimal fine-tuning as a function of the lower bound on the Higgs mass  $m_h$  calculated with `FeynHiggs` 2.6.0 ( $\tan\beta = 10$ ,  $m_A = 250$  GeV,  $m_t = 170.9$  GeV). Throughout this paper the fine-tuning is minimized subject to a constraint on  $m_h$ , where  $m_h$  is estimated with a one-loop formula as described in Section 3.4.1. The different lines arise from different assumptions made about  $A_t$ , or  $\mu$  and  $M_2$ , when minimizing the fine-tuning. These different assumptions give rise to different low-energy spectra that present the least fine-tuned parameter choices satisfying these assumptions. These low-energy spectra may then be used in `FeynHiggs` to calculate  $m_h$ . Although  $M_2$ ,  $\mu$  and the sign of  $A_t$  do not affect the one-loop estimate of  $m_h$  which only contains the dominant corrections, they do affect the `FeynHiggs` estimate of  $m_h$ . For the solid black line no constraint was set on  $A_t$ , and  $\mu$  and  $M_2$  were only required to be above 100 GeV. It is the same line as in Figure 3.7, but with  $m_h$  estimated by `FeynHiggs` instead of the one-loop formula. The dashed blue line assumes  $A_t$  is positive and near maximal mixing, also with  $M_2$  and  $\mu$  only required to be above 100 GeV. The dash-dot green curve makes no assumption about  $A_t$  but sets  $\mu = 100$  GeV and  $M_2 = 100$  GeV. The dotted red line assumes  $A_t = 0$ , and again only requires  $\mu$  and  $M_2$  to be larger than 100 GeV. Further details and explanations are given in the text.

there is a transition from  $A_t \simeq -2m_{\tilde{t}}$  to  $A_t \simeq +2m_{\tilde{t}}$  of the minimal fine-tuned region as  $m_h^{\text{FH}}$  increases. This behavior is again not captured by  $m_h^{1\ell}$  which is independent of the sign of  $A_t$ . The transition occurs when the minimal FT is already quite large (about 0.2%).

This transition from negative to positive  $A_t$  is not smooth, in the sense that the first derivative of the curve at the transition point is not continuous<sup>5</sup>. To show this, the FT may be minimized with the constraint  $A_t = 0$ . The resulting low-energy spectrum may then again be used to calculate  $m_h^{\text{FH}}$ , and the result is shown by the dotted red line in Figure 3.8. The value of  $m_h^{\text{FH}}$  for vanishing stop-mixing,  $A_t = 0$ , is much lower than for the two maximal mixing scenarios,  $A_t \simeq \pm 2m_{\tilde{t}}$ , and it is clear that the MFT region does not interpolate smoothly between them as a function of  $A_t$ .

The main point of the analysis in this section is that although the MSSM is already fine-tuned at least at about the 5% level (if the messenger scale equals the GUT scale), there is not much room left for the Higgs mass to increase before the FT becomes much worse.

Note that for a lower messenger scale the Higgs mass can have a slightly larger value before the MFT begins to increase enormously. For example, for  $M_S = 200$  TeV, the MFT is 1% for  $m_h \simeq 123$  GeV. So even for a lower messenger scale the Higgs mass cannot be that much beyond 120 GeV before the MFT increases dramatically.

### 3.6 Conclusions

In this paper the minimally tuned Minimal Supersymmetric Standard Model, or MTMSSM, was presented. The MSSM parameter region that has the minimal model-independent fine-tuning (FT) of EWSB was found. Model - independent means that no relations were assumed between the soft SUSY breaking parameters at the scale at which they are generated (the messenger scale). Instead, all of the important parameters were allowed to be independent and free at the messenger scale, and were taken to contribute to the total FT of the EWSB scale. The messenger scale itself was varied between 2 TeV and  $M_{\text{GUT}}$  and the effect of this on the minimal

---

<sup>5</sup>One may perhaps refer to this as the *first order phase transition of fine-tuning*.

FT was presented.

The most important parameters that contribute to the tuning are  $|\mu|^2$ ,  $m_{H_u}^2$ , the gaugino masses  $M_1$ ,  $M_2$  and  $M_3$ , the stop soft masses  $m_{\tilde{t}_L}^2$  and  $m_{\tilde{t}_R}^2$ , and the stop soft trilinear coupling  $A_t$ . The MSSM spectra which lead to the minimal model-independent FT were found by numerically minimizing the FT expression subject to constraints on the Higgs, stop, and gaugino masses (the Higgs mass was found to always be the most important low-energy constraint). The high-energy spectra are characterized by tachyonic stop soft masses, even for messenger scales as low as 2 TeV (but note that threshold effects in the RG-running were neglected throughout). The potential existence of charge and/or color breaking minima turns out not to be a problem. The gluino mass,  $M_3$ , is much smaller than the wino mass,  $M_2$ , and  $M_2$  in turn is much smaller than the bino mass  $M_1$ . The low-scale spectra are characterized by negative  $A_t$  near the maximal mixing scenario that maximizes the Higgs mass. The large stop mixing leads to a large splitting between the two stop mass eigenstates. Interesting phenomenological signatures include the possibility of a stop LSP.

The minimal FT was also found as a function of the lower bound on the Higgs mass (with the messenger scale set to  $M_{\text{GUT}}$ ). Although in the numerical minimization procedure the dominant one-loop expression for  $m_h$  was used as a constraint, the resulting least fine-tuned spectra were used to calculate  $m_h$  more accurately with `FeynHiggs`. A plot of the minimal FT as a function of  $m_h$  was presented. There are several striking features of this plot. For  $m_h$  larger than about 120 GeV the FT increases very rapidly. This value of  $m_h$  is rather low, perhaps surprisingly so. It is only slightly dependent on the parameters in the Higgs sector. Near it, the value of  $A_t$  in the least FT region also makes a sudden transition from lying near  $-2m_{\tilde{t}}$  to lying near  $+2m_{\tilde{t}}$ , where  $m_{\tilde{t}}$  is the average of the two stop soft masses. The upshot of this particular analysis is that although the MSSM is already fine-tuned at least at about the 5% level (if the messenger scale equals the GUT scale), there is not much room left for the Higgs mass to increase before the FT becomes much worse. The magnitude and rate of increase of the minimal FT as  $m_h$  increases beyond about 120 GeV is very striking.

### 3.7 Appendix: Semi-numerical Solutions of the MSSM One-Loop RG-Equations

This appendix reviews the procedure for solving the MSSM one-loop RG equations semi-numerically [35, 36]. The low scale  $M_0$  is set to be  $m_Z$ , and the high (messenger) scale  $M_S$  is taken to lie anywhere between  $m_Z$  and  $M_{\text{GUT}}$ . Threshold corrections are neglected when solving the RG-equations.

The main goal is to obtain an expression for  $m_Z^2$  in terms of high-scale input parameters as in equation (3.5). Assuming that  $\tan\beta$  is not too small, this requires solving  $|\mu(m_Z)|^2$  and  $m_{H_u}^2(m_Z)$  in terms of high-scale parameters (for moderate values of  $\tan\beta$ ,  $m_{H_d}^2$  may be neglected, see equation (3.4)). The fine-tuning may then be calculated and naturally expressed in terms of high-scale parameters as in equation (3.10). However, in order to minimize the fine-tuning taking into account low-scale constraints on the Higgs, stop, and gaugino masses, it is more appropriate to rewrite the fine-tuning expression in terms of low scale parameters. This requires that  $\mu$  as well as all the soft supersymmetry breaking parameters appearing in equation (3.10) be written in terms of low scale parameters.

In solving the RG-equations, only the contributions from the third generation particles will be included, since the third generation Yukawa couplings are much larger than those from the first and second generations. Moreover, the contributions from the bottom/sbottom and tau/stau sectors are neglected as  $\tan\beta$  is taken to be not too large.

The high-scale parameters may in general be written in terms of low scale-parameters as

$$m_i^2(M_S) = \sum_{j,k} c_{ijk}(\tan\beta, M_0, M_S) m_j(M_0) m_k(M_0). \quad (3.20)$$

For example, for  $M_S = M_{\text{GUT}}$ , the expressions for the most important high-scale parameters

written in terms of low-scale parameters are

$$\hat{M}_i = d_i M_i \quad \{d_1, d_2, d_3\} = \{2.42, 1.22, 0.35\} \quad (3.21)$$

$$\hat{A}_t = 3.15 A_t + 2.33 M_3 + 1.03 M_2 + 0.26 M_1 \quad (3.22)$$

$$\begin{aligned} \hat{m}_{H_u}^2 &= 2.07 m_{H_u}^2 + 1.07 m_{\tilde{t}_L}^2 + 1.07 m_{\tilde{t}_R}^2 + 0.19 M_3^2 - 0.98 M_2^2 \\ &\quad - 0.31 M_1^2 + 3.38 A_t^2 + 3.69 A_t M_3 + 1.19 A_t M_2 + 0.24 A_t M_1 \\ &\quad + 0.76 M_3 M_2 + 0.15 M_3 M_1 + 0.05 M_2 M_1 + 0.06 S_Y \end{aligned} \quad (3.23)$$

$$\begin{aligned} \hat{m}_{\tilde{t}_L}^2 &= 0.36 m_{H_u}^2 + 1.36 m_{\tilde{t}_L}^2 + 0.36 m_{\tilde{t}_R}^2 - 0.72 M_3^2 - 0.81 M_2^2 \\ &\quad - 0.06 M_1^2 + 1.13 A_t^2 + 1.23 A_t M_3 + 0.40 A_t M_2 + 0.08 A_t M_1 \\ &\quad + 0.25 M_3 M_2 + 0.05 M_3 M_1 + 0.02 M_2 M_1 + 0.02 S_Y \end{aligned} \quad (3.24)$$

$$\begin{aligned} \hat{m}_{\tilde{t}_R}^2 &= 0.72 m_{H_u}^2 + 0.72 m_{\tilde{t}_L}^2 + 1.72 m_{\tilde{t}_R}^2 - 0.65 M_3^2 - 0.18 M_2^2 \\ &\quad - 0.46 M_1^2 + 2.26 A_t^2 + 2.46 A_t M_3 + 0.80 A_t M_2 + 0.16 A_t M_1 \\ &\quad + 0.50 M_3 M_2 + 0.10 M_3 M_1 + 0.04 M_2 M_1 - 0.09 S_Y \end{aligned} \quad (3.25)$$

$$\hat{\mu} = 0.95 \mu. \quad (3.26)$$

Similar type of expressions hold for low-scale parameters as a function of high-scale parameters.

The gauge couplings  $g_\alpha$ ,  $\alpha \in \{1, 2, 3\}$ , and the top Yukawa coupling  $\lambda_t$  are fixed at the low scale by their experimental values [41]. Section 3.7.1 gives the solution of their RG-equations.

The MSSM one-loop  $\beta$ -functions that need to be solved come in three different functional forms [68]. The RG-equations of the gaugino masses  $M_\alpha$ , the supersymmetric Higgsino mass  $\mu$ , and  $S_Y$  are of the form

$$\frac{dm_i}{dt} = f_i(\lambda_t, g_\alpha) m_i, \quad m_i \in \{M_\alpha, \mu, S_Y\}, \quad (3.27)$$

where  $t = \ln(M_S/M_0)$ . Their solution is given by

$$m_i(t) = m_i(0) \exp \int_0^t dt' f_i(\lambda_{t'}, g_\alpha). \quad (3.28)$$

The stop soft trilinear coupling has the functional form

$$\frac{dA_t}{dt} = a(\lambda_t) A_t + b(g_\alpha, M_\alpha). \quad (3.29)$$

The solution of this equation is more involved due to the presence of both homogeneous and inhomogeneous terms, and requires the solution for the gaugino masses (3.28). It may be written as (see Section 3.7.3)

$$A_t(t) = e^{\int dt' a(\lambda_{t'})} A_t(0) + e^{\int dt' a(\lambda_{t'})} \int_0^t dt'' e^{-\int dt''' a(\lambda_{t''})} b(g_\alpha, M_\alpha). \quad (3.30)$$

Finally, the RG-equations of the up-type Higgs soft mass and the stop soft masses form a system of coupled inhomogeneous differential equations,

$$\frac{dm_i^2}{dt} = \sum_j u_{ij}(\lambda_t) m_j^2 + v_i(g_\alpha, M_\alpha, S_Y, A_t), \quad m_i^2 \in \{m_{H_u}^2, m_{\tilde{t}_L}^2, m_{\tilde{t}_R}^2\}. \quad (3.31)$$

This may be solved (see Section 3.7.4) using the solutions for the gaugino masses and  $S_Y$  (3.28) as well as the solution for the stop soft trilinear coupling (3.30),

$$m_i^2(t) = \left( e^{\int dt' u(\lambda_{t'})} m^2(0) + e^{\int dt' u(\lambda_{t'})} \int_0^t dt'' e^{-\int dt''' u(\lambda_{t''})} v(g_\alpha, M_\alpha, S_Y, A_t) \right)_i. \quad (3.32)$$

### 3.7.1 Gauge and Yukawa Couplings

The one-loop  $\beta$ -functions for the gauge and top Yukawa couplings in the MSSM are

$$8\pi^2 \beta_{g_\alpha^2} = b_\alpha g_\alpha^4, \quad \{b_Y, b_2, b_3\} = \{11, 1, -3\} \quad (3.33)$$

$$16\pi^2 \beta_{\lambda_t} = \lambda_t \left( 6\lambda_t^2 - \frac{16}{3}g_3^2 - 3g_2^2 - \frac{13}{9}g_Y^2 \right). \quad (3.34)$$

Their solutions are

$$g_\alpha^2(t) = g_\alpha^2(0) \xi_\alpha^{-1}(t) \quad (3.35)$$

$$\lambda_t^2(t) = \lambda_t^2(0) E(t; \vec{n}_0) G(t; \vec{n}_0)^{-1}, \quad (3.36)$$

where  $\vec{n}_0 = \left( \frac{13}{9b_1}, \frac{3}{b_2}, \frac{16}{3b_3} \right) = \left( \frac{13}{99}, 3, -\frac{16}{9} \right)$ , and for future convenience the functions

$$\xi_\alpha(t) = 1 - \frac{b_\alpha}{8\pi^2} g_\alpha^2(0)t \quad (3.37)$$

$$E(t; \vec{n}) = \prod_{\alpha=1}^3 \xi_\alpha^{(\vec{n})_\alpha}(t) \quad (3.38)$$

$$F(t; \vec{n}) = \int_0^t dt' E(t'; \vec{n}) \quad (3.39)$$

$$G(t; \vec{n}) = 1 - \frac{3}{4\pi^2} \lambda_t^2(0) F(t; \vec{n}) \quad (3.40)$$

have been introduced. The solution (3.36) is analytic if  $g_2$  and  $g_Y$  are set to zero [69, 70], whereas non-zero values of  $g_2$  and  $g_Y$  require a numerical integration.

### 3.7.2 Gaugino Masses, $\mu$ -term and $S_Y$

The RG-equations for the gaugino masses,  $\mu$  and  $S_Y$  are

$$\beta_{M_\alpha} = \frac{M_\alpha}{g_\alpha^2} \beta_{g_\alpha^2} \quad (3.41)$$

$$16\pi^2 \beta_\mu = \mu (3\lambda_t^2 - 3g_2^2 - g_Y^2) \quad (3.42)$$

$$8\pi^2 \beta_{S_Y} = g_Y^2 \sum_{\text{scalars } i} \left(\frac{Y_i}{2}\right)^2 S_Y. \quad (3.43)$$

The general solution is of the form (3.28), and may be written as

$$M_\alpha(t) = M_\alpha(0) \xi_\alpha^{-1}(t) \quad (3.44)$$

$$\mu(t) = \mu(0) G(t; \vec{n}_0)^{-\frac{1}{4}} \xi_2^{\frac{3}{2}}(t) \xi_1^{\frac{1}{22}}(t) \quad (3.45)$$

$$S_Y(t) = S_Y(0) \xi_1^{-1}(t) \quad (3.46)$$

with the notation of Section 3.7.1. The solutions for the gaugino masses and  $S_Y$  are analytic while  $\mu$  must be solved numerically unless the contributions from  $g_2$  and  $g_Y$  are neglected.

### 3.7.3 Stop Soft Trilinear Coupling

The  $\beta$ -function of the stop soft trilinear coupling is

$$8\pi^2 \beta_{A_t} = \left( 6\lambda_t^2 A_t - \frac{16}{3} g_3^2 M_3 - 3g_2^2 M_2 - \frac{13}{9} g_Y^2 M_1 \right). \quad (3.47)$$

Using the solutions for the gaugino masses (3.44), this equation may be integrated and written as

$$A_t(t) = \frac{1}{G(t; \vec{n}_0)} \left[ A_t(0) + \sum_{\alpha=1}^3 (\vec{n}_0)_\alpha \frac{M_\alpha(0)}{\xi_\alpha(t)} \left( G(t; \vec{n}_0) - \xi_\alpha(t) G(t; \vec{n}_0 - \vec{e}^\alpha) \right) \right] \quad (3.48)$$

where  $(\vec{e}^\alpha)_\beta = \delta_\beta^\alpha$  are the usual unit vectors. If  $g_2$  and  $g_Y$  are zero, the solution does not require a numerical integration.

### 3.7.4 Up-type Higgs Soft Mass and Stop Soft Masses

The  $\beta$ -functions of  $m_{H_u}^2$ ,  $m_{\tilde{t}_L}^2$  and  $m_{\tilde{t}_R}^2$  are

$$8\pi^2\beta_{m_{H_u}^2} = 3\lambda_t^2 \left[ m_{H_u}^2 + m_{\tilde{t}_L}^2 + m_{\tilde{t}_R}^2 + |A_t|^2 \right] - 3g_2^2 |M_2|^2 - g_Y^2 |M_1|^2 - \frac{1}{2}g_Y^2 S_Y \quad (3.49)$$

$$8\pi^2\beta_{m_{\tilde{t}_L}^2} = \lambda_t^2 \left[ m_{H_u}^2 + m_{\tilde{t}_L}^2 + m_{\tilde{t}_R}^2 + |A_t|^2 \right] - \frac{16}{3}g_3^2 |M_3|^2 - 3g_2^2 |M_2|^2 - \frac{1}{9}g_Y^2 |M_1|^2 - \frac{1}{6}g_Y^2 S_Y \quad (3.50)$$

$$8\pi^2\beta_{m_{\tilde{t}_R}^2} = 2\lambda_t^2 \left[ m_{H_u}^2 + m_{\tilde{t}_L}^2 + m_{\tilde{t}_R}^2 + |A_t|^2 \right] - \frac{16}{3}g_3^2 |M_3|^2 - \frac{16}{9}g_Y^2 |M_1|^2 - \frac{2}{3}g_Y^2 S_Y. \quad (3.51)$$

They form a system of coupled inhomogeneous differential equations. Note that  $A_t$  appears quadratically in these  $\beta$ -functions which gives cross-terms between  $M_\alpha(0)$  and  $A_t(0)$  (see equation (3.48)). The equations can be solved as in (3.32) but it is possible to simplify the analysis by the change of variables

$$X = m_{H_u}^2 - m_{\tilde{t}_L}^2 - m_{\tilde{t}_R}^2 \quad (3.52)$$

$$Y = m_{H_u}^2 - 3m_{\tilde{t}_L}^2 \quad (3.53)$$

$$Z = m_{H_u}^2 + m_{\tilde{t}_L}^2 + m_{\tilde{t}_R}^2. \quad (3.54)$$

In terms of the new variables, the  $\beta$ -functions are

$$8\pi^2\beta_X = \frac{32}{3}g_3^2 |M_3|^2 + \frac{8}{9}g_Y^2 |M_1|^2 + g_Y^2 S_Y \quad (3.55)$$

$$8\pi^2\beta_Y = 16g_3^2 |M_3|^2 + 6g_2^2 |M_2|^2 - \frac{2}{3}g_Y^2 |M_1|^2 \quad (3.56)$$

$$8\pi^2\beta_Z = 6\lambda_t^2 Z + 6\lambda_t^2 |A_t|^2 - \frac{32}{3}g_3^2 |M_3|^2 - 6g_2^2 |M_2|^2 - \frac{26}{9}g_Y^2 |M_1|^2. \quad (3.57)$$

In this form,  $\beta_X$  and  $\beta_Y$  are easily integrated since they have no homogeneous term (which is due to the fact that the corresponding matrix  $u_{ij}$  in (3.31) has rank = 1)

$$X(t) = X(0) - \frac{16}{9} M_3^2(0) (\xi_3^{-2}(t) - 1) + \frac{4}{99} M_1^2(0) (\xi_1^{-2}(t) - 1) + \frac{1}{11} S_Y(0) (\xi_1^{-1}(t) - 1) \quad (3.58)$$

$$Y(t) = Y(0) - \frac{8}{3} M_3^2(0) (\xi_3^{-2}(t) - 1) + 3 M_2^2(0) (\xi_2^{-2}(t) - 1) - \frac{1}{33} M_1^2(0) (\xi_1^{-2}(t) - 1). \quad (3.59)$$

The equation for  $Z$  requires a numerical integration (even if  $g_2$  and  $g_Y$  are zero)

$$Z(t) = \frac{1}{G(t; \vec{n}_0)} \left[ Z(0) - \sum_{\alpha=1}^3 (\vec{n}_0)_\alpha \frac{M_\alpha^2(0)}{\xi_\alpha^2(t)} \left( G(t; \vec{n}_0) - \xi_\alpha^2(t) G(t; \vec{n}_0 - 2\vec{e}^\alpha) \right) + \frac{3}{4\pi^2} \lambda_t^2(0) \int_0^t dt' E(t'; \vec{n}_0) |A_t(t')|^2 \right]. \quad (3.60)$$

The solutions for  $m_{H_u}^2$ ,  $m_{t_L}^2$  and  $m_{t_R}^2$  in terms of  $X$ ,  $Y$  and  $Z$  are then

$$m_{H_u}^2(t) = \frac{1}{2} (X(t) + Z(t)) \quad (3.61)$$

$$m_{t_L}^2(t) = \frac{1}{6} (X(t) - 2Y(t) + Z(t)) \quad (3.62)$$

$$m_{t_R}^2(t) = \frac{1}{3} (-2X(t) + Y(t) + Z(t)). \quad (3.63)$$

### 3.8 Appendix: Fine-tuning Components

This appendix lists for completeness the expressions for the fine-tuning of  $m_Z^2$  with respect to  $M_3^2$ ,  $M_2^2$ ,  $M_1^2$ ,  $\mu^2$ ,  $A_t^2$ ,  $m_{H_u}^2$ ,  $m_{t_L}^2$  and  $m_{t_R}^2$ . The fine-tuning components as a function of high-scale parameters are easily found from the fine-tuning measure, equation (3.8), with the

observable  $m_Z^2$  written as in equation (3.5). For  $M_S = M_{\text{GUT}}$ , the fine-tuning components are

$$m_Z^2 \Delta(m_Z^2, \hat{M}_3^2) \simeq 5.24 \hat{M}_3^2 + 0.23 \hat{M}_3 \hat{M}_2 + 0.03 \hat{M}_3 \hat{M}_1 - 0.38 \hat{A}_t \hat{M}_3 \quad (3.64)$$

$$m_Z^2 \Delta(m_Z^2, \hat{M}_2^2) \simeq -0.44 \hat{M}_2^2 + 0.23 \hat{M}_3 \hat{M}_2 + 0.01 \hat{M}_2 \hat{M}_1 - 0.08 \hat{A}_t \hat{M}_2 \quad (3.65)$$

$$m_Z^2 \Delta(m_Z^2, \hat{M}_1^2) \simeq -0.01 \hat{M}_1^2 + 0.03 \hat{M}_3 \hat{M}_1 + 0.01 \hat{M}_2 \hat{M}_1 - 0.01 \hat{A}_t \hat{M}_1 \quad (3.66)$$

$$m_Z^2 \Delta(m_Z^2, \hat{\mu}^2) \simeq -2.19 \hat{\mu}^2 \quad (3.67)$$

$$m_Z^2 \Delta(m_Z^2, \hat{A}_t^2) \simeq 0.22 \hat{A}_t^2 - 0.38 \hat{A}_t \hat{M}_3 - 0.08 \hat{A}_t \hat{M}_2 - 0.01 \hat{A}_t \hat{M}_1 \quad (3.68)$$

$$m_Z^2 \Delta(m_Z^2, \hat{m}_{H_u}^2) \simeq -1.32 \hat{m}_{H_u}^2 \quad (3.69)$$

$$\begin{aligned} &\simeq -m_Z^2 - 2.19 \hat{\mu}^2 + 1.36 \hat{m}_t^2 + 5.24 \hat{M}_3^2 \\ &\quad - 0.44 \hat{M}_2^2 + 0.46 \hat{M}_3 \hat{M}_2 - 0.77 \hat{A}_t \hat{M}_3 - 0.17 \hat{A}_t \hat{M}_2 \\ &\quad - 0.01 \hat{M}_1^2 + 0.22 \hat{A}_t^2 \end{aligned}$$

$$m_Z^2 \Delta(m_Z^2, \hat{m}_{t_L}^2) \simeq 0.68 \hat{m}_{t_L}^2 \quad (3.70)$$

$$m_Z^2 \Delta(m_Z^2, \hat{m}_{t_R}^2) \simeq 0.68 \hat{m}_{t_R}^2. \quad (3.71)$$

Here it is understood that the absolute value of the right-hand sides of each of these equations is meant to be taken. The EWSB relation, equation (3.7), was used to eliminate  $\hat{m}_{H_u}^2$ . It is natural to eliminate  $\hat{m}_{H_u}^2$  instead of  $\hat{\mu}^2$  or any other soft supersymmetry breaking parameters since  $\hat{\mu}^2$  is supersymmetric while the other soft supersymmetry breaking parameters are not involved in the EWSB equation at the EW scale. With the help of equations (3.21)-(3.26), it is now straightforward to rewrite the FT expression (3.10) in terms of low-scale parameters.

## References

- [1] **ALEPH, DELPHI, L3 and OPAL** Collaboration, The LEP Working Group for Higgs Boson Searches, “Search for neutral MSSM Higgs bosons at LEP,” [hep-ex/0602042](#).
- [2] J. R. Ellis, K. Enqvist, D. V. Nanopoulos, and F. Zwirner, “Observables in Low-Energy Superstring Models,” *Mod. Phys. Lett.* **A1** (1986) 57.
- [3] R. Barbieri and G. F. Giudice, “Upper Bounds on Supersymmetric Particle Masses,” *Nucl. Phys.* **B306** (1988) 63.
- [4] B. de Carlos and J. A. Casas, “One loop analysis of the electroweak breaking in supersymmetric models and the fine tuning problem,” *Phys. Lett.* **B309** (1993) 320–328, [hep-ph/9303291](#).
- [5] B. de Carlos and J. A. Casas, “The Fine tuning problem of the electroweak symmetry breaking mechanism in minimal SUSY models,” [hep-ph/9310232](#).
- [6] G. W. Anderson and D. J. Castano, “Measures of fine tuning,” *Phys. Lett.* **B347** (1995) 300–308, [hep-ph/9409419](#).
- [7] P. Ciafaloni and A. Strumia, “Naturalness upper bounds on gauge mediated soft terms,” *Nucl. Phys.* **B494** (1997) 41–53, [hep-ph/9611204](#).
- [8] P. H. Chankowski, J. R. Ellis, and S. Pokorski, “The fine-tuning price of LEP,” *Phys. Lett.* **B423** (1998) 327–336, [hep-ph/9712234](#).
- [9] K. Agashe and M. Graesser, “Improving the fine tuning in models of low energy gauge mediated supersymmetry breaking,” *Nucl. Phys.* **B507** (1997) 3–34, [hep-ph/9704206](#).
- [10] K. L. Chan, U. Chattopadhyay, and P. Nath, “Naturalness, weak scale supersymmetry and the prospect for the observation of supersymmetry at the Tevatron and at the LHC,” *Phys. Rev.* **D58** (1998) 096004, [hep-ph/9710473](#).
- [11] D. Wright, “Naturally nonminimal supersymmetry,” [hep-ph/9801449](#).
- [12] G. L. Kane and S. F. King, “Naturalness implications of LEP results,” *Phys. Lett.* **B451** (1999) 113–122, [hep-ph/9810374](#).
- [13] M. Bastero-Gil, G. L. Kane, and S. F. King, “Fine-tuning constraints on supergravity models,” *Phys. Lett.* **B474** (2000) 103–112, [hep-ph/9910506](#).
- [14] J. A. Casas, J. R. Espinosa, and I. Hidalgo, “The MSSM fine tuning problem: A way out,” *JHEP* **01** (2004) 008, [hep-ph/0310137](#).
- [15] J. A. Casas, J. R. Espinosa, and I. Hidalgo, “A relief to the supersymmetric fine tuning problem,” [hep-ph/0402017](#).
- [16] J. A. Casas, J. R. Espinosa, and I. Hidalgo, “Implications for new physics from fine-tuning arguments. I: Application to SUSY and seesaw cases,” *JHEP* **11** (2004) 057, [hep-ph/0410298](#).

- [17] P. C. Schuster and N. Toro, “Persistent fine-tuning in supersymmetry and the NMSSM,” [hep-ph/0512189](#).
- [18] R. Dermisek and J. F. Gunion, “Escaping the large fine tuning and little hierarchy problems in the next to minimal supersymmetric model and  $h \rightarrow a a$  decays,” *Phys. Rev. Lett.* **95** (2005) 041801, [hep-ph/0502105](#).
- [19] R. Dermisek and H. D. Kim, “Radiatively generated maximal mixing scenario for the Higgs mass and the least fine tuned minimal supersymmetric standard model,” *Phys. Rev. Lett.* **96** (2006) 211803, [hep-ph/0601036](#).
- [20] J. A. Casas, J. R. Espinosa, and I. Hidalgo, “Expectations for LHC from naturalness: Modified vs. SM Higgs sector,” [hep-ph/0607279](#).
- [21] T. Kobayashi, H. Terao, and A. Tsuchiya, “Fine-tuning in gauge mediated supersymmetry breaking models and induced top Yukawa coupling,” *Phys. Rev.* **D74** (2006) 015002, [hep-ph/0604091](#).
- [22] P. Athron and D. J. Miller, “A New Measure of Fine Tuning,” [arXiv:0705.2241 \[hep-ph\]](#).
- [23] M. Frank *et al.*, “The Higgs boson masses and mixings of the complex MSSM in the Feynman-diagrammatic approach,” [hep-ph/0611326](#).
- [24] G. Degrandi, S. Heinemeyer, W. Hollik, P. Slavich, and G. Weiglein, “Towards high-precision predictions for the MSSM Higgs sector,” *Eur. Phys. J.* **C28** (2003) 133–143, [hep-ph/0212020](#).
- [25] S. Heinemeyer, W. Hollik, and G. Weiglein, “The masses of the neutral CP-even Higgs bosons in the MSSM: Accurate analysis at the two-loop level,” *Eur. Phys. J.* **C9** (1999) 343–366, [hep-ph/9812472](#).
- [26] S. Heinemeyer, W. Hollik, and G. Weiglein, “FeynHiggs: A program for the calculation of the masses of the neutral CP-even Higgs bosons in the MSSM,” *Comput. Phys. Commun.* **124** (2000) 76–89, [hep-ph/9812320](#).
- [27] S. Heinemeyer, W. Hollik, H. Rzehak, and G. Weiglein, “The Higgs sector of the complex MSSM at two-loop order: QCD contributions,” [arXiv:0705.0746 \[hep-ph\]](#).
- [28] Y. Okada, M. Yamaguchi, and T. Yanagida, “Upper bound of the lightest Higgs boson mass in the minimal supersymmetric standard model,” *Prog. Theor. Phys.* **85** (1991) 1–6.
- [29] J. R. Ellis, G. Ridolfi, and F. Zwirner, “Radiative corrections to the masses of supersymmetric Higgs bosons,” *Phys. Lett.* **B257** (1991) 83–91.
- [30] H. E. Haber and R. Hempfling, “Can the mass of the lightest Higgs boson of the minimal supersymmetric model be larger than  $m(Z)$ ?” *Phys. Rev. Lett.* **66** (1991) 1815–1818.
- [31] H. E. Haber, R. Hempfling, and A. H. Hoang, “Approximating the radiatively corrected Higgs mass in the minimal supersymmetric model,” *Z. Phys.* **C75** (1997) 539–554, [hep-ph/9609331](#).
- [32] M. Carena, J. R. Espinosa, M. Quiros, and C. E. M. Wagner, “Analytical expressions for radiatively corrected Higgs masses and couplings in the MSSM,” *Phys. Lett.* **B355** (1995) 209–221, [hep-ph/9504316](#).
- [33] M. Carena, M. Quiros, and C. E. M. Wagner, “Effective potential methods and the Higgs mass spectrum in the MSSM,” *Nucl. Phys.* **B461** (1996) 407–436, [hep-ph/9508343](#).

- [34] R. Essig, “Implications of the LEP Higgs bounds for the MSSM stop sector,” *Phys. Rev.* **D75** (2007) 095005, [hep-ph/0702104](#).
- [35] L. E. Ibanez and C. Lopez, “N=1 Supergravity, the Weak Scale and the Low-Energy Particle Spectrum,” *Nucl. Phys.* **B233** (1984) 511.
- [36] M. Carena, P. H. Chankowski, M. Olechowski, S. Pokorski, and C. E. M. Wagner, “Bottom-up approach and supersymmetry breaking,” *Nucl. Phys.* **B491** (1997) 103–128, [hep-ph/9612261](#).
- [37] J. A. Casas, J. R. Espinosa, and I. Hidalgo, “Implications for new physics from fine-tuning arguments. II: Little Higgs models,” *JHEP* **03** (2005) 038, [hep-ph/0502066](#).
- [38] P. Athron and D. J. Miller, “Fine Tuning in Supersymmetric Models,” [arXiv:0707.1255 \[hep-ph\]](#).
- [39] A. B. Lahanas and D. V. Nanopoulos, “The Road to No Scale Supergravity,” *Phys. Rept.* **145** (1987) 1.
- [40] CDF Collaboration, “A combination of CDF and D0 results on the mass of the top quark,” [hep-ex/0703034](#).
- [41] W.-M. Yao *et al.*, “Review of Particle Physics,” *Journal of Physics G* **33** (2006) 1+.
- [42] M. Drees, R. Godbole, and P. Roy, *Theory & Phenomenology of Sparticles*. World Scientific Publishing Company, 2004.
- [43] M. Carena and H. E. Haber, “Higgs boson theory and phenomenology. ((V)),” *Prog. Part. Nucl. Phys.* **50** (2003) 63–152, [hep-ph/0208209](#).
- [44] S. P. Martin, “A supersymmetry primer,” [hep-ph/9709356](#).
- [45] S. Heinemeyer, W. Hollik, and G. Weiglein, “The mass of the lightest MSSM Higgs boson: A compact analytical expression at the two-loop level,” *Phys. Lett.* **B455** (1999) 179–191, [hep-ph/9903404](#).
- [46] G. L. Kane, T. T. Wang, B. D. Nelson, and L.-T. Wang, “Theoretical implications of the LEP Higgs search,” *Phys. Rev.* **D71** (2005) 035006, [hep-ph/0407001](#).
- [47] R. Kitano and Y. Nomura, “Supersymmetry, naturalness, and signatures at the LHC,” *Phys. Rev.* **D73** (2006) 095004, [hep-ph/0602096](#).
- [48] P. M. Ferreira, I. Jack, and D. R. T. Jones, “Infrared soft universality,” *Phys. Lett.* **B357** (1995) 359–364, [hep-ph/9506467](#).
- [49] M. Lanzagorta and G. G. Ross, “Infrared fixed point structure of soft supersymmetry breaking mass terms,” *Phys. Lett.* **B364** (1995) 163–174, [hep-ph/9507366](#).
- [50] B. Pendleton and G. G. Ross, “Mass and Mixing Angle Predictions from Infrared Fixed Points,” *Phys. Lett.* **B98** (1981) 291.
- [51] J. M. Frere, D. R. T. Jones, and S. Raby, “Fermion Masses and Induction of the Weak Scale by Supergravity,” *Nucl. Phys.* **B222** (1983) 11.
- [52] J. P. Derendinger and C. A. Savoy, “Quantum Effects and SU(2) x U(1) Breaking in Supergravity Gauge Theories,” *Nucl. Phys.* **B237** (1984) 307.
- [53] J. F. Gunion, H. E. Haber, and M. Sher, “Charge / Color Breaking Minima And A-Parameter Bounds In Supersymmetric Models,” *Nucl. Phys.* **B306** (1988) 1.

- [54] J. A. Casas, A. Lleyda, and C. Munoz, “Strong constraints on the parameter space of the MSSM from charge and color breaking minima,” *Nucl. Phys.* **B471** (1996) 3–58, [hep-ph/9507294](#).
- [55] C. Le Mouel, “Charge and color breaking conditions associated to the top quark Yukawa coupling,” *Phys. Rev.* **D64** (2001) 075009, [hep-ph/0103341](#).
- [56] A. Kusenko, P. Langacker, and G. Segre, “Phase Transitions and Vacuum Tunneling Into Charge and Color Breaking Minima in the MSSM,” *Phys. Rev.* **D54** (1996) 5824–5834, [hep-ph/9602414](#).
- [57] A. Riotto and E. Roulet, “Vacuum decay along supersymmetric flat directions,” *Phys. Lett.* **B377** (1996) 60–66, [hep-ph/9512401](#).
- [58] R. Dermisek, H. D. Kim, and I.-W. Kim, “Mediation of supersymmetry breaking in gauge messenger models,” *JHEP* **10** (2006) 001, [hep-ph/0607169](#).
- [59] **SUSY Working Group** Collaboration, R. Culbertson *et al.*, “Low-scale and gauge-mediated supersymmetry breaking at the Fermilab Tevatron Run II,” [hep-ph/0008070](#).
- [60] C.-L. Chou and M. E. Peskin, “Scalar top quark as the next-to-lightest supersymmetric particle,” *Phys. Rev.* **D61** (2000) 055004, [hep-ph/9909536](#).
- [61] U. Sarid and S. D. Thomas, “Mesino-antimesino oscillations,” *Phys. Rev. Lett.* **85** (2000) 1178–1181, [hep-ph/9909349](#).
- [62] M. Perelstein and C. Spethmann, “A collider signature of the supersymmetric golden region,” *JHEP* **04** (2007) 070, [hep-ph/0702038](#).
- [63] R. Dermisek and I. Low, “Probing the stop sector and the sanity of the MSSM with the Higgs boson at the LHC,” [hep-ph/0701235](#).
- [64] J. R. Espinosa and R.-J. Zhang, “MSSM lightest CP-even Higgs boson mass to  $O(\alpha(s)\alpha(t))$ : The effective potential approach,” *JHEP* **03** (2000) 026, [hep-ph/9912236](#).
- [65] M. Carena *et al.*, “Reconciling the two-loop diagrammatic and effective field theory computations of the mass of the lightest CP-even Higgs boson in the MSSM,” *Nucl. Phys.* **B580** (2000) 29–57, [hep-ph/0001002](#).
- [66] S. Heinemeyer, “MSSM Higgs physics at higher orders,” [hep-ph/0407244](#).
- [67] M. Carena, S. Heinemeyer, C. E. M. Wagner, and G. Weiglein, “Suggestions for improved benchmark scenarios for Higgs- boson searches at LEP2,” [hep-ph/9912223](#).
- [68] S. P. Martin and M. T. Vaughn, “Two loop renormalization group equations for soft supersymmetry breaking couplings,” *Phys. Rev.* **D50** (1994) 2282, [hep-ph/9311340](#).
- [69] C. T. Hill, “Quark and Lepton Masses from Renormalization Group Fixed Points,” *Phys. Rev.* **D24** (1981) 691.
- [70] M. Lanzagorta and G. G. Ross, “Infrared fixed points revisited,” *Phys. Lett.* **B349** (1995) 319–328, [hep-ph/9501394](#).

## Chapter 4

# Meta-Stable Dynamical Supersymmetry Breaking Near Points of Enhanced Symmetry

This chapter appears in print in JHEP09(2007)032, arxiv:0707.0007 [hep-th], and in arXiv:0710.4311 [hep-th], and includes work done with Kuver Sinha and Gonzalo Torroba.

We construct a model with long-lived metastable vacua in which all the relevant parameters, including the supersymmetry breaking scale, are generated dynamically by dimensional transmutation. Our model consists of two sectors coupled by a singlet and combines dynamical supersymmetry breaking with an O’Raifeartaigh mechanism in terms of confined variables. The metastable vacua appear along a pseudo-runaway direction near a point of enhanced symmetry as a result of a balance between non-perturbative and perturbative quantum effects. We show that metastable supersymmetry breaking is a rather generic feature near certain enhanced symmetry points of gauge theory moduli spaces.

### 4.1 Introduction

The idea that our universe may be in a long-lived metastable state in which supersymmetry is broken has recently led to an increased interest in developing models of supersymmetry breaking. This has opened many new possibilities in constructing field theory and string theory models.

On the field theoretic side, the work of Intriligator, Seiberg and Shih (ISS) [1] presented calculable metastable vacua using Seiberg duality. This motivated related field theory constructions, involving gauge mediation [2, 3, 4, 5], generalized O’Raifeartaigh models [6], retrofitting [7], adjoint matter [8], applications to particle physics [9, 10, 11], etc. Similar developments

have been seen in string theory based on a number of different tools, such as intersecting or wrapping branes [12, 13, 14, 15], flux compactifications [16, 17, 18, 19, 20], Calabi-Yau's with particular geometric properties [21, 22, 23, 24], IIA/M-theory configurations [25, 26, 27] and others. Statistical analyses of the supersymmetry breaking scale on the landscape of effective field theories were done, for instance, in [28, 29, 30].

The ISS model consists of supersymmetric QCD (SQCD) in the free magnetic range, and metastable vacua appear after taking into account one-loop corrections that lift the pseudo-moduli. Their work suggests that nonsupersymmetric vacua are rather generic, if one requires them to be only local, rather than global, minima of the potential. The construction still contained relevant couplings in the form of masses for the quarks though, and the search for models with all the relevant parameters generated dynamically has proven difficult; see [31, 32, 33, 34] for recent work in this direction.

One lesson from ISS is that certain properties of moduli spaces can hint at the existence of metastable vacua. In their case, it was the existence of supersymmetric vacua coming in from infinity that signaled an approximate R-symmetry. Here we will point out that one should also look for another feature, namely, enhanced symmetry points, which are defined by the appearance of massless particles. We claim that if the moduli space has certain coincident enhanced symmetry points, metastable vacua with all the relevant couplings arising by dimensional transmutation may be obtained.

Let us motivate this claim. In order to generate relevant couplings dynamically, a gauge sector is required, which gives nonperturbative contributions to the superpotential. However, in general this leads to a runaway behavior. We will show that starting with two gauge sectors, the runaway may now be stabilized by one loop effects from the additional gauge sector, but only around enhanced symmetry points where quantum corrections are large enough. Such runaways which are stabilized by perturbative quantum corrections will be called ‘pseudo-runaways’. Surprisingly, the gauge theories where this occurs turn out to be generic.

The model considered here consists of two SQCD sectors, each with independent rank and

number of flavors, coupled by a singlet. It involves only marginal operators with all scales generated dynamically. At the origin of moduli space, the singlet vanishes and the quarks of both sectors become massless simultaneously. There are thus two coincident enhanced symmetry points at the origin. While one of the SQCD sectors is in the electric range and produces a runaway, the other has a magnetic dual description as an O’Raifeartaigh-like model. Near the enhanced symmetry point, the Coleman-Weinberg corrections stabilize the nonperturbative instability producing a long-lived metastable vacuum. A feature of our model is that it may be possible to gauge parts of its large global symmetry to obtain renormalizable, natural models of direct gauge mediated supersymmetry breaking with a singlet. R-symmetry is broken both spontaneously and explicitly in our model.

The plan of the paper is as follows. In Section 2, our model is introduced and its supersymmetric vacua are studied. In Section 3, we analyze in detail the non-supersymmetric vacua and argue that they are parametrically long-lived. In Section 4, we give a detailed analysis of the particle spectrum and the R-symmetry properties. In Section 5, we argue that such metastable vacua may be generic near points of enhanced symmetry in the landscape of effective field theories. In Section 6, we give our conclusions.

## 4.2 The Model and its Supersymmetric Vacua

We consider models with two supersymmetric QCD (SQCD) sectors characterized by  $(N_c, N_f, \Lambda)$  and  $(N'_c, N'_f, \Lambda')$ , respectively, that are coupled to the same singlet field  $\Phi$ . The field  $\Phi$  provides the mass of the quarks in both sectors. In Section 2.1, the general properties of such models will be discussed and their global symmetries analyzed. In Section 2.2, we analyze the supersymmetric vacua. Section 2.3 will discuss for which range of the parameters  $(N_c, N_f, \Lambda)$  and  $(N'_c, N'_f, \Lambda')$  metastable vacua will be shown to exist. The upshot will be that one sector has to be taken in the electric range and the other sector in the free magnetic range.

### 4.2.1 Description of the Model

The matter content of the models considered here consists of two copies of supersymmetric QCD, each with independent rank and number of flavors, and a single gauge singlet chiral superfield:

$$\begin{array}{cccc}
 & SU(N_c) & SU(N'_c) & \\
 Q_i & \square & 1 & i = 1, \dots, N_f \\
 \bar{Q}_i & \bar{\square} & 1 & \\
 P_{i'} & 1 & \square & i' = 1, \dots, N'_f \\
 \bar{P}_{i'} & 1 & \bar{\square} & \\
 \Phi & 1 & 1 & 
 \end{array} \tag{4.1}$$

The most general tree-level superpotential with only relevant or marginal terms in four dimensions for the matter content (4.1) with  $N_c, N'_c \geq 4$  is

$$W = (\lambda_{ij}\Phi + \xi_{ij})Q_i\bar{Q}_j + (\lambda'_{i'j'}\Phi + \xi'_{i'j'})P_{i'}\bar{P}_{j'} + w(\Phi), \tag{4.2}$$

where  $w(\Phi)$  is a cubic polynomial in  $\Phi$ . Remarkably, we shall find metastable vacua even in the simplest case of  $w(\Phi) = 0$ , which we assume from now on. The general situation is discussed in Section 5 (in [33], the case  $w(\Phi) = \kappa\Phi^3$  was used to stabilize  $\Phi$  supersymmetrically).

At the classical level, the superpotential with  $w(\Phi) = 0$  has an  $U(1)_R \times U(1)_V \times U(1)'_V$  global symmetry under which the fields transform as

$$\begin{array}{cccc}
 & U(1)_R & U(1)_V & U(1)'_V \\
 Q_i & +1 & +1 & 0 \\
 \bar{Q}_i & +1 & -1 & 0 \\
 P_{i'} & +1 & 0 & +1 \\
 \bar{P}_{i'} & +1 & 0 & -1 \\
 \Phi & 0 & 0 & 0 \\
 \Lambda^{3N_c - N_f} & 2N_c & 0 & 0 \\
 \Lambda'^{3N'_c - N'_f} & 2N'_c & 0 & 0
 \end{array} \tag{4.3}$$

where the normalizations of the  $U(1)_V \times U(1)'_V$  charges are arbitrary. In the quantum theory the  $U(1)_R$  symmetry is anomalous with respect to the  $SU(N_c)$  and  $SU(N'_c)$  gauge dynamics. The theta angles  $\theta$  and  $\theta'$  transform inhomogeneously under  $U(1)_R$ , and the holomorphic dynamical scale,

$$(\Lambda/\mu)^{3N_c - N_f} = e^{-8\pi^2/g^2(\mu) + i\theta}, \quad (4.4)$$

and likewise for  $\Lambda'^{3N'_c - N'_f}$ , transform with charges given in (4.3). The  $U(1)_R$  symmetry is broken explicitly by the anomalies to the anomaly free discrete subgroups  $Z_{2N_c} \subset U(1)_R$  and  $Z_{2N'_c} \subset U(1)_R$ , respectively. The largest simultaneous subgroup of both  $Z_{2N_c}$  and  $Z_{2N'_c}$  which is left invariant by the superpotential (4.2) which couples the two gauge sectors through  $\Phi$  interactions is  $Z_{\text{GCD}(2N_c, 2N'_c)} \subset U(1)_R$ , where  $\text{GCD}(2N_c, 2N'_c)$  is the greatest common divisor of  $2N_c$  and  $2N'_c$ .

In the  $SU(N_f)_V \times SU(N'_f)_V$  global symmetry limit the superpotential (4.2) (with  $w(\Phi) = 0$ ) reduces to

$$W = (\lambda\Phi + \xi)\text{tr}(Q\bar{Q}) + (\lambda'\Phi + \xi')\text{tr}(P\bar{P}). \quad (4.5)$$

This superpotential has the same  $U(1)_R \times U(1)_V \times U(1)'_V$  global symmetry as (4.2), as well as a  $Z_2 \times Z_2$  conjugation symmetry under which  $Q_i \leftrightarrow \bar{Q}_i$  and  $P_i \leftrightarrow \bar{P}_i$ , respectively. The form of the superpotential (4.5) may be enforced for any  $N_c$  and  $N'_c$  by weakly gauging the  $SU(N_f)_V \times SU(N'_f)_V$  symmetry. One of the masses,  $\xi$  or  $\xi'$ , may always be absorbed into a shift of  $\Phi$ . For  $\xi = \xi'$  both masses may simultaneously be absorbed into a shift of  $\Phi$ , and the tree level superpotential in this case reduces to

$$W = \lambda\Phi \text{tr}(Q\bar{Q}) + \lambda'\Phi \text{tr}(P\bar{P}). \quad (4.6)$$

This form agrees with the naturalness requirement that there be no relevant couplings.  $\Phi = 0$  is an enhanced symmetry point for both sectors, where the respective quarks become massless. The case  $\xi \neq \xi'$  is analyzed in Section 5.

At the classical level this superpotential has an  $U(1)_R \times U(1)_A \times U(1)_V \times U(1)'_V$  global

symmetry

$$\begin{array}{ccccc}
& U(1)_R & U(1)_A & U(1)_V & U(1)'_V \\
Q_i & +1 & -\frac{1}{2} & +1 & 0 \\
\bar{Q}_i & +1 & -\frac{1}{2} & -1 & 0 \\
P_{i'} & +1 & -\frac{1}{2} & 0 & +1 \\
\bar{P}_{i'} & +1 & -\frac{1}{2} & 0 & -1 \\
\Phi & 0 & +1 & 0 & 0 \\
\Lambda^{3N_c-N_f} & 2N_c & -N_f & 0 & 0 \\
\Lambda'^{3N'_c-N'_f} & 2N'_c & -N'_f & 0 & 0
\end{array} \tag{4.7}$$

where the normalizations of the  $U(1)_A \times U(1)_V \times U(1)'_V$  charges are arbitrary. The  $U(1)_R$  charges are only defined up to an addition of an arbitrary multiple of the  $U(1)_A$  charges. In the quantum theory both the  $U(1)_R$  and  $U(1)_A$  symmetries are anomalous. With the classical charge assignments (4.7) the  $U(1)_R$  symmetry is broken explicitly by the  $SU(N_c)$  and  $SU(N'_c)$  gauge dynamics to the anomaly free discrete subgroup  $Z_{\text{GCD}(2N_c, 2N'_c)} \subset U(1)_R$  as described above. Likewise, the  $U(1)_A$  symmetry is broken explicitly by  $SU(N_c)$  and  $SU(N'_c)$  gauge dynamics to anomaly free discrete subgroups  $Z_{N_f} \subset U(1)_A$  and  $Z_{N'_f} \subset U(1)_A$ , respectively. The largest simultaneous subgroup of both  $Z_{N_f}$  and  $Z_{N'_f}$  which is left invariant by the superpotential (4.6) is  $Z_{\text{GCD}(N_f, N'_f)} \subset U(1)_A$ . The form of the potential (4.6) may be enforced by gauging the non-anomalous discrete  $Z_{\text{GCD}(N_f, N'_f)}$  symmetry if it is non-trivial, along with weakly gauging the  $SU(N_f)_V \times SU(N'_f)_V$  symmetry. This forbids the presence of a polynomial dependence  $w(\Phi)$ .

The marginal tree-level superpotential (4.6) is, up to irrelevant terms, of rather generic form within many UV completions of theories with moduli dependent masses. It requires only that the masses of the flavors of both gauge groups are moduli dependent functions, and that all flavors become massless at a single point in moduli space, here defined to be  $\Phi = 0$ .

Importantly for the discussion of metastable dynamical supersymmetry breaking below, the superpotential (4.6) contains only marginal terms, so that any relevant mass scales must arise from dimensional transmutation. Generalizations to other gauge groups and matter contents in vector-like representations with the superpotential (4.6) are straightforward.

The classical moduli space for the theory (4.1) with superpotential (4.6) depends on the gauge group ranks and number of flavors. For  $\lambda = \lambda' = 0$  the moduli space is parameterized by  $\Phi$ , meson invariants  $M_{ij} = Q_i \bar{Q}_j$  and  $M'_{i'j'} = P_{i'} \bar{P}_{j'}$  and for  $N_f \geq N_c$  and/or  $N'_f \geq N'_c$  baryon and anti-baryon invariants  $B_{i_1 i_2 \dots i_{N_c}} = Q_{[i_1} Q_{i_2} \dots Q_{i_{N_c}]}$ ,  $\bar{B}_{i_1 i_2 \dots i_{N_c}} = \bar{Q}_{[i_1} \bar{Q}_{i_2} \dots \bar{Q}_{i_{N_c}]}$ , and/or  $B'_{i_1 i_2 \dots i_{N'_c}} = P_{[i_1} P_{i_2} \dots P_{i_{N'_c}]}$ ,  $\bar{B}'_{i_1 i_2 \dots i_{N'_c}} = \bar{P}_{[i_1} \bar{P}_{i_2} \dots \bar{P}_{i_{N'_c}]}$  respectively. For  $\lambda, \lambda' \neq 0$  the superpotential (4.6) lifts all the moduli parameterized by the mesons. The remaining moduli space has a branch parameterized by  $\Phi$ . For  $\Phi \neq 0$  the flavors are massive and the baryon and anti-baryon directions are lifted along this branch. For  $N_f \geq N_c$  and/or  $N'_f \geq N'_c$  there is a second branch of the moduli space parameterized by the baryons and anti-baryons with  $\Phi = 0$ . The two branches touch at the point where all the moduli vanish.

## 4.2.2 Supersymmetric Vacua

The classical moduli space of vacua is lifted by nonperturbative effects in the quantum theory. Since the metastable supersymmetry breaking vacua discussed below arise for  $\Phi \neq 0$ , only this branch of the moduli space will be considered in detail. On this branch, holomorphy, symmetries, and limits fix the exact superpotential written in terms of invariants, to be

$$\begin{aligned}
W = & \lambda \Phi \operatorname{Tr} M + (N_c - N_f) \left[ \frac{\Lambda^{3N_c - N_f}}{\det M} \right]^{1/(N_c - N_f)} \\
& + \lambda' \Phi \operatorname{Tr} M' + (N'_c - N'_f) \left[ \frac{\Lambda^{3N'_c - N'_f}}{\det M'} \right]^{1/(N'_c - N'_f)}
\end{aligned} \tag{4.8}$$

For gauge sectors in the free magnetic range, the nonperturbative contribution refers to the Seiberg dual. Since the meson invariants are lifted on this branch, they may be eliminated by equations of motion,  $\partial W / \partial M_{ij} = 0$  and  $\partial W / \partial M'_{i'j'} = 0$ , to give the exact superpotential in

terms of the classical modulus  $\Phi$

$$W = N_c [(\lambda\Phi)^{N_f} \Lambda^{3N_c - N_f}]^{1/N_c} + N'_c [(\lambda'\Phi)^{N'_f} \Lambda'^{3N'_c - N'_f}]^{1/N'_c}. \quad (4.9)$$

The supersymmetric minima are given by stationary points of the superpotential,  $\partial W/\partial\Phi = 0$ , for which

$$N_f [(\lambda\Phi)^{N_f} \Lambda^{3N_c - N_f}]^{1/N_c} + N'_f [(\lambda'\Phi)^{N'_f} \Lambda'^{3N'_c - N'_f}]^{1/N'_c} = 0. \quad (4.10)$$

Physically distinct supersymmetric vacua are distinguished by the expectation value of the superpotential.

### 4.2.3 Parameter ranges for the gauge sectors

Under mild assumptions we thus end up considering two SQCD sectors, characterized by  $(N_c, N_f, \Lambda)$  and  $(N'_c, N'_f, \Lambda')$ , respectively, and superpotential couplings (4.6). Different choices may be considered here; to restrict them, it is important to note that calculable quantum corrections can be generated in two different limits.

For  $\lambda_i\Phi \gg \Lambda_i$ , with  $\Lambda_i = \Lambda$  or  $\Lambda'$ , the corresponding gauge group is weakly coupled and hence generates small calculable corrections to the Kähler potential. Integrating out the massive quarks, for energies below  $\Phi$ , leads to gaugino condensation, which gives nonperturbative contributions as in (4.9).

On the other hand, for  $\lambda_i\Phi \ll \Lambda_i$ , the corresponding gauge sector becomes strongly coupled. The calculable case corresponds to having the gauge theory in the free magnetic range. For concreteness, we choose this sector to be  $SU(N_c)$  (the unprimed sector), so that  $N_c + 1 \leq N_f < \frac{3}{2}N_c$ .

For the  $(N'_c, N'_f, \Lambda')$  (primed) sector, the interesting case arises for  $N'_f < N'_c$  and  $\lambda'\Phi \gg \Lambda'$ . Although the classical superpotential pushes  $\Phi$  to zero, the primed dynamics generates a nonperturbative term which makes the potential energy diverge as  $\Phi \rightarrow 0$ , in agreement with the fact that  $\Phi = 0$  corresponds to an enhanced symmetry point where  $P$  and  $\bar{P}$  become massless. Balancing the primed and unprimed contributions leads to a runaway direction in moduli space

which will be lifted by one loop corrections. This stabilizes  $\Phi$  at a nonzero value. Calculability demands working in the energy range  $E \gg \Lambda'$  and  $E \ll \Lambda$  so the dynamically generated scales must satisfy  $\Lambda' \ll \Lambda$ .

The semiclassical limit corresponds to energies  $E \gg \Lambda, \Lambda'$ , where both sectors are weakly coupled. Since  $\Lambda' \ll \Lambda$ ,  $SU(N_c)$  confines first when flowing to the IR. For  $\Lambda' \ll E \ll \Lambda$ , the primed sector is weakly interacting while the unprimed sector has a dual weakly coupled description [35] in terms of the magnetic gauge group  $SU(\tilde{N}_c)$  with  $\tilde{N}_c = N_f - N_c$ ,  $N_f^2$  singlets  $M_{ij}$ , and  $N_f$  magnetic quarks  $(q_i, \tilde{q}_j)$ . In terms of this description, the full non-perturbative superpotential reads

$$\begin{aligned}
W = & m\Phi\text{tr}M + h\text{tr}qM\tilde{q} + \lambda'\Phi\text{tr}P\bar{P} + (N'_c - N'_f) \left( \frac{\Lambda'^{3N'_c - N'_f}}{\det P\bar{P}} \right)^{1/(N'_c - N'_f)} \\
& + (N_f - N_c) \left( \frac{\det M}{\tilde{\Lambda}^{3N_c - 2N_f}} \right)^{1/(N_f - N_c)}. \tag{4.11}
\end{aligned}$$

Hereafter,  $M_{ij} = Q_i\bar{Q}_j/\Lambda$ , and  $m := \lambda\Lambda$ . The magnetic sector has a Landau pole at  $\tilde{\Lambda} = \Lambda$ .

In this description, the meson  $M$  and the primed quarks  $(P, \bar{P})$  become massless at  $\Phi = 0$ .  $M = 0$  is also an enhanced symmetry point since here the magnetic quarks  $(q, \tilde{q})$  become massless.

### 4.3 Metastability near enhanced symmetry points

In this section, metastable vacua near the origin of moduli space will be shown to exist for the theory with superpotential (4.11). In Section 3.1, we analyze the branches of the moduli space and determine where Coleman-Weinberg effects may lift the runaway. Next, in 3.2, we focus on the region containing metastable vacua. In 3.3, we argue that other quantum corrections are under control and do not affect the stability of these vacua. Finally, in Section 3.4 the metastable vacua are shown to be parametrically long-lived.

### 4.3.1 Exploring the moduli space

Starting from the superpotential (4.11), the discussion is simplified by taking the limit  $\tilde{\Lambda} \rightarrow \infty$ , while keeping  $m$  fixed. The nonperturbative  $\det M$  term is only relevant for generating supersymmetric vacua, as discussed in (4.9), and not important for the details of the metastable vacua that will arise near  $M = 0$ . Thus, for  $M/\tilde{\Lambda} \rightarrow 0$  and  $\Phi/\tilde{\Lambda} \rightarrow 0$ , it is enough to consider the superpotential

$$W = m\Phi \operatorname{tr} M + h \operatorname{tr} qM\tilde{q} + \lambda'\Phi \operatorname{tr} P\bar{P} + (N'_c - N'_f) \left( \frac{\Lambda'^{3N'_c - N'_f}}{\det P\bar{P}} \right)^{1/(N'_c - N'_f)}. \quad (4.12)$$

In this limit all the fields are canonically normalized and the classical potential is

$$V = V_D + V'_D + \sum_a |W_a|^2 \quad (4.13)$$

where  $W_a = \partial_a W$ , and  $a$  runs over all the fields.  $V_D$  and  $V'_D$  are the usual D-term contributions from  $SU(\tilde{N}_c)$  and  $SU(N'_c)$ . Since both gauge sectors are weakly coupled, it is enough to consider the F-terms on the D-flat moduli space, parametrized by the chiral ring. This restriction has no impact on the analysis of the metastable vacua.

Let us study the regime  $P\bar{P} \rightarrow \infty$ . Then nonperturbative effects from  $SU(N'_c)$  may be neglected, and the classical superpotential

$$W_{cl} = m\Phi \operatorname{tr} M + h \operatorname{tr} qM\tilde{q} + \lambda'\Phi \operatorname{tr} P\bar{P} \quad (4.14)$$

is recovered. Setting

$$W_{M_{ij}} = m\Phi\delta_{ij} + hq_i\tilde{q}_j = 0, \quad (4.15)$$

we obtain  $\Phi = 0$  and  $hq\tilde{q} = 0$ . This implies  $W_{\operatorname{tr}P\bar{P}} = W_q = 0$ . The locus  $W_\Phi = 0$  then defines a classical moduli space of supersymmetric vacua.

Let us keep  $P\bar{P}$  large, but include the non-perturbative effects from  $SU(N'_c)$ . Then  $W_{\operatorname{tr}P\bar{P}} = 0$  sets  $P\bar{P} \rightarrow \infty$  and  $W_\Phi = 0$  implies  $M \rightarrow \infty$ . Therefore the model does not have a stable vacuum in the limit  $\tilde{\Lambda} \rightarrow \infty$ . As discussed above, for  $\tilde{\Lambda}$  finite and  $M$  large enough, the nonperturbative  $\det M$  term introduces supersymmetric vacua as in (4.9).

All the F-terms are small in the limit  $M \rightarrow \infty$ ,  $\Phi \rightarrow 0$ , which thus corresponds to  $M_{\bar{F}}^2 \gg |F|$ . The one-loop corrections give logarithmic dependences on the fields  $(\Phi, M)$  and these cannot stop the power-law runaway behavior.

Thus we are led to consider the region near the enhanced symmetry point  $M = 0$ . As we shall see below, this still has a runaway. Crucially, it turns out that one-loop corrections stop this runaway (this novel effect is characterized as a ‘pseudo-runaway’). The reason for this is that the Coleman-Weinberg formula [36]

$$V_{CW} = \frac{1}{64\pi^2} \text{Str } M^4 \ln M^2 \quad (4.16)$$

will have polynomial (instead of logarithmic) dependence. This will be explained next.

A global plot of the potential is provided in Fig. 4.1, where  $M$  has been expanded around zero as below in equation (3.8). In the graphic, the ‘drain’ towards the supersymmetric vacuum corresponds to the curve  $W_{\Phi} = 0$ .

### 4.3.2 Metastability Along the Pseudo-Runaway Direction

In the region  $\Phi \neq 0$ ,  $(P, \bar{P})$  may be integrated out by equations of motion provided that  $\Lambda' \ll \lambda' \Phi$ . This is a good description if we are not exactly at the origin but near it, as given by  $\Phi/\tilde{\Lambda} \ll 1$ . Taking, as before,  $\tilde{\Lambda} \rightarrow \infty$  and  $m$  fixed, the superpotential reads

$$W = m\Phi \text{tr } M + h \text{tr } qM\tilde{q} + N'_c [\lambda'^{N'_f} \Lambda'^{3N'_c - N'_f} \Phi^{N'_f}]^{1/N'_c}. \quad (4.17)$$

This description corresponds to an O’Raifeartaigh-type model in terms of magnetic variables but with no flat directions.

Given that  $\phi = \langle \Phi \rangle \neq 0$ , we will expand around the point of maximal symmetry

$$q = \begin{pmatrix} q_0 & 0 \end{pmatrix}, \quad \tilde{q} = \begin{pmatrix} \tilde{q}_0 \\ 0 \end{pmatrix}, \quad M = \begin{pmatrix} 0 & 0 \\ 0 & 0 + X \cdot I_{N_c \times N_c} \end{pmatrix}. \quad (4.18)$$

Here  $q_0$  and  $\tilde{q}_0$  are  $\tilde{N}_c \times \tilde{N}_c$  matrices satisfying

$$hq_{0i}\tilde{q}_{0j} = -m\phi \delta_{ij}, \quad i, j = \tilde{N}_c + 1, \dots, N_f, \quad (4.19)$$

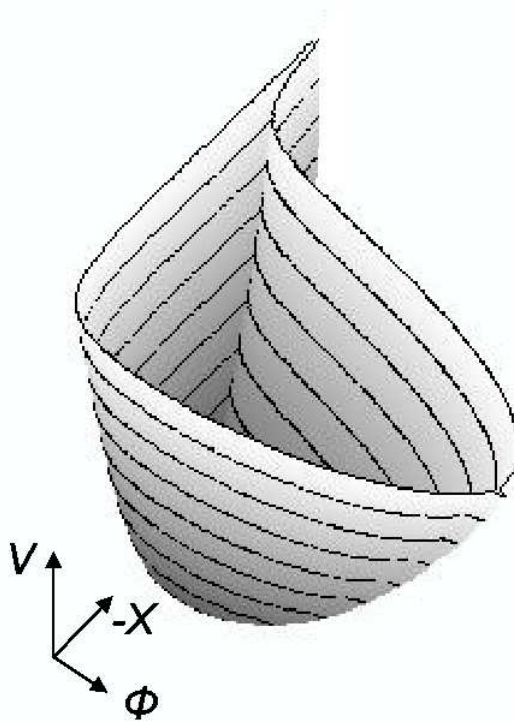


Figure 4.1: A plot showing the global shape of the potential.  $M$  has been expanded around zero as in equation (3.8). Note the runaway in the direction  $X \rightarrow -\infty$  and  $\phi \rightarrow 0$ . The singularity at  $\phi = 0$  and the “drain”  $W_\phi = 0$  are clearly visible. Also visible is the Coleman-Weinberg channel near  $X = 0$  and  $\phi$  large, discussed later. This plot was generated with the help of [37].

and the nonzero block matrix in  $M$  has been taken to be proportional to the identity; indeed, only  $\text{tr } M$  appears in the potential. This minimizes  $W_M$  and sets  $W_q = W_{\bar{q}} = 0$ . The spectrum of fluctuations around (4.18) is studied in detail in Section 4, where it is shown that the lightest degrees of freedom correspond to  $(\phi, X)$  with mass given by  $m$ . The effective potential derived from (4.17) is

$$V(\phi, X) = N_c m^2 |\phi|^2 + \left| m N_c X + N'_f \lambda'^{N'_f/N'_c} \left( \frac{\Lambda'^{3N'_c - N'_f}}{\phi^{N'_c - N'_f}} \right)^{1/N'_c} \right|^2 + V_{CW}(\phi, X), \quad (4.20)$$

where the second term comes from  $W_\phi$ . The Coleman-Weinberg contribution will be discussed shortly.

As a starting point, set  $X = 0$  and  $V_{CW} \rightarrow 0$ . Minimizing  $V(\phi, X = 0)$  gives

$$|\phi_0|^{(2N'_c - N'_f)/N'_c} = \sqrt{\frac{N'_c - N'_f}{N_c N'_c}} N'_f \frac{\lambda'^{N'_f/N'_c}}{m} \Lambda'^{(3N'_c - N'_f)/N'_c}, \quad (4.21)$$

and since  $W_{\phi\phi} \sim m$ ,  $V(\phi_0 + \delta\phi, X = 0)$  corresponds to a parabola of curvature  $m$ . The nonperturbative term only affects  $\phi_0$  but not the curvature  $m$ ; this will be important in the discussion of subsection 3.4.

Next, allowing  $X$  to fluctuate (but still keeping  $V_{CW} \rightarrow 0$ ),  $V(\phi_0, X)$  gives a parabola centered at

$$X_{W_\phi=0} = -\sqrt{\frac{N'_c}{N_c(N'_c - N'_f)}}|\phi_0| \quad (4.22)$$

and curvature  $m$ . In other words,  $X = 0$  is on the side of a hill of curvature  $m$  and height  $V(\phi_0, 0) \sim m^2|\phi_0|^2$ .

To create a minimum near  $X = 0$ ,  $V_{CW}$  should contain a term  $m_{CW}^2|X|^2$ , with  $m_{CW} \gg m$ ; this would overwhelm the classical curvature. As explained in Section 4, the massive degrees of freedom giving the dominant contribution to  $V_{CW}$  come from integrating out the massive fluctuations along  $q_0$  and  $\tilde{q}_0$ . The result is

$$V_{CW} = N_c b h^3 m |\phi| |X|^2 + \dots \quad (4.23)$$

with  $b = (\log 4 - 1)/8\pi^2 \tilde{N}_c$  [1], and ‘...’ represent contributions that are unimportant for the present discussion. In this computation,  $X$  and  $\phi$  are taken as background fields. It is crucial to notice that the quadratic  $X$  dependence appears because  $X = 0$  is an enhanced symmetry point.

In order to be able to produce a local minimum, the marginal parameters  $(\lambda, \lambda')$  will have to be tuned to satisfy

$$\epsilon \equiv \frac{m^2}{m_{CW}^2} = \frac{m}{b h^3 |\phi|} \ll 1. \quad (4.24)$$

In this approximation, the value of  $\phi$  at the minimum is still given by (4.21); also,  $X$  is stabilized at the nonzero value

$$X_0 = -e^{-i \frac{N'_c - N'_f}{N'_c} \alpha_\phi} \frac{N'_f}{b h^3} \lambda'^{N'_f/N'_c} \left( \frac{\Lambda'^{3N'_c - N'_f}}{|\phi_0|^{2N'_c - N'_f}} \right)^{1/N'_c}. \quad (4.25)$$

The phases of  $\phi$  and  $X$  are thus related by

$$\alpha_X + \frac{N'_c - N'_f}{N'_c} \alpha_\phi = \pi. \quad (4.26)$$

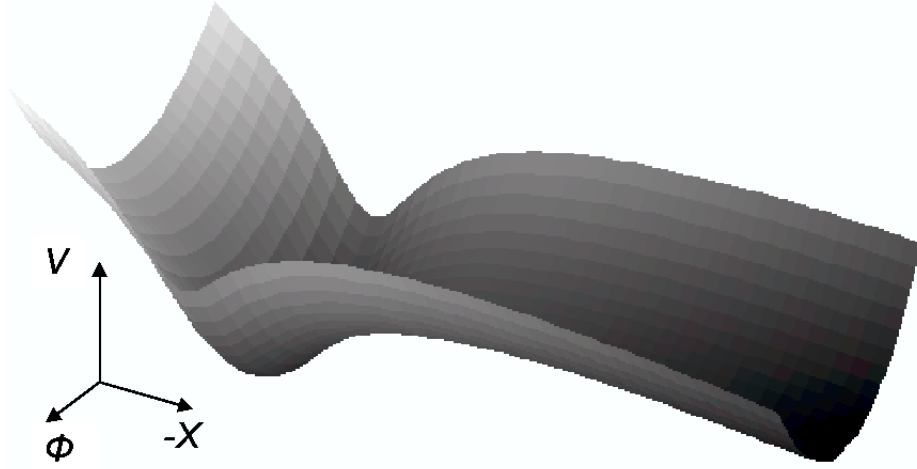


Figure 4.2: A plot showing the shape of the potential, including the one-loop Coleman-Weinberg corrections, near the metastable minimum. In the  $\phi$ -direction the potential is a parabola, whereas in the  $X$ -direction it is a side of a hill with a minimum created due to quantum corrections. This plot was generated with the help of [37].

Inserting (4.21) into (4.25) gives

$$|X_0| = \sqrt{\frac{N_c N'_c}{N'_c - N'_f} \frac{m}{bh^3}}. \quad (4.27)$$

At the minimum, (4.24) gives

$$(m/\Lambda')^{3N'_c - N'_f} \ll (bh^3)^{(2N'_c - N'_f)/N'_c} \lambda'^{N'_f} \quad (4.28)$$

so the Yukawa coupling  $\lambda$  in  $m = \lambda\Lambda$  must be taken small for the analysis to be self-consistent.

The calculability condition  $\Lambda' \ll \lambda'\Phi$  follows as a consequence of this. At the minimum,  $X_0 \ll \phi_0$ . The F-terms are given by

$$W_\phi \approx \sqrt{\frac{N_c N'_c}{N'_c - N'_f}} m \phi_0 \sim W_X. \quad (4.29)$$

and from (4.21) the scale of supersymmetry breaking is thus controlled by the dynamical scales of both gauge sectors. In the next subsection, the vacuum will be shown to be long-lived if (4.24) is satisfied.

Thus the model has a metastable vacuum near the origin, created by a combination of quantum corrections and nonperturbative gauge effects. The pseudo-runaway towards  $X = X_{W_\phi=0}$  has been lifted by the Coleman-Weinberg contribution, as anticipated. This is the origin of the  $1/b$  dependence in (4.27). The local minimum is depicted in Fig. 4.2.

### 4.3.3 Stability under other quantum corrections

The metastable vacuum appears from a competing effect between a runaway behavior in the primed sector and one loop corrections for the meson field  $X$ . One is naturally led to ask if, under these circumstances, other quantum effects are under control. These include higher loop terms from the massive particles producing  $V_{CW}$  as well as perturbative  $g'$  corrections.

Let us first study higher loop contributions from the massive fields in  $(q, \tilde{q})$ . They can correct the potential by additive terms of the form  $X^n$ ,  $n > 2$ ; these are automatically subleading, because  $|X_0|^2 \ll m|\phi_0|$ . They can also produce higher  $\phi$  powers. However, such quantum corrections can only depend on the combination  $m\phi$ , and thus will be suppressed by powers of the UV cutoff  $\Lambda_0$ . For instance, a quartic term would appear as  $(m\phi)^4/\Lambda_0^4$ . We conclude that all these effects are subleading to (4.23).

Furthermore, since nonperturbative effects from  $SU(N'_c)$  were used, we should make sure that perturbative  $g'$  effects are not important. First note that the nonperturbative term in (4.20) is of the same order as the classical height of the potential  $m^2|\phi|^2$  (see eq. (4.29)). It thus suffices to show that  $g'$  perturbative corrections to this height are subleading. A simple argument for this is as follows. Loops generate typical quartic terms in the Kähler potential

$$\delta K = \frac{\alpha}{\Lambda_0^2} (\Phi^* \Phi)^2 \quad (4.30)$$

which change the scalar potential by

$$\left[ \frac{\alpha}{\Lambda_0^2} |\phi|^2 \right] (m^2 |\phi|^2). \quad (4.31)$$

The prefactor is parametrically small, making these contributions negligible.

### 4.3.4 Tunneling Out of the Metastable Vacuum

This section will show that the metastable non-supersymmetric vacuum can be made parametrically long-lived by taking the parameter  $\epsilon \equiv \frac{m}{bh^3|\phi_0|}$  sufficiently small. The lifetime of the metastable vacuum may be estimated using semiclassical techniques and is proportional to the exponential of the bounce action,  $e^B$  [38].

First, the direction of tunneling in field space needs to be determined. Recall that the metastable vacuum in the  $(|\phi|, X)$  space lies at

$$|\phi_0|^{\frac{2N'_c - N'_f}{N'_c}} = \sqrt{\frac{N'_c - N'_f}{N_c N'_c}} N'_f \frac{\lambda'^{\frac{N'_f}{N'_c}}}{m} \Lambda'^{\frac{3N'_c - N'_f}{N'_c}}, \quad X_0 = -\sqrt{\frac{N_c N'_c}{N'_c - N'_f}} \frac{m}{bh^3}. \quad (4.32)$$

(The phase of  $\phi$ , not of qualitative importance for the present discussion, has been chosen to be zero. This fixes  $X$  to be real - see equation (4.26).) For fixed  $X$  the potential has a minimum at  $|\phi| = |\phi_0|$ ; while quantum corrections may change this value by an order one number, corrections to the curvature of the potential in the  $|\phi|$  direction are negligible. This curvature is positive, and thus the potential increases as  $|\phi|$  moves away from  $|\phi_0|$ . The field therefore does not tunnel in the  $|\phi|$  direction (see (4.2)). Along the  $X$  direction, however, the potential without quantum corrections near the enhanced symmetry point is like the side of a hill. For fixed  $|\phi| = |\phi_0|$ , the potential decreases in the negative  $X$  direction, and the classical curvature at  $X = 0$  is  $m$ .

Quantum corrections are qualitatively important when  $|X|$  is sufficiently small. For  $|X|^2 \ll |W_X|$ , their size grows quadratically as a function of  $X$  and they are sufficient to change the slope of the classical potential enough to introduce a minimum. For  $|X|^2 \simeq |W_X|$ , the growth of the quantum corrections is only logarithmic, and the slope of the classical potential again starts to dominate. Hence, the total potential has a peak that parametrically may be estimated to lie near

$$X_{\text{peak}} \simeq -\sqrt{|W_X|} = -\sqrt{N_c m |\phi_0|}. \quad (4.33)$$

For  $|X| > |X_{\text{peak}}|$ , the potential decreases as  $X$  becomes more negative until  $X$  reaches the ‘drain’  $W_\phi = 0$ ,

$$X_{W_\phi=0} = -\sqrt{\frac{N'_c}{N_c(N'_c - N'_f)}} |\phi_0|. \quad (4.34)$$

The direction in field space to tunnel out of the false vacuum is towards negative  $X$  with fixed  $|\phi| = |\phi_0|$ . It thus suffices to consider the tunneling in the one-dimensional potential,  $V(X) \equiv V(|\phi_0|, X)$ . Note that parametrically  $|X_0| \ll |X_{\text{peak}}| \ll |X_{W_\phi=0}|$  as  $\epsilon \rightarrow 0$ .

For negative  $X$ , using equations (4.20) and (4.32), the one-dimensional potential may be written as

$$V(X) = \left( \frac{2N'_c - N'_f}{N'_c - N'_f} \right) N_c m^2 |\phi_0|^2 + N_c^2 b h^3 m^2 |\phi_0|^2 f\left(\frac{-|X|}{b h^3 |\phi_0|}\right). \quad (4.35)$$

In the region  $|X| \ll |X_{\text{peak}}|$ , the function  $f(x)$  is dominated by quantum corrections and may be approximated by

$$f(x) \simeq \frac{b h^3}{N_c \epsilon} x^2, \quad (4.36)$$

where a constant piece coming from the quantum corrections, again not important for the calculation of the bounce action, has been neglected. On the other hand, in the region  $|X_{\text{peak}}| \ll |X| \ll |X_{W_\phi=0}|$ , the constant slope of the classical potential dominates. The potential in this region may be approximated by the classical potential plus a constant contribution from the quantum corrections whose size is roughly given by the height of the potential barrier. The height of the potential barrier is, from (4.36), of order  $f(X_{\text{peak}}/b h^3 |\phi_0|) = 1$ , and it is thus loop-suppressed compared to the overall magnitude of the potential near the metastable minimum. The potential in this region will be parametrized by a straight line

$$f(x) \simeq 1 - 2 \sqrt{\frac{N'_c}{N_c(N'_c - N'_f)}} (x - x_{\text{peak}}). \quad (4.37)$$

In order to estimate the bounce action it is not appropriate to use the thin-wall approximation [38]. Instead, the potential may be modeled as a triangular barrier [39]. Using the results of [39], the value to which the field tunnels to is

$$\tilde{X} \sim -b h^3 |\phi_0|. \quad (4.38)$$

Note that parametrically  $|X_0| \ll |X_{\text{peak}}| \ll |\tilde{X}|$  as  $\epsilon \rightarrow 0$ , and that  $|\tilde{X}|$  is loop-suppressed compared to  $|X_{W_\phi=0}|$ . The bounce action scales as

$$B \sim \frac{\tilde{X}^4}{V(X_{\text{peak}}) - V(X_0)} \sim b h^3 \frac{1}{\epsilon^2}. \quad (4.39)$$

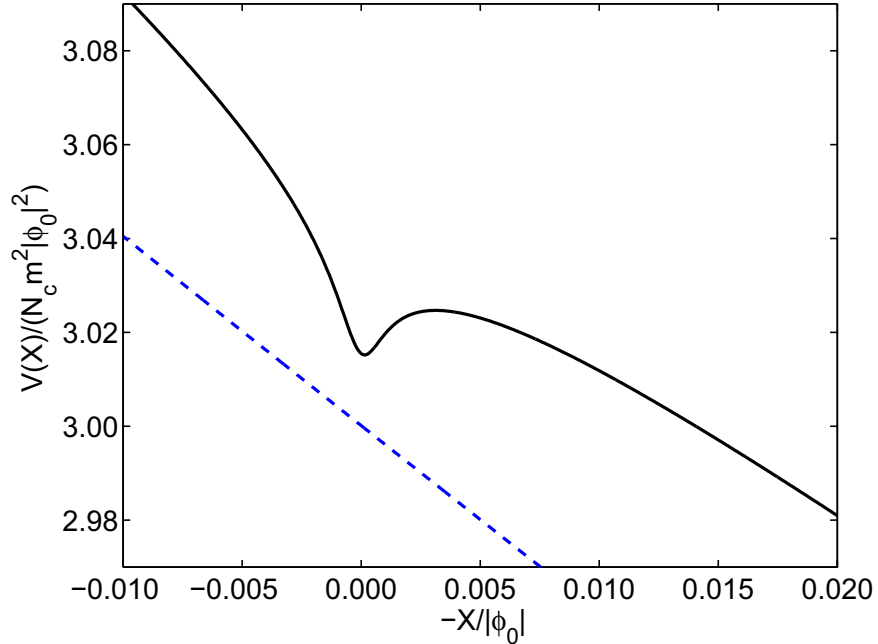


Figure 4.3: A plot of the classical potential (dashed line) and the total potential including one-loop corrections (solid line) for fixed  $|\phi| = |\phi_0|$ , where  $|\phi_0|$  is the position of the metastable minimum in the  $\phi$ -direction, defined in (4.32). In the figure,  $N_f = 3$ ,  $N_c = 2$ ,  $N'_f = 1$  and  $N'_c = 2$ . The values were scaled so that the position of the “drain”,  $W_\phi = 0$ , equals 1 on both axes. In these units, the position of the metastable minimum is on the order of  $10^{-4}$ . This plot was generated with the help of [37].

Therefore  $B \rightarrow \infty$  as  $\epsilon \rightarrow 0$ , and the metastable vacuum is parametrically long-lived.

The total potential  $V(X)$ , including the full one-loop Coleman-Weinberg potential computed numerically with the help of [37], is shown in Fig. 4.3. The program of [37] also allowed us to check numerically the previous tunneling properties.

#### 4.4 Particle Spectrum and R-symmetry

In this section, we discuss in more detail the particle spectrum of the model and comment on the R-symmetry properties.

The fluctuations of the fields around the metastable minimum may be parametrized following ISS,

$$\phi = \phi_0 + \delta\phi, \quad M = \begin{pmatrix} Y_{\tilde{N}_c \times \tilde{N}_c} & Z_{\tilde{N}_c \times (N_f - \tilde{N}_c)}^T \\ \tilde{Z}_{(N_f - \tilde{N}_c) \times \tilde{N}_c} & X_0 + X_{(N_f - \tilde{N}_c) \times (N_f - \tilde{N}_c)} \end{pmatrix} \quad (4.40)$$

	Fermions			Bosons		
	Weyl mult.	mass <sup>2</sup>	$U(N_f - 1)$	Real mult.	mass <sup>2</sup>	$U(N_f - 1)$
$\phi, \text{tr}X$	2	$\mathcal{O}(m^2)$	$1_0$	1 3	0 $\mathcal{O}(m^2)$	$1_0$ $1_0$
$X_{ij} - \text{tr}X$	$(N_f - 1)^2 - 1$	0	Adj <sub>0</sub>	$2((N_f - 1)^2 - 1)$	0	Adj <sub>0</sub>
$Y, \chi, \tilde{\chi}$	1	0	$1_0$	1 1 4	$0_{\text{GB}}$ $0_{\text{NCGB}}$ $\mathcal{O}(hm \phi_0 )$	$1_0$ $1_0$ $1_0$
$Z, \tilde{Z}, \rho, \tilde{\rho}$	$2(N_f - 1)$	$\mathcal{O}(hm \phi_0 )$	$\square_1 + \overline{\square}_{-1}$	$2(N_f - 1)$ $2(N_f - 1)$ $2(N_f - 1)$ $2(N_f - 1)$	$0_{\text{GB}}$ $\mathcal{O}(hm \phi_0 )$ $\mathcal{O}(hm \phi_0 )$ $\mathcal{O}(hm \phi_0 )$	$\square_1$ $\overline{\square}_{-1}$ $(\square_1 + \overline{\square}_{-1})$ $\overline{\square}_{-1}$

Figure 4.4: Table showing the classical mass spectrum, grouped in sectors of  $\text{Str} M^2 = 0$  for  $N_f = N_c + 1$ . The  $\mathcal{O}(m^2)$  fields in  $(\phi, \text{tr} X)$  are not degenerate. Although supersymmetry is spontaneously broken, there is no goldstino at the classical level.

$$q = \begin{pmatrix} q_0 + \chi_{\tilde{N}_c \times \tilde{N}_c} \\ \rho_{(N_f - \tilde{N}_c) \times \tilde{N}_c} \end{pmatrix}, \quad \tilde{q} = \begin{pmatrix} \tilde{q}_0 + \tilde{\chi}_{\tilde{N}_c \times \tilde{N}_c} \\ \tilde{\rho}_{(N_f - \tilde{N}_c) \times \tilde{N}_c} \end{pmatrix}, \quad (4.41)$$

where  $q_0 \tilde{q}_0 := -m\phi_0/h$ . All fields are complex;  $\phi_0$  and  $X_0$  are the values at the metastable minimum.

The relevant mass scales are

$$M^2 = 0, \quad m^2, \quad m_{CW}^2 = bh^3 m|\phi_0|, \quad hm|\phi_0|. \quad (4.42)$$

The particles may be divided into three ‘sectors’ with small mixing amongst themselves. Up to quadratic order, the superpotential is

$$\begin{aligned} W = & W_{\phi\phi} \delta\phi\delta\phi + mN_c \delta\phi(X_0 + X) + m\delta\phi \sum_{\alpha=1}^{\tilde{N}_c} Y_{\alpha\alpha} \\ & + mN_c \phi_0(X_0 + X) + h \sum_{f=1}^{N_c} [q_0 (\tilde{\rho} Z^T)_{ff} + \tilde{q}_0 (\rho \tilde{Z}^T)_{ff} + X_0 (\rho \tilde{\rho}^T)_{ff}] \\ & + h \sum_{\alpha=1}^{\tilde{N}_c} [q_0 (\tilde{\chi} Y)_{\alpha\alpha} + \tilde{q}_0 (\chi Y)_{\alpha\alpha}]. \end{aligned} \quad (4.43)$$

The first line is related to the new dynamical field  $\delta\phi$ ; unlike ISS, now  $X$  is not a pseudo-flat direction. The second and third lines are as in ISS.

Consider the case  $N_f = N_c + 1$ ; the spectrum of classical masses is shown in Fig. 4.4, and the spectrum of the masses including one-loop CW corrections is shown in Fig. 4.5. The fields are grouped in sectors of  $\text{STr} M^2 = 0$ .

	Fermions			Bosons		
	Weyl mult.	mass <sup>2</sup>	$U(N_f - 1)$	Real mult.	mass <sup>2</sup>	$U(N_f - 1)$
$\phi, \text{tr} X$	1 1	0 $\mathcal{O}(m^2)$	$1_0$ $1_0$	1 1 2	0 $\mathcal{O}(m^2)$ $\mathcal{O}(m_{CW}^2)$	$1_0$ $1_0$ $1_0$
$X_{ij} - \text{tr} X$	$(N_f - 1)^2 - 1$	0	Adj <sub>0</sub>	$2((N_f - 1)^2 - 1)$	$\mathcal{O}(m_{CW}^2)$	Adj <sub>0</sub>
$Y, \chi, \tilde{\chi}$	1 2	0 $\mathcal{O}(hm \phi_0 )$	$1_0$ $1_0$	1 1 4	$0_{\text{GB}}$ $\mathcal{O}(m_{CW}^2)$ $\mathcal{O}(hm \phi_0 )$	$1_0$ $1_0$ $1_0$
$Z, \tilde{Z}, \rho, \tilde{\rho}$	$2(N_f - 1)$ $2(N_f - 1)$	$\mathcal{O}(hm \phi_0 )$ $\mathcal{O}(hm \phi_0 )$	$\square_1 + \bar{\square}_{-1}$ $\square_1 + \bar{\square}_{-1}$	$2(N_f - 1)$ $2(N_f - 1)$ $2(N_f - 1)$ $2(N_f - 1)$	$0_{\text{GB}}$ $\mathcal{O}(hm \phi_0 )$ $\mathcal{O}(hm \phi_0 )$ $\mathcal{O}(hm \phi_0 )$	$\square_1$ $\bar{\square}_{-1}$ $(\square_1 + \bar{\square}_{-1})$ $\bar{\square}_{-1}$

Figure 4.5: Table showing the mass spectrum, including one-loop corrections, grouped in sectors of  $\text{Str } M^2 = 0$  for  $N_f = N_c + 1$ . Notice the appearance of the goldstino in the  $(\phi, \text{tr} X)$  sector. The  $\mathcal{O}(m^2)$  fields in  $(\phi, \text{tr} X)$  are not degenerate; here  $m_{CW}^2 = bh^3m|\phi_0|$ .

	Fermions				Bosons			
	Weyl mult.	mass <sup>2</sup>	$U(N_f - \tilde{N}_c)$	$SU(\tilde{N}_c)_D$	Real mult.	mass <sup>2</sup>	$U(N_f - \tilde{N}_c)$	$SU(\tilde{N}_c)_D$
$\phi, \text{tr} X$	2	$\mathcal{O}(m^2)$	$1_0$	1	1 3	0 $\mathcal{O}(m^2)$	$1_0$ $1_0$	1 1
$X_{ij} - \text{tr} X$	$(N_f - \tilde{N}_c)^2 - 1$	0	Adj <sub>0</sub>	1	$2((N_f - \tilde{N}_c)^2 - 1)$	0	Adj <sub>0</sub>	1
$Y, \chi, \tilde{\chi}$	$\tilde{N}_c^2$ $2\tilde{N}_c^2$	0 $\mathcal{O}(hm \phi_0 )$	$1_0$ $1_0$	Adj Adj	$\tilde{N}_c^2$ $\tilde{N}_c^2$ $4\tilde{N}_c^2$	$0_{\text{GB}}$ $0_{\text{NCGB}}$ $\mathcal{O}(hm \phi_0 )$	$1_0$ $1_0$ $1_0$	Adj Adj Adj
$Z, \tilde{Z}, \rho, \tilde{\rho}$	$2\tilde{N}_c(N_f - \tilde{N}_c)$ $2\tilde{N}_c(N_f - \tilde{N}_c)$	$\mathcal{O}(hm \phi_0 )$ $\mathcal{O}(hm \phi_0 )$	$\square_1 + \bar{\square}_{-1}$ $\square_1 + \bar{\square}_{-1}$	$\square + \bar{\square}$ $\square + \bar{\square}$	$2\tilde{N}_c(N_f - \tilde{N}_c)$ $2\tilde{N}_c(N_f - \tilde{N}_c)$ $2\tilde{N}_c(N_f - \tilde{N}_c)$ $2\tilde{N}_c(N_f - \tilde{N}_c)$	$0_{\text{GB}}$ $\mathcal{O}(hm \phi_0 )$ $\mathcal{O}(hm \phi_0 )$ $\mathcal{O}(hm \phi_0 )$	$\square_1$ $\bar{\square}_{-1}$ $(\square_1 + \bar{\square}_{-1})$ $\bar{\square}_{-1}$	$\square$ $\square$ $(\bar{\square} + \square)$ $\square$

Figure 4.6: Table showing the classical mass spectrum, grouped in sectors of  $\text{Str } m^2 = 0$ , for  $N_f > N_c + 1$ . After gauging  $SU(\tilde{N}_c)$ , the traceless goldstone bosons from  $(\chi, \tilde{\chi})$  are eaten, giving a mass  $m_W^2 = g^2m|\phi_0|/h$  to the gauge bosons. Further, from  $V_D = 0$ , the noncompact goldstones also acquire a mass  $m_W^2$ . Including CW corrections,  $\text{tr} X$  acquires mass  $m_{CW}^2$  and one of the fermions becomes massless.

The fields  $(Y, \chi, \tilde{\chi})$  form three chiral superfields, with supersymmetric masses, and hence do not contribute when integrated out at one loop. The Coleman-Weinberg potential is generated by the fields  $(Z, \tilde{Z}, \rho, \tilde{\rho})$ , which are the heaviest in the spectrum. Including such quantum corrections,  $\text{tr} X$  acquires a mass  $m_{CW}^2$ , while the mass of  $\phi$  is not modified. Interestingly, at the classical level there is no massless goldstino, since the expansion is not around a critical point of the classical potential. Including quantum corrections, one of the massive fermions in the  $(\phi, \text{tr} X)$ -sector becomes massless, as may be seen in Fig. 4.5. A similar situation, in the opposite limit of small supersymmetry breaking, has been discussed recently in [40].

The case  $\tilde{N}_c = N_f - N_c > 1$  can be similarly analyzed, and is shown in Fig. 4.6.

The Standard Model gauge group can be embedded inside the global symmetry group of this model. In this way, renormalizable models of direct gauge mediated supersymmetry breaking may be constructed.

#### 4.4.1 Breaking the R-symmetry

To have gaugino masses, any R-symmetry must be broken, explicitly and/or spontaneously [1], [40]. The low energy superpotential 4.17 has the following  $U(1)_R$  symmetry:

$$R_\phi = 2\frac{N'_c}{N'_f}, \quad R_X = 2\frac{N'_f - N'_c}{N'_f}, \quad R_q = R_{\bar{q}} = \frac{N'_c}{N'_f}. \quad (4.44)$$

Since the VEV's of these fields are nonzero in the metastable vacuum, the R-symmetry is spontaneously broken, and there is an R-axion  $a$ . In terms of the phase of the  $i$ -th field, the axion is

$$\phi_i = \frac{1}{\sqrt{2}} \frac{f_R}{R_i} e^{iR_i(a/f_R)}, \quad (4.45)$$

where the decay constant  $f_R$  is defined as

$$f_R = \left[ \sum_i (\sqrt{2}R_i|\langle\phi_i\rangle|)^2 \right]^{1/2} \quad (4.46)$$

and  $R_i$  is the R-charge of  $\phi_i$ . In [6] it was pointed out that if R-symmetry is broken spontaneously in an O' Raifeartaigh model, then the theory should contain a field with R-charge different than 0 or 2. This is also the case in the present situation, although our model does not contain the linear O' Raifeartaigh term.

For finite  $\tilde{\Lambda}$ , the det  $X$  contributions need to be taken into account, and the  $U(1)_R$  symmetry becomes anomalous. Adding this term induces a tadpole for  $Y$ , which now acquires an expectation value of order

$$Y \sim \left[ \frac{X_0}{\tilde{\Lambda}} \right]^{\frac{3N_c - 2N_f}{N_f - N_c}} X_0, \quad (4.47)$$

so that  $|Y| \ll |X_0|$ . Then the mass of the R-axion follows from

$$|W_X|^2 \sim \left| m\phi + cX_0^2 \left[ \frac{X_0}{\tilde{\Lambda}} \right]^{\frac{3N_c - 2N_f}{N_f - N_c}} \right|^2. \quad (4.48)$$

Deriving twice the cross-term, which is proportional to  $\cos(a/f)$ , yields the axion mass

$$m_a^2 \sim m^2 \left( \left[ \frac{\lambda}{bh^3} \right]^2 \frac{3N_c - 2N_f}{N_f - N_c} \frac{\epsilon}{bh^3} \right) \ll m^2, \quad (4.49)$$

where  $\lambda$  is the Yukawa coupling appearing in  $m = \lambda\Lambda$ . Thus, R-symmetry is both spontaneously and explicitly broken.

## 4.5 Meta-Stability Near Generic Points of Enhanced Symmetry

In this section, the existence and genericity of metastable vacua near enhanced symmetry points is explored. Statistical analyses of the supersymmetry breaking scale up to date have not taken into account loop quantum effects ([28], [29], [30]) as these corrections are hard to evaluate on an ensemble of field theories. However, metastable vacua introduced by the Coleman-Weinberg potential, with all the relevant parameters generated dynamically, may change such results. Before considering the general case, let us analyze (4.5).

### 4.5.1 Non-coincident enhanced symmetry points

Consider two gauge sectors as in (4.5), with enhanced symmetry points at  $\Phi = 0$  and  $\Phi = \xi$ , respectively. The free magnetic sector is taken to be massless at  $\Phi = 0$ ; integrating over the other primed sector gives

$$W = m\Phi \operatorname{tr} M + h \operatorname{tr} qM\tilde{q} + N'_c [\lambda'^{N'_f} \Lambda'^{3N'_c - N'_f} (\Phi + \xi)^{N'_f}]^{1/N'_c}. \quad (4.50)$$

Since metastable vacua were shown to exist for  $\xi = 0$ , here the discussion is restricted to the limit of  $\xi$  much bigger than all the energy scales in the problem. This is consistent with the fact that naturalness demands any relevant coupling to be of order the UV cutoff.

Introducing the notation

$$\alpha = N'_f/N'_c, \quad K = N'_c \lambda'^{N'_f/N'_c} \Lambda'^{(3N'_c - N'_f)/N'_c}, \quad (4.51)$$

the equations of motion for  $\phi$  and  $X$  give

$$N_c m^2 \phi = \alpha^2 (1 - \alpha) \frac{K^2}{\xi^{3-2\alpha}}. \quad (4.52)$$

$$|X| = \frac{N_c}{\alpha(1-\alpha)} \frac{m^2 \xi^{2-\alpha}}{K}. \quad (4.53)$$

Without fine-tuning  $m$  or  $K$ ,  $X$  tends to be driven away from the origin as  $\xi$  increases. The fine-tuning may be seen, for instance, from the requirement  $m_{CW} \gg m$ , which implies

$$m^3 \ll bh^3 \frac{K^2}{\xi^{3-2\alpha}}. \quad (4.54)$$

Although this resembles the calculability condition (4.28), now there are powers of the large scale  $\xi$  in the denominator. For  $\xi$  of order the UV cutoff, this represents a big fine-tuning, either on the coefficient  $K$  or on the small mass parameter  $m$ .

The conclusion is that, while metastable vacua can occur for far away enhanced symmetry points, this situation is not generic and requires fine-tuning. This is to be expected, once relevant parameters are allowed to appear in the superpotential.

#### 4.5.2 General Analysis

A generic structure in the landscape of effective field theories corresponds to a gauge theory with vector-like matter and mass given by a singlet, whose dynamics is related to another sector. The superpotential may be written as

$$W = f(\Phi) + \lambda \Phi \text{tr}(Q\bar{Q}). \quad (4.55)$$

Here,  $(Q, \bar{Q})$  are  $N_f$  quarks in  $SU(N_c)$  SQCD;  $f(\Phi)$  may be generated, for instance, from a flux superpotential, by nonrenormalizable interactions [7], or, as in the case studied in this work, by another gauge sector. Next, it is required that the SQCD sector be in the free magnetic range; this is still a generic situation. The dual magnetic description is weakly coupled near the enhanced symmetry point  $\Phi = 0$ , where the superpotential reads

$$W = f(\Phi) + m\Phi \text{tr} M + h \text{tr} qM\tilde{q}. \quad (4.56)$$

The question that will be addressed here is: what restrictions need to be imposed on  $f(\Phi)$ , so that the one loop potential  $V_{CW}$  can create a metastable vacuum near  $M = 0$ ? Since we are

interested in the novel effect of pseudo-runaway directions we will demand  $f'(\Phi) \neq 0$ . The case  $f'(\Phi) = 0$  is standard in such analyses, see e.g. [33].

As discussed in Section 3, this is possible only if

$$m_{CW}^2 := N_c b h^3 m |\phi| \gg m^2 \quad (4.57)$$

where  $\phi$  denotes the expectation value of  $\Phi$  at the metastable vacuum. Further, one needs to impose that

$$h^2 |X|^2 \ll m |\phi| \quad (4.58)$$

in order for the Taylor expansion of  $V_{CW}$  around  $X = 0$  to converge. Evaluating the potential as in (4.20),

$$V = N_c m^2 |\phi|^2 + |f'(\phi) + m N_c X|^2 + m_{CW}^2 |X|^2. \quad (4.59)$$

The rank condition, an essential ingredient in the discussion, just follows from having SQCD in the free magnetic range. This fixes the first term, which comes from  $W_M$ , and the block structure of the matrix  $M$ ;  $X$  was defined in (4.18).

Extremizing  $V(\phi, X = 0)$  leads to

$$N_c m^2 \phi = -f'(\phi) f''(\phi)^*. \quad (4.60)$$

On the other hand, minimization with respect to  $X$  in the approximation  $m_{CW}^2 \gg m^2$ , gives the metastable vacuum

$$m_{CW}^2 X = -N_c m f'(\phi). \quad (4.61)$$

Notice that  $m_{CW}^2 \gg m^2$  makes this value parametrically smaller than the position of the ‘drain’  $f'(\phi) + m N_c X = 0$ . This ensures the stability of the nonsupersymmetric vacuum. Replacing (4.60) in (4.61) (with  $m_{CW}^2 = N_c b h^3 |\phi|$ ) yields

$$|X| = \frac{N_c m^2}{b h^3} \frac{1}{|f''(\phi)|}. \quad (4.62)$$

It is possible to combine the conditions (4.57) and (4.58) with the values at the metastable vacuum (4.60), (4.62), to derive constraints on  $f(\phi)$ : (4.57) now reads

$$\frac{|f'(\phi) f''(\phi)|}{m^3} \gg \frac{1}{b h^3}, \quad (4.63)$$

while (4.58) gives

$$h^2|f'(\phi)|^2 \ll m(bh^3)^2|\phi|^3. \quad (4.64)$$

Summarizing, the necessary conditions to have metastable vacua near  $X = 0$  are (4.63) and (4.64). As illustrated in §4.5.1, they require fine-tuning the coefficients of  $f(\phi)$ , except in the case of coincident enhanced symmetry points, where there are no relevant scales.

## 4.6 Conclusions

We constructed a model with long-lived metastable vacua in which all the relevant parameters, including the supersymmetry breaking scale, are generated dynamically by dimensional transmutation. The model consists of two  $N = 1$  supersymmetric QCD sectors with flavors whose respective masses are controlled by the same singlet field. One of the gauge sectors is in the free magnetic range while the other is in the electric range. The metastable vacua are produced near a point of enhanced symmetry by a combination of nonperturbative gauge effects and, crucially, perturbative effects coming from the one-loop Coleman-Weinberg potential.

The model has the following desirable features: an explicitly and spontaneously broken  $R$ -symmetry, a singlet, a large global symmetry, naturalness and renormalizability.

There are two points that have to be stressed. First, a salient feature of the model is the existence of pseudo-runaway directions. They correspond to a runaway behavior that is lifted by one loop quantum corrections. This has not been observed before, the closest analog corresponding for example to the pseudo-moduli of [1]. It is quite plausible that this phenomenon appears in other models as well. The criterion is that the height of the potential has to be parametrically larger than the curvature, as quantified in Section 3. The strength of the quadratic Coleman-Weinberg corrections is set by this height, thus introducing a local minimum of high curvature in the (otherwise) runaway potential.

In dynamical supersymmetry breaking models ([41], [42], [43], [44], [45], [46]), nonsupersymmetric vacua generally arise due to competing effects between a nonperturbative runaway and a classical term in the superpotential, as in the (3,2) model [47]. Our analysis shows that it is

possible to stabilize such runaways even without tree-level terms, provided that one is close to certain enhanced symmetry points.

The second feature worth emphasizing is the connection between enhanced symmetry points in gauge theory moduli spaces and metastable dynamical supersymmetry breaking. There are reasons to believe that such vacua are generic. At the field theory level this is associated to the fact that a nonzero Witten index [48] may still allow an approximate R-symmetry [49]. While dynamical ISS models are not hard to construct, in general these mechanisms involve discrete R-symmetries [7]. This is very suppressed in the landscape of string vacua, corresponding to a high codimension locus in the flux lattice [50]. On the other hand, the construction presented here does not suffer from the previous difficulty. Therefore, it would be interesting to study how statistical estimates of the scale of supersymmetry breaking change, once the model is embedded in string theory.

## References

- [1] K. Intriligator, N. Seiberg, and D. Shih, “Dynamical SUSY breaking in meta-stable vacua,” *JHEP* **04** (2006) 021, [hep-th/0602239](#).
- [2] O. Aharony and N. Seiberg, “Naturalized and simplified gauge mediation,” *JHEP* **02** (2007) 054, [hep-ph/0612308](#).
- [3] M. Dine and J. Mason, “Gauge mediation in metastable vacua,” *Phys. Rev.* **D77** (2008) 016005, [hep-ph/0611312](#).
- [4] R. Kitano, H. Ooguri, and Y. Ookouchi, “Direct mediation of meta-stable supersymmetry breaking,” *Phys. Rev.* **D75** (2007) 045022, [hep-ph/0612139](#).
- [5] D.-E. Diaconescu, B. Florea, S. Kachru, and P. Svrcek, “Gauge - mediated supersymmetry breaking in string compactifications,” *JHEP* **02** (2006) 020, [hep-th/0512170](#).
- [6] D. Shih, “Spontaneous R-symmetry breaking in O’Raifeartaigh models,” *JHEP* **02** (2008) 091, [hep-th/0703196](#).
- [7] M. Dine, J. L. Feng, and E. Silverstein, “Retrofitting O’Raifeartaigh models with dynamical scales,” *Phys. Rev.* **D74** (2006) 095012, [hep-th/0608159](#).
- [8] A. Amariti, L. Girardello, and A. Mariotti, “Non-supersymmetric meta-stable vacua in SU(N) SQCD with adjoint matter,” *JHEP* **12** (2006) 058, [hep-th/0608063](#).
- [9] T. Banks, “Remodeling the pentagon after the events of 2/23/06,” [hep-ph/0606313](#).
- [10] T. Banks, “Cosmological supersymmetry breaking and the power of the pentagon: A model of low energy particle physics,” [hep-ph/0510159](#).
- [11] T. Banks, S. Echols, and J. L. Jones, “Baryogenesis, dark matter and the pentagon,” *JHEP* **11** (2006) 046, [hep-ph/0608104](#).
- [12] A. Giveon and D. Kutasov, “Gauge symmetry and supersymmetry breaking from intersecting branes,” *Nucl. Phys.* **B778** (2007) 129–158, [hep-th/0703135](#).
- [13] M. Aganagic, C. Beem, J. Seo, and C. Vafa, “Geometrically induced metastability and holography,” *Nucl. Phys.* **B789** (2008) 382–412, [hep-th/0610249](#).
- [14] H. Ooguri and Y. Ookouchi, “Meta-stable supersymmetry breaking vacua on intersecting branes,” *Phys. Lett.* **B641** (2006) 323–328, [hep-th/0607183](#).
- [15] S. Franco, I. Garcia-Etxebarria, and A. M. Uranga, “Non-supersymmetric meta-stable vacua from brane configurations,” *JHEP* **01** (2007) 085, [hep-th/0607218](#).
- [16] S. B. Giddings, S. Kachru, and J. Polchinski, “Hierarchies from fluxes in string compactifications,” *Phys. Rev.* **D66** (2002) 106006, [hep-th/0105097](#).
- [17] S. Kachru, R. Kallosh, A. Linde, and S. P. Trivedi, “De Sitter vacua in string theory,” *Phys. Rev.* **D68** (2003) 046005, [hep-th/0301240](#).

- [18] M. R. Douglas, J. Shelton, and G. Torroba, “Warping and supersymmetry breaking,” [arXiv:0704.4001 \[hep-th\]](#).
- [19] C. P. Burgess *et al.*, “Warped supersymmetry breaking,” [hep-th/0610255](#).
- [20] S. Kachru, J. Pearson, and H. L. Verlinde, “Brane/flux annihilation and the string dual of a non-supersymmetric field theory,” *JHEP* **06** (2002) 021, [hep-th/0112197](#).
- [21] D.-E. Diaconescu, A. Garcia-Raboso, and K. Sinha, “A D-brane landscape on Calabi-Yau manifolds,” *JHEP* **06** (2006) 058, [hep-th/0602138](#).
- [22] D.-E. Diaconescu, A. Garcia-Raboso, R. L. Karp, and K. Sinha, “D-brane superpotentials in Calabi-Yau orientifolds (projection),” [hep-th/0606180](#).
- [23] S. Franco and A. M. . Uranga, “Dynamical SUSY breaking at meta-stable minima from D-branes at obstructed geometries,” *JHEP* **06** (2006) 031, [hep-th/0604136](#).
- [24] D.-E. Diaconescu, R. Donagi, and B. Florea, “Metastable quivers in string compactifications,” *Nucl. Phys.* **B774** (2007) 102–126, [hep-th/0701104](#).
- [25] O. DeWolfe, A. Giryavets, S. Kachru, and W. Taylor, “Type IIA moduli stabilization,” *JHEP* **07** (2005) 066, [hep-th/0505160](#).
- [26] T. Banks and K. van den Broek, “Massive IIA flux compactifications and U-dualities,” *JHEP* **03** (2007) 068, [hep-th/0611185](#).
- [27] I. Bena, E. Gorbatov, S. Hellerman, N. Seiberg, and D. Shih, “A note on (meta)stable brane configurations in MQCD,” *JHEP* **11** (2006) 088, [hep-th/0608157](#).
- [28] F. Denef and M. R. Douglas, “Distributions of nonsupersymmetric flux vacua,” *JHEP* **03** (2005) 061, [hep-th/0411183](#).
- [29] F. Denef and M. R. Douglas, “Distributions of flux vacua,” *JHEP* **05** (2004) 072, [hep-th/0404116](#).
- [30] M. R. Douglas, “Statistical analysis of the supersymmetry breaking scale,” [hep-th/0405279](#).
- [31] R. Argurio, M. Bertolini, S. Franco, and S. Kachru, “Gauge/gravity duality and meta-stable dynamical supersymmetry breaking,” *JHEP* **01** (2007) 083, [hep-th/0610212](#).
- [32] R. Argurio, M. Bertolini, S. Franco, and S. Kachru, “Metastable vacua and D-branes at the conifold,” *JHEP* **06** (2007) 017, [hep-th/0703236](#).
- [33] F. Brummer, “A natural renormalizable model of metastable SUSY breaking,” *JHEP* **07** (2007) 043, [arXiv:0705.2153 \[hep-ph\]](#).
- [34] D. Malyshev, “Del Pezzo singularities and SUSY breaking,” [arXiv:0705.3281 \[hep-th\]](#).
- [35] K. A. Intriligator and N. Seiberg, “Lectures on supersymmetric gauge theories and electric-magnetic duality,” *Nucl. Phys. Proc. Suppl.* **45BC** (1996) 1–28, [hep-th/9509066](#).
- [36] S. R. Coleman and E. Weinberg, “Radiative Corrections as the Origin of Spontaneous Symmetry Breaking,” *Phys. Rev.* **D7** (1973) 1888–1910.
- [37] K. van den Broek, “Vscape V1.1.0: An interactive tool for metastable vacua,” *Comput. Phys. Commun.* **178** (2008) 52–72, [arXiv:0705.2019 \[hep-ph\]](#).
- [38] S. R. Coleman, “The Fate of the False Vacuum. 1. Semiclassical Theory,” *Phys. Rev.* **D15** (1977) 2929–2936.

- [39] M. J. Duncan and L. G. Jensen, “Exact tunneling solutions in scalar field theory,” *Phys. Lett.* **B291** (1992) 109–114.
- [40] K. Intriligator and N. Seiberg, “Lectures on Supersymmetry Breaking,” *Class. Quant. Grav.* **24** (2007) S741–S772, [hep-ph/0702069](#).
- [41] E. Witten, “Dynamical Breaking of Supersymmetry,” *Nucl. Phys.* **B188** (1981) 513.
- [42] I. Affleck, M. Dine, and N. Seiberg, “Exponential Hierarchy from Dynamical Supersymmetry Breaking,” *Phys. Lett.* **B140** (1984) 59.
- [43] I. Affleck, M. Dine, and N. Seiberg, “Calculable Nonperturbative Supersymmetry Breaking,” *Phys. Rev. Lett.* **52** (1984) 1677.
- [44] I. Affleck, M. Dine, and N. Seiberg, “Dynamical Supersymmetry Breaking in Chiral Theories,” *Phys. Lett.* **B137** (1984) 187.
- [45] I. Affleck, M. Dine, and N. Seiberg, “Dynamical Supersymmetry Breaking in Supersymmetric QCD,” *Nucl. Phys.* **B241** (1984) 493–534.
- [46] I. Affleck, M. Dine, and N. Seiberg, “Supersymmetry Breaking by Instantons,” *Phys. Rev. Lett.* **51** (1983) 1026.
- [47] I. Affleck, M. Dine, and N. Seiberg, “Dynamical Supersymmetry Breaking in Four-Dimensions and Its Phenomenological Implications,” *Nucl. Phys.* **B256** (1985) 557.
- [48] E. Witten, “Constraints on Supersymmetry Breaking,” *Nucl. Phys.* **B202** (1982) 253.
- [49] K. Intriligator, N. Seiberg, and D. Shih, “Supersymmetry Breaking, R-Symmetry Breaking and Metastable Vacua,” *JHEP* **07** (2007) 017, [hep-th/0703281](#).
- [50] M. Dine and Z. Sun, “R symmetries in the landscape,” *JHEP* **01** (2006) 129, [hep-th/0506246](#).

## Chapter 5

### Direct Detection of Non-Chiral Dark Matter

This chapter appears in print in *Phys. Rev. D* **78**, 015004 (2008), arxiv:0710.1668 [hep-ph].

Direct detection experiments rule out fermion dark matter that is a chiral representation of the electroweak gauge group. Non-chiral real, complex and singlet representations, however, provide viable fermion dark matter candidates. Although any one of these candidates will be virtually impossible to detect at the LHC, it is shown that they may be detected at future planned direct detection experiments. For the real case, an irreducible radiative coupling to quarks may allow a detection. The complex case in general has an experimentally ruled out tree-level coupling to quarks via  $Z$ -boson exchange. However, in the case of two  $SU(2)_L$  doublets, a higher dimensional coupling to the Higgs can suppress this coupling, and a remaining irreducible radiative coupling may allow a detection. Singlet dark matter could be detected through a coupling to quarks via Higgs exchange. Since all non-chiral dark matter can have a coupling to the Higgs, at least some of its mass can be obtained from electroweak symmetry breaking, and this mass is a useful characterization of its direct detection cross-section.

#### 5.1 Introduction

The evidence for the existence of non-baryonic dark matter is overwhelming. Within the concordance  $\Lambda$ CDM cosmological model, the required dark matter relic density is now known to remarkable accuracy [1]. The nature of the dark matter particles within this model, however, is unknown.

There is a possibility that new physics associated with electroweak symmetry breaking

(EWSB) might contain a dark matter candidate with the correct relic density. This is because *weakly interacting massive particles* (WIMPs) can have the observed dark matter relic density through thermal freeze-out if their mass is on the order of the electroweak (EW) scale. In addition, it is possible to stabilize WIMPs by including a symmetry that forbids their decay into other particles. This allows them to be good dark matter candidates.

The preferred mass of WIMPs suggests the possibility that they may be produced and detected at the upcoming Large Hadron Collider (LHC) at CERN. Two other types of experiments attempting to detect dark matter are indirect and direct detection experiments. While the indirect detection experiments look for the particles that are produced from annihilating dark matter, the direct detection experiments attempt to infer the presence of dark matter particles as they scatter off nuclei within detectors by looking for the resulting nuclear recoil.

The rationale for the direct detection experiments is that the dark matter lies in a halo which encompasses our Milky Way galaxy. As the earth and sun rotate around the galactic center, detectors on the earth move through the halo and intersect the path of dark matter particles, which are expected to scatter off the nuclei inside the detectors. Since the local dark matter density is not known better than to within a factor of two, there is some uncertainty in the expected scattering rate [2]. Depending on the experimental setup, the nuclear recoil from the scattering would produce ionization, phonons or scintillation, any of which can be observed. Examples of direct dark matter detection experiments include CDMS, DAMA, NaIAD, PICASSO, ZEPLIN, EDELWEISS, CRESST, XENON and WARP [3, 4, 5, 6, 7, 8, 9, 10, 11, 12, 13].

The dark matter scattering off nuclei within a detector can proceed via two fundamentally different types of interactions. There is, on the one hand, a spin-independent, or coherent, interaction between the dark matter and the nucleons. In this case the contribution of each nucleon to the total scattering cross-section interferes constructively across the nucleus. Scattering off nuclei is therefore enhanced roughly by a factor of  $A^2$  in the cross-section, where  $A$  is the number of nucleons in the nucleus. This large enhancement factor is absent for the other type of interaction, which is spin-dependent, and couples the dark matter spin to the spin of the

nuclei. The large enhancement factor is also the main reason that much tighter constraints (a factor of about  $10^5 - 10^6$ ) exist on the SI cross-section, normalized to cross-section per nucleon, than on the SD cross-section.

In this paper, fermion dark matter transforming under the EW gauge group  $SU(2)_L \times U(1)_Y$  will be added to the standard model (SM), and the observational consequences at a direct detection experiment will be discussed. In particular, chiral and non-chiral (real and complex) representations of  $SU(2)_L \times U(1)_Y$  will be considered in §5.2 and §5.3, respectively, and the focus will be on spin-independent interactions for the reasons discussed in the previous paragraph. §5.4 discusses how the direct detection cross-section may be characterized in terms of the fraction of the dark matter mass that is obtained through EWSB. This characterization is particularly useful for EW singlet dark matter. The conclusions are presented in §5.5.

The results of this paper are summarized in Figure 5.3. Shown are the current experimental upper bounds on the spin-independent cross-section for WIMP scattering off nucleons from XENON10 (solid line) [14], the projected upper bounds for SuperCDMS 2-ST at Soudan (blue dashed line), SuperCDMS 25kg / 7-ST at Snolab (green dashed line), XENON1T (magenta dashed line) and SuperCDMS Phase C (red dashed line) [15, 16, 17]. The cross-sections for chiral and non-chiral dark matter are shown, in addition to the Higgs contribution to the direct detection cross-section for a variety of parameter choices.

## 5.2 Chiral Electroweak Dark Matter

Chiral EW matter is forbidden to have an explicit mass term in the Lagrangian since such a mass term is not gauge invariant. It instead has a Yukawa coupling to the Standard Model Higgs field and gains all its mass from EWSB through the Higgs mechanism. Chiral EW dark matter particles are thus Dirac fermions.

EW precision measurements put tight constraints on additional chiral matter. For example, an additional doublet of colorless heavy fermions gives a contribution of  $1/6\pi$  to the electroweak

$S$ -parameter, which is about  $1.8\sigma$  away from its measured central value. An additional degenerate generation is disfavored even more strongly at the 99.95% confidence level [18].

Although EW precision measurements still allow room for chiral EW dark matter, direct detection experiments rule it out as a viable dark matter candidate. The reason is that it has a vector coupling to the  $Z$ -boson and can therefore scatter coherently off the nuclei inside the detector via a tree-level  $Z$ -boson exchange. The resulting cross-section is large enough that such dark matter particles would already have been seen [19].

In general, the cross-section per nucleon for dark matter scattering coherently off nuclei via the exchange of a  $Z$ -boson is given by

$$\sigma \simeq \frac{G_F^2}{2\pi} m_{\chi N}^2 \frac{1}{A^2} \left[ (1 - 4\sin^2\theta_W)Z - (A - Z) \right]^2 \bar{Y}^2. \quad (5.1)$$

Here,  $G_F$  is the Fermi coupling constant,  $m_{\chi N}$  is the reduced mass of the dark matter mass ( $m_\chi$ ) and nucleon mass ( $m_N$ ),  $A$  ( $Z$ ) is the mass (atomic) number of the nucleus,  $\theta_W$  is the weak mixing angle, and  $\bar{Y} \equiv \frac{1}{2}(Y_L + Y_R)$ , where  $Y_L$  and  $Y_R$  are the hypercharge of the left- and right-handed components of the dark matter particle [19]. The convention chosen here is  $Q = T_3 + \frac{1}{2}Y$ , where  $Q$  is the electric charge,  $T_3$  is the third component of the isospin, and  $Y$  is the hypercharge of the particle. The term proportional to  $Z$  in the square brackets is for the dark matter scattering off the protons inside the nucleus. It is suppressed since  $1 - 4\sin^2\theta_W$  is very small. The term proportional to  $A - Z$  is for the dark matter scattering off the neutrons inside the nucleus, and it dominates. The factor of  $1/A^2$  normalizes the cross-section to a cross-section per nucleon.

Chiral EW dark matter has  $Y_R = Y_L \pm 1$ , i.e.  $\bar{Y} = Y_L \pm \frac{1}{2}$ . For the CDMS experiment, for example, which uses Germanium ( ${}_{32}^{73}\text{Ge}$ ), the scattering cross-section per nucleon then becomes

$$\sigma \gtrsim 5 \times 10^{-40} \text{ cm}^2, \quad (5.2)$$

for  $\bar{Y} \geq \frac{1}{2}$ . This result is roughly independent of the mass of the dark matter, at least for a

large enough dark matter mass. A Dirac neutrino<sup>1</sup> saturates the lower bound as it has  $Y_L = 1$  and  $Y_R = 0$ , and thus  $\bar{Y} = \frac{1}{2}$ . For  $m_\chi$  above roughly 10 GeV, the cross-section is larger than current bounds, see Figure 5.3, and such chiral EW dark matter is therefore ruled out as a viable dark matter candidate. Note that for  $m_\chi$  less than about 10 GeV (and down to about 2 eV, at which point the dark matter ceases to be “cold”), the direct detection cross-section is not larger than the experimental bound. However, since these particles couple to the  $Z$ -boson, the  $Z$  could have decayed into them. The precise CERN LEP measurement of the invisible decay of the  $Z$ -boson rules out this possibility.

### 5.3 Non-Chiral Dark Matter

Non-chiral, or vector, matter is different from chiral matter in that an explicit mass term in the Lagrangian is allowed. Even though, a priori, there is nothing that protects this explicit mass term from being large, its size can nevertheless naturally be on the order of the EW scale. This may happen if, for example, the underlying high-scale theory has a global chiral symmetry that is spontaneously broken at the EW scale, but that forbids an explicit mass term at higher scales.

Non-chiral matter is not subject to the same tight constraints from EW precision measurements as is chiral matter. This is because there is no renormalizable coupling to the Higgs field. Although there is a higher dimensional (non-renormalizable) coupling to the Higgs, this does not cause any conflict with EW precision measurements. Instead, this coupling implies that non-chiral matter gains some small fraction of its mass from EWSB. It will be seen that the fraction of the dark matter particle’s mass that comes from EWSB is useful characterization of the dark matter’s direct detection cross-section. This will be discussed further in §5.4.

Stability and electric neutrality are basic requirements of any dark matter particle. Since massive non-chiral representations are allowed to carry conserved quantum numbers, which

---

<sup>1</sup>A Dirac neutrino also has an axial vector coupling to the  $Z$ -boson and therefore a spin-dependent interaction with nuclei.

prohibits their mixing with Standard Model fermions, the lightest state of such an additional representation can indeed be stable. Moreover, such representations contain both new neutral and new charged particles. The charged particles are several hundred MeV *heavier* than the neutral particles due to EWSB. Intuitively one can understand the mass difference as arising from different one-loop corrections to the masses and wave-functions: the charged components receive corrections from both virtual photons and Z-bosons in the loop, whereas the neutral components receive corrections only from virtual Z-bosons [20]. This means that the lightest state of an additional massive non-chiral representation can also be expected to be neutral.

It is useful to divide non-chiral representations up further into real and complex representations. Each of these will now be discussed by focusing on an explicit example.

### 5.3.1 Real representations of $SU(2)_L \times U(1)_Y$

If the dark matter particle is part of a real representation of  $SU(2)_L \times U(1)_Y$ , then its hypercharge,  $Y$ , must be zero. Since the charge,  $Q$ , of the dark matter must be zero, this also implies  $T_3 = Q - \frac{1}{2}Y = 0$ . The dark matter particle, now a Majorana fermion, therefore does not couple to the Z-boson, and there is no coherent tree-level scattering off nuclei. This makes it “safe” from the current experimental bounds.

As an example, consider the dark matter to be part of an  $SU(2)_L$  triplet with zero hypercharge,

$$L = \begin{pmatrix} L^+ \\ L^0 \\ L^- \end{pmatrix}. \quad (5.3)$$

Here the neutral component  $L^0$  is a possible dark matter candidate. The explicit mass term in the Lagrangian is given by

$$\mathcal{L} \supset -\frac{m}{2}(2L^+L^- + L^0L^0). \quad (5.4)$$

The non-renormalizable operator that, after EWSB, splits the mass of the neutral components from the mass of the charged components by several hundred MeV is given by [20]

$$\mathcal{L} \supset \epsilon^{abc} L^a L^b H^\dagger T^c H, \quad (5.5)$$

where the  $T^a$ ,  $a = 1, 2, 3$ , are the  $SU(2)_L$  generators, and  $H$  is the Standard Model Higgs field.

The interactions of  $L^0$  with the Standard Model gauge bosons and the charged fields  $L^\pm$  are given by

$$gW_\mu^+(-L^{+\dagger}\bar{\sigma}^\mu L^0 + L^{0\dagger}\bar{\sigma}^\mu L^-) + gW_\mu^-(-L^{0\dagger}\bar{\sigma}^\mu L^+ + L^{-\dagger}\bar{\sigma}^\mu L^0). \quad (5.6)$$

Two-component spinor notation for the dark matter is employed throughout this paper, while four-component Dirac notation will be used below for the quark fields (in equation (5.6),  $\sigma^\mu = (I_2, \vec{\sigma})$  and  $\bar{\sigma}^\mu = (I_2, -\vec{\sigma})$ , where  $\vec{\sigma}$  are the usual Pauli matrices).

Note the absence of any coupling of the neutral component  $L^0$  to the  $Z$ -boson. This means there is no tree-level scattering for  $L^0$  off nuclei, making this a viable dark matter candidate. There is, however, an irreducible one-loop coupling to nucleons, which will be discussed in §5.3.3.

The particle  $L^0$  behaves like a wino-like lightest supersymmetric particle (LSP) found in the Minimal Supersymmetric Standard Model (MSSM). Assuming that  $L^0$  makes up all of the dark matter in the universe, it may be shown that it must have a mass of about

$$m_{L^0} \simeq 2 \text{ TeV} \quad (5.7)$$

to give the correct dark matter relic density. This mass was estimated from Figure 4 in [21]. Non-perturbative electroweak corrections to the dark matter annihilation cross-section as included in [22] require the dark matter to have a mass of about 2.7 TeV to obtain the correct relic density.

It is interesting to note that if  $L^0$  makes up most of the dark matter component in the universe, it will most likely be very difficult to detect at the LHC. Although a detailed collider study is beyond the scope of this paper, the following comments are meant to give an indication

of this difficulty. Since the  $L^{\pm,0}$  are heavy and weakly interacting, their production cross-sections are small. They may be very roughly estimated to be on the order of  $10^{-5} - 10^{-4}$  pb, as may be extrapolated from Figure 2 in [23], which shows the production cross-section for the related wino-like neutralinos and charginos in the MSSM. Moreover, the charged states  $L^{\pm}$  are split from the neutral state  $L^0$  only by a small amount, so that even though they produce ionizing charged tracks, they do so only within the inner portion of the detector, before they each decay into the neutral state by emitting a soft pion [20]. The missing energy from the two neutral particles escaping the detector balances, so that there is not much visible missing energy. At the LHC it is very difficult to trigger on this, and such dark matter particles will thus be extremely difficult to detect at the LHC. It is possible but unlikely that a detailed collider study will change this conclusion.

### 5.3.2 Complex representation of $SU(2)_L \times U(1)_Y$

If the dark matter particle is part of a complex representation of  $SU(2)_L \times U(1)_Y$ , then its hypercharge is nonzero. Since the charge of the dark matter must be zero,  $T_3 = -\frac{1}{2}Y$ . The dark matter particle, now a Dirac fermion, therefore couples to the  $Z$ -boson at tree-level. In the notation of equation (5.1),  $Y_L = Y_R \equiv Y$ , and the cross-section per nucleon for scattering off nuclei is given by

$$\sigma \simeq \frac{G_F^2}{2\pi} m_{\chi N}^2 \frac{1}{A^2} \left[ (1 - 4 \sin^2 \theta_W) Z - (A - Z) \right]^2 Y^2. \quad (5.8)$$

For the CDMS experiment, using Germanium, the scattering cross-section per nucleon then becomes

$$\sigma \simeq 2 \times 10^{-39} Y^2 \text{ cm}^2, \quad (5.9)$$

which is experimentally ruled out.

If this tree-level coupling of the dark matter particle to the  $Z$ -boson can be avoided or at least suppressed, this type of dark matter again becomes viable. This can be achieved for example by adding additional matter, cf. [24, 25, 26, 27, 28]. In the case of dark matter that is

a doublet of  $SU(2)_L$ , however, it can be achieved by a non-renormalizable operator that couples the dark matter particle to the Higgs.

The example of two  $SU(2)_L$  doublets of opposite hypercharge will now be discussed in detail. Denote the two  $SU(2)_L$  doublets by

$$L_1 = \begin{pmatrix} L_1^0 \\ L_1^- \end{pmatrix} \quad L_2 = \begin{pmatrix} -L_2^+ \\ L_2^0 \end{pmatrix}, \quad (5.10)$$

where  $L_1$  has hypercharge  $Y = -1$ , and  $L_2$  has hypercharge  $Y = +1$ . The explicit mass term in the Lagrangian is given by

$$\mathcal{L} \supset -mL_1L_2, \quad (5.11)$$

where the  $SU(2)_L$  indices are contracted as  $\epsilon_{\alpha\beta}L_1^\alpha L_2^\beta$ . The neutral components of each doublet together form a neutral Dirac fermion.

There is an accidental  $U(1)_{L_1L_2}$  symmetry under which  $L_1$  and  $L_2$  transform opposite to each other. This symmetry requires the neutral components to be part of a Dirac fermion, and thus allows the tree-level scattering off nuclei via  $Z$ -boson exchange. An operator which violates this symmetry can, however, split the Dirac state into a pseudo-Dirac state, which consists of two Majorana fermions that have a tiny mass splitting. This splitting can substantially suppress the tree-level scattering.

The non-renormalizable operator that, after EWSB, splits the mass of the neutral components from the mass of the charged components by several hundred MeV is given by

$$\mathcal{L} \supset L_2 T^a L_1 H^\dagger T^a H, \quad (5.12)$$

where the  $T^a$  are the  $SU(2)$  generators [20]. This operator, however, only affects the splitting of the charged states from the neutral states. Since it does not violate the  $U(1)_{L_1L_2}$  symmetry, it does not affect the neutral Dirac state, whose scattering off nuclei remains unchanged.

However, a non-renormalizable operator that does violate the  $U(1)_{L_1L_2}$  symmetry is given by

$$\mathcal{L} \supset -\frac{c}{M}(L_1H)(L_1H) + h.c. - \frac{c^*}{M}(L_2H^c)(L_2H^c) + h.c., \quad (5.13)$$

where brackets indicate that the  $SU(2)_L$  indices are contracted,  $H^c = i\sigma_2 H^*$ , and  $H$  has been assigned hypercharge  $Y = -1$ . The scale  $M$  is some high mass scale at which this operator is generated, and  $c$  is an  $O(1)$  coefficient. Note that in writing down this term, the discrete symmetry  $L_1 \leftrightarrow (L_2)^c$  was assumed, so that the coefficients are the same up to complex conjugation (removing this assumption leaves unchanged the main conclusion, namely that the neutral Dirac state will be split). This operator only exists for dark matter that has hypercharge  $|Y| = 1$ .

Once the Higgs field obtains a vacuum expectation value,  $v$ , and EW symmetry has been broken, the neutral components get an additional contribution to the mass, which can be written as  $\delta = \frac{c}{M} v^2$ .  $M$  will have to be large enough to ensure  $|\delta| \ll m$ . Including corrections up to  $\mathcal{O}\left(\frac{\text{Im}\delta}{m}\right)$  or  $\mathcal{O}\left(\frac{\text{Re}\delta}{m}\right)$ , the mass term may be written as

$$\begin{aligned} & -\frac{1}{2} \begin{pmatrix} L_1^0 & L_2^0 \end{pmatrix} \begin{pmatrix} \delta & m \\ m & \delta^* \end{pmatrix} \begin{pmatrix} L_1^0 \\ L_2^0 \end{pmatrix} \\ & = -\frac{1}{2} \begin{pmatrix} \chi_2 & \chi_1 \end{pmatrix} \begin{pmatrix} m + \text{Re}\delta & 0 \\ 0 & m - \text{Re}\delta \end{pmatrix} \begin{pmatrix} \chi_2 \\ \chi_1 \end{pmatrix}, \end{aligned} \quad (5.14)$$

where the neutral mass eigenstates are given by

$$\chi_1 \simeq \frac{i}{\sqrt{2}} \left( \left( -1 + \frac{1}{2} \frac{\text{Im}\delta}{m} \right) L_1^0 + \left( 1 + \frac{1}{2} \frac{\text{Im}\delta}{m} \right) L_2^0 \right) \quad (5.15)$$

$$\chi_2 \simeq \frac{1}{\sqrt{2}} \left( \left( 1 + \frac{1}{2} \frac{\text{Im}\delta}{m} \right) L_1^0 + \left( 1 - \frac{1}{2} \frac{\text{Im}\delta}{m} \right) L_2^0 \right) \quad (5.16)$$

These are the two Majorana fermions that make up the pseudo-Dirac state. Ignoring higher order corrections, the mass eigenstates may also be written as

$$\chi_1 \simeq \frac{i}{\sqrt{2}} (-L_1^0 + L_2^0), \quad m_1 = m - \text{Re}\delta \quad (5.17)$$

$$\chi_2 \simeq \frac{1}{\sqrt{2}} (L_1^0 + L_2^0), \quad m_2 = m + \text{Re}\delta. \quad (5.18)$$

Here  $\chi_1$ , the lighter of the two Majorana particles, is the dark matter particle. It behaves like a higgsino-like LSP found in the MSSM. Assuming that  $\chi_1$  makes up all of the dark matter in

the universe, it must have a mass of about

$$m_{\chi_1} \simeq 1 \text{ TeV}, \quad (5.19)$$

to give the correct dark matter relic density. This mass was estimated from Figure 4 in [21].

Non-perturbative electroweak corrections are negligible as discussed in [22].

At lowest order, the couplings among the neutral fields,  $\chi_1$  and  $\chi_2$ , and the charged fields,  $L_1^-$  and  $L_2^+$ , are given by

$$\begin{aligned} & L_1^\dagger(i\bar{\sigma}^\mu\partial_\mu)L_1 + L_2^\dagger(i\bar{\sigma}^\mu\partial_\mu)L_2 + gW_\mu^+ \left[ \frac{1}{2}(\chi_2^\dagger - i\chi_1^\dagger)\bar{\sigma}^\mu L_1^- \right. \\ & \left. - \frac{1}{2}L_2^{+\dagger}\bar{\sigma}^\mu(\chi_2 - i\chi_1) \right] + gW_\mu^- \left[ -\frac{1}{2}(\chi_2^\dagger + i\chi_1^\dagger)\bar{\sigma}^\mu L_2^+ + \frac{1}{2}L_1^{-\dagger}\bar{\sigma}^\mu(\chi_2 + i\chi_1) \right] \\ & + \frac{g}{\cos\theta_W} Z_\mu \left[ L_1^{-\dagger}\bar{\sigma}^\mu \left( -\frac{1}{2} + \sin^2\theta_W \right) L_1^- + L_2^{+\dagger}\bar{\sigma}^\mu \left( \frac{1}{2} - \sin^2\theta_W \right) L_2^+ \right. \\ & \left. + \frac{i}{2}(\chi_2^\dagger\bar{\sigma}^\mu\chi_1 - \chi_1^\dagger\bar{\sigma}^\mu\chi_2) \right] + eA_\mu \left[ -L_1^{-\dagger}\bar{\sigma}^\mu L_1^- + L_2^{+\dagger}\bar{\sigma}^\mu L_2^+ \right]. \end{aligned} \quad (5.20)$$

Including the next higher order correction, the coupling of the dark matter to the  $Z$ -boson becomes

$$\frac{g}{2\cos\theta_W} Z_\mu \left[ i(\chi_2^\dagger\bar{\sigma}^\mu\chi_1 - \chi_1^\dagger\bar{\sigma}^\mu\chi_2) + \frac{\text{Im}\delta}{m}(\chi_2^\dagger\bar{\sigma}^\mu\chi_2 - \chi_1^\dagger\bar{\sigma}^\mu\chi_1) \right]. \quad (5.21)$$

Equations (5.20) and (5.21) show that the only coupling  $\chi_1$  has to itself at tree-level is suppressed by a factor of  $\frac{\text{Im}\delta}{m}$ . The dominant coupling of  $\chi_1$  is to  $\chi_2$ , and it is possible for  $\chi_1$  to scatter *inelastically* off nucleons via  $Z$ -boson exchange ( $\chi_1 \rightarrow \chi_2$ ). This inelastic scattering will be kinematically inaccessible if the mass splitting between  $\chi_1$  and  $\chi_2$  ( $\sim 2\text{Re}(\delta)$ ) is large enough. Since the typical recoil energies of the nuclei in the detector are expected to be on the order of a few 10's of keV, a splitting of a few 10's of keV is required in order to forbid the inelastic scattering via  $Z$ -boson exchange<sup>2</sup> [2, 30]. This means that  $\frac{\text{Im}\delta}{m}$  can be as small as  $\sim 10^{-7} - 10^{-8}$ , so that the cross-section for the scattering of  $\chi_1$  to  $\chi_1$  off nuclei is suppressed by a factor of  $\left(\frac{\text{Im}\delta}{m}\right)^2 \sim 10^{-14} - 10^{-16}$ , which ensures it lies well below the current experimental bound. Note

---

<sup>2</sup>The question of whether the scattering is kinematically allowed or not depends critically on the mass of the nucleus in the detector. It is thus possible to carefully choose  $\delta$  in such a way that scattering will take place in a heavier target such as NaI used by DAMA, but not in a lighter target such as Ge used by CDMS. The possibility of using this to explain the DAMA signal, in the absence of a signal by CDMS and others, was discussed in [29, 25]. (The fact that the dark matter in the halo would follow a Maxwell-Boltzmann distribution of velocities complicates, but does not invalidate, the statements just made.)

also that this requires the scale of the new physics which generates the operator that breaks the  $U(1)_{L_1 L_2}$  symmetry to be roughly  $M \lesssim 10^8 - 10^9$  GeV.

For appropriate values of the mass splitting the dark matter can therefore not scatter off the nuclei at tree-level. This makes it “safe” from current experimental bounds. There is, however, again an irreducible one-loop coupling to nucleons, which will be discussed in §5.3.3.

It should be noted that  $\chi_1$  will most likely be extremely difficult to detect at the LHC. The reasoning is similar to that mentioned at the end of §5.3.1 for the case of the  $SU(2)_L$  triplet with zero hypercharge. The LHC production cross-section of  $\chi_1$  here is only marginally larger (since it is less massive), about  $10^{-4} - 10^{-3}$  pb. This was estimated from Figure 2 in [31], which shows the production cross-section for the related higgsino-like neutralinos and charginos in the MSSM. Moreover, the direct production of this type of dark matter and the associated charged particles will again only give rise to signals that are very difficult to trigger on at the LHC. Their associated production with jets, for example, has a cross-section that is too small to be visible above background events (see [32], which looked at collider signatures for a higgsino-like lightest supersymmetric particle). The non-chiral dark matter proposed in this paper thus seems to be extremely difficult to detect at the LHC. Although a detailed LHC collider study is beyond the scope of this paper, it seems unlikely that it would change this conclusion.

### 5.3.3 Direct detection of non-chiral dark matter

The previous two subsections considered non-chiral dark matter that is either a real or a complex representation of  $SU(2)_L \times U(1)_Y$ . For real representations, there is no tree-level coupling between the dark matter and the nuclei. For complex representations, the tree-level coupling is completely negligible, if the Dirac state has been appropriately split into a pseudo-Dirac state. Although the absence of any tree-level coupling allows non-chiral dark matter particles to be consistent with current experimental limits, there is an irreducible one-loop coupling which is

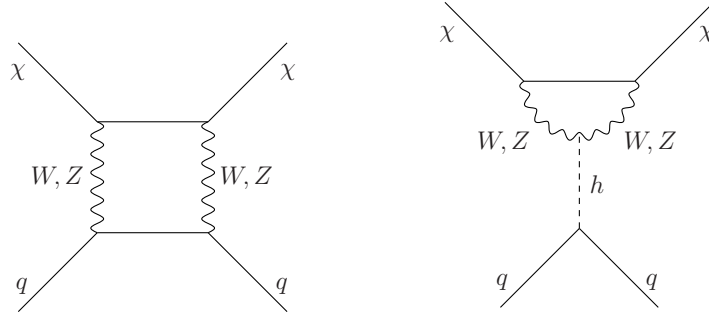


Figure 5.1: Feynman diagrams for the irreducible one-loop couplings between non-chiral dark matter and quarks. For real representations of  $SU(2)_L \times U(1)_Y$ , there are only  $W$ -bosons within the loop. For complex representations of  $SU(2)_L \times U(1)_Y$ , there are both  $W$ - and  $Z$ -bosons in the loop. The symbol  $h$  denotes the Standard Model Higgs boson,  $\chi$  denotes the dark matter particle, and  $q$  refers to quarks. There is also a cross-diagram for the diagram on the left which needs to be included.

large enough for it to be detectable in future direct detection experiments.<sup>3</sup> These irreducible one-loop couplings are given in Figure 5.1.

For real representations, the one-loop diagrams involve the  $W$ -bosons, but not the  $Z$ -boson. As an explicit example, consider the  $SU(2)_L$  triplet with zero hypercharge ( $L^0$ ). Its couplings to the  $W$ -bosons and to the additional charged states ( $L^\pm$ ) are given in equation (5.6). The effective Lagrangian for the coherent interaction between the dark matter and the quarks is

$$\begin{aligned}
4\alpha_2^2\pi \sum_q \left[ \frac{1}{8} f_I^W(m_W/m_{L^0}) \frac{1}{m_W m_h^2} (L^0 L^0 + L^{0\dagger} L^{0\dagger}) m_q \bar{q} q \right. \\
+ \frac{1}{12} f_{II}^W(m_W/m_{L^0}) \frac{1}{m_W^3 m_{L^0}} (L^0 i D^\mu \sigma^\nu L^{0\dagger} + L^{0\dagger} i D^\mu \bar{\sigma}^\nu L^0) \times \\
\left. \bar{q} (\gamma_\mu i D_\nu + \gamma_\nu i D_\mu - \frac{1}{2} g_{\mu\nu} i \not{D}) q \right]. \quad (5.22)
\end{aligned}$$

This result<sup>4</sup> was obtained by assuming that the momentum carried by the quarks in the Feynman diagram on the left in Figure 5.1 is small but non-zero; in the Feynman diagram on the right the momentum of the quarks was set to zero, and therefore no momentum was assumed to flow

<sup>3</sup>For indirect dark matter detection rates and for prospects of detecting the associated charged particles among the ultra-high energy cosmic rays see [22].

<sup>4</sup>The result for the one-loop computation agrees on-shell with [33], although here the operator  $(\frac{1}{2} L^0 L^0 + \frac{1}{2} L^{0\dagger} L^{0\dagger}) \bar{q} i \not{D} q$  is found to vanish, and the coefficient of the twist-two operator is a factor of two larger than in [33]. The results of this paper do not agree off- or on-shell with [34], who considered wino-like and higgsino-like lightest supersymmetric particles in the MSSM. Since the operators agree on-shell with [33], the final cross-sections calculated in this paper also basically agree. (It is more difficult to compare the cross-sections with those of [34] since their's is dependent on various MSSM parameters.)

through the Higgs propagator. The functions  $f_I^W$  and  $f_{II}^W$  are given by

$$f_I^W(x) = \frac{1}{3\pi} \left( \frac{12 - 12x^2 + 2x^4}{\sqrt{4-x^2}} \arctan\left(\frac{1}{x}\sqrt{4-x^2}\right) + 2x + (4x - x^3) \ln x^2 \right) \quad (5.23)$$

$$f_{II}^W(x) = \frac{1}{4\pi} \left( \frac{16 + 12x^2 - 12x^4 + 2x^6}{\sqrt{4-x^2}} \arctan\left(\frac{1}{x}\sqrt{4-x^2}\right) - 5x + 2x^3 + (4x^3 - x^5) \ln x^2 \right). \quad (5.24)$$

These functions have been normalized to equal one in the limit  $x \rightarrow 0$ . This is a useful normalization since here  $x \equiv m_W/m_{L^0} \ll 1$ .

For higher dimensional representations, there is an additional factor in equation (5.22). For an  $n$ -tuple of  $SU(2)_L$  with zero hypercharge this additional factor is given by  $(n^2 - 1)/8$ .

For complex representations, the one-loop diagrams involve the  $W$ - and  $Z$ -bosons. As an explicit example, consider the dark matter candidate from two  $SU(2)_L$  doublets of opposite hypercharge ( $\chi_1$ ). Its couplings to the  $W$ - and  $Z$ -bosons, to the additional charged states  $L_1^-$  and  $L_2^+$ , and to the slightly heavier neutral state  $\chi_2$  are given in equation (5.20). The effective coherent interaction between the dark matter and the quarks due to  $W$ -bosons in the loop is given by equation (5.22) by replacing  $L^0$  with  $\chi_1$  and by including a factor of  $1/4$  which multiplies the whole equation. The effective Lagrangian for the coherent interaction between the dark matter and the quarks due to a  $Z$ -boson in the loop is given by

$$\begin{aligned} \frac{\alpha_2^2 \pi}{\cos^4 \theta_W} \sum_q \left[ \left( -\frac{1}{16} f_I^Z(m_Z/m_{\chi_1}) \frac{(c_V^q)^2 - (c_A^q)^2}{m_Z^3} + \frac{1}{16} f_{II}^Z(m_Z/m_{\chi_1}) \frac{1}{m_Z m_h^2} \right) \right. \\ \times \left( \chi_1 \chi_1 + \chi_1^\dagger \chi_1^\dagger \right) m_q \bar{q} q \\ \left. + \frac{1}{24} f_{III}^Z(m_Z/m_{\chi_1}) \frac{(c_V^q)^2 + (c_A^q)^2}{m_Z^3 m_{\chi_1}} \left( \chi_1 i D^\mu \sigma^\nu \chi_1^\dagger + \chi_1^\dagger i D^\mu \bar{\sigma}^\nu \chi_1 \right) \right. \\ \left. \times \bar{q} \left( \gamma_\mu i D_\nu + \gamma_\nu i D_\mu - \frac{1}{2} g_{\mu\nu} i \not{D} \right) q \right] \quad (5.25) \end{aligned}$$

where the functions  $f_I^Z$ ,  $f_{II}^Z$  and  $f_{III}^Z$  are given by

$$f_I^Z(x) = \frac{1}{\pi} \left( \frac{4 - 2x^2 + x^4}{\sqrt{4 - x^2}} \arctan \left( \frac{1}{x} \sqrt{4 - x^2} \right) + x - \frac{1}{2} x^3 \ln x^2 \right) \quad (5.26)$$

$$f_{II}^Z(x) = \frac{1}{\pi} \left( \frac{4 + 4x^2 - 2x^4}{\sqrt{4 - x^2}} \arctan \left( \frac{1}{x} \sqrt{4 - x^2} \right) - 2x + x^3 \ln x^2 \right) \quad (5.27)$$

$$f_{III}^Z(x) = \frac{1}{8\pi} \left( \frac{32 + 16x^2 - 32x^4 + 8x^6}{\sqrt{4 - x^2}} \arctan \left( \frac{1}{x} \sqrt{4 - x^2} \right) - 4x + 8x^3 + (8x^3 - 4x^5) \ln x^2 \right). \quad (5.28)$$

These functions have also been normalized to equal one in the limit  $x \rightarrow 0$ . This is again a useful normalization since here  $x \equiv m_Z/m_{\chi_1} \ll 1$ . On the quark line the coupling of the  $Z$  boson to the quarks is given by  $-\frac{g}{\cos \theta_W} \gamma^\mu \frac{1}{2} (c_V^q - c_A^q \gamma^5)$ , where  $c_V^q = T_q^3 - 2 \sin^2 \theta_W Q_q$ ,  $c_A^q = T_q^3$ ,  $Q_q$  is the quark charge, and  $T_q^3 = +\frac{1}{2}$  ( $-\frac{1}{2}$ ) for up (down)-type quarks.

For higher dimensional complex representations, there are additional factors in the  $W$ -bosons contribution in equation (5.22) and in the  $Z$ -boson contribution in equation (5.25). For an  $n$ -tuple of  $SU(2)$  with  $n = Y + 1$ , there is an additional factor of  $(n^2 - (1 - Y)^2)/16$  multiplying equation (5.22). However, if  $n > Y + 1$ , then there are more charged states that the dark matter particle can couple to, and the additional factor multiplying equation (5.22) is given by  $(n^2 - (1 + Y^2))/8$ . For an  $n$ -tuple of hypercharge  $Y$ , the factor that needs to multiply equation (5.25) is given by  $Y^2$ .

The effective coupling between dark matter and the quarks involves several operators at a scale of order  $m_Z$  (which is the value of the dominant momentum in the loops of the diagrams in Figure 5.1). These operators are the scalar operator  $m_q \bar{q}q$ , the trace operator  $\bar{q} i \not{D} q$  (which was found to vanish, but there is no symmetry reason for why it should vanish), and the traceless twist-two operator  $\frac{1}{2} \bar{q} (\gamma_\mu i D_\nu + \gamma_\nu i D_\mu - \frac{1}{2} g_{\mu\nu} i \not{D}) q$ . The traceless twist-two operator and trace operator are part of the quark energy momentum tensor given by  $\bar{q} \gamma^{(\mu} i D^{\nu)} q$ .

The nucleon matrix element of the scalar operator  $m_q \bar{q}q$  for light quarks is [2, 35]

$$\langle N | m_q \bar{q}q | N \rangle = f_{T_q}^N m_N \bar{N} N, \quad (5.29)$$

where on the right hand side of the equation  $N$  denotes a nucleon, and

$$\begin{aligned} f_{T_u}^p &\simeq 0.020 \pm 0.004, & f_{T_d}^p &\simeq 0.026 \pm 0.005, & f_{T_s}^p &\simeq 0.118 \pm 0.062 \\ f_{T_u}^n &\simeq 0.014 \pm 0.003, & f_{T_d}^n &\simeq 0.036 \pm 0.008, & f_{T_s}^n &\simeq 0.118 \pm 0.062. \end{aligned} \quad (5.30)$$

The main contribution comes from the strange quark content of the nucleon, which also has the largest uncertainty. Heavy quarks,  $Q$ , also contribute to the mass of the nucleon. This can be derived by making use of the anomaly relating the heavy quarks to the gluons [2],

$$\langle N | m_Q \bar{Q} Q | N \rangle = \langle N | -\frac{\alpha_s}{12\pi} G_{\mu\nu}^a G^{a\mu\nu} | N \rangle = \frac{2}{27} f_{TG}^N m_N \bar{N} N, \quad (5.31)$$

where,

$$\frac{2}{27} f_{TG}^N = \frac{2}{27} \left( 1 - \sum_{u,d,s} f_{T_q}^N \right) \simeq 0.062. \quad (5.32)$$

Although we found that the trace operator  $\bar{q} i \not{D} q$  vanishes and that there is thus no need to know its nucleon matrix element, we mention it here for completeness. The nucleon matrix element for light quarks may be estimated as

$$\langle N | \bar{q} i \not{D} q | N \rangle = \langle N | m_q \bar{q} q | N \rangle. \quad (5.33)$$

An accurate determination of the nucleon matrix element for the trace operator with heavy quarks involves the calculation of higher loop diagrams as shown in Figure 5.2, and is beyond the scope of this paper (see for example [36]). Instead, as a crude approximation, equation (5.33) may also be used for the heavy quarks  $Q$ , together with (5.31).

The twist-two quark operator is given by

$$\mathcal{O}_q^{(2)\mu\nu} = \frac{1}{2} \bar{q} (\gamma^\mu i D^\nu + \gamma^\nu i D^\mu - \frac{1}{2} g^{\mu\nu} i \not{D}) q. \quad (5.34)$$

A linear combination of scale-dependent twist-two quark operators,

$$\sum_q \lambda_q [\mathcal{O}_q^{(2)}]_{m_Z^2}, \quad (5.35)$$

is generated at the scale  $m_Z$ , with coefficients  $\lambda_q$  that may be read from equations (5.22) and (5.25). For the  $W$ -contribution to the scattering amplitude, the coefficients are the same for

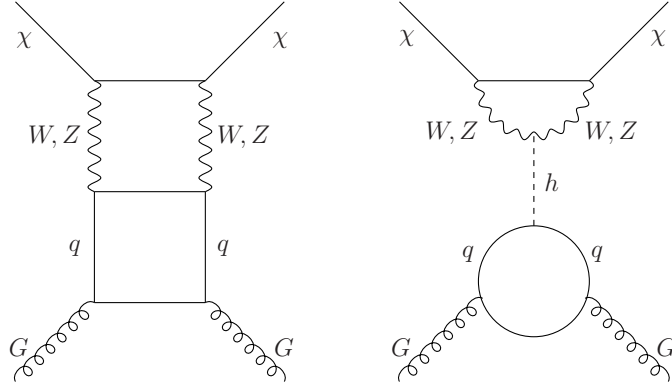


Figure 5.2: Feynman diagrams generating a coupling between dark matter  $\chi$  and gluons  $G$ . For real representations of  $SU(2)_L \times U(1)_Y$ , there are only  $W$ -bosons within the loop. For complex representations of  $SU(2)_L \times U(1)_Y$ , there are both  $W$ - and  $Z$ -bosons in the loop. The symbol  $h$  denotes the Standard Model Higgs boson and  $q$  refers to quarks.

all quarks  $q$ , but for the  $Z$ -contribution they differ for up- and down-type quarks. Under QCD rescaling, the twist-two quark operator mixes with the twist-two gluon operator. This may be taken into account by rewriting equation (5.35) as a linear combination of operators that rescale multiplicatively [37]. One of these operators is the QCD energy-momentum tensor  $T^{\mu\nu}$

$$T^{\mu\nu} = \sum_q \mathcal{O}_q^{(2)\mu\nu} + \mathcal{O}_G^{(2)\mu\nu}, \quad (5.36)$$

where  $\mathcal{O}_G^{(2)}$  is the twist-2 gluon operator given by

$$\mathcal{O}_G^{(2)\mu\nu} = G^{a\rho\mu} G_\rho^{a\nu} - \frac{1}{4} g^{\mu\nu} G^{a\rho\sigma} G_{\rho\sigma}^a. \quad (5.37)$$

Another operator that may be rescaled multiplicatively is

$$\mathcal{O}_-^{\mu\nu} = \frac{16}{3} \sum_q \mathcal{O}_q^{(2)\mu\nu} - n_f \mathcal{O}_G^{(2)\mu\nu}, \quad (5.38)$$

where  $n_f$  is the number of active quark flavors ( $n_f = 5$  at the scale  $m_Z$ ). In the case of the  $W$ -contribution, for which all  $\lambda_q$  are the same, equation (5.35) can be rewritten in terms of the operators (5.36) and (5.38). For the  $Z$ -contribution, however,  $\lambda_q$  differs for up- and down-type quarks, so that other operators that rescale multiplicatively are required. These are flavor non-singlet combinations of the individual quark operators  $\mathcal{O}_{q_i}^{(2)} - \mathcal{O}_{q_j}^{(2)}$  that do not mix with the gluon operator since the gluon contributions cancel out.

The linear combination of twist-two quark operators (5.35) can thus be rewritten in terms of operators whose QCD rescaling is simple. The operators may then be rescaled down to low scales, so that (5.35) may be written in terms of operators that are evaluated at low scales. The energy-momentum tensor  $T^{\mu\nu}$  has zero anomalous dimension, whereas  $\mathcal{O}_-^{\mu\nu}$  and the flavor non-singlet combinations  $\mathcal{O}_{q_i}^{(2)} - \mathcal{O}_{q_j}^{(2)}$  have positive anomalous dimension given by  $\frac{\alpha_s}{3\pi}(\frac{16}{3} + n_f)$  and  $\frac{16\alpha_s}{9\pi}$ , respectively. This means that running to the infrared,  $T^{\mu\nu}$  does not get renormalized whereas the other operators,  $\mathcal{O}_-^{\mu\nu}$  and  $\mathcal{O}_{q_i}^{(2)} - \mathcal{O}_{q_j}^{(2)}$ , both *decrease*. The dominant contribution at low scales to the linear combination of twist-two quark operators generated at  $m_Z$  is thus from the quark energy momentum tensor, whose contribution is known exactly. The other contributions are subdominant, and may be estimated from the parton distribution functions (PDFs); helpful for this is [38]. The expression for (5.35), written in terms of the operators evaluated at a lower scale, will not be reproduced here. However, it was checked that for a lower scale equal to 1 GeV, the subdominant contributions that require knowledge of the PDFs amount to only about 17% in the case of the  $W$ -contribution and 14% in the case of the  $Z$ -contribution (care was taken to decrease the active number of quark flavors from five to four at the scale of the bottom quark mass and from four to three at the scale of the charm quark mass). This shows that the nucleon matrix element of the twist-two quark operator can be estimated reliably.

The nucleon matrix element of the twist-two quark operators may be evaluated by using the expression [2]

$$\begin{aligned} \langle N(p) | \mathcal{O}_q^{(2)\mu\nu} | N(p) \rangle &= \frac{1}{m_N} \left( p^\mu p^\nu - \frac{1}{4} m_N^2 g^{\mu\nu} \right) \\ &\times \int_0^1 dx x (q(x, \mu^2) + \bar{q}(x, \mu^2)), \end{aligned} \quad (5.39)$$

where  $p^\mu$  denotes the momentum of the nucleon, and zero momentum transfer was assumed. The PDF  $q(x, \mu^2)$  (or  $\bar{q}(x, \mu^2)$ ) gives the probability density of finding the quark  $q$  (or anti-quark  $\bar{q}$ ) in the nucleon with momentum fraction  $x$ . The integral denotes the second moment of the

PDF, and one may define

$$q(2, \mu^2) = \int_0^1 dx x q(x, \mu^2). \quad (5.40)$$

The PDFs depends on the scale  $\mu$  at which the twist-two operator was generated, so that here  $\mu = m_Z$ . Using the website [38] and the results from the CTEQ group (CTEQ6M) [39], the second moment of the PDFs may be determined directly at this scale (equivalently,  $q(2, \mu^2)$  may be determined at  $\mu = 1$  GeV if the linear combination of twist-two quark operators is first rescaled down to 1 GeV). The second moment of the PDFs for the proton for  $\mu = m_Z$  are given by

$$\begin{aligned} u(2) &\simeq 0.221, & \bar{u}(2) &\simeq 0.034, \\ d(2) &\simeq 0.115, & \bar{d}(2) &\simeq 0.039, \\ s(2) &\simeq 0.026, & \bar{s}(2) &\simeq 0.026, \\ c(2) &\simeq 0.019, & \bar{c}(2) &\simeq 0.019, \\ b(2) &\simeq 0.012, & \bar{b}(2) &\simeq 0.012, \\ G(2) &\simeq 0.47. \end{aligned} \quad (5.41)$$

$G(2)$  is the PDF of the gluon, which is not needed here. For the neutron, the values of  $u(2)$  and  $\bar{u}(2)$  are interchanged with  $d(2)$  and  $\bar{d}(2)$ , respectively.

The nucleon matrix elements discussed above may now be used to write the spin-independent effective Lagrangian for non-chiral dark matter scattering off nucleons as

$$\mathfrak{L}_{\text{eff}, N}^{\chi} \simeq \mathcal{C} m_N \left( \frac{1}{2} \chi \chi + \frac{1}{2} \chi^\dagger \chi^\dagger \right) \bar{N} N, \quad (5.42)$$

where  $\mathcal{C}$  is determined from equations (5.22) and (5.25) and using the nucleon matrix elements. The cross-section for the non-chiral dark matter particle to scatter off nuclei (normalized to a single nucleon) is then

$$\sigma_N^{\chi} = \frac{1}{\pi} \mu_{\chi N}^2 m_N^2 \mathcal{C}^2, \quad (5.43)$$

where  $\mu_{\chi N}^2$  is the reduced mass of the nucleon and the dark matter. The cross-section for a dark matter particle from an  $SU(2)_L$  triplet with  $Y = 0$  is roughly the same when scattering

off a proton or a neutron, and the average is given by

$$\sigma_N^{L^0} \simeq 1.9 \times 10^{-45} \text{ cm}^2. \quad (5.44)$$

The cross-section for a dark matter particle from two  $SU(2)_L$  doublets with opposite hypercharge  $Y = \pm 1$ , after splitting the Dirac state into a pseudo-Dirac state, is also roughly the same when scattering off a proton or a neutron, and the average is given by

$$\sigma_N^{\chi^1} \simeq 2.1 \times 10^{-46} \text{ cm}^2. \quad (5.45)$$

A Higgs mass of  $m_h = 120$  GeV was assumed. For higher dimensional representations there are additional factors which increase the cross-section, as discussed below equations (5.22) and (5.25). For example, a quintuplet of  $SU(2)_L$  with  $Y = 0$  has a cross-section that is larger by a factor of 9 than the triplet cross-section, i.e.  $\sigma \simeq 1.7 \times 10^{-44} \text{ cm}^2$ .

Figure 5.3 shows the results for the cross-section and how they compare to current experimental exclusion bounds, as well as projected future bounds. The current upper bound on the direct detection cross-section is roughly two to three orders of magnitude higher than the calculated cross-sections in (5.44) and (5.45), respectively. Interestingly, XENON1T will get close to, but not quite reach, the required sensitivity to see an  $SU(2)_L$  triplet with zero hypercharge and should be able to detect an  $SU(2)_L$  quintuplet with zero hypercharge, while SuperCDMS 25kg / 7-ST at Snolab will not quite be able to detect the triplet, but will get close to detecting the quintuplet. Experiments planned for well into the future, such as the proposed SuperCDMS ‘‘Phase C’’ [16, 17], should be able to also probe the required parameter space for the case of the two  $SU(2)_L$  doublets with opposite hypercharge.

## 5.4 Higgs contribution to the Direct Detection

### Cross-Section and Singlet Dark Matter

In this section, singlet dark matter will be discussed, and a useful characterization of its direct detection cross-section will be given. Dark matter that is a singlet under  $SU(2)_L \times U(1)_Y$  does not have any irreducible couplings to quarks, unlike the non-chiral dark matter discussed

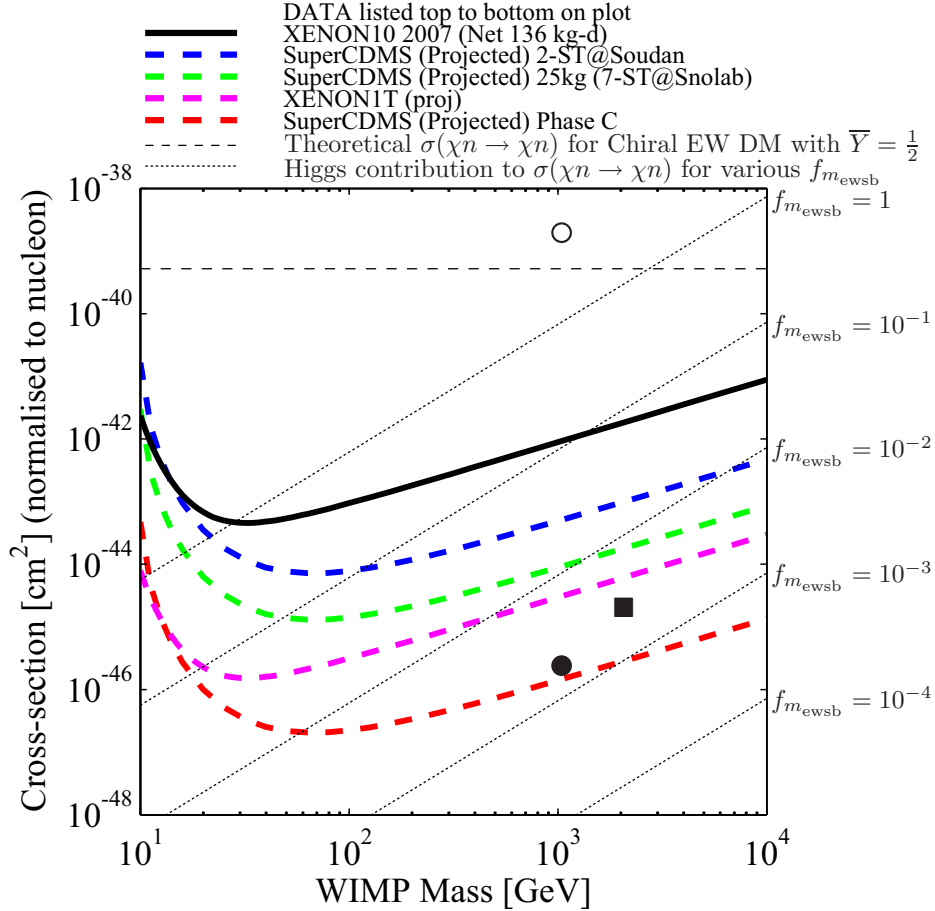


Figure 5.3: A comparison of the results presented in this paper with current and projected experimental bounds for the cross-section of dark matter scattering off a nucleon. Shown are the current experimental upper bounds from XENON10 (solid black line) [14], and the projected upper bounds for SuperCDMS 2-ST at Soudan (blue dashed line), SuperCDMS 25kg / 7-ST at Snolab (green dashed line), XENON1T (magenta dashed line) and SuperCDMS Phase C (red dashed line) [15, 16, 17]. The dashed black horizontal line is the theoretical lower bound on the cross-section for chiral electroweak dark matter scattering coherently off nuclei via the exchange of a  $Z$ -boson, see §5.2. The black dot (●) is the predicted cross-section for a 1 TeV non-chiral dark-matter particle part of two  $SU(2)_L$  doublets with opposite hypercharge (a complex representation of  $SU(2)_L$ ), assuming its coupling to the  $Z$ -boson is forbidden by splitting the Dirac state into a pseudo-Dirac state; see §5.3.2. Without the latter assumption, the cross-section is given by the open circle (○) and would be ruled out. The black square (■) is the predicted cross-section for a 2 TeV non-chiral dark matter particle part of an  $SU(2)_L$  triplet with zero hypercharge (a real representation of  $SU(2)_L$ ), see §5.3.1. Dark matter from higher order real or complex representations has a larger direct-detection cross-section than those represented by the black square or by the black dot, respectively, see §5.3. The dotted diagonal lines represent the Higgs contribution to dark matter scattering off nucleons for a range of magnitudes of the Higgs to dark matter coupling. This coupling also determines what fraction,  $f_{m_{\text{ewsb}}} \equiv m_{\text{ewsb}}/m_\chi$ , of the dark matter mass comes from electroweak symmetry breaking, and the lines shown are for various  $f_{m_{\text{ewsb}}}$ . The experimental results shown in this figure were obtained through [40].

in §5.3. It will be assumed that the singlet dark matter does not couple to the Higgs at the renormalizable level and does not obtain a mass spontaneously. Rather, the singlet will be allowed in the Lagrangian to have an explicit mass term which is not associated with the EW scale. Although there is no renormalizable coupling between the singlet and the SM, no symmetries forbid the existence of a non-renormalizable interaction generated by new physics beyond the SM at some high scale. The gauge invariant operator coupling the dark matter  $\chi$  to the Higgs is an infinite sum of higher-dimensional operators,

$$\mathcal{L}_{h\chi\chi} = \frac{c_1}{\Lambda_1} \chi\chi H^\dagger H + \frac{c_2}{\Lambda_2^3} \chi\chi (H^\dagger H)^2 + \dots + \frac{c_n}{\Lambda_n^{2n-1}} \chi\chi (H^\dagger H)^n + \dots, \quad (5.46)$$

where one Higgs field is replaced by the physical Higgs boson  $h/\sqrt{2}$ , and all others acquire a vacuum expectation value of  $v/\sqrt{2} \simeq 174$  GeV. The  $c_n$  are dimensionless coefficients and the  $\Lambda_n$  are the scales at which the higher dimensional operators are generated by new physics.

The Higgs-dark-matter coupling (5.46) is allowed more generally for any non-chiral dark matter, whether it is a singlet or forms a non-trivial representation of the EW gauge group. For singlet dark matter, the coupling (5.46) is generated at a scale  $\Lambda_1$  by new physics. For non-chiral dark matter with non-trivial EW quantum numbers, the coupling is already generated at the EW scale by integrating out the  $W$ -bosons (and, for complex representations, also the  $Z$ -boson), as shown in Figure 5.1 in §5.3.

The existence of this Higgs to dark matter coupling also implies the existence of additional contributions to the dark matter mass when all of the Higgs fields in (5.46) acquire a vacuum expectation value. This means that non-chiral dark matter obtains at least some of its mass from EWSB. Denoting the dark matter mass by  $m_\chi$  and the mass that is not associated with EWSB by  $m_0$ , gives the relation

$$m_\chi = m_0 + m_{\text{ewsb}}, \quad (5.47)$$

where  $m_{\text{ewsb}} \simeq \frac{v^2}{2\Lambda_1} + \dots$  is the mass gained from EWSB.

The mass obtained by the dark matter from EWSB is a useful characterization of the Higgs

contribution to the direct detection cross-section. The latter is given by (see also [41], [42])

$$\sigma_N^\chi \simeq \frac{g^2}{4\pi m_W^2 m_h^4} \mu_{\chi N}^2 m_N^2 \left( \sum_q f_{T_q}^N \right)^2 g_{h\chi\chi}^2, \quad (5.48)$$

where  $g_{h\chi\chi} \simeq c_1 v / 2\Lambda_1 \simeq m_{\text{ewsb}}/v$  is the Higgs to dark matter coupling, and  $f_{T_q}^N$  may be taken from equations (5.29) – (5.32). Evaluating the cross-section for  $m_h \simeq 120$  GeV gives

$$\sigma_N^\chi \simeq 8 \times 10^{-47} \mu_{\chi N}^2 m_{\text{ewsb}}^2, \quad (5.49)$$

or,

$$\sigma_N^\chi \simeq 8 \times 10^{-47} \mu_{\chi N}^2 m_\chi^2 f_{m_{\text{ewsb}}}^2, \quad (5.50)$$

where

$$f_{m_{\text{ewsb}}} \equiv \frac{m_{\text{ewsb}}}{m_\chi} \quad (5.51)$$

is the dark matter mass fraction obtained from EWSB. The cross-section is seen to be directly proportional to the square of this fraction.

The various dotted lines in Figure 5.3 show the cross-section for  $f_{m_{\text{ewsb}}} = 1, 10^{-1}, 10^{-2}, 10^{-3}$ , and  $10^{-4}$ , as well as the current experimental bounds. (Constraints on  $m_\chi$  and  $f_{m_{\text{ewsb}}}$  from the known dark matter relic density are not included in the present discussion, but see for example [41], [42]). These lines represent the Higgs contribution to the direct detection cross-section. Modulo destructive interference with other contributions, they represent the lower bounds of the direct detection cross-section also for non-chiral dark matter that is not an EW singlet.

If the dark matter is associated with new physics at the EW scale, the fraction  $f_{m_{\text{ewsb}}}$  should not be too small. The current bound has ruled out dark matter with a mass heavier than about 1 TeV and that obtains more than 10% of its mass from EWSB. SuperCDMS “Phase C” would be able to rule out dark matter with a mass heavier than about 1 TeV and that obtains more than about 0.1% of its mass from EWSB. This means that, assuming  $c_1 \sim \mathcal{O}(1)$ , SuperCDMS “Phase C” would probe a scale of  $\Lambda_1 \sim \mathcal{O}(30 \text{ TeV})$ . As the direct detection experiments probe ever smaller values of  $f_{m_{\text{ewsb}}}$ , the absence of any direct detection signal would make relevant the question of whether one should abandon the idea that dark matter is associated with new physics at the EW scale.

## 5.5 Conclusions

Fermion dark matter transforming under the electroweak gauge group  $SU(2)_L \times U(1)_Y$  was added to the standard model, and the observational consequences at a direct detection experiment were discussed. Figure 5.3 summarizes the results.

Chiral electroweak dark matter is well known to be not a viable dark matter candidate, as it has a spin-independent coupling to nuclei via the  $Z$ -boson, which gives a cross-section that is ruled out by two to three orders of magnitude.

Non-chiral dark matter from real representations of  $SU(2)_L \times U(1)_Y$  has an irreducible one-loop spin-independent coupling to nuclei. The triplet has a mass of about 2 TeV and a cross-section that is about two order of magnitude below current experimental bounds. A future experiment with a very large sensitivity, such as the proposed XENON1T, may come close to probing the relevant region of parameter space. Higher order representations have a larger cross-section which makes it easier to detect them.

Non-chiral dark matter from complex representation of  $SU(2)_L \times U(1)_Y$  have a tree-level coupling to nuclei via  $Z$ -boson exchange, which would rule it out unless this tree-level coupling can be suppressed somehow. For two  $SU(2)_L$  doublets with opposite hypercharge the tree-level coupling can be suppressed by a dimension five operator that couples the Higgs to the dark matter particle and is able to split the neutral Dirac state into a pseudo-Dirac state. The remaining irreducible one-loop coupling allows such a dark matter particle to be detected at a very sensitive future planned direct detection experiment such as SuperCDMS “Phase C”. Its mass is required to be about 1 TeV to reproduce the observed dark matter relic density.

Although a detailed LHC collider study was not done, non-chiral dark matter particles are most likely extremely difficult to detect at the LHC. The reason is that not many of them will be produced since they are not only required to be heavy to reproduce the observed relic density, but they are also weakly interacting. This is in addition to the fact that they would not even provide a signal that can easily be triggered on.

Non-chiral dark matter has a coherent coupling to the standard model fermions through the Higgs field. The existence of this coupling to the Higgs also means that at least some of its mass is obtained from electroweak symmetry breaking. Non-chiral dark matter from non-trivial representations of the electroweak gauge group does indeed gain a small fraction, about  $10^{-3}$ , of its mass from electroweak symmetry breaking. For dark matter that is a singlet under the electroweak gauge group, a non-renormalizable coupling to the Higgs could allow it to be detected at a direct detection experiment (the singlet's dominant coupling to the Higgs was assumed to be through a dimension five operator). A useful characterization of the direct detection cross-section is given by the fraction of mass that the dark matter particle obtains through electroweak symmetry breaking, the amplitude being directly proportional to this fraction. The current experimental bound has ruled out dark matter with a mass heavier than about 1 TeV and that obtains more than 10% of its mass from EWSB. SuperCDMS “Phase C” would be able to rule out dark matter with a mass heavier than about 1 TeV and that obtains more than 0.1% of its mass from EWSB. As the direct detection experiments probe ever more of the available parameter space, the absence of any direct detection signal would at some point make relevant the question of whether one should abandon the idea that dark matter is associated with new physics at the EW scale.

## References

- [1] D. N. Spergel *et al.*, “Wilkinson Microwave Anisotropy Probe (WMAP) three year results: Implications for cosmology,” [astro-ph/0603449](#).
- [2] G. Jungman, M. Kamionkowski, and K. Griest, “Supersymmetric dark matter,” *Phys. Rept.* **267** (1996) 195–373, [hep-ph/9506380](#).
- [3] **CDMS** Collaboration, D. S. Akerib *et al.*, “Limits on spin-dependent WIMP nucleon interactions from the Cryogenic Dark Matter Search,” [astro-ph/0509269](#).
- [4] **CDMS** Collaboration, D. S. Akerib *et al.*, “Limits on spin-independent WIMP nucleon interactions from the two-tower run of the Cryogenic Dark Matter Search,” [astro-ph/0509259](#).
- [5] **DAMA** Collaboration, R. Bernabei *et al.*, “Search for WIMP annual modulation signature: Results from DAMA / NaI-3 and DAMA / NaI-4 and the global combined analysis,” *Phys. Lett.* **B480** (2000) 23–31.
- [6] R. Bernabei *et al.*, “Dark matter search,” *Riv. Nuovo Cim.* **26N1** (2003) 1–73, [astro-ph/0307403](#).
- [7] B. Ahmed *et al.*, “The NAIAD experiment for WIMP searches at Boulby mine and recent results,” *Astropart. Phys.* **19** (2003) 691–702, [hep-ex/0301039](#).
- [8] **PICASSO** Collaboration, M. Barnabe-Heider *et al.*, “Status of the PICASSO project,” *Nucl. Phys. Proc. Suppl.* **138** (2005) 160–162, [hep-ex/0312049](#).
- [9] **Boulby Dark Matter** Collaboration, V. A. Kudryavtsev, “Dark matter experiments at Boulby Mine,” *Springer Proc. Phys.* **98** (-143) [astro-ph/0406126](#).
- [10] A. Benoit *et al.*, “Improved exclusion limits from the EDELWEISS WIMP search,” *Phys. Lett.* **B545** (2002) 43–49, [astro-ph/0206271](#).
- [11] G. Angloher *et al.*, “Limits on WIMP dark matter using scintillating CaWO<sub>4</sub> cryogenic detectors with active background suppression,” *Astropart. Phys.* **23** (2005) 325–339, [astro-ph/0408006](#).
- [12] E. Aprile *et al.*, “Simultaneous Measurement of Ionization and Scintillation from Nuclear Recoils in Liquid Xenon as Target for a Dark Matter Experiment,” [astro-ph/0601552](#).
- [13] **WARP** Collaboration, P. Benetti *et al.*, “Measurement of the specific activity of Ar-39 in natural argon,” [astro-ph/0603131](#).
- [14] **XENON** Collaboration, J. Angle *et al.*, “First Results from the XENON10 Dark Matter Experiment at the Gran Sasso National Laboratory,” [arXiv:0706.0039 \[astro-ph\]](#).
- [15] **The XENON** Collaboration, E. Aprile, “The XENON dark matter experiment,” [astro-ph/0502279](#).
- [16] **CDMS-II** Collaboration, P. L. Brink *et al.*, “Beyond the CDMS-II dark matter search: SuperCDMS,” *ECONF* **C041213** (2004) 2529, [astro-ph/0503583](#).

- [17] **The SuperCDMS** Collaboration, R. W. Schnee *et al.*, “The superCDMS experiment,” [astro-ph/0502435](#).
- [18] S. Eidelman *et al.*, “Review of particle physics,” *Phys. Lett.* **B592** (2004) 1.
- [19] M. W. Goodman and E. Witten, “Detectability of certain dark-matter candidates,” *Phys. Rev.* **D31** (1985) 3059.
- [20] S. D. Thomas and J. D. Wells, “Massive doublet leptons,” *Phys. Rev. Lett.* **81** (1998) 34–37, [hep-ph/9804359](#).
- [21] S. Profumo and C. E. Yaguna, “A statistical analysis of supersymmetric dark matter in the MSSM after WMAP,” *Phys. Rev.* **D70** (2004) 095004, [hep-ph/0407036](#).
- [22] M. Cirelli, A. Strumia, and M. Tamburini, “Cosmology and Astrophysics of Minimal Dark Matter,” [arXiv:0706.4071](#) [[hep-ph](#)].
- [23] K. Cheung and C.-W. Chiang, “Splitting the split supersymmetry,” *Phys. Rev.* **D71** (2005) 095003, [hep-ph/0501265](#).
- [24] L. J. Hall, T. Moroi, and H. Murayama, “Sneutrino cold dark matter with lepton-number violation,” *Phys. Lett.* **B424** (1998) 305–312, [hep-ph/9712515](#).
- [25] D. Tucker-Smith and N. Weiner, “The status of inelastic dark matter,” *Phys. Rev.* **D72** (2005) 063509, [hep-ph/0402065](#).
- [26] P. C. Schuster and N. Toro, “Is dark matter heavy because of electroweak symmetry breaking? Revisiting heavy neutrinos,” [hep-ph/0506079](#).
- [27] G. Belanger, A. Pukhov, and G. Servant, “Dirac Neutrino Dark Matter,” [arXiv:0706.0526](#) [[hep-ph](#)].
- [28] F. D’Eramo, “Dark matter and Higgs boson physics,” *Phys. Rev.* **D76** (2007) 083522, [arXiv:0705.4493](#) [[hep-ph](#)].
- [29] D. R. Smith and N. Weiner, “Inelastic dark matter,” *Phys. Rev.* **D64** (2001) 043502, [hep-ph/0101138](#).
- [30] J. D. Lewin and P. F. Smith, “Review of mathematics, numerical factors, and corrections for dark matter experiments based on elastic nuclear recoil,” *Astropart. Phys.* **6** (1996) 87–112.
- [31] K. Cheung, C.-W. Chiang, and J. Song, “A minimal supersymmetric scenario with only  $\mu$  at the weak scale,” [hep-ph/0512192](#).
- [32] U. Chattopadhyay, D. Choudhury, M. Drees, P. Konar, and D. P. Roy, “Looking for a heavy higgsino LSP in collider and dark matter experiments,” *Phys. Lett.* **B632** (2006) 114–126, [hep-ph/0508098](#).
- [33] M. Cirelli, N. Fornengo, and A. Strumia, “Minimal dark matter,” [hep-ph/0512090](#).
- [34] J. Hisano, S. Matsumoto, M. M. Nojiri, and O. Saito, “Direct detection of the Wino- and Higgsino-like neutralino dark matters at one-loop level,” *Phys. Rev.* **D71** (2005) 015007, [hep-ph/0407168](#).
- [35] J. R. Ellis, A. Ferstl, and K. A. Olive, “Re-evaluation of the elastic scattering of supersymmetric dark matter,” *Phys. Lett.* **B481** (2000) 304–314, [hep-ph/0001005](#).
- [36] M. Drees and M. M. Nojiri, “New contributions to coherent neutralino - nucleus scattering,” *Phys. Rev.* **D47** (1993) 4226–4232, [hep-ph/9210272](#).

- [37] M. E. Peskin and D. V. Schroeder, *An Introduction to Quantum Field Theory*. Westview Press, 1995.
- [38] "<http://durpdg.dur.ac.uk/hepdata/pdf3.html>."
- [39] J. Pumplin *et al.*, "New generation of parton distributions with uncertainties from global QCD analysis," *JHEP* **07** (2002) 012, [hep-ph/0201195](#).
- [40] R. Gaitskell, V. Mandic, and J. Filippini, "<http://dendera.berkeley.edu/plotter/entryform.html>."
- [41] J. McDonald, "Gauge Singlet Scalars as Cold Dark Matter," *Phys. Rev.* **D50** (1994) 3637–3649, [hep-ph/0702143](#).
- [42] Y. G. Kim and K. Y. Lee, "The minimal model of fermionic dark matter," *Phys. Rev.* **D75** (2007) 115012, [hep-ph/0611069](#).

## Chapter 6

# Extracting Hadronic Resonances using Jet Ensemble Correlations

This chapter is a summary of work done with Shan-Huei Chuang, Eva Halkiadakis, Amit Lath, and Scott Thomas (to appear).

A search strategy is presented for the pair production of new heavy colored fermions transforming as an octet of the Standard Model color group and each decaying into three quarks without leptons or missing energy. The resulting six-jet final state suffers from a large Standard Model background, predominantly from pure QCD six-jet production, but also from the all-hadronic decay of the top quark. Innovative cuts making use of a variety of kinematic cuts and correlations and kinematic features found in observables formed from the signal jets, which are absent for the same observables formed from background jets, are required to extract the three-jet resonance from these new particle. In addition, use is made of an *ensemble* of reconstructed objects to increase signal efficiency. The mass reach is about 650-700 GeV for  $\mathcal{L} \gtrsim 10 \text{ fb}^{-1}$ . Particles with masses as large as 300 GeV can potentially be observed with only 100  $\text{pb}^{-1}$  of integrated luminosity, which can be obtained soon after the start of the LHC. The analysis method presented here is also applicable for extracting the top quark resonance in the all-hadronic channel, as well as for multi-jet signals in association with leptons and missing energy.

## 6.1 Introduction

There are a wide variety of possible discovery signatures for new physics at the Large Hadron Collider (LHC). One that has not been well studied involves multi-jet events, both with and without leptons and/or missing energy. Jets are produced in QCD hard scattering processes that create high transverse momentum quarks or gluons. Since quarks and gluons carry a color charge, QCD confinement does not allow them to be detected directly in their free form and instead they turn into a spray of hadrons confined to a narrow cone, called a jet. Jets are ubiquitously produced in standard model (SM) QCD processes which will dominate at the LHC, and this may easily hide new physics beyond the standard model that also produces jets. This is why much of the community is focused on extracting new physics from more conventional discovery signals, such as multi-leptons and missing energy with no, or very few, jets, which do not have such a large standard model background. However, there are many new physics signals that could only, or predominantly, involve jets, so an analysis of discovery signatures which involve many jets is essential. Moreover, since any new particles which produce multi-jet events couple strongly, their production cross-section at the LHC tends to be large. This opens up the possibility that they could be among the first things to be discovered at the LHC, provided that suitable search strategies are developed.

In this work, pair production of a new heavy colored particle  $Q$  that undergoes a three-body decay into jets will be considered. (Table 6.1 lists the possible representations and decay modes of new heavy colored particles. We focus on the case when  $Q$  is a fermion transforming as an octet under  $SU(3)_C$ .) One can imagine the existence of such a particle in many extensions of the Standard Model (SM). For example, these particles and their decay channel can appear in technicolor-like extensions of the SM, see e.g. [1, 2, 3, 4]. They also appear in supersymmetry, where the gluino (the superpartner of the gluon) is a colored adjoint Majorana fermion and can decay to three jets if R-parity is not conserved.

The signal of interest is therefore a six-jet final state with no leptons and no missing energy ( $QQ \rightarrow 6$  jets). (Such a signal was considered a long time ago in [5, 6].) This signal has a very

$SU(3)_C$	Lowest Multiplicity Production Modes	Low Multiplicity Decay Modes	Hadron Collider Signatures
Fermion			
<b>8</b>	$gg, q\bar{q} \rightarrow QQ$	$Q \rightarrow qq\bar{q}, \bar{q}q\bar{q}$	$(jjj)(jjj)$
<b>6, <math>\bar{6}</math></b>	$g\bar{q} \rightarrow Q, gq \rightarrow \bar{Q}$ $gg, q\bar{q} \rightarrow Q\bar{Q}$	$Q \rightarrow g\bar{q}, \bar{Q} \rightarrow gq$ $Q \rightarrow q\bar{q}\bar{q}, \bar{Q} \rightarrow \bar{q}q\bar{q}$	$(jj)$ $(jjj)$ $(jj)(jj)$ $(jjj)(jj)$ $(jjj)(jjj)$
<b>3, <math>\bar{3}</math></b>	$gq \rightarrow Q, g\bar{q} \rightarrow \bar{Q}$ $gg, q\bar{q} \rightarrow Q\bar{Q}$	$Q \rightarrow gq, \bar{Q} \rightarrow g\bar{q}$ $Q \rightarrow qq\bar{q}, \bar{Q} \rightarrow \bar{q}q\bar{q}$	$(jj)$ $(jjj)$ $(jj)(jj)$ $(jjj)(jj)$ $(jjj)(jjj)$
Scalar			
<b>8</b>	$gg, q\bar{q} \rightarrow Q$ $gg, q\bar{q} \rightarrow Q\bar{Q}$	$Q \rightarrow gg, q\bar{q}$	$(jj)$ $(jj)(jj)$
<b>6, <math>\bar{6}</math></b>	$qq \rightarrow Q, \bar{q}\bar{q} \rightarrow \bar{Q}$ $gg, q\bar{q} \rightarrow Q\bar{Q}$	$Q \rightarrow qq, \bar{Q} \rightarrow \bar{q}\bar{q}$	$(jj)$ $(jj)(jj)$
<b>3, <math>\bar{3}</math></b>	$\bar{q}\bar{q} \rightarrow Q, qq \rightarrow \bar{Q}$ $gg, q\bar{q} \rightarrow Q\bar{Q}$	$Q \rightarrow \bar{q}\bar{q}, \bar{Q} \rightarrow qq$	$(jj)$ $(jj)(jj)$

Table 6.1: Lorentz and gauge invariant color flow restrictions on resonant and two-body production and decay modes to quarks and gluons of fermion and scalar triplet, quix, and octet representations transforming as **3** or  $\bar{\mathbf{3}}$ , **6** or  $\bar{\mathbf{6}}$ , or **8** under  $SU(3)_C$ , respectively. Shown in parenthesis are the possible resonances.

large background coming from pure QCD six-jet production and a smaller background coming from the all-hadronic decay of the top quark, which also produces six jets. Since the new heavy particle  $Q$  decays via a three-body decay into three jets, it should be seen as a resonance when forming the invariant mass of three jets. However, innovative cuts are required in order to extract this resonance. This is due to the very large number of background events which can completely swamp the signal, and also due to the large amount of combinatoric confusion from not knowing how to select the three jets coming from the decay of one of the  $Q$ 's. This work will propose an innovative search strategy to look for these type of particles. It is worth emphasizing that the search strategies developed here are more widely applicable.

In §6.2, an overview of the simulation tools and the analysis strategy will be given. §6.3 contains the analysis and the results of this work. The conclusions are presented in §6.4. There are three appendices with more information in Sections 6.5, 6.6, and 6.7.

## 6.2 Simulation Tools and Overview of Analysis

### 6.2.1 Discussion of Simulation Tools

We are interested in detecting the pair production of a new heavy particle (denoted by  $Q$ ) that undergoes a three-body decay into quarks/gluons to produce a six-jet final state. In particular, we simulated with PYTHIA [7] the pair production of a colored adjoint Majorana fermion that undergoes a three-body decay into jets. Such a particle and decay mode may be found in the Minimal Supersymmetric Standard Model with R-parity violation, where the superpartner of the gluon (called a gluino) can be made to decay into three quarks. PYTHIA can simulate the production of two gluinos, each of which undergoes a three-body decay via an intermediate off-shell squark ( $\tilde{q}^*$ ) to produce a six-jet final state ( $\tilde{g}\tilde{g} \rightarrow \tilde{q}^*j\tilde{q}^*j \rightarrow 6j$ ), see Fig. 6.1. The mass of the gluino was chosen to lie between 300 GeV and 900 GeV (with the remainder of the MSSM particles decoupled).

For the SM background that also produces a six-jet final state, we included the all-hadronic

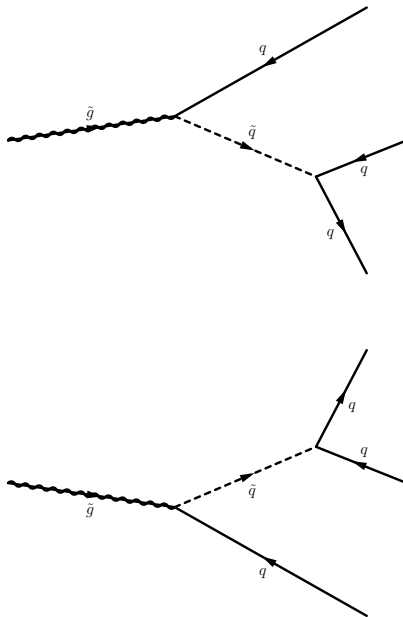


Figure 6.1: The decay of two gluinos to six quarks, via an intermediate off-shell squark, producing a six jet final state. Events of this type were generated with PYTHIA using the Minimal Supersymmetric Standard Model with R-parity violation.

decay of the top quark ( $\bar{t}t \rightarrow \bar{b}W^-bW^+ \rightarrow 6j$ ), which we generated with PYTHIA, and the pure QCD six-jet background. The pure QCD background was generated with the help of ALPGEN [8, 9, 10]. ALPGEN generates events with six-quarks in the final state. These events were then run through PYTHIA to simulate the showering and hadronization of the quarks.

The generated events were run through the “Pretty Good Simulation” (PGS 4) detector [11]. PGS 4 is a fast detector simulation which efficiently simulates the detection of jets, electrons, muons, and taus. In particular, the jet algorithm looks for jets within a cone whose diameter is  $\Delta R = 0.5$ . The hadronic calorimeter energy resolution is  $\sigma(E_T^{\text{jet}}) = 0.8\sqrt{E_T^{\text{jet}}}$ . Since PGS 4 is a fast detector simulation, a natural question to ask is whether it is realistic enough to simulate the very complicated CMS and ATLAS detectors at the LHC. To answer this question, the events were also run through the full detector simulation of the Compact Muon Solenoid (CMS) experimental collaboration using their CMS Software (CMSSW). We will discuss in an appendix (§6.5) the differences between PGS 4 and CMSSW, but the upshot is that the analysis done with PGS 4 is robust.

## 6.2.2 Overview of Analysis and Search Strategy

The analysis was done with ChROOT<sup>1</sup> which is based on ROOT<sup>2</sup>, the publicly available object oriented analysis framework from CERN. Many additional functions were written and added to ChROOT in order to do this analysis.

We now give an overview of the search strategy. The signal of interest in this work is a six-jet final state, with no leptons and no missing energy. The number of background events which also produce the same six-jet final state is extremely large and a priori swamps the number of signal events.<sup>3</sup> However, the jets coming from the new particle  $Q$  tend to have a significantly larger momentum transverse to the beam pipe than the jets coming from the pure QCD background and from the all-hadronic decay of the top quark. The ratio of signal events ( $S$ ) to background events ( $B$ ) can therefore be significantly increased by requiring the jets to have a large transverse momentum ( $p_T$ ). The particular kinematic cuts employed in this work include a cut on the sum of the transverse momenta of all the jets and a cut on the  $p_T$  of the sixth hardest jet. Even after these cuts, however, the ratio  $S/B$  is still less than one.

Each of the two  $Q$ 's undergoes a three-body decay into three jets, so that one way to separate the signal from the background is to look for resonances in three-body invariant mass distributions. One problem with this approach is that the cuts on the transverse momenta of the jets, which are necessary to obtain a manageable  $S/B$  ratio, tend to shape the three-body invariant mass distribution of the background events in such a way that it does not look too distinct from the three-body resonance shape from the signal events. It is desirable therefore to come up with a strategy (i.e. a set of cuts) which does shape the signal differently to the background.

---

<sup>1</sup>[http://v1.jthaler.net/olympicswiki/doku.php?id=lhc\\_olympics:chroot](http://v1.jthaler.net/olympicswiki/doku.php?id=lhc_olympics:chroot)

<sup>2</sup><http://root.cern.ch/>

<sup>3</sup>In fact, the *number* of background events is uncertain by at least a factor of three (M.L. Mangano, private communication). The reason for this uncertainty is that the six-jet pure QCD background is extremely difficult to calculate, and ALPGEN, which was used to generate this background, only does the tree-level amplitude exactly. This means that the normalization of the number of background events will have to be determined from actual data, rather than from calculations and simulations, and it is important to keep in mind this factor of three uncertainty when looking at numbers for  $S/B$  or  $S/\sqrt{B}$ . Moreover, the extreme size as well as the uncertainty in the background cross-sections are the two main reasons why simply counting the number of observed six jets events will not be sufficient to detect a signal.

A further problem with the simple strategy of looking for three-body invariant mass distributions is that it can only be effective if the three jets belonging to each of the two  $Q$ 's can be found among the six jets from the signal (which will be called “signal jets”). However, the number of ways that three jets can be picked from six is  $\binom{6}{3} = 20$ , so that there is a large amount of combinatoric confusion. (It is important to note that this combinatoric “background” is present without, and in addition to, the physics background from QCD and the all hadronic  $t\bar{t}$  decays.) A further problem, adding to the combinatoric confusion, is that there are basically always more than six jets in the signal events, since the signal jets radiate many more jets. Since these radiated jets tend to be softer, one might think that the six signal jets should be the hardest six jets in the event. However, it is possible that at least one of the radiated jets from a particular signal jet has a larger  $p_T$  than one of the other signal jets, so that the six signal jets are *not* always the six hardest jets in an event. In addition to this, initial state radiation (ISR) can produce a hard jet coming from a gluon radiated off the incoming protons just before the hard collision takes place. This jet can be harder than any of the six signal jets. This means that the six signal jets are often not found among the six hardest jets of a signal event. However, if one tries to find the three jets that come from one of the  $Q$ 's among the seven (or more) hardest jets, the combinatoric confusion becomes even more unmanageable (e.g.  $\binom{7}{3} = 35$ ). A priori, it is therefore not clear how to select the jets in order to produce a clean three-body resonance.

In this work, we will show that the above mentioned difficulties with separating background hadronic activity from new physics signals can be best dealt with by looking for distinguishing features or *correlations* among the jet observables. The main correlation that we will be interested in is that between the invariant mass of three jets versus the sum of the transverse momenta of the same three jets (although in an appendix (§6.6) we shall discuss correlations among a few other observables). Whereas the signal events display a clearly discernible correlation between these two quantities, the background events do not display the same correlation (or kinematic feature). The main use of the correlation is to allow us to identify, at least for some of the events, which three jets come from the decay of one of the  $Q$ 's. An appropriate

cut is then able to extract the events for which such an identification is possible. This greatly improves the ratio between the signal and the combinatoric and physics background.

Another important aspect to this work is the idea of making use of *an ensemble of jet combinations*. Recall that there is a large number of possible three-jet combinations that could come from the decay of a single  $Q$ . In order to determine the correct three-jet combinations, we can use Monte Carlo information to match the quarks coming from the decay of the  $Q$  with the jets that are found by the detector simulation. Ordering the jets according to their  $p_T$  this Monte Carlo information then tells us what fraction of the time any particular  $p_T$ -ordered three-jet combination is correct. In other words, it tells us what fraction of the time the first, second, and third hardest jet, or the first, second, and fourth hardest jet, or any other  $p_T$ -ordered three-jet combination in a signal event, is correct. For a large number of events, each of these three-jet combinations will be correct some of the time, but certain combinations are correct more often than others, and the Monte Carlo information allows us to determine the best ones.

Instead of using the kinematic feature or correlation discussed above to pull out those events for which only the best jet-triplet combination is correct, we can use an *ensemble* of jet-triplet combinations. The precise number of jet triplet combinations to use can be optimized, but we tested it with using 1, 8, and 16. The main point of using an ensemble is that it increases the number of signal events that pass all the cuts and can therefore increase the signal significance.

After all the cuts, the three-body invariant mass distribution for the signal together with the background looks like a narrow gaussian shape (from the signal) sitting on top of a broad hump (from the background). By carefully fitting for these two shapes we are able to extract the signal from the background with a significance of above five sigma for a wide range of  $Q$  masses, up to about 650 GeV - 700 GeV (the precise number of course depends on the normalization of the background).

	$\sigma$ (pb)	Events	$\mathcal{L}$ (fb <sup>-1</sup> )
$m_Q=290$ GeV	344	100000	0.3
$m_Q=420$ GeV	50	100000	2.0
$m_Q=660$ GeV	3.4	100000	29.6
$m_Q=890$ GeV	0.5	100000	215.5
6j, $p_T > 20$	407000	315069	0.00077
6j, $p_T > 50$	2400	434011	0.2
6j, $p_T > 80$	120	507428	4.2
6j, $p_T > 110$	14	448520	32.3
$t\bar{t}$	490	490000	1.0

Table 6.2: Data samples generated, their cross-sections, number of events in sample, and integrated luminosity. The cross-sections include a 5 GeV cut on the jets within PYTHIA, and assume  $|\eta| < 3.0$ .

## 6.3 Analysis and Results

### 6.3.1 Summary of Generated Data, Triggers, and Kinematic Cuts

We first summarize the data that we generated, see Table 6.2. The new physics signal is given by the production of a new  $QQ$  pair and its subsequent decay into six jets. Four data samples were generated with different masses for the  $Q$ 's, namely  $m_Q = 290$  GeV, 420 GeV, 660 GeV, and 880 GeV. The production cross-sections listed in Table 6.2 assume a very low cut on the jets of 5 GeV, with  $|\eta| \leq 3$ . The  $t\bar{t}$ -background was generated with the same cuts on the jets. Four samples for the six-jet QCD background were generated with ALPGEN assuming different cuts on the  $p_T$  of each of the six quarks, namely 20 GeV, 50 GeV, 80 GeV, and 110 GeV ( $\eta$  was assumed to lie within 3 in all cases). The ALPGEN generated six-quark events were then run through PYTHIA to do the showering and hadronization.

Next, we discuss the trigger-level cuts. At the LHC there are about  $10^9$  events every second, but only about 100 events per second can be recorded. A huge rejection rate is therefore required, and an event will only be recorded if it is deemed “interesting” and passes certain

$$\begin{aligned}
& |\eta_j| < 3 \quad j = 1, \dots, 6 \\
& \Delta R_{ij} > 0.5 \quad i, j = 1, \dots, 6 \\
& \left( \begin{aligned}
& p_{T,1} > 400 \text{ GeV} \quad \cup \\
& p_{T,2} > 350 \text{ GeV} \quad \cup \\
& p_{T,3} > 195 \text{ GeV} \quad \cup \\
& p_{T,4} > 80 \text{ GeV} \quad \cup \\
& \sum_{j=1}^6 p_{T,j} > 1000 \text{ GeV} \quad \cup
\end{aligned} \right) \\
& p_{T,6} > 30 \text{ GeV}
\end{aligned}$$

Table 6.3: High level triggers and event selection on  $p_T$  ordered jets. For the high level triggers see the CMS TDR [12, 13].

basic cuts, called “trigger-level” cuts. Also, although the events were generated with a very low cut on the jets of 5 GeV, such a low cut is not realistic. Thus, an additional “event selection cut” is made which requires the  $p_T$  of the sixth jet to be at least 30 GeV. The high level triggers and event selection cuts are summarized in Table 6.3. It turns out that the trigger which requires the fourth hardest jet to lie above 80 GeV dominates the others, and most events come in on this trigger.

A variety of kinematic cuts may be employed in order to increase the  $S/B$  ratio. We find that a cut on the sum of the transverse momenta of the six hardest jets ( $\sum_{i=1}^6 p_{T,i}$ ), as well as a cut on the transverse momentum of the sixth jet ( $p_{T,6}$ ), are two very useful cuts<sup>4</sup>. These cuts may be scaled with  $m_Q$ , i.e. harder cuts are used for larger  $m_Q$  (heavier  $Q$  will decay into jets that on average have a larger transverse momentum, since there is more phase space available for the jets). Figure 6.2(a) and 6.2(b) show the distribution of the events in the  $p_{T,6}$  versus  $\sum_{i=1}^6 p_{T,i}$  plane for the signal ( $m_Q = 290$  GeV) and the ALPGEN generated pure QCD background (assuming a  $p_T$  cut of 80 GeV on each of the six quarks), without any additional trigger- or

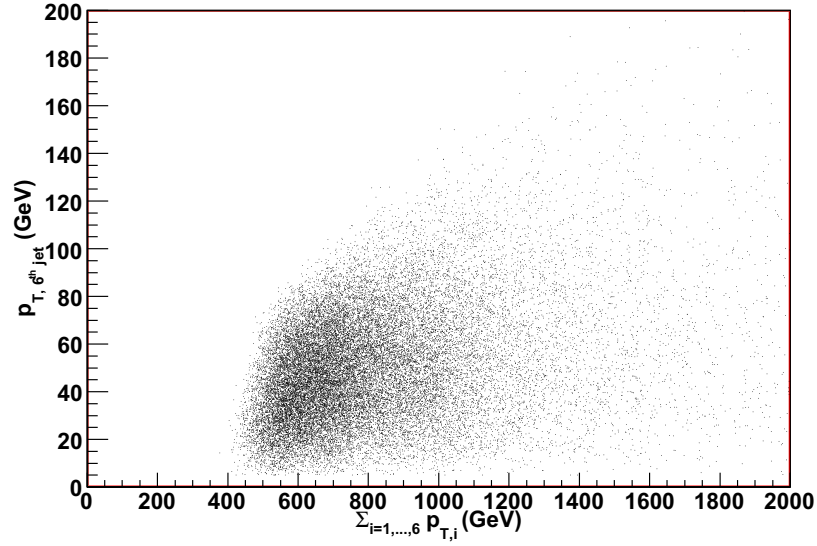
<sup>4</sup>There are other kinematic cuts that we tried, but found not to be so useful. Recall that one problem in selecting the correct six jets coming from the decay of the  $Q$ 's is that we cannot be sure that they are among the six hardest jets in an event. However, requiring the  $p_T$  of the seventh hardest jet to be very *small* increases the chances that the seventh hardest jet and the other softer jets are indeed radiated jets and not signal jets. It may be worth to further study such a cut.

analysis-level cuts, for  $\mathcal{L}=250 \text{ pb}^{-1}$ . Table 6.4 shows the cross-sections for the various data samples after trigger and event-selection cuts and after various cuts on the kinematic variables  $\sum_{i=1}^6 p_{T,i}$  and  $p_{T,6}$ . It is clear that the pure QCD background is much larger than the signal, even after all the cuts. Making the cuts even harder can increase the  $S/B$  ratio, but it will hurt the signal efficiency too much (i.e., there will not be enough signal events left over to perform an analysis on). Note that the  $t\bar{t}$  background is also very small after these kinematic cuts. For  $m_Q \simeq m_t$ , the  $QQ$  production cross-section is larger than the  $t\bar{t}$  production cross-section, since the  $Q$  is an octet and the top is a fundamental of  $SU(3)_C$ . For larger  $m_Q$  their production cross-section decreases, but the jets from the  $Q$ -decay are harder than the jets from the  $t\bar{t}$ -decay. Although the cross-sections after the kinematic cuts are roughly comparable for the large  $m_Q$  samples, the three-jet invariant mass distributions for the  $QQ$  sample peak at much larger values than for the  $t\bar{t}$  sample, so that it is easy to separate the  $QQ$  signal from the  $t\bar{t}$  background.

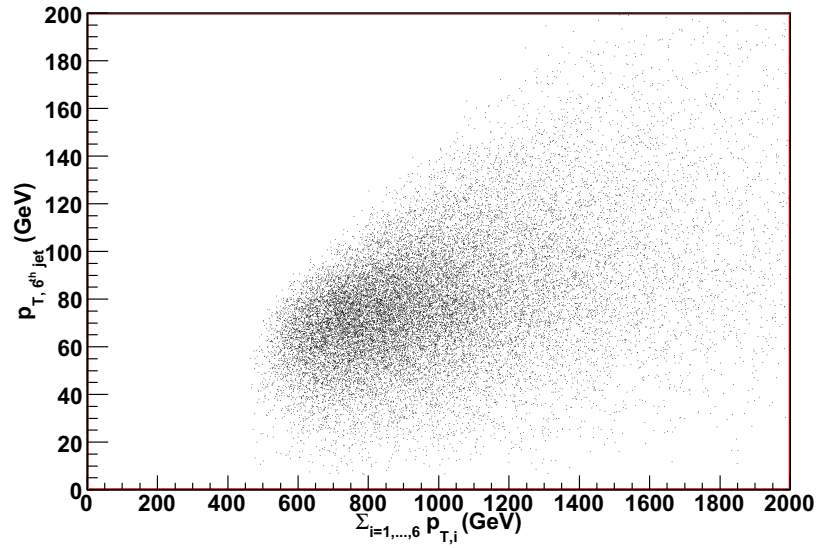
### 6.3.2 The search for the three-jet resonance

Each of the two  $Q$ 's undergoes a three-body decay into three jets, so that one way to separate the signal from the background is to look for resonances in three-body invariant mass distributions. These resonances should be present for the signal, but not for the QCD background. They will also be present for the  $t\bar{t}$  background, but the  $t\bar{t}$  background is easy to separate since it is either smaller than the pure QCD background, or the top quark resonance will be at much lower mass if  $m_Q$  is large (see discussion in §6.3.1).

Let us assume that the six signal jets are the six hardest jets in the signal event. We have seen that this is very often not actually true, see §6.2.2, but the combinatoric confusion will only get worse if we do not assume this. There are 20 ways to select three jets from six, and 10 pairs of three-jet combinations in which one member of the pair belongs to one of the  $Q$ 's, and the other member belongs to the other  $Q$ . How does one select the correct pair? One suggestion is to make use of the fact that the invariant mass of the two members of the pair must equal each other (and must equal  $m_Q$ , although when doing the analysis the value of



(a) Scatterplot for the signal  $m_Q = 290$  GeV, without any trigger- or analysis-level cuts, for  $\mathcal{L}=250$  pb $^{-1}$ .



(b) Scatterplot for the ALPGEN generated pure QCD background (assuming a  $p_T$  cut of 80 GeV on each of the six quarks), without any additional trigger- or analysis-level cuts, for  $\mathcal{L}=250$  pb $^{-1}$ .

Figure 6.2: The distribution of the events in the  $p_{T,6}$  versus  $\sum_{i=1}^6 p_{T,i}$  plane for signal and pure QCD background.

$m_Q$ (GeV)	$QQ$	$QQ$	$QQ$	$QQ$	QCD	$\bar{t}t$
	290	420	660	880	–	172
Trigger + Event Selection	98	30	2.8	0.42	10650	17
Cuts						
$\sum_{j=1}^6 p_{T,j}$ (GeV)	$p_{T,6}$ (GeV)					
600	30	83			8350	14
600	60	36			430	4.5
600	90	7.4			28	0.63
600	120	1.5			3.2	0.067
700	30		26		6000	11
700	60		14		360	3.7
700	90		4.5		28	0.61
700	120		1.2		3.2	0.067
1100	30			2.1	1150	2.4
1100	60			1.6	110	1.1
1100	90			0.94	17	0.29
1100	120			0.44	2.9	0.061
1500	30				0.28	210
1500	60				0.24	29
1500	90				0.18	6.4
1500	120				0.12	1.6

Table 6.4:  $\sigma(pp \rightarrow X \rightarrow 6j)$  cross sections in pb for adjoint Majorana fermion pair production, top quark pair production and QCD,  $X = \{QQ, t\bar{t}, \text{QCD}\}$ , with the triggers and event selection given in Table 6.3, and with additional  $\sum_{j=1}^6 p_{T,j}$  and  $p_{T,6}$  cuts on the  $p_T$  ordered jets.

$m_Q$  is of course unknown). This means that we can look for the pair which has the smallest difference in the invariant masses of the two members. The smaller of the two invariant masses satisfying this criterion is shown in Figure 6.3 for the signal with  $m_Q = 290$  GeV and for the pure QCD background (all the trigger-level, event selection, and kinematic cuts discussed in §6.3.1 are included). Looking at the signal in Fig.6.3(a), it is clear that there is a very large combinatoric background. With the rather hard kinematic cuts, the resonance is only barely visible at around 300 GeV, and the peak at around 600 GeV comes from the mismatching of the jet-triplets due to the combinatoric confusion. The background shown in Fig.6.3(b) is about four times larger and also peaks at about 600 GeV. This clearly shows the shaping of the signal and the background due to the hard kinematic cuts. It also suggests that selecting the pair of triplets that is closest in invariant mass does not help us much to extract the signal from the background. This conclusion remains roughly unchanged for other values of  $m_Q$  and for different kinematic cuts.

We also checked that requiring the difference of the invariant masses of the two members within the selected pair of triplets to be smaller than e.g. 60 GeV does not improve the signal shape significantly. Moreover, we checked that the difference in the invariant mass of the “best” pair is roughly the same as the difference in the invariant mass of the “second best” pair. This suggests that this method of selecting the correct triplets is not very good. In fact, we checked that selecting a random triplet is not significantly worse than selecting a triplet from the best pair.

The shape of the signal shown in Fig. 6.3 may be contrasted with the shape of the signal found from picking the correct triplets, shown in Fig. 6.4. The correct triplets may be found by using the Monte Carlo simulation information with which the quarks from the decay of the  $Q$ 's can be matched to the reconstructed jets. For each jet, the quark  $q$  or gluon  $g$  closest to it is found for which  $p_{T,q/g}/p_{T,\text{jet}} > 0.75$ . The value of  $\Delta R = \sqrt{(\Delta\phi)^2 + (\Delta\eta)^2}$  between the jet and the quark/gluon is required to be less than 0.5. We then check whether the parent, grandparent, or great-grandparent of the quark/gluon matched in this way is one of the  $Q$ 's. The efficiency

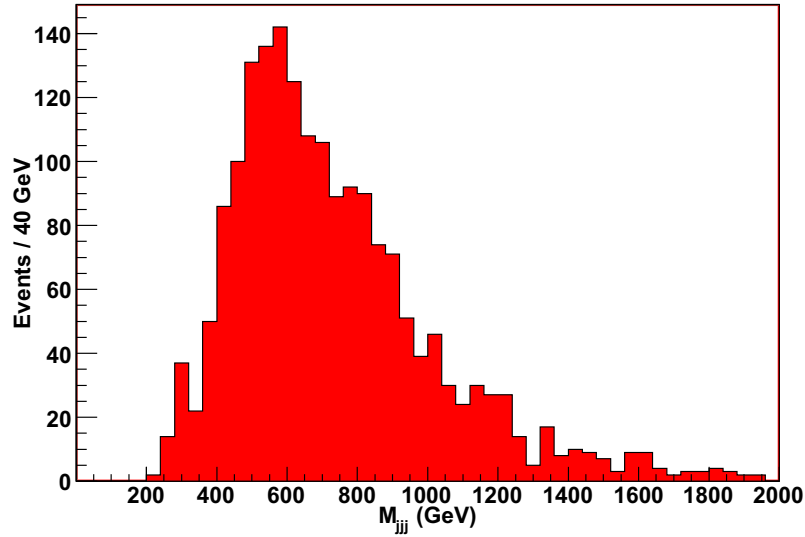
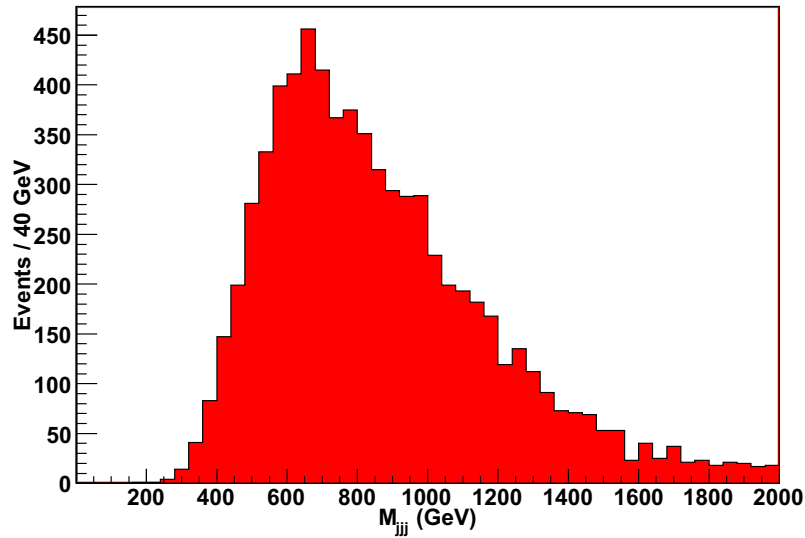
(a) Histogram for the signal  $m_Q = 290$  GeV.(b) Histogram for the pure QCD background (when generated with ALPGEN, a  $p_T$  cut of 80 GeV on each of the six quarks was assumed).

Figure 6.3: The figures show the three-jet invariant mass which was found as follows: form all 10 pairs of three-jet invariant mass combinations from the six hardest jets within an event and calculate the difference between the invariant masses of the two members of each pair. Find the pair with the smallest difference, and plot the smaller of the two invariant masses from this pair. All the trigger-level and event selection cuts as discussed in §6.3.1 are included. Also included are the two kinematic cuts  $\sum_{j=1}^6 p_{T,j} \geq 600$  GeV and  $p_{T,6} \geq 90$  GeV. The luminosity used in these plots is  $\mathcal{L}=250$  pb $^{-1}$ .

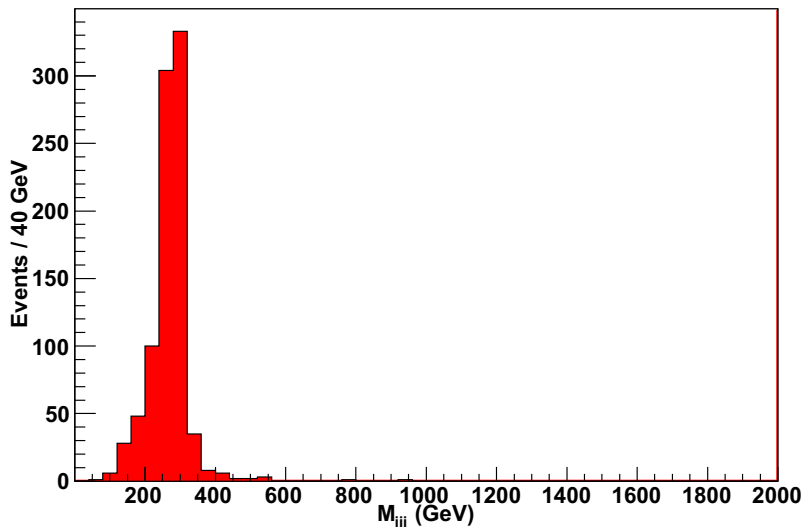


Figure 6.4: The three-jet invariant mass using Monte Carlo matching information for the same signal data as used in Fig. 6.3, i.e. for  $m_Q = 290$  GeV, including all the trigger-level and event selection cuts as discussed in §6.3.1, and also including the two kinematic cuts  $\sum_{j=1}^6 p_{T,j} \geq 600$  GeV and  $p_{T,6} \geq 90$  GeV. The luminosity used in this plot is  $\mathcal{L}=250$  pb $^{-1}$ .

of matching the quarks of at least one  $Q$  to the reconstructed jets is about 65-80%, depending on  $m_Q$ . The width of the resonance seen in Fig. 6.4 is due only to the imperfect hadronic calorimeter energy resolution (see further discussion of this in §6.5). Moreover, contrasting it with Fig. 6.3(a), it also clearly shows just how severe the combinatoric confusion is. The combinatoric background basically cannot be distinguished from the physics background from pure QCD.

The Monte Carlo matching of the reconstructed jets to the quarks from the decay of the  $Q$ 's can be used to determine which reconstructed jet-triplet combinations are correct most often. To do this, we first order the reconstructed jets according to their  $p_T$ , from high to low, and determine how often the reconstructed jet-triplet combination  $ijk$  can be matched to the quarks that come from the decay of a particular  $Q$  (here,  $i, j, k = 1, 2, \dots, 6$ , and  $p_{T,i} \geq p_{T,j} \geq p_{T,k}$ ). The probability fractions are shown in Table 6.5 for  $m_Q = 290$  GeV (the probability is calculated by dividing the number of events in which the particular reconstructed jet-triplet  $ijk$  can be matched to a particular  $Q$ , divided by the total number of events in which we were able to match

$p_T$ Ordered Jet Triplet	Correct Matching Fraction
235	0.060
234	0.057
245	0.053
145	0.047
236	0.045
146	0.040
156	0.034
246	0.034
136	0.031
135	0.031
345	0.031
256	0.024
134	0.021
346	0.021
126	0.016
356	0.016

Table 6.5: Correct matching probability fraction of  $p_T$  ordered reconstructed jet triplets to the parton level  $Q \rightarrow qqq, \bar{q}\bar{q}\bar{q}$  resonance for  $m_Q = 290$  GeV as obtained from Monte Carlo information. The probability fractions and the ordering of the reconstructed jet triplets remain roughly unchanged for different  $m_Q$ . Note that the table only shows the jet triplets that can be made up from the six hardest jet. The 11 best jet-triplets are found among triplets consisting only of the six hardest jets.

any of the jet-triplets to that same  $Q$ ). Note that only the jet-triplets that can be made up from the six hardest jets are shown. The 11 best jet-triplets are found among triplets consisting only of the six hardest jets. Note that the probability fractions and the ordering of the reconstructed jet-triplets remain roughly unchanged for different  $m_Q$ .

From Table 6.5, it can be seen that the combination 235, i.e. the second, third and fifth hardest jet, is the best one and is correct about 6% of the time. Note that the combination 123 is not among the top 16 combinations. This makes sense, since it is unlikely that one of the  $Q$ 's is going to decay into the three hardest jets in an event. It is much more likely that if the hardest jet comes from one  $Q$ , then the second hardest jet will come from the other  $Q$ .

A priori, it is not clear how to use the information gained from the Monte Carlo matching. However, we will now discuss a very useful kinematic correlation among observables made up from the signal jets, which will enable us to better deal with the large combinatoric and physics background. As we will see, it allows one to extract the signal, since both the combinatoric and physics background do not have the same correlation. The correlation that we will focus on here is found among the invariant mass of three jets versus the scalar sum of their transverse momenta. Other kinematic correlations exist, which are qualitatively of the same importance as the one discussed here, and they will be summarized in an appendix (§6.6).

The correlation between  $M_{ijk} \equiv \sqrt{(p_i + p_j + p_k)^2}$  and  $p_{T,ijk} \equiv |p_{T,i}| + |p_{T,j}| + |p_{T,k}|$ , where  $i, j, k$  refer to three different jets, exists basically for all  $p_T$ -ordered jet-triplets. The correlation is most pronounced, however, for the jet-triplets that are correct most of the time. We know which ones these are from the Monte Carlo matching information. However, instead of just using the best  $p_T$ -ordered jet-triplet (i.e. the triplet 235 according to Table 6.5), it is much better to include an *ensemble of jet-triplets*. This means that we include not just the best triplet, but rather a collection of them. The precise number of triplets that should be included can be optimized but was chosen here to be either the best 8 or the best 16 triplets. The main point of including an ensemble of jet-triplets, as opposed to just one jet triplet, is that it increases the significance of the signal.

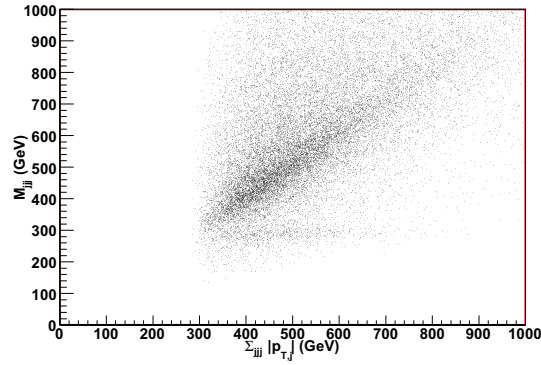
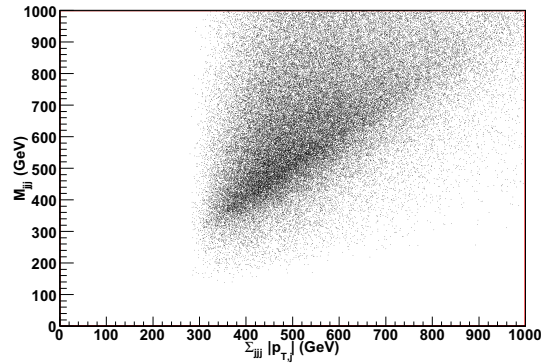
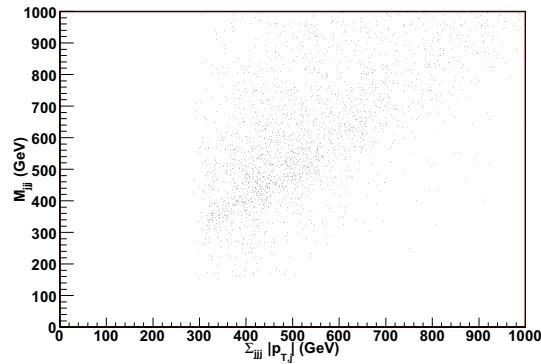
(a) Signal  $m_Q = 290$  GeV.(b) Pure QCD background (when generated with ALPGEN, a  $p_T$  cut of 80 GeV on each of the six quarks was assumed).(c)  $t\bar{t}$  background.

Figure 6.5: The figures show the invariant mass,  $M_{ijk} \equiv \sqrt{(p_i + p_j + p_k)^2}$ , versus the scalar sum of the transverse momenta,  $|p_{T,i}| + |p_{T,j}| + |p_{T,k}|$  for signal, pure QCD and  $t\bar{t}$ . Here  $ijk$  form a jet-triplet, and the figures include all the best 16 jet-triplets that most often come from the decay of a  $Q$ , as shown in Table 6.5. There are thus 16 entries for each event. All the trigger-level and event selection cuts as discussed in §6.3.1 are included, as well as the two kinematic cuts  $\sum_{j=1}^6 p_{T,j} \geq 600$  GeV and  $p_{T,6} \geq 90$  GeV. The luminosity shown here is  $\mathcal{L}=250$   $\text{pb}^{-1}$ .

A plot of  $M_{ijk}$  versus  $p_{T,ijk}$  is shown in Fig. 6.5 for the signal, QCD background and  $t\bar{t}$  background (note that each plot in this figure includes 16 entries per event). An interesting kinematic feature, or correlation, is clearly visible for the signal in Fig. 6.5(a), where it appears as a horizontal band around  $M_{ijk} \simeq m_Q = 290$  GeV. It is more pronounced for larger  $p_{T,ijk}$ , and is clearly distinct from the main diagonal band. This correlation is obviously absent for the pure QCD background, since it appears only due to the resonance that is present in the signal. The  $t\bar{t}$ -background also has a similar feature around  $M_{ijk} \simeq m_t \simeq 172$  GeV, which is just barely visible in Fig. 6.5(c) (it can be made more pronounced with softer kinematic cuts). Events on the horizontal branch come from correct jet-triplets consisting of highly boosted jets and thus will have a large value for  $p_{T,ijk}$ . Wrong jet-triplets which are highly boosted will not generally land on the horizontal band, but will instead prefer to lie along the diagonal band. The correct highly boosted jet-triplets will consist of jets that are close together in  $(\phi, \eta)$ -space. Thus one can also see a correlation if one plots  $M_{ijk}$  versus  $\Delta R_{ij} + \Delta R_{jk} + \Delta R_{ki}$ , where  $\Delta R_{ij} = \sqrt{(\phi_i - \phi_j)^2 + (\eta_i - \eta_j)^2}$ , and  $\phi_i$  ( $\eta_i$ ) is the value of  $\phi$  ( $\eta$ ) of the  $i$ -th jet (see §6.6).

The non-zero width of the horizontal band is from the imperfect energy resolution of the hadronic calorimeter. It is important to note that the combinatoric background is virtually absent from the horizontal band. Moreover, since the QCD background also does not have this kinematic feature, there is a strong contrast between the signal and the combinatoric and physics backgrounds on the horizontal branch. Isolating the horizontal branch isolates those events in which we are able to pick out the correct jet-triplet(s). This will lead to a good signal over background ratio.

The best way to isolate the horizontal branch is to place a diagonal cut in the plane of  $M_{ijk}$  versus  $p_{T,ijk}$  and keep everything below the diagonal line. More precisely, we keep an event if any of the jet-triplets chosen from the set of the 16 best triplets, as given in Table 6.5, satisfies the inequality

$$M_{ijk} \leq p_{T,ijk} + \text{offset}, \quad (6.1)$$

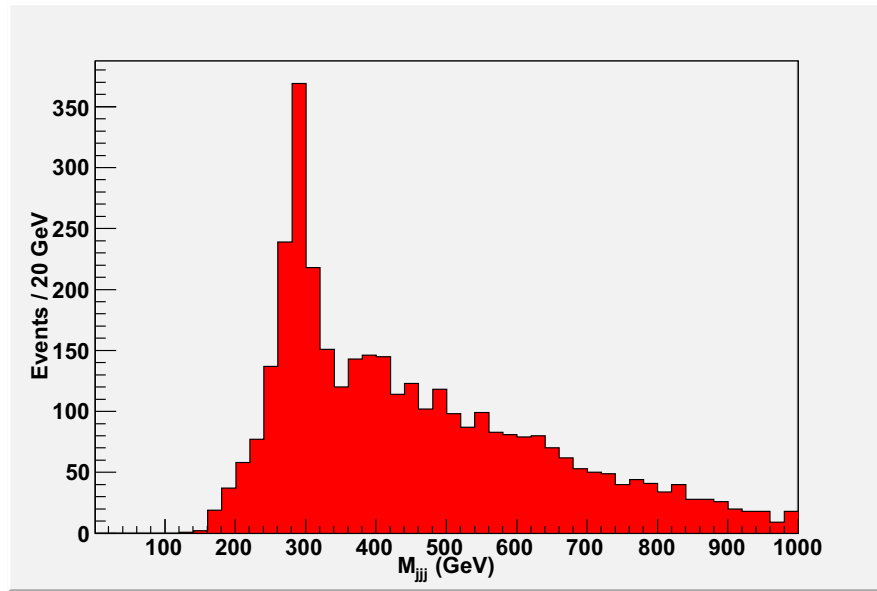
where “offset” was chosen to be either  $\infty$  (i.e. no cut), 0 GeV, -100 GeV, -200 GeV, -300 GeV,

or -400 GeV. The events that remain after this cut will have the property that at least one of its jet-triplets among the 16 best jet-triplets make the cut (6.1). It may of course happen that more than one of the jet-triplets make the cut.

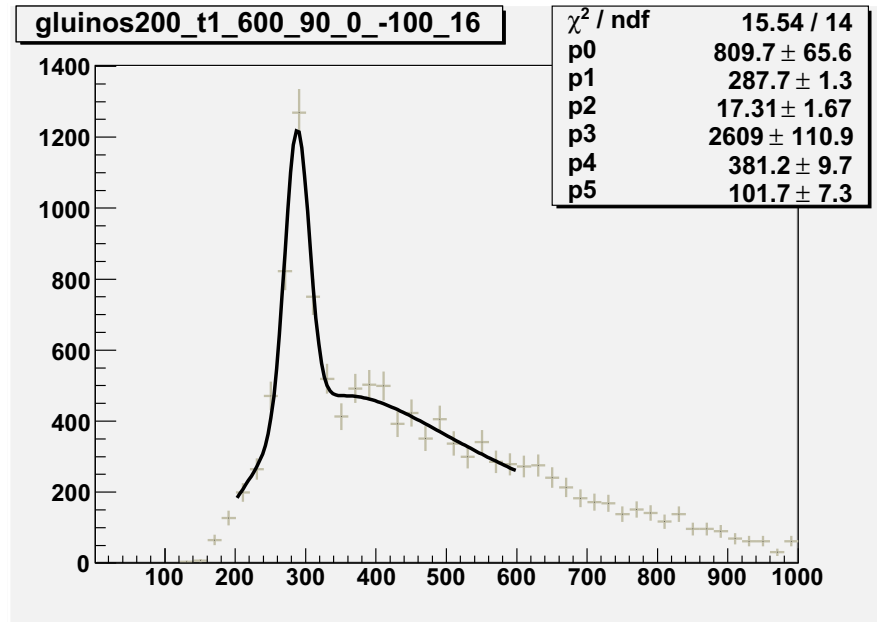
For all the jet-triplets that made the cut (6.1), we calculate their invariant mass. The result is shown in a histogram in Fig. 6.6(a), for  $m_Q = 290$  GeV and with an offset of -100 GeV (trigger, event selection, and kinematic cuts are included). Note that the number of entries for each event found in the total signal sample is between 0 and 16, and is equal to the number of jet-triplets, chosen from the 16 best jet-triplets, that make all the cuts, including (6.1). Comparing Fig. 6.6(a) with Fig. 6.3(a), it is clear that we have succeeded in isolating the resonance. There is still some combinatoric confusion, which can be removed further by increasing the offset. It is not always necessary to do this when trying to extract the signal from the background. In fact, if the offset is too large the signal efficiency becomes too low.

The shape of the signal shown in Fig. 6.6(a) shows a peak sitting on top of a broad background. In order to better model the statistical fluctuations, we now fit a function to this shape, and generate random data samples that average to this shape. The peak is well described by ROOT's Gaussian function, and the broad background can be described by ROOT's Landau function. The result of doing the fit, and rescaling everything to  $\mathcal{L} = 1 \text{ fb}^{-1}$ , is shown in Fig. 6.6(b). The parameters that are used in the fit are called  $p_i$ ,  $i = 0, 1, \dots, 5$ .  $p_0$ ,  $p_1$ , and  $p_2$  are respectively the normalization, mean, and sigma of the gaussian function.  $p_3$ ,  $p_4$ , and  $p_5$  are respectively the normalization, most probable value, and sigma of the landau function. The name on the top left of the plot has the format: "gluinosAAA.t1.BBB.CCC\_DDD\_EEE\_FFF", where

- "AAA" is the  $\overline{\text{MS}}$  mass  $m$  of  $Q$  (here referred to as a gluino):
  - $m = 200 \text{ GeV} \leftrightarrow m_Q = 290 \text{ GeV}$
  - $m = 300 \text{ GeV} \leftrightarrow m_Q = 420 \text{ GeV}$
  - $m = 500 \text{ GeV} \leftrightarrow m_Q = 660 \text{ GeV}$



(a) The luminosity shown here is  $\mathcal{L}=300 \text{ pb}^{-1}$ .



(b) This figure shows a fit to the shape in (a) above. See text for more details. The luminosity shown here is  $\mathcal{L}=1 \text{ fb}^{-1}$ .

Figure 6.6: The invariant mass of all the jet-triplets, chosen among the 16 best triplets, that satisfy (6.1) for the signal with  $m_Q = 290 \text{ GeV}$ . All the trigger-level and event selection cuts as discussed in §6.3.1 are included, as well as the two kinematic cuts  $\sum_{j=1}^6 p_{T,j} \geq 600 \text{ GeV}$  and  $p_{T,6} \geq 90 \text{ GeV}$ . The offset in equation (6.1) is  $-100 \text{ GeV}$  for this plot.

$$- m = 700 \text{ GeV} \leftrightarrow m_Q = 880 \text{ GeV}$$

- “t1” means that all the triggers from §6.3.1 are included
- “BBB” is the cut on  $\sum_{j=1}^6 p_{T,j}$
- “CCC” is the cut on  $p_{T,6}$
- “DDD” is the cut on  $|\vec{p}_{T,i} + \vec{p}_{T,j} + \vec{p}_{T,k}|$ , where  $\vec{p}_{T,i}$  is the two-component momentum vector transverse to the beam pipe (chosen to be zero in all of the plots presented)
- “EEE” is the value of the offset in equation (6.1)
- “FFF” is the number of jet-triplets included in the plot (here always 16)

The same curve fitting may be done to the pure QCD and  $t\bar{t}$ -background, and the plots may be stacked on top of each other. The pure QCD background may also be fit with ROOT’s Landau and Gaussian function. The  $t\bar{t}$  background is well fit with just a Gaussian function. The result is shown in Fig. 6.7. The signal can clearly be seen above both the QCD and  $t\bar{t}$  backgrounds.

This analysis may be repeated for a variety of kinematic cuts and for various values of  $m_Q$ . Several figures showing plots of the invariant mass distribution for the signal only, and for the signal stacked on top of the background, are shown in an appendix (§6.7) in Figs.6.11-6.16 and Figs.6.17-6.21, respectively.

The results of this analysis are summarized in Table 6.6. Shown are the various kinematic and diagonal cuts used in the analysis for different values of  $m_Q$ . Also shown is the “Diagonal Cut Yield on 16-Ensemble”, for the signal ( $QQ$ ) and the pure QCD background, which is the number of jet-triplets (out of a maximum of 16) from each event that on average pass all the cuts (including the diagonal cut). This number is obtained from averaging 1000 pseudo-experiments. The ratio  $S_{16}^{\text{res}}/B_{16}^{\text{res}}$  is the number of jet-triplets from the signal that are within the resonance peak after all the cuts, divided by the corresponding number for the pure QCD background. The significance given by  $S_{16}^{\text{res}}/\sqrt{B_{16}^{\text{res}}}$  for integrated luminosities  $\mathcal{L} = 0.1, 1, \text{ and } 10$

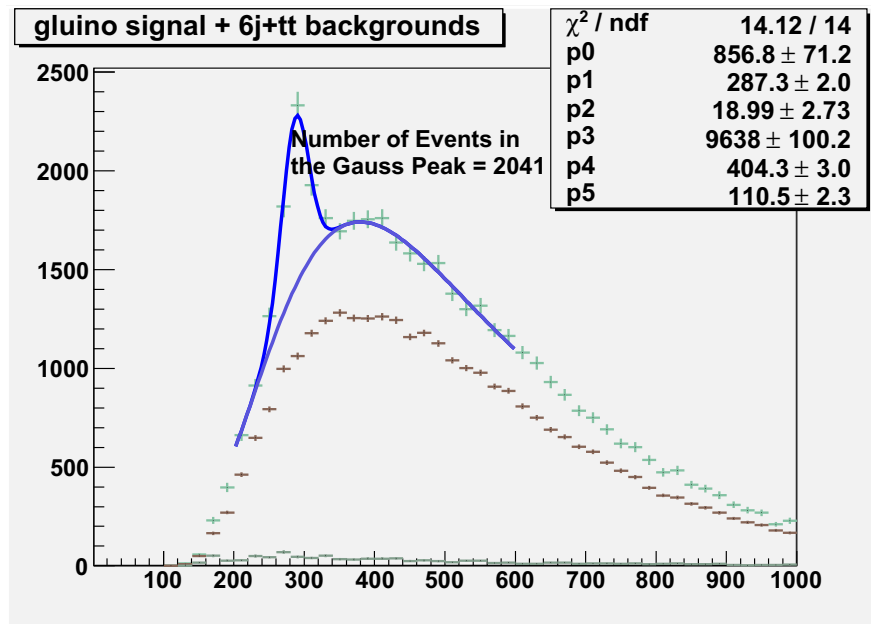


Figure 6.7: The invariant mass of the best 16 jet-triplets that satisfy (6.1) for the signal with  $m_Q = 290$  GeV, the pure QCD background, and the  $t\bar{t}$  background (stacked on top of each other from top to bottom, respectively). Included are all the trigger-level and event selection cuts as discussed in §6.3.1, as well as the two kinematic cuts  $\sum_{j=1}^6 p_{T,j} \geq 600$  GeV and  $p_{T,6} \geq 90$  GeV. The offset in equation (6.1) is -100 GeV. The luminosity shown here is  $\mathcal{L} = 1\text{fb}^{-1}$ .

$m_Q$ (GeV)	$\sum_{j=1}^6 p_{T,j}$ Cut (GeV)	$p_{T,6}$ Cut (GeV)	Diagonal Cut (GeV)	Diag. Cut Yield on 16-Ensemble	$S_{16}^{\text{res}}/B_{16}^{\text{res}}$ All	$S_{16}^{\text{res}}/\sqrt{B_{16}^{\text{res}}}$		
						0.1 fb $^{-1}$	1 fb $^{-1}$	10 fb $^{-1}$
290	600	30	-100	1.53 (0.74)	0.01	3.7	11	37
290	600	60	-100	1.40 (0.76)	0.09	3.2	9.3	28
290	600	90	-100	1.66 (1.03)	0.37	6.3	23	72
290	600	30	-200	0.43 (0.15)	0.02	5.5	19	60
290	600	60	-200	0.42 (0.19)	0.15	6.1	12	41
290	600	90	-200	0.63 (0.36)	0.50	7.3	23	76
290	600	60	-300	0.14 (0.05)	0.27	8.0	21	62
290	600	90	-300	0.23 (0.12)	0.62	2.6	13	46
420	700	30	-200	0.47 (0.21)	0.12	4.3	14	33
420	700	60	-200	0.45 (0.23)	0.06	2.6	8.0	29
420	700	90	-200	0.60 (0.36)	0.22	3.4	6.0	21
420	700	120	-200	0.89 (0.55)	0.49	1.0	3.5	11
420	700	60	-300	0.15 (0.06)	0.09	2.7	8.0	24
420	700	90	-300	0.23 (0.12)	0.36	1.7	5.9	17
420	700	120	-300	0.39 (0.23)	0.65	1.3	5.3	14
420	700	60	-400	0.06 (0.02)	0.11	3.8	11	32
420	700	90	-400	0.09 (0.04)	0.44	3.6	7.5	28
420	700	120	-400	0.17 (0.09)	0.79	3.3	6.5	21
660	1100	60	-200	0.94 (0.61)	0.02	0.9	3.5	11
660	1100	90	-200	0.88 (0.55)	0.06	0.9	2.3	8.8
660	1100	120	-200	0.89 (0.60)	0.15	0.9	2.9	7.5
660	1100	60	-300	0.34 (0.20)	0.03	0.5	1.4	4.0
660	1100	90	-300	0.33 (0.35)	0.08	0.5	1.4	4.2
660	1100	120	-300	0.37 (0.25)	0.20	0.4	0.8	3.7
660	1100	60	-400	0.13 (0.07)	0.03	0.8	3.8	8.8
660	1100	90	-400	0.13 (0.07)	0.11	0.8	3.1	5.5
660	1100	120	-400	0.16 (0.10)	0.30	0.7	2.3	5.9

Table 6.6: Shown are the various kinematic and diagonal cuts used in the analysis for different values of  $m_Q$ . Also shown is the “Diagonal Cut Yield on 16-Ensemble”, for the signal ( $QQ$ ) and the pure QCD background, which is the number of jet-triplets (out of a maximum of 16) from each event that on average pass all the cuts (including the diagonal cut). The ratio  $S_{16}^{\text{res}}/B_{16}^{\text{res}}$  is the number of jet-triplets from the signal that are within the resonance peak after all the cuts, divided by the corresponding number for the pure QCD background. The significance given by  $S_{16}^{\text{res}}/\sqrt{B_{16}^{\text{res}}}$  for integrated luminosities  $\mathcal{L} = 0.1, 1, \text{ and } 10 \text{ fb}^{-1}$ , respectively, are also given in the table. All numbers are obtained from averaging 1000 pseudo-experiments.

$\text{fb}^{-1}$ , respectively, are also given in the table. These numbers are also obtained from averaging 1000 pseudo-experiments.

The significance is around the discovery threshold of  $5\sigma$  if  $\mathcal{L} \gtrsim 0.1 \text{ fb}^{-1}$  for low  $m_Q \sim 300$  GeV. This luminosity should be reached rather soon after the start of the LHC. About  $\mathcal{L} \gtrsim 1 \text{ fb}^{-1}$  is required to discover  $Q$ 's with  $m_Q \sim 450$  GeV, while  $Q$ 's with  $m_Q \sim 700$  GeV require  $\mathcal{L} \gtrsim 10 \text{ fb}^{-1}$ . Note that the significance will decrease by a factor of  $\sqrt{3}$  if the QCD background has a 3 times larger cross-section than what was assumed here. The same numbers as shown in the table would then be obtained if  $\mathcal{L}$  is increased by a factor of 3. These remarks assume that only the background normalization changes, not its shape. However, even if the background shape changes slightly it is unlikely that it will mimic the shape of the signal for all the cuts that have been proposed here. So it should still be possible to extract the signal from the background even in this case, although this statement would certainly need further study.

Finally, recall that the trigger-level cuts select  $Q$ 's that are very boosted. For very low  $m_Q$ , the trigger-level cuts select events that not only have highly boosted jets from the  $Q$ 's, but the  $Q$ 's themselves are highly boosted when produced. It is possible that the three jets from the decay of one of the  $Q$ 's begin to merge. Instead of a three-jet resonance there could then be a two-jet resonance. The effect of the merging on the analysis method discussed here requires further study.

## 6.4 Conclusions

The results of this work are summarized in Table 6.6. They show that searches for new particles that produce multi-jet signals without any leptons or missing energy *can* be done. In particular, it was found that a new heavy adjoint Majorana fermion  $Q$  decaying into three jets forms a resonance that can be extracted from the large hadronic background. The mass reach is about  $m_Q \sim 650\text{-}700$  GeV for  $\mathcal{L} \gtrsim 10 \text{ fb}^{-1}$ .  $Q$ 's with masses as large as 300 GeV can potentially be observed with only  $100 \text{ pb}^{-1}$  of integrated luminosity, which can be obtained soon after the start of the LHC. The signal can be extracted using a variety of kinematic cuts and making use

of correlations or kinematic features in observables formed from the signal jets which are absent for the same observables formed from background jets.

The analysis method presented here is more widely applicable. It may be used to search for  $t\bar{t}$  production in the all hadronic channel. In fact, there is additional information that can be used in this case, such as b-tagging and the intermediate W-boson resonance, which makes the search slightly easier. Moreover, it may be that the  $Q$ 's that get produced do not undergo a three-body decay, but instead decay via an intermediate on-shell resonance, just like the top quark. Our analysis method can also be used in this case. It is also applicable and should work very well for multi-jet signals which are produced in conjunction with leptons and/or missing energy. Such signals can, for example, be found in supersymmetry with R-parity violation.

The analysis here can no doubt be optimized further. Since a variety of cuts are used, it may be useful to employ a neural network to do the optimization.

The two main ideas contained in this work are the idea of using *correlations* to extract kinematic features and the idea of using an *ensemble* of reconstructed objects. The kinematic features allow one to extract events with well-defined properties (e.g. in this work, the kinematic feature allows one to extract events in which we can identify the jet-triplets that come from the decay of the  $Q$ 's). Using an ensemble then increases the efficiency and thus the significance of the signal. These ideas are very widely applicable and not just confined to multi-jet signals.

## 6.5 Appendix: Comparison of the PGS 4 and CMSSW detector simulations

Since PGS 4 is a fast detector simulation, a natural question to ask is whether it is realistic enough to simulate the very complicated CMS and ATLAS detectors at the LHC. To answer this question, the events were also run through the full detector simulation of the Compact Muon Solenoid (CMS) experimental collaboration using their CMS Software (CMSSW). Including only the trigger-level cuts, Figs. 6.8(a) and 6.8(b) show the Monte Carlo matched three-jet invariant mass assuming  $m_Q \simeq 290$  GeV for the PGS and for the CMSSW detector simulation,

respectively. The gaussian invariant mass peak has a width of about  $\sigma \simeq 26$  GeV and  $\sigma \simeq 33$  GeV with the PGS and the CMSSW detector, respectively. As expected, the width is wider with the more realistic CMSSW detector simulation, and the PGS 4 detector is “too good”.

In PGS, the hadronic calorimeter jet energy resolution is given by

$$\sigma(E_T^{\text{jet}}) \propto 0.8 \times \sqrt{E_T^{\text{jet}}}. \quad (6.2)$$

In CMSSW (see the CMS TDR [12, 13]), the jet energy resolution for central jets is

$$\sigma(E_T^{\text{jet}}, |\eta| < 1.4) = (5.8 \text{ GeV}) \oplus (1.25 \times \sqrt{E_T^{\text{jet}}}) \oplus (0.033 \times E_T^{\text{jet}}), \quad (6.3)$$

while the jet energy resolution for forward jets is

$$\sigma(E_T^{\text{jet}}, |\eta| < 3.0) = (4.8 \text{ GeV}) \oplus (0.89 \times \sqrt{E_T^{\text{jet}}}) \oplus (0.043 \times E_T^{\text{jet}}). \quad (6.4)$$

The CMSSW jet energy resolution thus contains a constant and a linear term. The symbol  $\oplus$  indicates that the terms should be added in quadrature.

Every jet in every event that comes from PGS may be made more realistic by giving its energy an additional smearing. This can be done by multiplying the  $p_T$  of each jet by a gaussian random number, centered at 1, with a width given by the difference of the CMSSW  $\sigma$ -value given in (6.3) and the PGS  $\sigma$ -value given in (6.2). The result of this is shown in Fig. 6.8(c). The gaussian peak has a width of about  $\sigma \simeq 35$  GeV, which agrees well with the CMSSW peak width.

The CMSSW jets and the newly smeared PGS jets both should get an *additional* systematic smearing to make them even more realistic, see the CMS TDR [12, 13]. This additional smearing is given by taking the  $p_T$  or  $E_T$  of the jet and adding a gaussian random number centered at 0 with a width given by  $0.46 \times \sigma(E_T^{\text{jet}}, |\eta|)$ , i.e.

$$E_T^{\prime\text{jet}} = E_T^{\text{jet}} + \text{Gaus}[0, 0.46 \times \sigma(E_T^{\text{jet}}, |\eta|)]. \quad (6.5)$$

This further broadens the overall jet energy resolution by about 10%. The result of this, for the already smeared PGS jets, is shown in Fig. 6.8(d). The gaussian peak here has a width of about  $\sigma \simeq 37$  GeV.

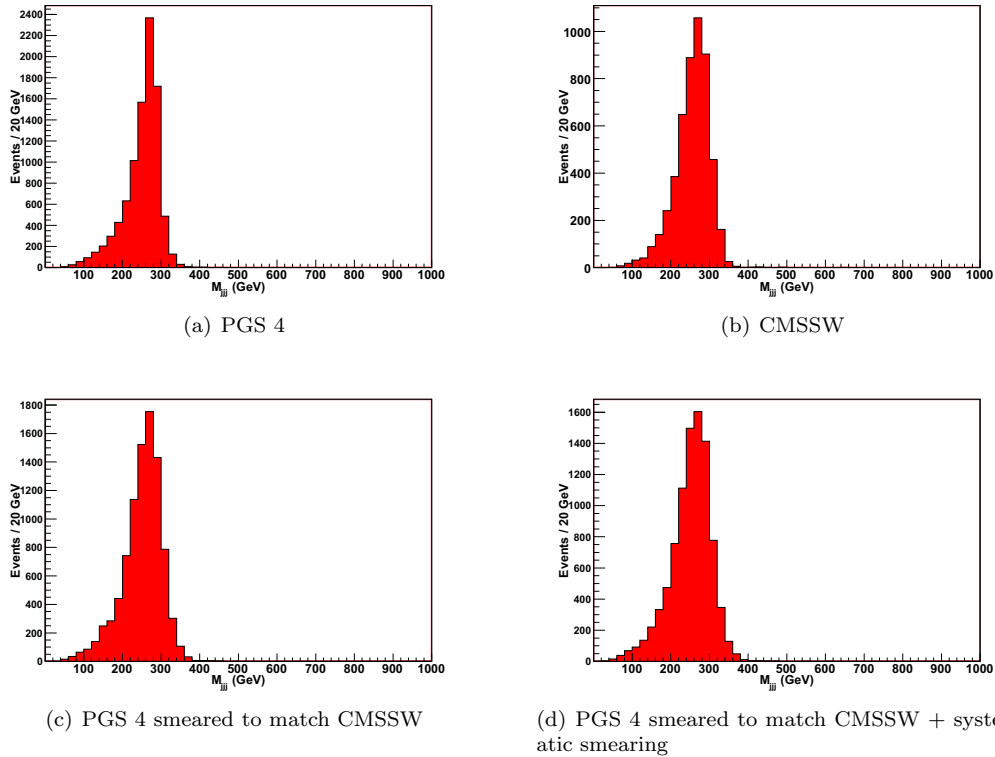


Figure 6.8: The Monte Carlo matched jet-triplet invariant masses for different detector simulations and, in some cases, with an additional smearing of the jet energy resolution. The signal has  $m_Q = 290$  GeV. Only trigger-level cuts are included, without any additional kinematic cuts. In Figure (a), the events were run through the PGS 4 detector simulation, while in Figure (b) they were run through the full CMSSW detector simulation. Figure (c) includes events run through PGS 4, but each jet receives an additional smearing as described in the text, in order to have an overall jet energy resolution as that found in CMSSW. Figure (d) includes jets run through PGS 4, with the same additional smearing as in Figure (c), but with an additional smearing of about 10% as given by (6.5). This additional 10% smearing is described in the CMS TDR as being more realistic, but is not included in the CMSSW detector simulation. The luminosity shown in the figures is about  $\mathcal{L} \simeq 300 \text{ pb}^{-1}$ .

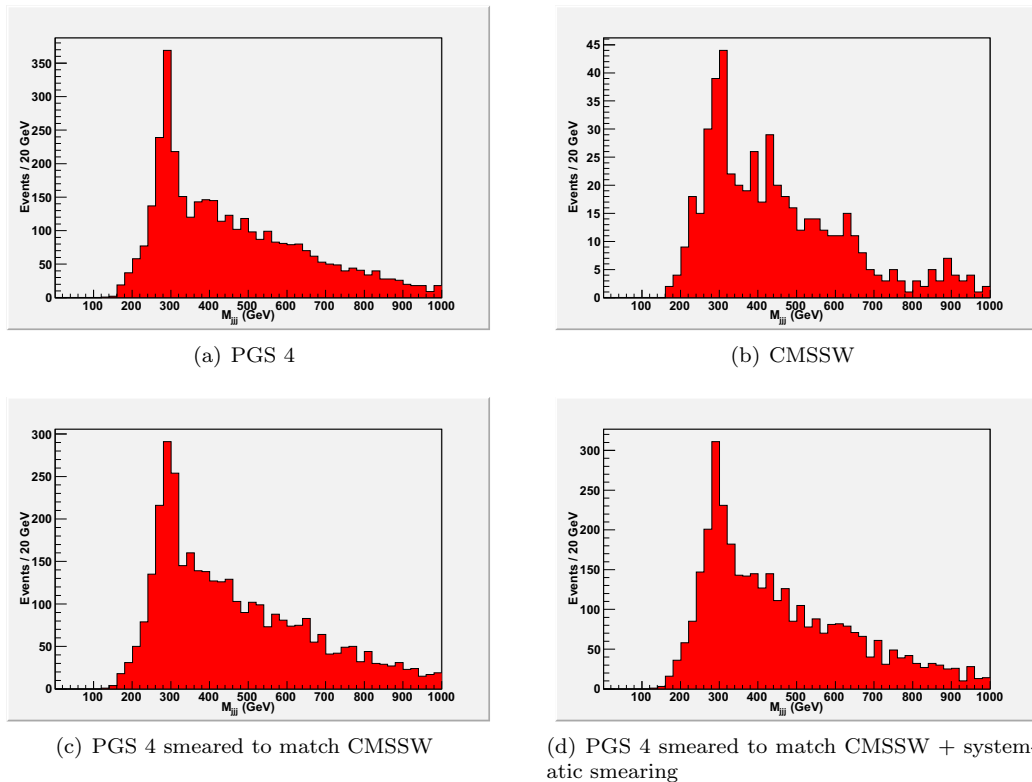


Figure 6.9: The invariant mass of the best 16 jet-triplets that satisfy (6.1) for the signal with  $m_Q = 290$  GeV. Included are all the trigger-level and event selection cuts as discussed in §6.3.1, as well as the two kinematic cuts  $\sum_{j=1}^6 p_{T,j} \geq 600$  GeV and  $p_{T,6} \geq 90$  GeV. The offset in equation (6.1) is -100 GeV. The luminosity shown here is  $\mathcal{L} = 300$  pb $^{-1}$ , except for Figure (d) which only has  $\mathcal{L} = 58$  pb $^{-1}$  and suffers slightly from low statistics. Figures (a)-(d) assume the same detector/jet energy resolution as described in Fig. 6.8.

A feel for the effect of the more realistic jet energy resolution on the analysis can be gained by looking at the signal shape after all the analysis cuts. This is shown in Fig. 6.9 for the PGS and the CMSSW detector simulation and for different jet energy resolutions as discussed above. The signal is at  $m_Q = 290$  GeV. Included are all the trigger-level and event selection cuts as discussed in §6.3.1, as well as the two kinematic cuts  $\sum_{j=1}^6 p_{T,j} \geq 600$  GeV and  $p_{T,6} \geq 90$  GeV. The offset in equation (6.1) is -100 GeV. The effect of the additional smearing is small, although it can be seen by eye. Although a systematic study of the effect of this on the results as described in Table 6.6 has not been done, it is clear that the results will only change by a small amount, since the smearing does not have too large an effect. This means that our results and analysis obtained with PGS (and no additional smearing) are reliable.

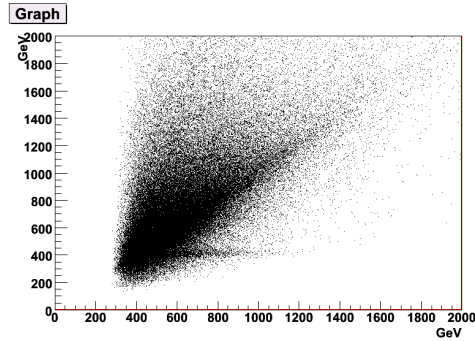
## 6.6 Appendix: Other Kinematic Correlations

We have seen that a very interesting correlation or kinematic feature can be seen for the signal when plotting the invariant mass  $M_{ijk} \equiv \sqrt{(p_i + p_j + p_k)^2}$  versus the scalar sum of the transverse momenta  $p_{T,ijk} \equiv |p_{T,i}| + |p_{T,j}| + |p_{T,k}|$ , where  $p_{T,i}$  is the transverse momentum of the  $i$ -th jet, and  $ijk$  forms a ( $p_T$ -ordered) jet-triplet. This is shown in Fig. 6.10(a) for  $m_Q = 420$  GeV. In this appendix, we shall briefly mention two other kinematic correlations that we investigated.

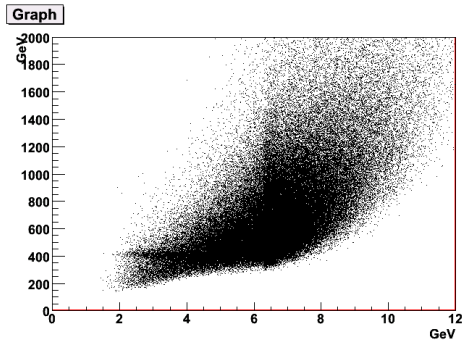
The first one is a correlation in  $M_{ijk}$  versus  $P \equiv \Delta R_{ij} + \Delta R_{jk} + \Delta R_{ki}$ , where  $\Delta R_{ij} = \sqrt{(\phi_i - \phi_j)^2 + (\eta_i - \eta_j)^2}$ , and  $\phi_i$  ( $\eta_i$ ) is the value of  $\phi$  ( $\eta$ ) of the  $i$ -th jet. This is shown in Fig. 6.10(b). Again the correct jet-triplets can be found on a horizontal band around  $M_{ijk} \simeq m_Q$ , this time for small values of  $P$ . The three jets in a triplet form a triangle in  $(\phi, \eta)$ -space, and  $P$  calculates the perimeter of this triangle. Events on the horizontal band again contain highly boosted jets. Since they are so highly boosted, the three jets in the correct triplet will lie close together, and thus the value of  $P$  will be small.

Another correlation can be found in  $M_{ijk}$  versus  $V \equiv |\vec{p}_{T,i} + \vec{p}_{T,j} + \vec{p}_{T,k}|$ , where  $\vec{p}_{T,i}$  is the two-component momentum vector transverse to the beam pipe. This correlation is shown in Fig. 6.10(c).  $V$  is the magnitude of the vector formed by summing the three transverse momentum vectors. A horizontal branch is also visible here. Events on this horizontal branch again contain highly boosted jets for which  $V$  is large.

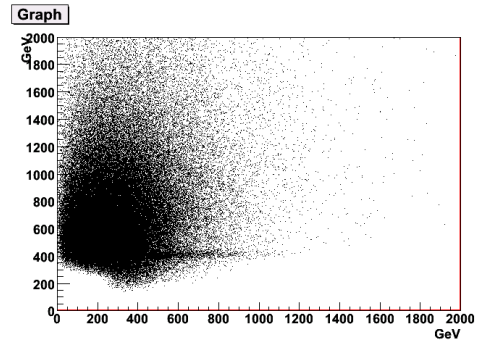
It is possible to make use of all of these correlations in an analysis, but it is also clear that they all provide basically the same information, since they always pick out highly boosted jets. Since there is no qualitative difference between the various correlations, we chose to focus our analysis on using just one of them ( $M_{ijk}$  versus  $p_{T,ijk}$ ). One can no doubt optimize the significance slightly by using all of the correlations.



(a)  $M_{ijk}$  versus  $p_{T,ijk} \equiv |p_{T,i}| + |p_{T,j}| + |p_{T,k}|$ , where  $p_{T,i}$  is the transverse momentum of the  $i$ -th jet.



(b)  $M_{ijk}$  versus  $P \equiv \Delta R_{ij} + \Delta R_{jk} + \Delta R_{ki}$ , where  $\Delta R_{ij} = \sqrt{(\phi_i - \phi_j)^2 + (\eta_i - \eta_j)^2}$ , and  $\phi_i$  ( $\eta_i$ ) is the value of  $\phi$  ( $\eta$ ) of the  $i$ -th jet.



(c)  $M_{ijk}$  versus  $V \equiv |\vec{p}_{T,i} + \vec{p}_{T,j} + \vec{p}_{T,k}|$ , where  $\vec{p}_{T,i}$  is the two-component momentum vector transverse to the beam pipe.

Figure 6.10:  $M_{ijk} \equiv \sqrt{(p_i + p_j + p_k)^2}$  versus various other kinematic quantities made out of three jets, for the signal with  $m_Q = 420$  GeV. Here  $ijk$  form a jet-triplet, and the figures include all the best 16 jet-triplets that most often come from the decay of a  $Q$ , as shown in Table 6.5. Each plot thus contains 16 entries for each event. All the trigger-level and event selection cuts as discussed in §6.3.1 are included, as well as the two kinematic cuts  $\sum_{j=1}^6 p_{T,j} \geq 600$  GeV and  $p_{T,6} \geq 90$  GeV. The luminosity shown here is  $\mathcal{L} = 2 \text{ fb}^{-1}$ .

## 6.7 Appendix: Three-Jet Resonance Figures

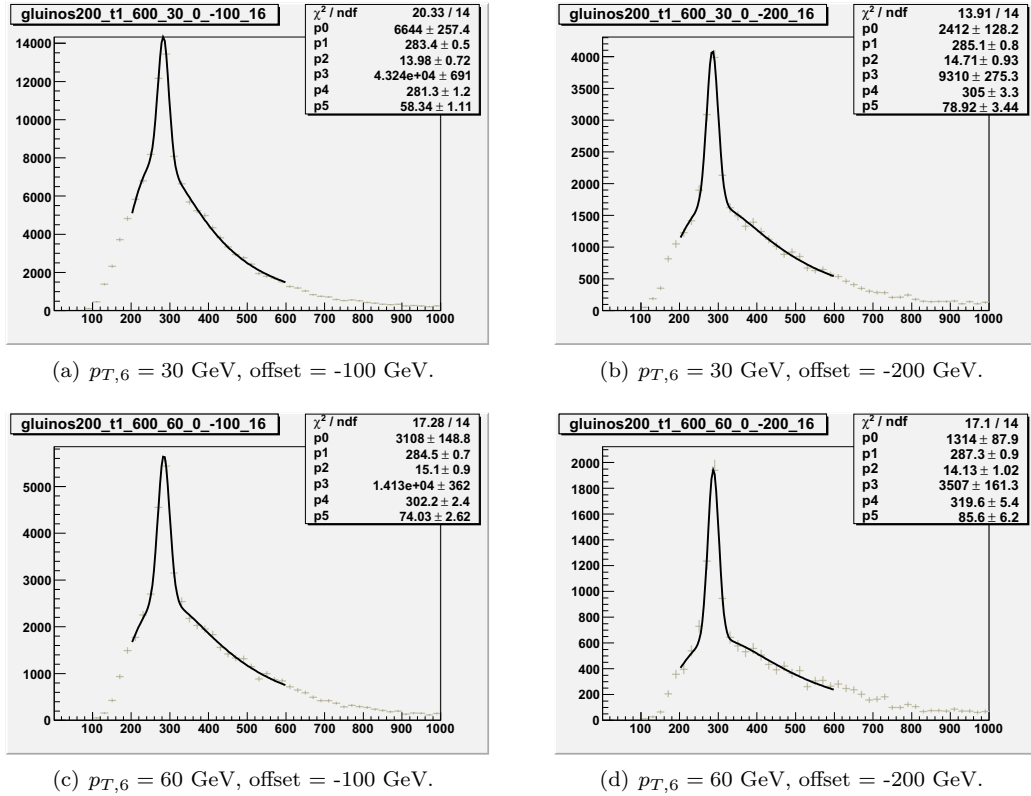


Figure 6.11: The invariant mass of the 16 best jet-triplets that satisfy (6.1) for the signal with  $m_Q = 290$  GeV and offset value given in each subfigure caption. Included are all the trigger-level and event selection cuts (§6.3.1), a kinematic cut  $\sum_{j=1}^6 p_{T,j} \geq 600$  GeV, and a cut on  $p_{T,6}$  as detailed in each subfigure caption.  $\mathcal{L} = 1\text{fb}^{-1}$ .

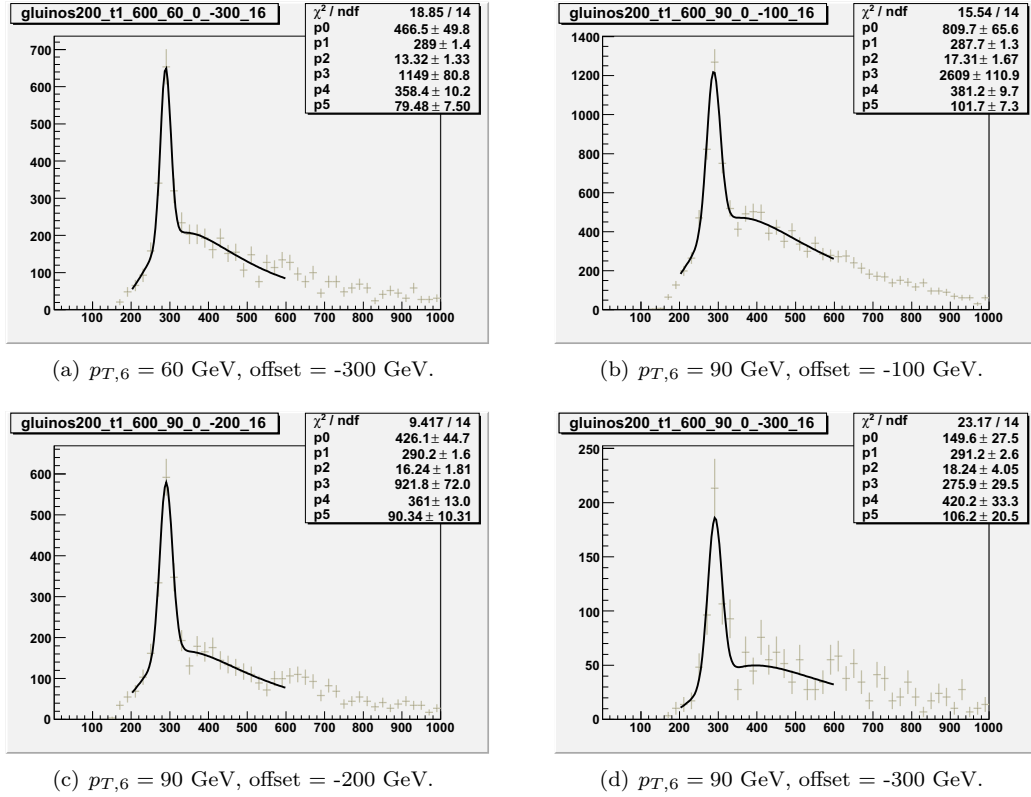


Figure 6.12: The invariant mass of the 16 best jet-triplets that satisfy (6.1) for the signal with  $m_Q = 290$  GeV and offset value given in each subfigure caption. Included are all the trigger-level and event selection cuts (§6.3.1), a kinematic cut  $\sum_{j=1}^6 p_{T,j} \geq 600$  GeV, and a cut on  $p_{T,6}$  as detailed in each subfigure caption.  $\mathcal{L} = 1\text{fb}^{-1}$ .

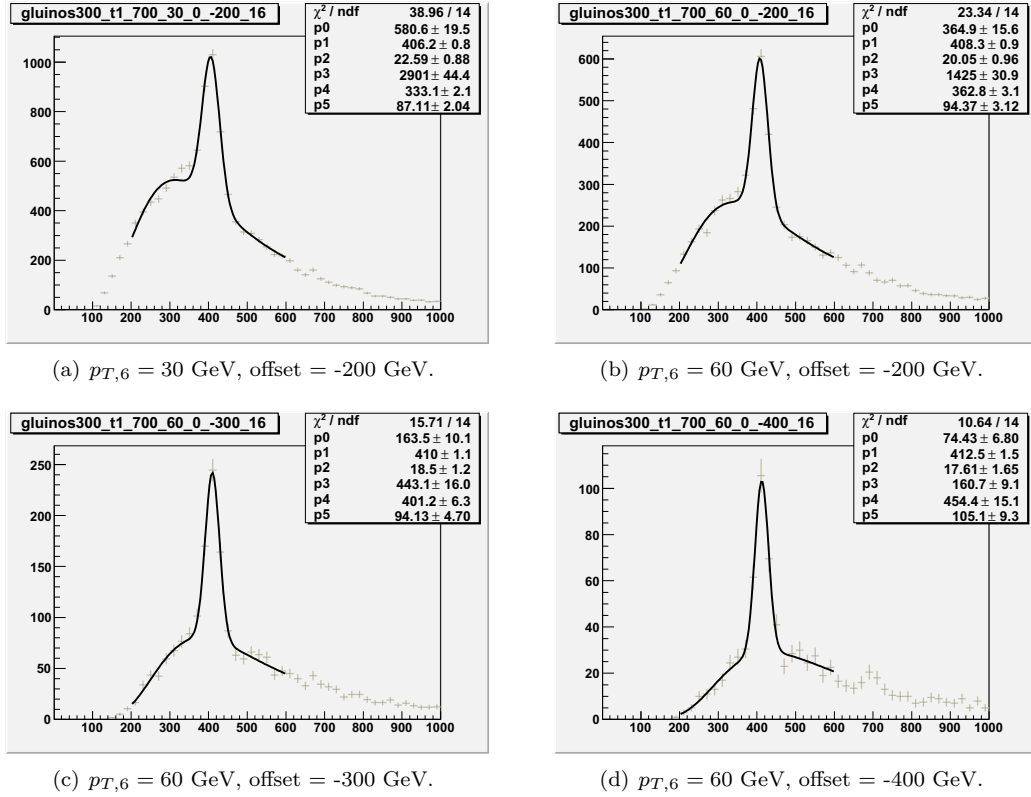


Figure 6.13: The invariant mass of the 16 best jet-triplets that satisfy (6.1) for the signal with  $m_Q = 420$  GeV and offset value given in each subfigure caption. Included are all the trigger-level and event selection cuts (§6.3.1), a kinematic cut  $\sum_{j=1}^6 p_{T,j} \geq 700$  GeV, and a cut on  $p_{T,6}$  as detailed in each subfigure caption.  $\mathcal{L} = 1\text{fb}^{-1}$ .

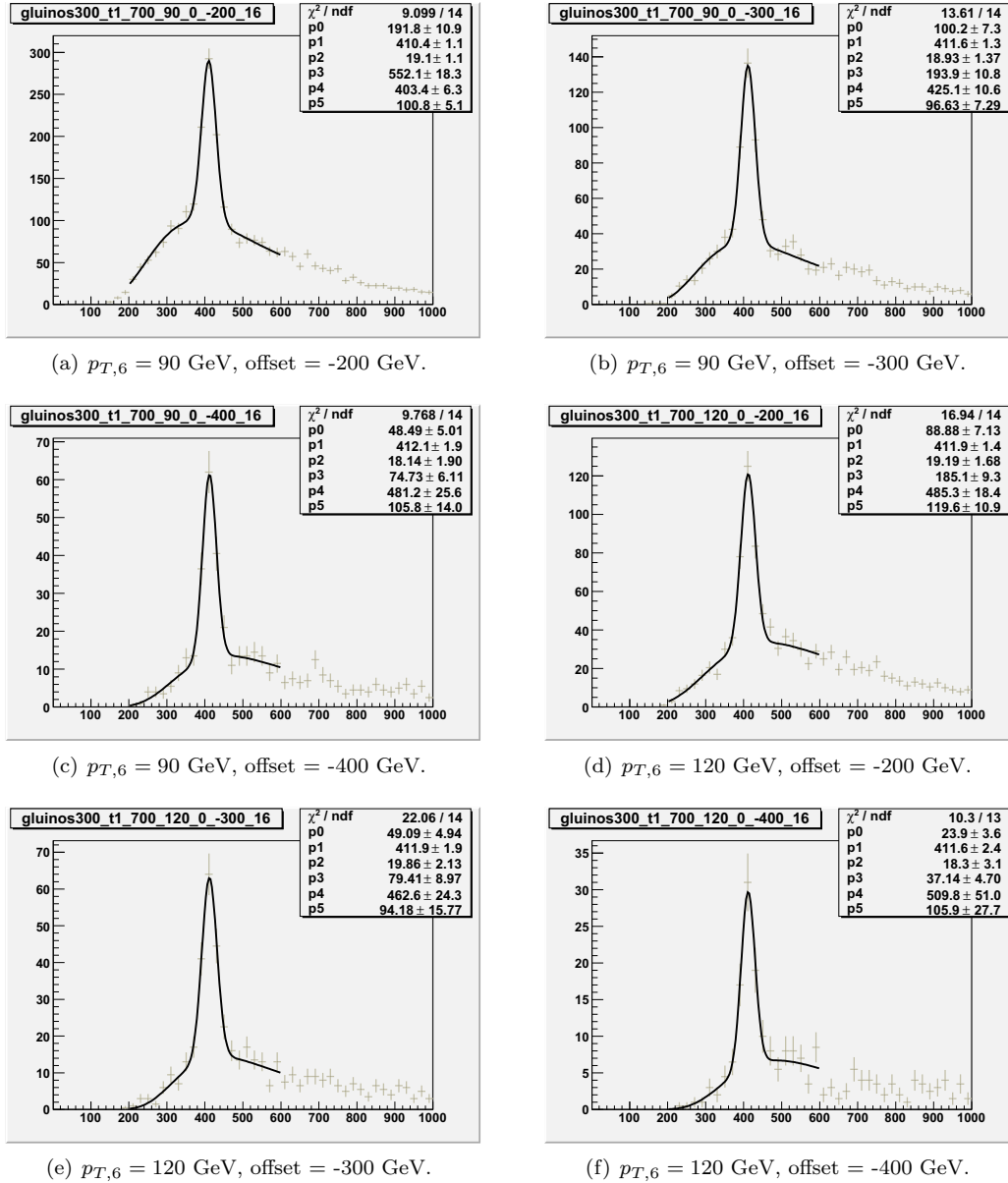


Figure 6.14: The invariant mass of the 16 best jet-triplets that satisfy (6.1) for the signal with  $m_Q = 420$  GeV and offset value given in each subfigure caption. Included are all the trigger-level and event selection cuts (§6.3.1), a kinematic cut  $\sum_{j=1}^6 p_{T,j} \geq 700$  GeV, and a cut on  $p_{T,6}$  as detailed in each subfigure caption.  $\mathcal{L} = 1\text{fb}^{-1}$ .

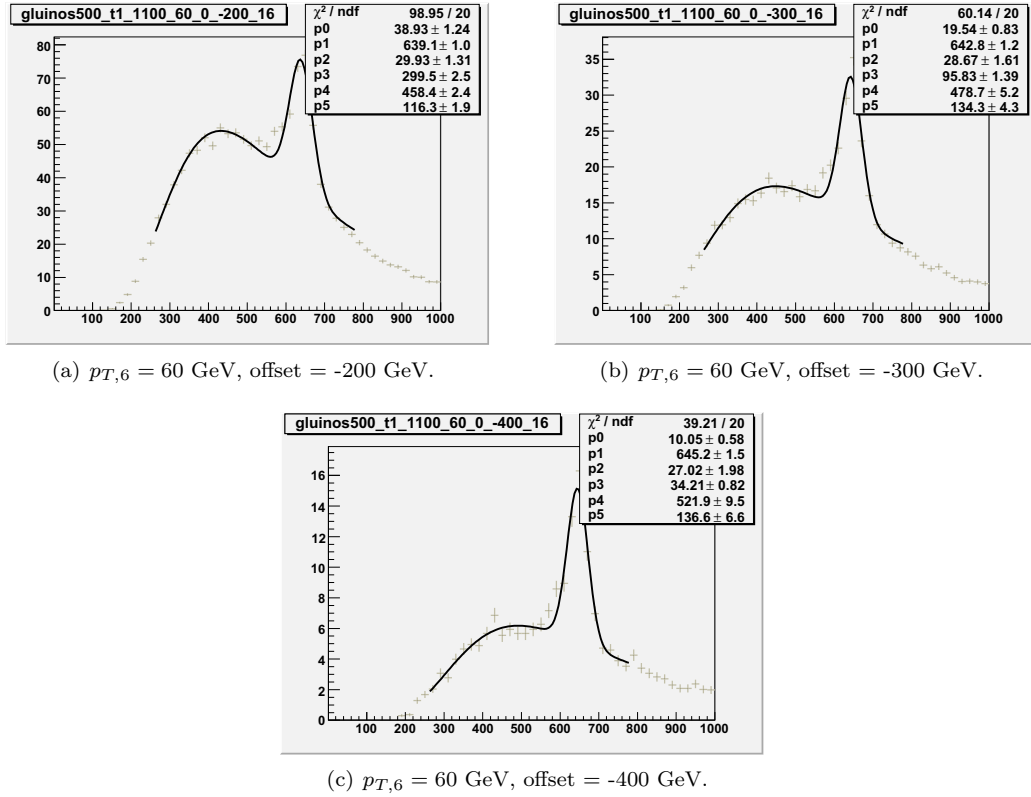


Figure 6.15: The invariant mass of the 16 best jet-triplets that satisfy (6.1) for the signal with  $m_Q = 660$  GeV and offset value given in each subfigure caption. Included are all the trigger-level and event selection cuts (§6.3.1), a kinematic cut  $\sum_{j=1}^6 p_{T,j} \geq 1100$  GeV, and a cut on  $p_{T,6}$  as detailed in each subfigure caption.  $\mathcal{L} = 1\text{fb}^{-1}$ .

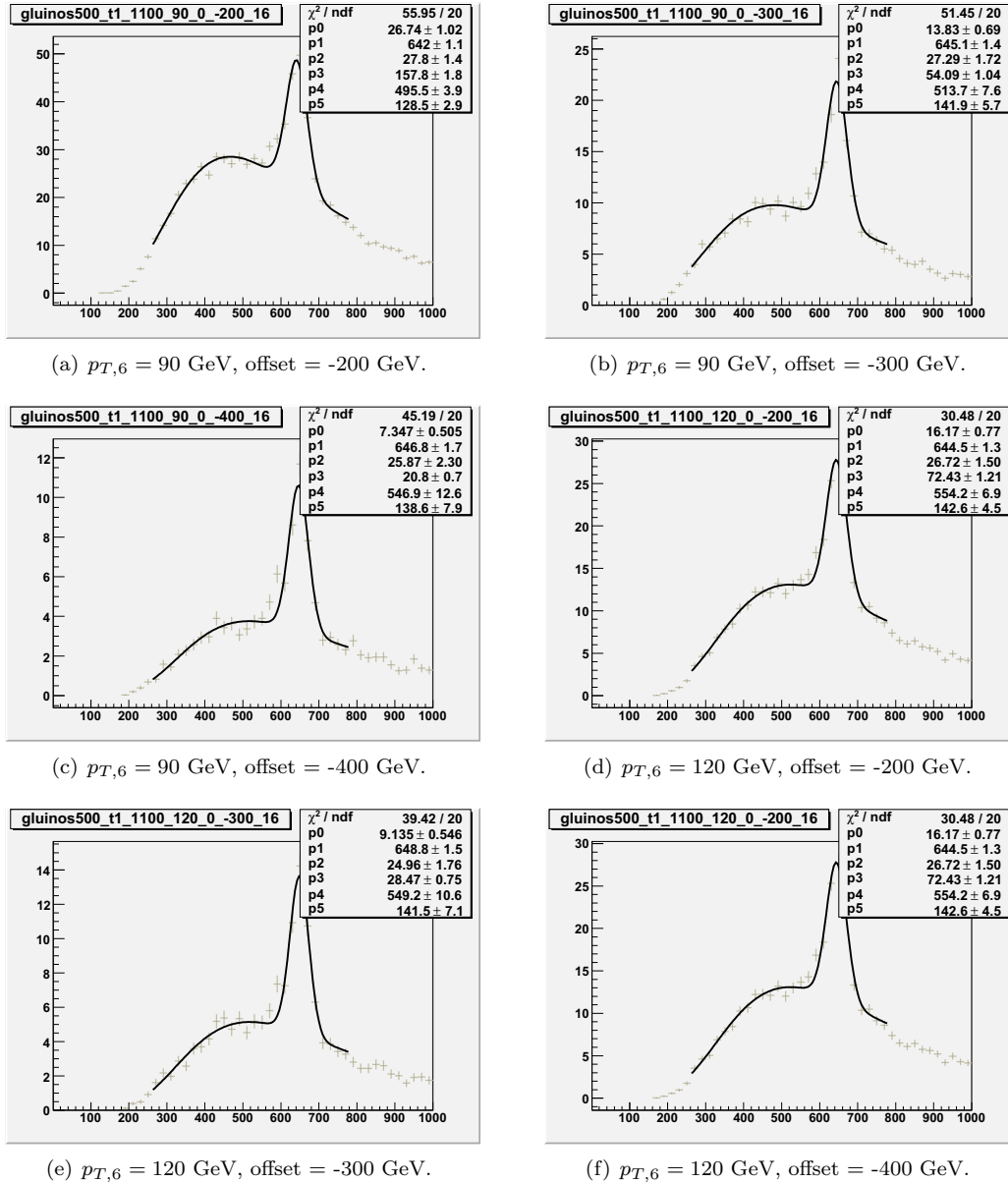


Figure 6.16: The invariant mass of the 16 best jet-triplets that satisfy (6.1) for the signal with  $m_Q = 660$  GeV and offset value given in each subfigure caption. Included are all the trigger-level and event selection cuts (§6.3.1), a kinematic cut  $\sum_{j=1}^6 p_{T,j} \geq 1100$  GeV, and a cut on  $p_{T,6}$  as detailed in each subfigure caption.  $\mathcal{L} = 1\text{fb}^{-1}$ .

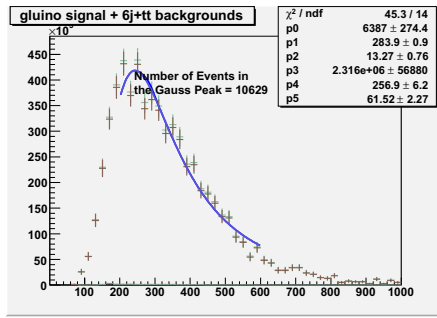
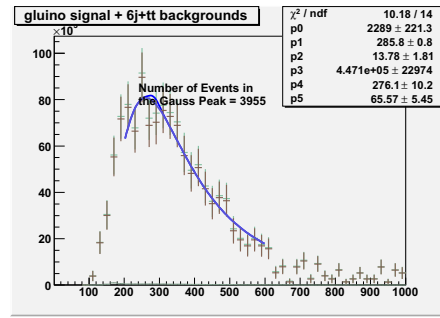
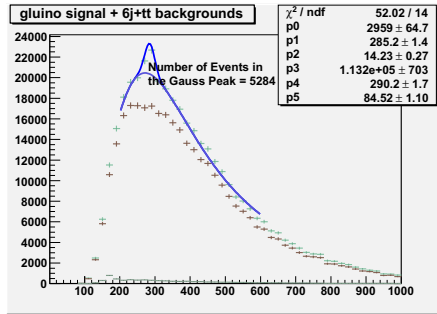
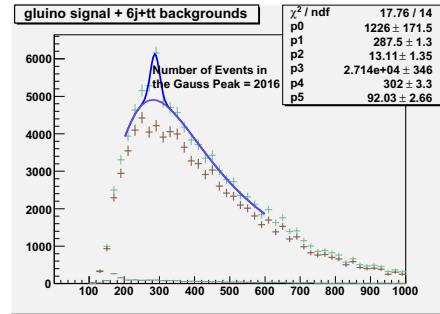
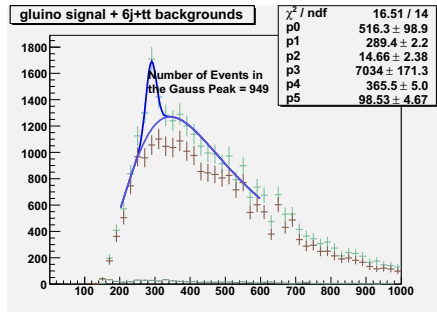
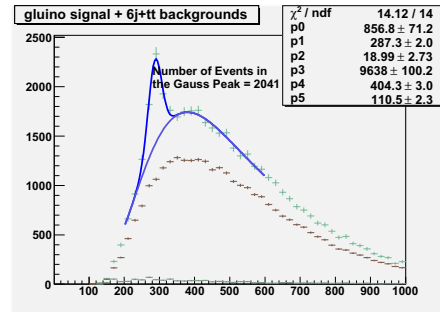
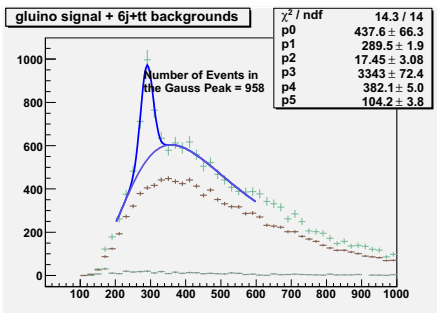
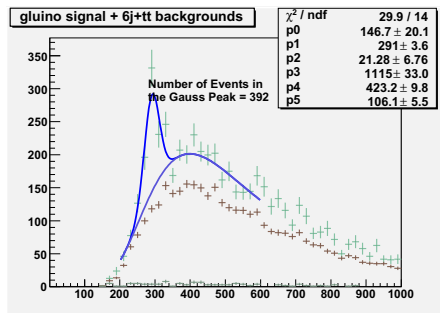
(a)  $p_{T,6} = 30$  GeV, offset = -100 GeV.(b)  $p_{T,6} = 30$  GeV, offset = -200 GeV.(c)  $p_{T,6} = 60$  GeV, offset = -100 GeV.(d)  $p_{T,6} = 60$  GeV, offset = -200 GeV.(e)  $p_{T,6} = 60$  GeV, offset = -300 GeV.(f)  $p_{T,6} = 90$  GeV, offset = -100 GeV.(g)  $p_{T,6} = 90$  GeV, offset = -200 GeV.(h)  $p_{T,6} = 90$  GeV, offset = -300 GeV.

Figure 6.17: The invariant mass of the 16 best jet-triplets that satisfy (6.1), with an offset value given in each subfigure caption, for the signal with  $m_Q = 290$  GeV, the pure QCD background, and the  $t\bar{t}$  background. Included are all the trigger-level and event selection cuts (§6.3.1), a kinematic cut  $\sum_{j=1}^6 p_{T,j} \geq 600$  GeV, and a cut on  $p_{T,6}$  as detailed in each subfigure caption.  $\mathcal{L} = 1\text{fb}^{-1}$ .

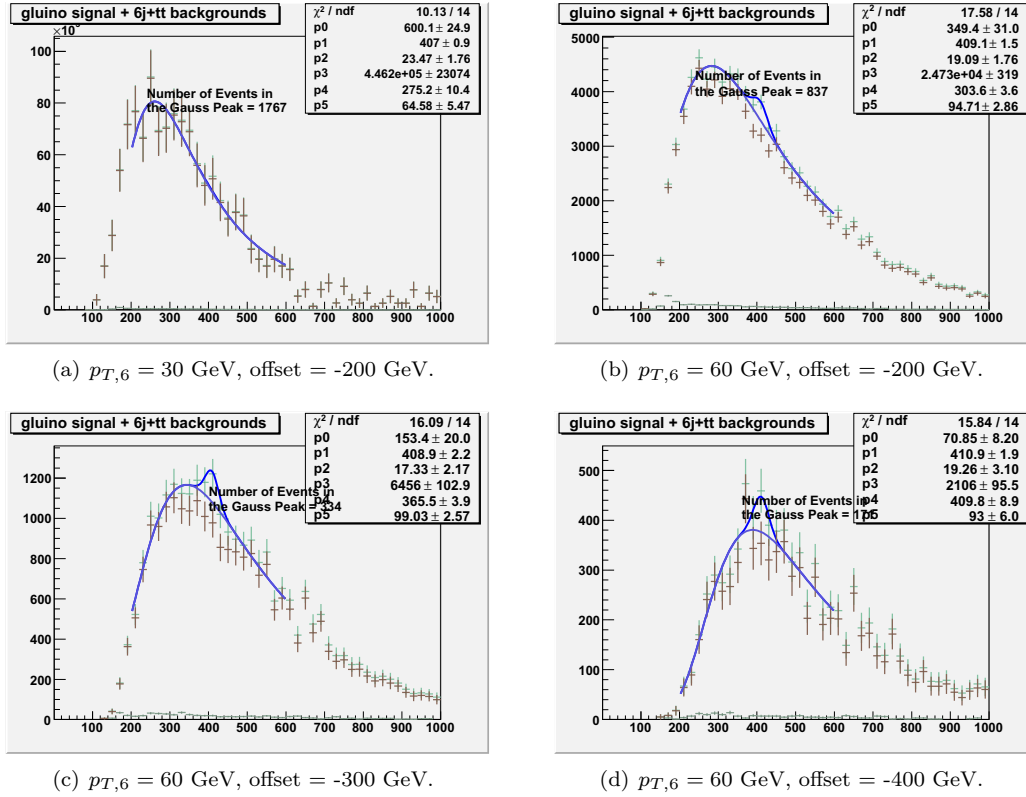


Figure 6.18: The invariant mass of the 16 best jet-triplets that satisfy (6.1), with an offset value given in each subfigure caption, for the signal with  $m_Q = 420$  GeV, the pure QCD background, and the  $t\bar{t}$  background. Included are all the trigger-level and event selection cuts (§6.3.1), a kinematic cut  $\sum_{j=1}^6 p_{T,j} \geq 700$  GeV, and a cut on  $p_{T,6}$  as detailed in each subfigure caption.  $\mathcal{L} = 1\text{fb}^{-1}$ .

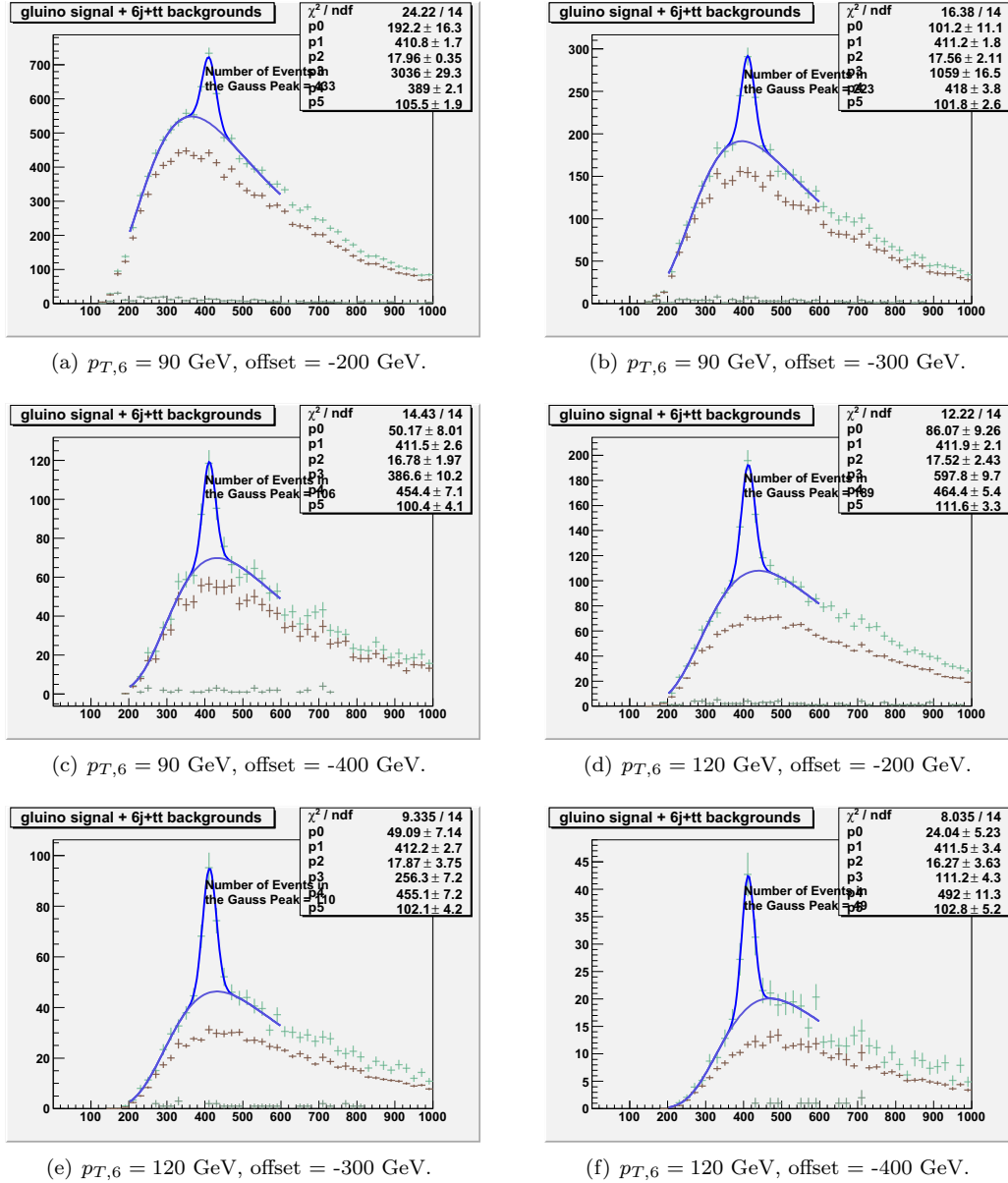


Figure 6.19: The invariant mass of the 16 best jet-triplets that satisfy (6.1), with an offset value given in each subfigure caption, for the signal with  $m_Q = 420$  GeV, the pure QCD background, and the  $t\bar{t}$  background. Included are all the trigger-level and event selection cuts (§6.3.1), a kinematic cut  $\sum_{j=1}^6 p_{T,j} \geq 700$  GeV, and a cut on  $p_{T,6}$  as detailed in each subfigure caption.  $\mathcal{L} = 1\text{fb}^{-1}$ .

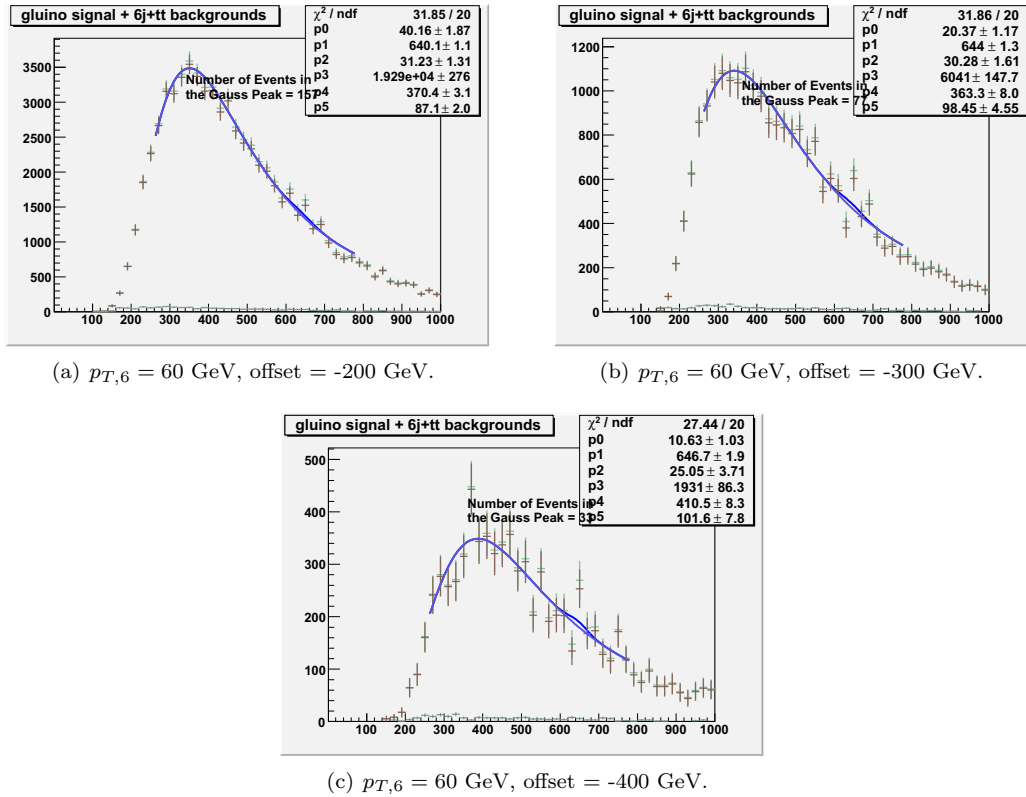


Figure 6.20: The invariant mass of the 16 best jet-triplets that satisfy (6.1), with an offset value given in each subfigure caption, for the signal with  $m_Q = 660$  GeV, the pure QCD background, and the  $t\bar{t}$  background. Included are all the trigger-level and event selection cuts (§6.3.1), a kinematic cut  $\sum_{j=1}^6 p_{T,j} \geq 1100$  GeV, and a cut on  $p_{T,6}$  as detailed in each subfigure caption.  $\mathcal{L} = 1\text{fb}^{-1}$ .

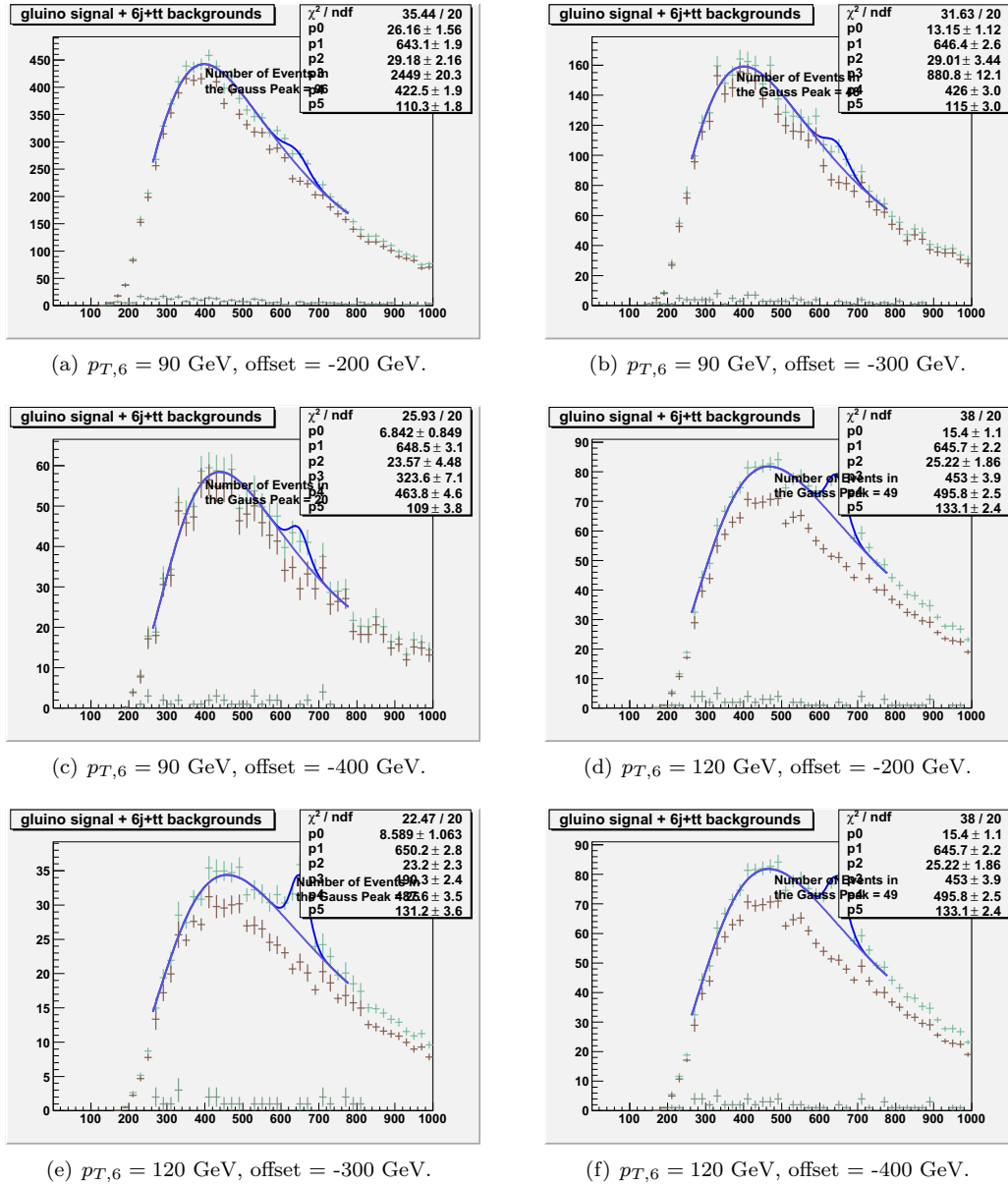


Figure 6.21: The invariant mass of the 16 best jet-triplets that satisfy (6.1), with an offset value given in each subfigure caption, for the signal with  $m_Q = 660$  GeV, the pure QCD background, and the  $t\bar{t}$  background. Included are all the trigger-level and event selection cuts (§6.3.1), a kinematic cut  $\sum_{j=1}^6 p_{T,j} \geq 1100$  GeV, and a cut on  $p_{T,6}$  as detailed in each subfigure caption.  $\mathcal{L} = 1\text{fb}^{-1}$ .

## References

- [1] E. Farhi and L. Susskind, “A Technicolored G.U.T,” *Phys. Rev.* **D20** (1979) 3404–3411.
- [2] W. J. Marciano, “Exotic New Quarks and Dynamical Symmetry Breaking,” *Phys. Rev.* **D21** (1980) 2425.
- [3] P. H. Frampton and S. L. Glashow, “Unifiable Chiral Color with Natural GIM Mechanism,” *Phys. Rev. Lett.* **58** (1987) 2168.
- [4] P. H. Frampton and S. L. Glashow, “Chiral Color: An Alternative to the Standard Model,” *Phys. Lett.* **B190** (1987) 157.
- [5] R. S. Chivukula, M. Golden, and E. H. Simmons, “Six jet signals of highly colored fermions,” *Phys. Lett.* **B257** (1991) 403–408.
- [6] R. S. Chivukula, M. Golden, and E. H. Simmons, “Multi - jet physics at hadron colliders,” *Nucl. Phys.* **B363** (1991) 83–96.
- [7] T. Sjostrand, S. Mrenna, and P. Skands, “PYTHIA 6.4 physics and manual,” *JHEP* **05** (2006) 026, [hep-ph/0603175](#).
- [8] F. Caravaglios, M. L. Mangano, M. Moretti, and R. Pittau, “A new approach to multi-jet calculations in hadron collisions,” *Nucl. Phys.* **B539** (1999) 215–232, [hep-ph/9807570](#).
- [9] M. L. Mangano, M. Moretti, and R. Pittau, “Multijet matrix elements and shower evolution in hadronic collisions: W b anti-b + (n)jets as a case study,” *Nucl. Phys.* **B632** (2002) 343–362, [hep-ph/0108069](#).
- [10] M. L. Mangano, M. Moretti, F. Piccinini, R. Pittau, and A. D. Polosa, “ALPGEN, a generator for hard multiparton processes in hadronic collisions,” *JHEP* **07** (2003) 001, [hep-ph/0206293](#).
- [11] **Higgs Working Group** Collaboration, M. S. Carena *et al.*, “Report of the Tevatron Higgs working group,” [hep-ph/0010338](#).
- [12] **CMS** Collaboration, G. L. Bayatian *et al.*, “CMS physics: Technical design report,”. CERN-LHCC-2006-001.
- [13] **CMS** Collaboration, G. L. Bayatian *et al.*, “CMS technical design report, volume II: Physics performance,” *J. Phys.* **G34** (2007) 995–1579.

## Vita

### ROUVEN ESSIG

#### Education

- 2002-2008 Rutgers University, New Brunswick, NJ  
Ph.D. in Physics and Astronomy
- 1998–2002 University of the Witwatersrand, South Africa  
BSc, BSc (Hons) in Physics, BSc (Hons) in Mathematics

#### Publications

1. **Rouven Essig**, “Direct Detection of Non-Chiral Dark Matter”, *Phys. Rev. D* **78**, 015004 (2008), arXiv:0710.1668 [hep-ph].
2. **Rouven Essig**, “Implications of the CERN LEP Higgs Bounds for the MSSM Stop Sector”, *Phys. Rev. D* **75**, 095005 (2007), arXiv:hep-ph/0702104.
3. **Rouven Essig**, Jean-François Fortin, “The Minimally Tuned Minimal Supersymmetric Standard Model”, *JHEP04(2008)073*, arXiv:0709.0980 [hep-ph].
4. **Rouven Essig**, Kuver Sinha, Gonzalo Torroba, “Meta-stable Dynamical Supersymmetry Breaking near Points of Enhanced Symmetry”, *JHEP09(2007)032*, arXiv:0707.0007 [hep-th].
5. **Rouven Essig**, Kuver Sinha, Gonzalo Torroba, “Enhanced symmetry points and metastable supersymmetry breaking along pseudo-runaway directions”, *To appear in the proceedings of SUSY07, Karlsruhe, Germany, 26 Jul - 1 Aug 2007*, arXiv:0710.4311 [hep-th].
6. Shan-Huei Chuang, **Rouven Essig**, Eva Halkiadakis, Amit Lath, Scott Thomas, “Extracting Hadronic Resonances using Jet Ensemble Correlations”, in preparation.